



# LUND UNIVERSITY

## Laser Remote Sensing for Environmental Monitoring

Guan, Zuguang

2010

[Link to publication](#)

*Citation for published version (APA):*

Guan, Z. (2010). *Laser Remote Sensing for Environmental Monitoring*. [Doctoral Thesis (compilation), Atomic Physics]. Division of Atomic Physics, Department of Physics, Faculty of Engineering, LTH, Lund University.

*Total number of authors:*

1

### General rights

Unless other specific re-use rights are stated the following general rights apply:

Copyright and moral rights for the publications made accessible in the public portal are retained by the authors and/or other copyright owners and it is a condition of accessing publications that users recognise and abide by the legal requirements associated with these rights.

- Users may download and print one copy of any publication from the public portal for the purpose of private study or research.
- You may not further distribute the material or use it for any profit-making activity or commercial gain
- You may freely distribute the URL identifying the publication in the public portal

Read more about Creative commons licenses: <https://creativecommons.org/licenses/>

### Take down policy

If you believe that this document breaches copyright please contact us providing details, and we will remove access to the work immediately and investigate your claim.

LUND UNIVERSITY

PO Box 117  
221 00 Lund  
+46 46-222 00 00

# LASER REMOTE SENSING FOR ENVIRONMENTAL MONITORING

Zuguang Guan

Doctoral Thesis  
2010



LUND UNIVERSITY



LASER REMOTE SENSING FOR ENVIRONMENTAL MONITORING

© 2010 Zuguang Guan

All rights reserved

Printed in Sweden by Media-Tryck, Lund, 2010

Division of Atomic Physics

Department of Physics

Faculty of Engineering, LTH

Lund University

P.O. Box 118

SE-221 00 Lund

Sweden

<http://www.atomic.physics.lu.se>

ISSN 0281-2762

Lund Reports on Atomic Physics, LRAP-421

ISBN: 978-91-7473-001-2

*To Grace, and my Parents*



# ABSTRACT

---

This thesis studies the techniques of laser remote sensing and their applications in environmental monitoring, as documented in several published papers.

The environment where the human being live is degrading with an accelerating speed. Quantitative monitoring characterizes the quality of the environment and offers possibilities to solve environmental problems. Laser remote sensing actively probes physical quantities with advantages of, e.g., large spatial coverage and little environmental influence, and hence becomes a very suitable tool for environmental analysis.

Light detection and ranging (LIDAR) measures the backscattered light from remote targets using a short-pulsed laser. Three varieties of LIDAR techniques, based on a vehicle-carried laboratory, have been developed in the work within the thesis. Elastic LIDAR measures the elastic backscattering from the atmospheric aerosols, and has been used to comparatively study their vertical distribution above a Swedish rural area and a Chinese Magacity. Differential absorption LIDAR (DIAL) is able to analyze the distribution of trace pollutants in the atmosphere. Vertical measurements of two serious pollutants, atomic mercury and nitrogen monoxide, have been performed in the same Chinese city. Further, DIAL is also proved to be valid for remote gas analysis in multiple-scattering media. Fluorescence LIDAR can recognize the molecules contained in a remote target, through analyzing the laser-induced fluorescence fingerprint. Such a technique is employed in this thesis mainly for ecological studies, particularly for insect and bird monitoring. Promising performances have been revealed through feasibility tests and field experiments.

Tunable diode laser absorption spectroscopy (TDLAS) attracts research attention for its compactness, cost-effectiveness, and high sensitivity. The signal-to-noise ratio of a TDLAS can be conventionally improved by applying modulation; while in the thesis, a different idea is proposed and demonstrated by operating the absorption spectroscopy on a zero light background. Proof-of-principle experiments are performed and considerations regarding real-world applications are discussed. GAs in Scattering Media

Absorption Spectroscopy (GASMAS) employs diode lasers for gas analysis as well, and wavelength modulation is frequently applied for sensitivity enhancement. Such an advanced TDLAS tool is applied in the thesis for food package monitoring.

Finally, fiber-optic remote sensing realizes the environmental monitoring by employing fiber-optic devices, e.g., fiber Bragg gratings (FBGs). Applications of these sensors are usually limited to temperature and stain monitoring. By using a methane catalyst which transfers the ambient methane into heat, FBG sensors become sensitive to methane. The sensitivity can be improved if the sensing FBG is interrogated by another reference grating having a matched spectrum. The multiplexing of such twin-grating-structure sensors is realized, and thus a distributed sensor network is possible to construct.

# POPULÄRVETENSKAPLIG SAMMANFATTNING

---

Sedan den industriella revolutionen har världen konfronterats med många miljöproblem, t.ex. luftföroreningar, surt regn, global uppvärmning, farligt avfall, ozonhålsproblematik, "smog" och vattenföroreningar. Det är viktigt att utveckla mätteknik för att objektivt kunna fastställa miljöförhållandena för att sedan kunna göra adekvata åtgärder. Miljön kan direkt karakteriseras, t.ex. genom att mäta koncentrationen av föroreningar i luft och vatten, eller också kan indirekta effekter påvisas, t.ex. på insekter och fåglar, som ofta är mera känsliga för miljöförändringar än människor. Andra frågor av allmänt intresse är säkerhet i livsmedelshantering, och hälsa på arbetsplatsen. Detta är även miljöfrågor i vidsträckt mening, och utan mätteknik och reglering kan här större hälsorisker föreligga än de härrörande från den yttre miljön. Alla ovannämnda aspekter innefattas inom det breda ämnesområdet miljömätteknik, som är ämnet för föreliggande avhandling.

Fjärranalys med laser erbjuder avancerade och kraftfulla tekniker för miljömätning. Dessa metoder har två karakteristiska drag: En artificiell strålningskälla, som oftast är en laser, utnyttjas. Vidare utförs mätningarna beröringsfritt eller på avstånd. En laser är en ljuskälla som har uppenbara fördelar - t.ex. kan ljuset sändas ut i extremt korta pulser med mycket hög toppeffekt. Laserljus kan göras mycket mera parallellt än vanligt ljus vilket gör att det kan sändas över långa avstånd. Möjligheten till mätning på avstånd gör att miljön kan studeras utan yttre påverkan.

Tre typer av laserbaserade fjärranalystekniker beskrivs i denna avhandling och exempel på olika intressanta tillämpningar ges. I likhet med radar- och sonar-teknik studeras i LIDAR (LIght De-tection And Ranging)-tekniken ekon efter transmission av en puls. Avståndet från ljuskällan till målet kan bestämmas genom att mäta flykttiden för de fotoner som reflekteras tillbaka till mot-tagaren. LIDAR-ekon kan även erhållas från partiklar fördelade i atmosfären, och aerosoler kan därför studeras effektivt. Om

lasern justeras till specifika våglängder som absorberas av t.ex.  $\text{SO}_2$  och  $\text{NO}_2$ , kommer återspridningen från partiklarna att dämpas. Genom att göra avståndsupplösta mätningar av detta slag kan fördelningen av dylika föroreningar i atmosfären kartläggas. Ett eko från ett fast strålmål kan också analyseras med avseende på fluorescens. Det är välkänt att sedlar och värdehandlingar, t.ex. pass, uppvisar synliga tecken och bilder vid belysning med ultraviolett ljus i ett mörklagt rum. Fluorescens teknik används allmänt för att upptäcka förfalskningar. Ett fluorescens-LIDAR-system, som sänder ut ultraviolettera pulser, kan registrera signaler från mål på avstånd upp till hundratals meter. Genom att analysera signalerna kan målet karakteriseras. Metoden har i denna avhandling använts för att bestämma art och kön för flygande insekter och fåglar.

Diodlasrar är kompakta och effektiva ljuskällor. En diodlasers aktiva del har en storlek på några hundra mikrometer och drivströmmen varierar från tiotals till hundratals milliampere. Våglängden hos en diodlaser kan varieras något genom att ändra laserns temperatur och drivström. Detta möjliggör gasanalys därigenom att gasers specifika absorptionsvåglängder kan uppsökas ledande till ljusdämpning. Om laserljuset sänds genom ett medium som sprider ljus, kommer strålens parallellitet att förstöras. Istället kommer ljuset att diffust lämna provet i alla riktningar. Mätningar under sådana omständigheter kallas GASMAS (GAS in Scattering Media Absorption Spectroscopy) och har i denna avhandling använts för mätningar på livsmedelsförpackningar.

Optiska fibrer för kommunikation har liknande tjocklek som mänskligt hår, och kan även användas i mättillämpningar. Man talar då om fibersensorer. En viktig fiberbaserad anordning är sk Bragg-gitter (FBG) som diskuteras i föreliggande avhandling. När vitt ljus som utbreder sig i en fiber möter en dylik anordning kommer en bestämd våglängdskomponent att reflekteras medan de övriga passerar igenom. Det reflekterade ljusets färg är känsligt för omgivningstemperatur och spänningar i fibern. Därigenom kan dylika anordningar användas som sensorer. Det finns katalysatorer som under inverkan av en omgivande metankoncentration utvecklar värme. En kombination av den dylik katalysator och en FBG-anordning för att mäta metankoncentrationer presenteras i denna avhandling. Dylika sensorer kan förbindas med optiska kommunikationsfibrer i ett nätverk, där mätvärden från olika platser kan sändas till en central för övervakning. Ett dylikt nätverk kan vara mycket lämpligt för att öka säkerheten i kolgruvor, som nu ofta drabbas av förödande explosioner.

# LIST OF PUBLICATIONS

---

This thesis is based on the following papers, which will be referred to by their Roman numerals in the text.

- I **Vertical lidar sounding of atomic mercury and nitric oxide in a major Chinese city**  
Z.G. Guan, P. Lundin, L. Mei, G. Somesfalean, S. Svanberg.  
*Applied Physics B* **Published online**, (August 2010).
- II **Gas analysis within remote porous targets using LIDAR multi-scatter techniques**  
Z.G. Guan, M. Lewander, R. Grönlund, H. Lundberg, S. Svanberg.  
*Applied Physics B* **93**, 657 - 663 (2008).
- III **Aerosol sounding at a rural Swedish area and in a major Chinese city - A comparative study with the Lund lidar system**  
P. Lundin, Z.G. Guan, L. Mei, G. Somesfalean, E. Swietlicki, S. Svanberg.  
*Proceedings of the 25th International Laser Radar Conference Volume I (S4P - 50)*, 663 - 666 (2010).
- IV **Insect monitoring with fluorescence lidar techniques: feasibility study**  
M. Brydegaard, Z.G. Guan, M. Wellenreuther, S. Svanberg.  
*Applied Optics* **48**, 5668 - 5677 (2009).
- V **Insect monitoring with fluorescence lidar techniques: field experiments**  
Z.G. Guan, M. Brydegaard, P. Lundin, M. Wellenreuther, A. Runemark, E.I. Svensson, S. Svanberg.  
*Applied Optics* **49**, (2010).



**VI Feasibility study: fluorescence lidar for remote bird classification**

M. Brydegaard, P. Lundin, Z.G. Guan, A. Runemark,  
S. Åkesson, S. Svanberg.  
*Applied Optics* **46**, 4531 - 4544 (2010).

**VII Quasi zero-background tunable diode laser absorption spectroscopy employing a balanced Michelson interferometer**

Z.G. Guan, M. Lewander, S. Svanberg.  
*Optics Express* **16**, 21714 - 21720 (2008).

**VIII Active feed-back regulation of a Michelson interferometer to achieve zero-background absorption measurements**

P. Lundin, Z.G. Guan, S. Svanberg.  
Submitted to *Applied Optics* (2010).

**IX Food monitoring based on diode laser gas spectroscopy**

M. Lewander, Z.G. Guan, L. Persson, A. Olsson,  
S. Svanberg.  
*Applied Physics B* **93**, 619 - 625 (2008).

**X Clinical system for non-invasive *in situ* monitoring of gases in the human paranasal sinuses**

M. Lewander, Z.G. Guan, K. Svanberg, S. Svanberg,  
T. Svensson.  
*Optics Express* **17**, 10849-10863 (2009).

**XI Assessment of photon migration in scattering media using heterodyning techniques with a frequency modulated diode laser**

Z.G. Guan, P. Lundin, S. Svanberg.  
*Optics Express* **17**, 16291 - 16299 (2009).

**XII An optical sensing system for the concentration of methane based on fiber Bragg gratings**

B. Zhou, G. Liu, Z.G. Guan, S. He.  
*Journal of Optoelectronics and Laser (China)* **19**, 378 - 380 (2008).

**XIII Coherence multiplexing of distributed sensors based  
on pairs of fiber Bragg gratings of low reflectivity**

Z.G. Guan, D. Chen, S. He.

*Journal of Lightwave Technology* **25**, 2143 - 2148 (2007).

Other publications not included in this thesis:

**XIV Agricultural pest monitoring with fluorescence LIDAR techniques: feasibility study**

L. Mei, Z.G. Guan, J. Lv, C. Löfstedt, H.J. Zhou,  
F.J. Chen, Z.R. Zhu, J.A. Cheng, S. Svanberg,  
G. Somesfalean.  
Manuscript in preparation (2010).

**XV Low coherent optical frequency domain reflectometry interrogates fiber Bragg grating sensors**

B. Zhou, C. Yan, Z.G. Guan, S. He.  
*Journal of Lighthwave Technology* in press, (2010).

**XVI Broad-band multi-spectral microscope for imaging transmission spectroscopy employing an array of light-emitting diodes**

M. Brydegaard, Z.G. Guan, S. Svanberg.  
*American Journal of Physics* **77**, 104 - 110 (2009).

**XVII Interrogation technique for a fiber Bragg grating sensing array based on a Sagnac interferometer and an acousto-optic modulator**

B. Zhou, Z.G. Guan, C. Yan, S. He.  
*Optics Letters* **33**, 2485 - 2487 (2008).

**XVIII Multiplexing of fiber Bragg grating pairs for sensing based on optical low coherence technology**

W. Liu, Z.G. Guan.  
*Microwave and Optical Technology Letters* **50**, 2437 - 2439 (2008).

**XIX Optical low-coherence reflectometry for a distributed sensor array of fiber Bragg gratings**

W. Liu, Z.G. Guan, G. Liu, C. Yan, S. He.  
*Sensors and Actuators A* **144**, 64 - 68 (2008).

**XX Coherence multiplexing system based on asymmetric Mach-Zehnder interferometer for Faraday sensors**

Z.G. Guan, S. He.  
*IEEE Photonics Technology Letters* **19**, 1907 - 1909 (2007).

- XXI **Quasi-distributed absorption sensing system based on a coherent multiplexing technique**  
 Z.G. Guan, B. Zhou, G. Liu, S. He.  
*IEEE Photonics Technology Letters* **19**, 792 - 194 (2007).
- XXII **Wavelength detection of coherence-multiplexed fiber-optic sensors based on long-period grating pairs**  
 Z.G. Guan, A.P. Zhang, R. Liao, S. He.  
*IEEE Sensors Journal* **7**, 36 - 37 (2007).
- XXIII **Multiplexing scheme for self-interfering long-period fiber grating using a low-coherence reflectometry**  
 M. Jiang, Z.G. Guan, S. He.  
*IEEE Sensors Journal* **7**, 1663 - 1667 (2007).
- XXIV **Low-coherence interrogation scheme for multiplexed sensors based on long-period-grating Mach-Zehnder interferometer**  
 Z.G. Guan, A.P. Zhang, M. Jiang, S. He.  
*IEEE Photonics Technology Letters* **15**, 832 - 834 (2006).
- XXV **Optical low-coherence reflectometry based on long-period grating Mach-Zehnder interferometers**  
 A.P. Zhang, Z.G. Guan, S. He.  
*Applied Optics* **45**, 5733 - 5739 (2006).
- XXVI **Optimization and fabrication of stitched long-period gratings for gain flattening of ultrawide-band EDFAs**  
 A.P. Zhang, X.W. Chen, J.H. Yan, Z.G. Guan, S.L. He, H.Y. Tam.  
*IEEE Photonics Technology Letters* **17**, 2559 - 2561 (2005).
- XXVII **Optimization of step-changed long-period gratings for gain-flattening of EDFAs**  
 A.P. Zhang, X.W. Chen, Z.G. Guan, S.L. He, H.Y. Tam, W.H. Chung.  
*IEEE Photonics Technology Letters* **17**, 121 - 123 (2005).



# ABBREVIATIONS

---

|        |  |
|--------|--|
| APS    | aerodynamic particle sizer                                     |
| BBO    | $\beta$ -barium borate   |
| CAP    | controlled atmosphere packaging                                |
| CCD    | charge-coupled device  |
| DAQ    | data acquisition   |
| DFB    | distributed feedback   |
| DIAL   | differential absorption LIDAR                                  |
| dWMS   | digital wavelength modulation spectroscopy                     |
| DOAS   | differential optical absorption spectroscopy                   |
| DOM    | dissolved organic matter                                       |
| EMI    | electromagnetic interference                                   |
| FBG    | fiber Bragg grating  |
| FBGP   | FBG pair   |
| FCW    | frequency modulated continuous wave                            |
| GASMAS | gas in scattering media absorption spectroscopy                |
| HITRAN | high-resolution transmission, molecular spectroscopic database |
| I-CCD  | intensified CCD  |
| IR     | infrared   |
| LED    | light-emitting diode   |
| LIDAR  | light detection and ranging                                    |
| LIF    | laser-induced fluorescence                                     |
| LPG    | long-period fiber grating                                      |
| MAP    | modified atmosphere packaging                                  |
| MIR    | middle infrared  |
| Nd:YAG | neodymium-doped yttrium aluminium garnet                       |
| OMA    | optical multi-channel analyzer                                 |
| OPD    | optical pathlength difference                                  |

|       |   |
|-------|---|
| OPO   | optical parametric oscillator               |
| OSA   | optical spectrum analyzer                   |
| PCI   | peripheral component interconnect           |
| PID   | proportional-integral-derivative            |
| PM2.5 | particulate matter below 2.5 micrometer     |
| PM10  | particulate matter below 10 micrometer      |
| PMT   | photomultiplier tube                        |
| PZT   | piezo-electric transducer                   |
| QCL   | quantum cascade laser                       |
| RAM   | residual amplitude modulation               |
| SLED  | superluminescent LED                        |
| SMPS  | scanning mobility particle sizer            |
| SNR   | signal-to-noise ratio                       |
| TCSPC | time-correlated single photon counting      |
| TDLAS | tunable diode laser absorption spectroscopy |
| TDM   | time division multiplexing                  |
| TEOM  | tapered-element oscillating microbalance    |
| TTL   | transistor-transistor logic                 |
| UV    | ultra violet                                |
| VCSEL | vertical-cavity surface-emitting laser      |
| WDM   | wavelength division multiplexing            |
| WMS   | wavelength modulation spectroscopy          |

# CONTENTS

---

|          |   |           |
|----------|---|-----------|
| <b>1</b> | <b>Introduction</b>                                       | <b>1</b>  |
| 1.1      | Organization of the Ph.D. program . . . . .               | 1         |
| 1.2      | Structure of the thesis . . . . .                         | 2         |
| <b>2</b> | <b>Environmental Remote Sensing</b>                       | <b>5</b>  |
| 2.1      | Environmental monitoring . . . . .                        | 5         |
| 2.1.1    | Atmospheric monitoring . . . . .                          | 6         |
| 2.1.2    | Ecological monitoring . . . . .                           | 8         |
| 2.1.3    | Food and occupational monitoring . . . . .                | 10        |
| 2.2      | Laser remote sensing . . . . .                            | 11        |
| 2.2.1    | LIDAR . . . . .   | 12        |
| 2.2.2    | TDLAS . . . . .   | 14        |
| 2.2.3    | Fiber-optic sensor . . . . .                              | 15        |
| <b>3</b> | <b>Light Detection and Ranging</b>                        | <b>17</b> |
| 3.1      | Elastic LIDAR . . . . .                                   | 18        |
| 3.1.1    | LIDAR equation and analytical solution . . . . .          | 18        |
| 3.1.2    | LIDAR system . . . . .                                    | 19        |
| 3.1.3    | Measurements and data analysis . . . . .                  | 20        |
| 3.2      | Differential absorption LIDAR (DIAL) . . . . .            | 23        |
| 3.2.1    | DIAL equation and solution . . . . .                      | 23        |
| 3.2.2    | DIAL system . . . . .                                     | 25        |
| 3.2.3    | Pollutant measurements in the atmosphere . . . . .        | 27        |
| 3.2.4    | Gas analysis in multi-scattering media . . . . .          | 33        |
| 3.3      | Fluorescence LIDAR . . . . .                              | 36        |
| 3.3.1    | Laser-induced fluorescence (LIF) . . . . .                | 36        |
| 3.3.2    | Remote LIF . . . . .                                      | 37        |
| 3.3.3    | Ecological studies . . . . .                              | 39        |
| <b>4</b> | <b>Tunable Diode Laser Absorption Spectroscopy</b>        | <b>47</b> |
| 4.1      | Background knowledge . . . . .                            | 48        |
| 4.1.1    | Gas absorption spectrum . . . . .                         | 48        |
| 4.1.2    | Diode laser . . . . .                                     | 49        |
| 4.1.3    | Sensitivity . . . . .                                     | 50        |
| 4.2      | Zero-background TDLAS . . . . .                           | 50        |
| 4.2.1    | Working principle . . . . .                               | 50        |
| 4.2.2    | Real-world application considerations . . . . .           | 52        |
| 4.3      | Gas in scattering media absorption spectroscopy . . . . . | 54        |
| 4.3.1    | Principle and technique . . . . .                         | 54        |
| 4.3.2    | Food monitoring . . . . .                                 | 57        |
| 4.3.3    | Path-length assessment . . . . .                          | 60        |
| <b>5</b> | <b>Fiber-optic Sensors</b>                                | <b>65</b> |
| 5.1      | Fiber Bragg Grating (FBG) . . . . .                       | 66        |
| 5.1.1    | Basics of FBG . . . . .                                   | 66        |



|          |   |           |
|----------|---|-----------|
| 5.1.2    | FBG sensors . . . . .                     | 67        |
| 5.1.3    | Interrogation schemes . . . . .           | 68        |
| 5.2      | FBG methane sensor . . . . .              | 69        |
| 5.2.1    | Methane transducer . . . . .              | 70        |
| 5.2.2    | Reference-FBG interrogation . . . . .     | 70        |
| 5.3      | Multiplexing schemes . . . . .            | 72        |
| 5.3.1    | Low-coherence multiplexing . . . . .      | 73        |
| 5.3.2    | Multiplexing of methane sensors . . . . . | 74        |
| <b>6</b> | <b>Future Work</b>                        | <b>77</b> |
|          | <b>Comments on the Papers</b>             | <b>79</b> |
|          | <b>Acknowledgements</b>                   | <b>85</b> |
|          | <b>References</b>                         | <b>87</b> |

---

Papers

---

|      |   |     |
|------|---|-----|
| I    | Vertical lidar sounding of atomic mercury and nitric oxide in a major Chinese city                                      | 99  |
| II   | Gas analysis within remote porous targets using LIDAR multi-scatter techniques  | 107 |
| III  | Aerosol sounding at a rural Swedish area and in a major Chinese city - A comparative study with the Lund lidar system   | 117 |
| IV   | Insect monitoring with fluorescence lidar techniques: feasibility study   | 123 |
| V    | Insect monitoring with fluorescence lidar techniques: field experiments   | 135 |
| VI   | Feasibility study: fluorescence lidar for remote bird classification  | 147 |
| VII  | Quasi zero-background tunable diode laser absorption spectroscopy employing a balanced Michelson interferometer         | 163 |
| VIII | Active feed-back regulation of a Michelson interferometer to achieve zero-background absorption measurements            | 173 |
| IX   | Food monitoring based on diode laser gas spectroscopy   | 181 |
| X    | Clinical system for non-invasive <i>in situ</i> monitoring of gases in the human paranasal sinuses                      | 191 |
| XI   | Assessment of photon migration in scattering media using heterodyning techniques with a frequency modulated diode laser | 209 |
| XII  | An optical sensing system for the concentration of methane based on fiber Bragg gratings                                | 221 |
| XIII | Coherence multiplexing of distributed sensors based on pairs of fiber Bragg gratings of low reflectivity                | 229 |



# INTRODUCTION

---

## 1.1 Organization of the Ph.D. program

At the Atomic Physics Division of Lund University, laser techniques have been developed for environmental monitoring since 1980 under the leadership of Prof. Sune Svanberg (the main supervisor of this thesis). Being attracted by the academic standing of the Lund group in the field of laser spectroscopy, the author came from China to Sweden as a visiting student in 2007. Afterwards, he became a Ph.D. candidate in the group through a regular application and selection. Most research work contributing to this thesis was performed between 2007 and 2010, during which the Ph.D. position was supported by the Swedish Research Council (VR). In addition, a SIDA/VR grant supported the Sino-Swedish collaboration, and important equipment was funded by the Kunt and Alice Wallenberg Foundation.

Clearly, the thesis studies a multidisciplinary subject, which must be based on good collaborations among researchers from different fields. The project of aerosol LIDAR sounding at Vavihill (Sweden) was collaborated with the Aerosol Group (Prof. Erik Swietlicki) at the Nuclear Physics Division of Lund University, in the spring of 2009; while a comparative study was carried out at Hangzhou (China) using the same LIDAR system, through a Sino-Swedish project with Zhejiang University in China. The author was at the Photonics Group (headed by Prof. Sailing He, who is also a professor at Royal Institution of Technology, Sweden) at Zhejiang before coming to Lund, and Dr. Gabriel Somesfalean (a co-supervisor of the thesis), who is a Lund graduate, is now working at the same Chinese group as an associate professor. The main supervisor, Prof. Sune Svanberg, is also a honorary professor at the Zhejiang University. In the project, totally 12 tons of Lund mobile LIDAR facility was deployed to China for 6 months (October 2009 to April 2010) of scientific activities. Besides the

aerosol sounding, two atmospheric pollutants, atomic mercury and nitrogen monoxide, were also vertically measured, using differential absorption LIDAR techniques. The demonstration of agriculture pest monitoring using fluorescence LIDAR techniques was also performed when the mobile system was in China, based on collaborations with biologists at Zhejiang University and Nanjing Agricultural University (Nanjing, China), through the relationship of the Ecology Department (Prof. Christer Löfstedt) of Lund University. Other biological monitoring discussed in the thesis, including two weeks of field experiments of damselfly monitoring at Veberöd, and field experiments of bird migration monitoring at Kullaberg, were carried out in Sweden, together with biologists (led by Profs Susanne Åkesson and Erik Svensson) from the Biology Department of Lund University.

The GAS in Scattering Media Absorption Spectroscopy (GASMAS) technique discussed in Chapter 4 is utilized for food monitoring. This part of research work directly promoted a collaboration with Tetra Pak, one of the world's largest suppliers of food packaging systems. An industrial project regarding juice package monitoring is now on-going at the Atomic Physics Division. Compared with GASMAS, the zero-background tunable diode laser absorption spectroscopy is at an early stage, and only proof-of-principle experiments were performed, with a clear purpose to improve the measurement sensitivity in real applications.

The chapter of fiber-optic sensors is partly adopted from the research work that the author performed at Zhejiang University of China, for the reason that the topic of the remote methane measurement fits well into the thesis, and by considering the firm collaboration between the Swedish and Chinese research groups.

## 1.2 Structure of the thesis

Principally, each single chapter through the thesis can be read independently. However, for those new to the field, Chapter 2, which generally overviews environmental monitoring techniques and applications, is strongly recommended to be read first before going deeper into Chapters 3 to 5, which detail three types of active optical remote sensing techniques and their specific applications in environmental monitoring.

In Chapter 3, three varieties of LIDAR techniques, i.e., elastic LIDAR, differential absorption LIDAR (DIAL) and fluorescence LIDAR, are introduced in Section 3.1, Section 3.2, and Section 3.3, respectively. This chapter is based on Papers I to VI. In Paper III, elastic LIDAR is employed for aerosol remote sensing, while in Papers I and II, DIAL techniques are used for atmospheric pollutant measurements, and remote gas analysis in multiple scattering media, respectively. The applications of the fluorescence LIDAR

for remote biological target analysis are reported in Papers **IV** to **VI**.

In Chapter 4, another important laser remote sensing technique, tunable diode laser absorption spectroscopy (TDLAS), is discussed. After reviewing some basic knowledge about the TDLAS in Section 4.1, the novel zero-background TDLAS and the advanced gas analyzing tool for scattering media, GASMAS, are introduced in Section 4.2 and Section 4.3, respectively. The techniques regarding the zero-background TDLAS are presented in Papers **VII** and **VIII**, while the applications of the GASMAS technique in food and clinical monitoring are reported in Papers **IX** and **X**. Paper **XI** proposes a novel technique to define pathlengths in the presence of multiple scattering, which is of great importance for GASMAS measurements.

The introduction of the third type of remote sensing techniques, fiber-optic sensors, is given in Chapter 5. Firstly, in Section 5.1, the basics and techniques related to an important sensing device, the fiber Bragg grating (FBG), are generally reviewed. Then, combining with Paper **XII**, Section 5.2 describes the technical details of a novel fiber-optic methane sensor, based on a pair of FBGs and a methane catalyst, which can transfer the ambient methane concentration into a temperature increase. The multiplexing possibility of such methane sensors is also considered in Section 5.3, by using the coherence multiplexing technique presented in Paper **XIII**.

Finally, future research possibilities are discussed in Chapter 6.



# ENVIRONMENTAL REMOTE SENSING

---

Environmental problems have different appearances, such as air pollution, acidification of water and soil, global warming etc. Quantitative measurements of atmospheric aerosols and trace gases form the basis for estimating such problems. Differently, ecological research reveals the environmental changes through, e.g., studying the movements and migration patterns of insects and birds. Unlike the natural or ecological environment, the social environment is surrounding human activities. For the sake of the health and safety of people, regular and strict surveillance should apply on critical public issues such as food quality and occupational safety. Techniques developed for studying the above-mentioned aspects are generally treated as *environmental monitoring* in this thesis.

Laser remote sensing is a powerful technique for environmental monitoring, since large spatial scales can be covered and very little environmental perturbation is induced. As examples, the techniques and applications of laser radar, diode laser spectroscopy and fiber-optic sensors are briefly introduced in this chapter.

## 2.1 Environmental monitoring

Environmental issues are modern problems ranging from local water/air pollution to global climate change, which are of great concern to human life and health. To control and improve environmental conditions, the quantitative monitoring is the first step that characterizes the quality of the environment and offers possibilities of further strategies.

As one most important natural environment on planet Earth, the atmosphere is a complex, dynamic gaseous system that is essential to support life. Compared with other natural resources like water and soil, air is more fragile to pollutants. One main atmo-



spheric pollutant, aerosols, defined as fine solid particles or liquid droplets suspended in gases, is abundantly produced from combustion or industries, and affects the climate and human health strongly. Many other pollutants ( $\text{CO}_2$ ,  $\text{SO}_2$ ,  $\text{NO}_x$ ,  $\text{C}_x\text{H}_y$ , Hg, etc.), existing as trace gases in the atmosphere, can also cause serious harm or discomfort to humans and can damage the natural environment. Monitoring the distribution and concentration of aerosols and trace gases in the atmosphere is critical for climate analysis and environmental protection.

Ecology studies the interactions between the organisms and their environment. Many organisms are highly sensitive to the environmental/climate change, and can thus be used as bio-markers by ecologists. The movement and migration of insects and birds are especially interesting for climate and epidemiological studies, and are specially studied in this thesis.

Compared with the polluted natural environment and abnormal ecosystem, unexpected accidents in human activities are more direct and dangerous to the health and safety of human being. For instance, food safety and occupational health are two hot topics which are discussed annually at, e.g., the Global Food Safety Conference [1] and the Occupational Health and Safety Conference [2]. As believed, techniques developed for assessment of the food quality and occupational environment are as important as (if not more important than) other environmental monitoring activities.

## 2.1.1 Atmospheric monitoring

### Aerosols

Aerosols are defined as solid or liquid particles suspended in mixtures of gases. For instance, smokes and fogs are two types of aerosols with solid and liquid cores, respectively. The sources of the aerosol particles are complicated, but can be generally separated into naturally generated and anthropogenic. Natural sources include volcano, sea-spray, erosion, etc. In an industrialized world, combustion is a prominent source of aerosols. The size of the aerosol particles ranges from several tens of nm (called the nuclear mode) to several tens of  $\mu\text{m}$  (called the coarse particle mode). The notation PM10 is used to describe particles of 10  $\mu\text{m}$  or less and PM2.5 represents particles less than 2.5  $\mu\text{m}$  in aerodynamic diameter [3].

Broadly speaking, aerosol particles tend to scatter energy back to space and cool the planet down. This tends to offset the warming associated with greenhouse gases in the atmosphere, which act like a blanket, trapping longwave radiation and warming the planet. Most aerosol particles have the opposite effect since they reflect some of the incoming solar radiation. Some types of particles, however, can absorb solar radiation and contribute to warm-

ing of the local atmosphere. An example of light absorbing particles is carbon soot generated from combustion processes or forest fires. Since aerosols have much shorter lifetimes and more varied distributions than greenhouse gases, the net effect on global climate is hard to predict. Besides the environmental effects, fine aerosols, mainly from the combustion, can be directly harmful to human health. For instance, PM<sub>2.5</sub> accumulates in human alveolar through breath, and has been shown to result in a number of diseases including ‘silicosis’ and ‘black lung’ [4].

Many point-monitoring techniques are available for aerosol measurements, including cascade impactors [5], tapered-element oscillating microbalance (TEOM) [6], aerodynamic particle sizer (APS) [7], scanning mobility particle sizer (SMPS) [8] etc. SMPS is especially interesting, since the concentration of aerosol particles can be measured in a spectroscopic fashion, i.e., aerosols can be separated according their sizes and the particle numbers can be counted. For remote and range-resolved measurement of aerosols, laser radar (or LIDAR) is the only technique. More details on LIDAR techniques used for aerosol analysis will be discussed in Section 3.1 and Paper III.

### Trace gases

Trace gases are those with concentration less than 1 % by volume in the atmosphere. Except nitrogen (78 %) and oxygen (21 %), all other gases in the natural atmosphere are trace gases.

Many trace gases are anthropogenic pollutants, and can be extremely harmful to human health and the natural environment. For instance, sulfur dioxide (SO<sub>2</sub>) is naturally produced by volcanoes, while considerably more from combustion of coal and petroleum containing sulfur compounds. Nitrogen oxides (NO<sub>x</sub>) are mainly from local traffic and have become a typical Megacity problem. Both gases ultimately contribute to acidification problems at washout, and the water and soil are then further polluted.

Mercury is a toxic pollutant, mostly in atomic form (gas phase) in the atmosphere. Mercury pollution has been extensively studied over the world, since the extremely toxic compound methyl mercury can be formed over time, and serious brain damage in humans can be caused. International conferences devoted to this topic are arranged every third year (see, e.g. [9]). The sources of such pollution are mainly coal combustion, waste incineration, chlor-alkali industries and mining activities. For instance, concentrations of 1  $\mu\text{g}/\text{m}^3$  can be found in the direct vicinity of mercury mines and ore smelters. More generally, mercury exists in the low atmospheric layer (since it is a type of heavy atom) with very low concentration. The background level above the Atlantic is around 2  $\text{ng}/\text{m}^3$ , and the urban concentrations can be 10 times higher or more.



**Figure 2.1.** An aerosol source, adapted from the Internet.

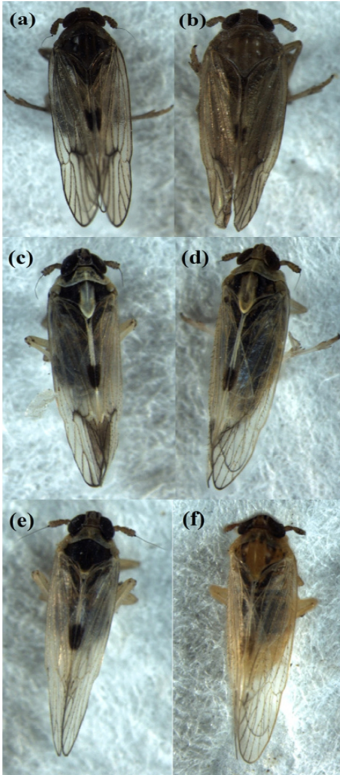


**Figure 2.2.** Agricultural pests: *Nilaparvata lugens*, male (a) and female (b); *Sogatella furcifera*, male (c) and female (d); *Laodelphax striatellus*, male (e) and female (f), adapted from [19].

Other, non-toxic, gases, such as carbon dioxide ( $\text{CO}_2$ ) and methane ( $\text{CH}_4$ ), are produced mainly by plants, microorganisms and from natural geophysical sources [10]. They keep the earth warm through the green-house effect, by absorbing radiation within the thermal infrared range. However, too much emission of  $\text{CO}_2$  from anthropogenic activities induces global warming problems, which were greatly discussed at the Copenhagen Conference in 2009. Reducing the emission of carbon for the future of mankind has become a common understanding of people. Compared with  $\text{CO}_2$ , methane has a even higher global warming potential by a factor of 72 (calculated over a period of 20 years) or 25 (for a time period of 100 years) [11].

Optical spectroscopic techniques have been developed for measuring trace gases. Point monitoring devices operating on different principles are available and widely used by environmental authorities. Gas samples are first sucked into a cell before being analyzed. Taking  $\text{SO}_2$  as an example, the measurement is based on UV-induced fluorescence [12].  $\text{NO}_x$  can be measured by detecting the photons from the chemiluminescence process with ozone ( $\text{O}_3$ ) [13].  $\text{CH}_4$ ,  $\text{CO}_2$  and Hg can be accurately quantified with high-resolution absorption spectroscopies [14, 15]. Optical remote sensing instrumentation has advantages, since wider areas are covered and sampling issues are avoided. Among such optical techniques, differential optical absorption spectroscopy (DOAS) [16], gas correlation techniques [17, 18], tunable diode laser absorption spectroscopy (TDLAS) and differential absorption LIDAR (DIAL) can be mentioned. The latter two techniques are specially studied in Chapter 3 and Chapter 4 of the thesis.

## 2.1.2 Ecological monitoring

### Insect monitoring

Monitoring insects and studying their movements and migration are of great importance in biological research and environmental monitoring. For instance, there exist groups of agricultural pests world-widely, including in Southeast Asia. They are mostly moths with sizes from  $1 \times 1$  to  $5 \times 5 \text{ mm}^2$  (see Figure 2.2). Between the spring and summer every year, some species migrate from the Indo-China peninsula, through the Guangdong and Guangxi provinces of China, and even penetrate into the Yangtze area of China. During the migrating, with local amount density as high as 1 million/ $\text{m}^2$ , they cause serious economical damage by feeding on rice crops. It is clearly important to understand their migrating strategy for controlling the agricultural loss. Developed techniques include conventional mark-and-recapture methods and microwave radar recently applied for automatic measurements. The feasibility

ity of fluorescence LIDAR to study such insects will be discussed in the thesis and the potential of the technique will be shown.

Damselflies constitute another type of insects, which are studied in the thesis. Damselfly larvae live in the water and have been used as biomarkers [20], since they are highly sensitive to oxygen concentration and water pollution. Damselfly adults are sensitive to ambient temperature, and the tendency of global warming can be known from the fact that many species have undergone a northwards shift in their distribution [21]. Moreover, dispersal studies of insects are critical to understand the role of gene dispersal between populations over wide spatial scales [22]. As for migration monitoring of agricultural pests, the traditional method in the past decades was limited to mark individuals with different fluorescence dyes and then collecting individuals from neighboring populations [23]. Very recently, pioneering work using elastic LIDAR to study honey bees for land mine detection has been reported in [24, 25]. In this thesis, the capability of fluorescence LIDAR on monitoring damselflies in the natural environment will be further revealed through a feasibility study and two weeks of field experiments. More details can be found in Papers IV and V.

## Bird migration

Many bird species migrate long distance seasonally for fitting the environment. Generally, migratory birds fly towards north in the spring and breed there in the summer, while in the autumn they fly back to warm regions in the south for spending the winter. Some birds perform really long migration flights across vast inhospitable areas, such as the Sahara desert and the Mediterranean Sea (e.g. [26, 27]). Studies of migrating birds are interesting not only to biologists, for identifying the species, ages and sexes, and how they select time of migration, flight direction relative to winds and topography as well as altitude of migration, but also to epidemiologists seeking to understand the spread of diseases carried by birds, including avian flu and malaria [27, 28].

A large proportion of migratory songbirds fly at night and at high altitudes (>500 m) between these remote destinations (e.g. [29]). In this way, the bird flight will be relatively less disturbed by turbulent wind conditions [30], and the risk of being taken by predators can be reduced (e.g. [31]). For this reason, the traditional visual observation is almost impossible for studying the migration status of these birds. Instead, tracking radars, infrared cameras, and their combination [29] enable observers to get a good estimate of the spatial distribution and numbers of birds passing. However, these remote methods are limited to not being able to detect the species of the free-flying birds. Compared with tracking radar, fluorescence LIDAR techniques can achieve additional infor-



**Figure 2.3.** A male *Calopteryx Splendens* damselfly, adapted from Paper IV.



**Figure 2.4.** Migrating birds, adapted from the Internet.



**Figure 2.5.** *Packaged food, adapted from the Internet.*

mation from the fluorescence signature of the remote targets, and has been successfully demonstrated by us to classify bird species.

### 2.1.3 Food and occupational monitoring

#### Food safety

Food safety is an important public issue regarding food handling, preservation and packaging. From long times, people have known that physical packages can protect food from shock, vibration, compression and temperature, and stop the penetration of external oxygen, water vapor and dust. Later, people further realized that the natural presence of oxygen in food products fastens the chemical breakdown and microbial spoilage of the food products. Oxidative processes are responsible, and it is therefore important to control the concentration of oxygen in food packaging. Traditional packaging methods are now largely replaced by newer techniques, e.g., modified atmosphere packaging (MAP) and controlled atmosphere packaging (CAP), which replace the natural oxygen content inside the package with other gases such as carbon dioxide ( $\text{CO}_2$ ) or nitrogen ( $\text{N}_2$ ). Carbon dioxide is an effective replacement as an anti-microbiological gas, while nitrogen behaves like an inert gas in food packaging.

Assessment of packed food to ensure its quality and suitability for consumption is of great importance for such a public issue. In order to maintain package integrity and reduce the waste of samples, the technique for assessment is preferred to be non-intrusive, which is particularly important in the MAP community. One possible way is to analyze the gas concentration in the sealed package using optical methods. TDLAS is a spectroscopic technique conventionally developed for gas monitoring in free space; while headspace monitoring in wine bottles has also been demonstrated [32]. In this thesis, however, the technique is employed to analyze the gases in food packages, combining the knowledge of light scattering in turbid media. Details can be found in Section 4.3 and Paper IX.

#### Occupational safety

Occupational health and safety are still of great concern in many developing countries. In China, for instance, frequent coal-mine accidents kill thousands of workers per year. The direct reason for 95% of coal-mine accidents is the high concentration of methane. The risk of mine blast become very high if the concentration of methane is above 5% in the local air.

A distributed sensor system that can monitoring the concentration of methane at multiple locations would be effective to avoid most mine accidents. Considering the electromagnetic interference (EMI) and the safety reason in the working environment under

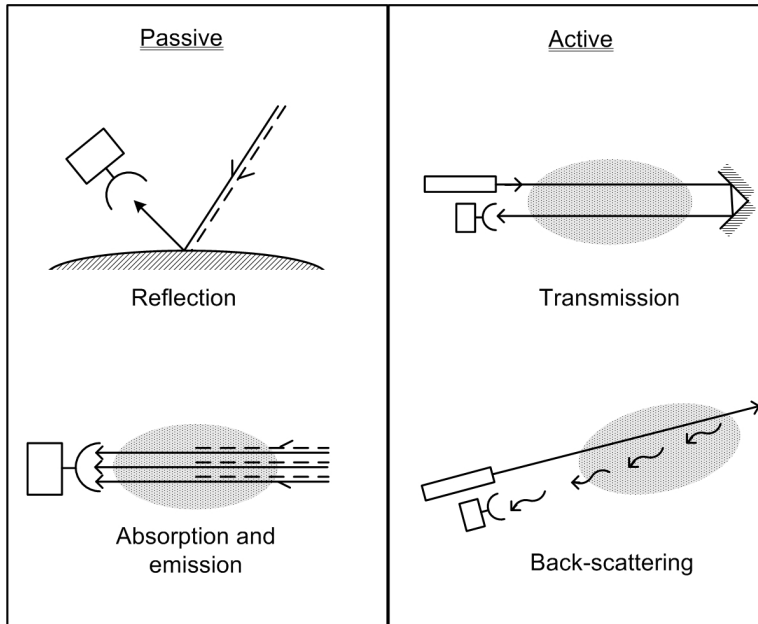


**Figure 2.6.** Passive and active optical remote sensing techniques [33].

ground, fiber-optic sensors have advantages over electronic sensors. Meanwhile, system cost is also an important issue that will be considered especially by Third World countries. Fiber-optic sensors are possible to be connected into a sensor network, which share a common light source and detection system, and in this case, the cost of each sensor is reduced.

## 2.2 Laser remote sensing

Remote sensing is small- or large-scale acquisition of information, without physical or intimate contact with the measured object. Optical remote sensing can be divided into active and passive techniques, according to whether an artificial light source is used, or not. Figure 2.6 illustrates different passive and active remote-sensing techniques. In passive modes, measurements are carried out using natural background radiation, such as sun-light and sky-light. In active modes, a laser is usually employed as the light source due to its obvious advantages like high intensity and single frequency properties. Related techniques are thus called laser remote sensing.

Laser remote sensing is extremely interesting for environmental monitoring. For atmospheric measurements in free air, laser re-

remote sensing has many advantages over point monitoring devices, since wider areas are covered and sampling technique issues are avoided. In ecological studies, laser remote sensing is much more effective and with less environmental influence compared with traditional ‘mark-and-collect’ methods used for studies of migrating insects and birds. Inherent properties (like non-contact and intrusiveness) make such techniques also very suitable for assessment of food packages. In the application of methane monitoring in, e.g., coal mines, fiber-optic sensors, as another type of important remote sensing technique, can be connected into a geometrically flexible sensor network, and signals can be collected and transmitted by a single communication fiber to a central office hundreds kilometers away.

Three types of laser (active optical) remote sensing techniques are discussed in this thesis. They are light detection and ranging (LIDAR), tunable diode laser absorption spectroscopy (TDLAS), and fiber-optic sensors. Brief descriptions of them are given in the following.

### 2.2.1 LIDAR

LIDAR, an acronym for light detection and ranging, is a radar-fashion technique using a pulsed laser instead of microwave radiation. As illustrated in right lower part of Figure 2.6, the reflection/back-scattering from targets is detected by a photosensitive device and recorded in the time domain. The ranges of targets can therefore be determined according to  $R = ct/2$ , where  $c$  is the light speed, and  $t$  is the time delay at which the detector receives the reflection/back-scattering signal. One main application of LIDAR technique is ranging, which is clearly of great military interest. However, laser range finder also has many civil applications. For instance, using such a technique, it is possible to map out the geometry of complex volumes like grottoes, underground storage rooms and mines [33].

Back-scattering from distributed particles and molecules in the atmosphere can also be captured by the sensitive detector. The LIDAR curve in the time domain can therefore be used to analyze the scattering coefficient along the laser beam. With scattering coefficients measured at many wavelengths and according to Mie scattering and Rayleigh scattering theories, the densities and sizes of the floating particles (aerosols) are possible to be determined [34]. LIDAR is a unique technique for atmospheric analysis. At low atmospheric layers, not only the aerosol distribution, but also wind speed/direction can be measured if the Doppler shift, due to the motion of the aerosols, is analyzed by using coherent technique or narrow-band-filter techniques [35].

At middle and upper atmospheric layers, due to the low density of the aerosols and molecules, resonance fluorescence LIDAR tech-

niques are employed instead for wind/temperature analysis [36]. Since Na, K, Li, Ca and Fe ions are present in the mesopause region, the resonance fluorescence spectra of them can be scanned out by a narrow-linewidth laser at certain wavelengths. The broadening of the spectra reveals the temperature information while the spectral shift reveals the wind information. All above-mentioned atmospheric measurements are remote and range-resolved due to the inherent property of LIDAR.

At short distance (several hundreds meters), the fluorescence LIDAR techniques have been proved to be able to analyze the components of remote targets [37]. With a UV laser as an excitation source, the fluorescence signature at longer wavelengths is the finger print that can recognize the molecules contained in the target. Applications of such a technique range from analyzing water samples, recognizing vegetation, diagnosing historical monuments [38, 39], to remotely classifying migrating insects and birds [Papers **IV-VI**].

Another type of advanced LIDAR technique, named differential absorption LIDAR, combines the LIDAR technique and absorption spectroscopic techniques [40]. By swiftly switching the laser wavelength ‘on’ and ‘off’ an absorption dip of one specific molecule/atom, the range-resolved concentration can be deduced from the difference between the ‘on’ and ‘off’ LIDAR curve. Such a technique can map out the concentration of trace gases in the atmosphere.

However, since the wavelength range that a DIAL can cover is usually limited, such a technique is conventionally not valid for pollutants (e.g. biological aerosol) with broadband spectral properties. Instead, a technique called femtosecond white-light LIDAR [41] was developed with unique advantages originating from the employment of a powerful mobile terawatt laser system – Teramobile [42]; a broadband of spectrum can be analyzed in measurements. Laser pulses of several tens of femtoseconds in pulse width and of several terawatts in peak power are transmitted into the atmosphere. Before that the group velocity dispersion is compensated by the chirped pulse amplification technique. Based on the high-intensity-induced nonlinear effects, actually, the dynamical equilibrium between self-focusing due to the Kerr effect and defocusing effects due to the ionization of air, the laser beam can propagate a very long distance in the atmosphere. During the propagation, multiphoton ionization and plasma production existing in the medium induce white-light backscattering along the laser beam, and thus an extremely broad spectral range can be covered. This new technique has been demonstrated for atmospheric remote sensing [43].



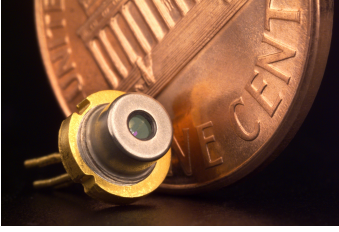


**Figure 2.7.** A laser diode next to a one-cent coin, adapted from the Internet.

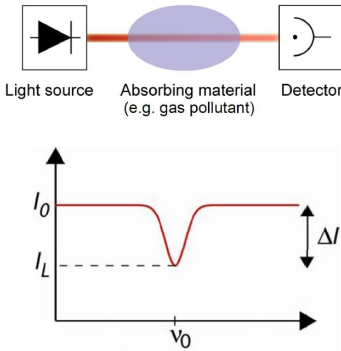


**Figure 2.8.** The working principle of TDLAS.

### 2.2.2 TDLAS

Diode lasers, due to their compactness and cost-effective advantages, have become important candidate light sources for absorption spectroscopy. The wavelength of a diode laser can be simply tuned by changing the temperature or driving current. The output light is usually collimated by a single piece of lens to free space or coupled into optical fibers. Electronic cooling is enough to keep the chip working at room temperature. Easy operation makes tunable diode laser absorption spectroscopy (TDLAS) very suitable for remote sensing applications. With the rapid development of semiconductor materials, the wavelengths of diode lasers are now (non-continually) selectable from the ultra-violet (UV) to the middle infrared (MIR) region. The absorption lines of most trace gases on Earth can be found in this broad range, and thus TDLAS is widely used for free-gas analysis [44–47].

Many techniques have been studied and developed to improve the sensitivity of TDLASs [47]. Since the absorption signal increases according to the product of the gas concentration and the optical path length, one direct way is to extend the effective optical path length, e.g. using a White cell. Another commonly used method is to modulate the light source at high frequency, so that the noise level largely reduces at the detector. Modulation methods include intensity modulation, wavelength modulation and frequency modulation.

Except employing long path-length and modulation, a high sensitivity of absorption spectroscopy can be realized by measuring the absorption signal on a zero background, which keeps the noise at the detector at a very low level. Examples include laser-induced fluorescence spectroscopy [48, 49], photoacoustic spectroscopy [50], and polarization spectroscopy [51]. Based on a balanced Michelson interferometer working in a destructive interference fashion [Paper VII], the TDLAS can realize background-free measurements also. This technique is discussed in Section 4.2.

A new type of TDLAS technique is developed by the Lund research group, to analyze the gas components and concentration in scattering media such as food. It is called gas in scattering media absorption spectroscopy (GASMAS) [52–60]. On a background of broadband absorption of solid media, the narrow absorption lines of gases are still possible to be recognized, by using wavelength modulation techniques. Importantly, multiple scattering naturally extends the effective propagating length of the light, and improves the sensitivity for free. Such a technique is discussed in the thesis mainly for food package monitoring, and is also explored for medical applications.

### **2.2.3 Fiber-optic sensor**

One main advantage of fiber-optic sensing systems is that the signal can be transferred by a single communication fiber from a remote location to the central office, between which the distance might be over 100 km. Together with other advantages like immunity to EMI, geometric versatility, etc., fiber-optic sensors are very suitable for environmental monitoring, e.g., in coal mines. Especially many sensors are possible to be connected by one fiber to form a sensor array. With an effective multiplexing scheme, these sensors can share one light source and the signals can be distinguished by one detection system, and in this way, the system cost are shared by and dramatically reduced for each sensor.

One of the most important candidates for fiber-optic sensors is the fiber Bragg grating (FBG), which is a periodic index modulation in fiber core [61, 62]. A narrow band (ca. 0.1 nm) of light that matches the phase condition will be selected and reflected by the grating, while the rest of the light will pass through. Since the reflective wavelength is sensitive to environmental temperature and strain, FBG sensors are widely used for structure monitoring. The reflection spectrum of each FBG can be separated from those of others, if its grating period is designed to be different. Wavelength domain multiplexing is hence a typical multiplexing scheme for FBG sensing arrays.

Using some specific catalysts, the concentration information of  $\text{CH}_4$  in the air can be transferred into temperature information and hence measured by FBG sensors [63] [Paper **XII**]. Combining other temperature and strain FBG sensors, multiple physical parameters at multiple locations are possible to be monitored using one distributed FBG sensing system. Such a system is expected to reduce the risk of accidents in Chinese coal mines.



---

# LIGHT DETECTION AND RANGING

---

Light detection and ranging (LIDAR) is a remote sensing technique that can provide range-resolved information, commonly by employing a laser as the light source. LIDAR techniques have been developed since the 1960s with most applications for atmospheric monitoring. Aerosols, water vapor, clouds, wind, trace constituents, and temperature are typical parameters for understanding complex mechanisms governing the atmosphere [34, 64]. Meanwhile, LIDAR has also been proved to be effective for hydrological and vegetation monitoring [37]. This powerful technique can provide four-dimensional (space and time) maps of the quantities during the measurements and thus is critical for environmental monitoring.

Different measurements are carried out by different LIDAR varieties, which can be separated by their working principles and functions. Three important ones are introduced in details in this chapter. The atmospheric aerosols and particles can be measured by analyzing the elastic back-scattering light, that is with the same frequency as that of the emitted light, and in accordance, such LIDAR technique/equipment is called elastic LIDAR, with its techniques and applications discussed in Section 3.1. For trace gas monitoring, the LIDAR curves are obtained at two wavelengths with different absorption coefficients due to the gas, and their ratio contains the information of the gas concentration. Such LIDAR techniques are therefore named differential absorption LIDAR (DIAL), and are discussed in Section 3.2. Laser-induced fluorescence (LIF) is the finger print for material recognition, since it includes molecular structure information. The remote/LIDAR version of LIF technique is named fluorescence LIDAR and is very helpful in ecological research, through remotely recognizing vegetation, monitoring flying insects and birds, etc. This part of the description is given in Section 3.3

### 3.1 Elastic LIDAR

#### 3.1.1 LIDAR equation and analytical solution

Elastic LIDAR, as the name indicates, measures the elastic backscattering, which is defined as ‘scattering with no apparent wavelength change and the sum of Mie scattering and Rayleigh scattering’ [34]. The elastic LIDAR systems are popular for atmospheric aerosol analysis, since the range-resolved scattering coefficient can be deduced from the LIDAR equation, Equation (3.1), where single scattering is assumed.

$$P(R) = K\beta(R)\exp\left(-2\int_0^R\alpha(r)dr\right)/R^2 \quad (3.1)$$

Here,  $P(R)$  is the backscattering signal power,  $K$  the system constant,  $\beta$  the backscattering coefficient, and  $\alpha$  the extinction coefficient.  $R$  and  $r$  indicate the LIDAR range.

By assuming a simple relation between  $\beta$  and  $\alpha$ , the scattering coefficient can be obtained from Equation (3.1). Two kinds of retrieval methods can be mentioned for giving analytical solution. One is called the Klett method [65], which ignores the scattering from the air molecules, and is only suitable in case of dense aerosol concentrations. The other one, called the Fernald method [66], considers the effects from both the aerosols and the molecules, and thus can give a more accurate solution, especially in clear weather conditions. In the Fernald method, the backscattering coefficient and the extinction coefficient are expressed as the sum of two components, i.e.,

$$\begin{aligned}\beta &= \beta_a + \beta_m \\ \alpha &= \alpha_a + \alpha_m\end{aligned} \quad (3.2)$$

Subscripts  $a$  and  $m$  indicate ‘aerosol’ and ‘molecule’, respectively. The relationships between the extinction and backscattering coefficients are simply assumed as,

$$\begin{aligned}\alpha_a(R) &= S_a(R)\beta_a(R) \\ \alpha_m(R) &= S_m\beta_m(R)\end{aligned} \quad (3.3)$$

where  $S_{a(m)}$  is called the extinction-to-backscattering ratio.  $S_a$  depends on the properties of aerosols and is a function of  $R$ , while  $S_m$  is a constant,  $8\pi/3$ , according to, e.g., [66].  $\alpha_m(R)$  and  $\beta_m(R)$  can be calculated through the atmospheric pressure model, which indicates the exponential decrease with altitude [67].

With the above assumptions, the solution of  $\alpha_a$  from Equation (3.1) can be expressed as,

$$\alpha_a(R) = -\frac{S_a(R)}{S_m} \alpha_m(R) + \frac{X(R)}{X(R_f)} \cdot S_a(R) \exp[I(R)] \times \left( \frac{\alpha_a(R_f)}{S_a(R_f)} + \frac{\alpha_m(R_f)}{S_m} \right) + J(R) \quad (3.4)$$

where

$$I(R) = 2 \int_R^{R_f} \left( S_a(r)/S_m - 1 \right) \alpha_m(r) dr$$

$$J(R) = 2 \int_R^{R_f} S_a(r) X(r) \exp[I(r)] dr \quad (3.5)$$

In Equation (3.4) and Equation (3.5),  $X(R) = P(R)R^2$ , where the range compensation factor  $R^2$  is applied for the raw curve. One can notice that, to get the solution of  $\alpha_a(R)$  in the full LIDAR range, at least one value ( $\alpha_a(R_f)$ ) at a reference distance ( $R_f$ ) needs to be known. In real operations, this reference can be from a point-monitoring taken close to the ground, or the stable, close-to-zero value at a high altitude, where the presence of aerosols can be ignored.

Since the scattering performance of aerosols is described by Rayleigh and Mie theories, which are laser-wavelength and particle-size dependent, the size distribution of the aerosols can be retrieved if scattering coefficients at many wavelengths are available. Principally, such a retrieval can become more accurate if more wavelengths are employed, while in real applications, four- or even two- wavelength measurements are sufficient by assuming aerosol size distributions with different models [34].

### 3.1.2 LIDAR system

The LIDAR campaigns carried out during this thesis work are mainly based on a well-developed vehicle-based mobile LIDAR system (see Figure 3.1) [68], which is importantly modified for different measurements. The system has two emission sources. One is a Nd:YAG laser with output at 1064 nm, and at 532 nm and 355 nm for the second and third harmonic frequencies. The other one is an optical parametric oscillator (OPO) pumped by the third harmonic frequency of another Nd:YAG laser. In elastic LIDAR measurements, the 355-nm radiation of the first Nd:YAG (SpectraPhysics, GCR-290) is used for eye-safety reasons. The laser is running in Q-switched mode with a pulse width of 8 ns, pulse energy of about 100 mJ and repetition rate of 20 Hz. The laser beam is expanded by a Keplerian telescope into a 4 cm diameter beam, and the divergence can be controlled to be less than 2 mrad. The expanded laser beam is transmitted vertically to the atmosphere without any

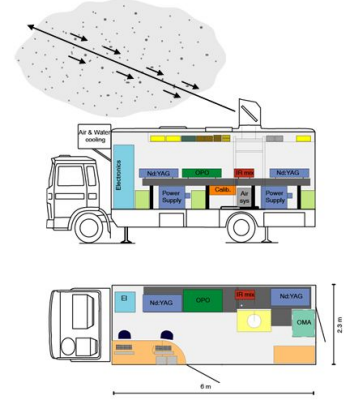


**Figure 3.1.** The mobile LIDAR system, adapted from [68].

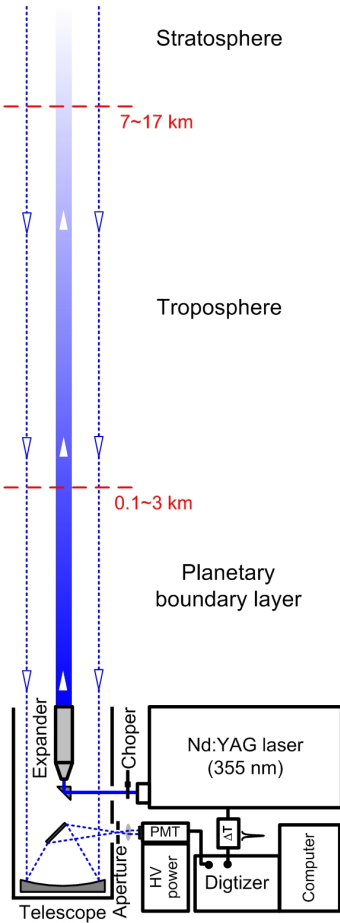


**Figure 3.2.** *The elastic LIDAR system.*

further optics; the dome containing a folding mirror for scanning was removed in vertical LIDAR measurements. The backscattered light is collected by a co-axial Newtonian telescope and focused onto a photomultiplier tube (PMT) (EMI 9816QA). At the focus point, an iris aperture is used to control the telescope field-of-view matching the divergence of the laser beam. The schematic diagram of the LIDAR system for elastic measurements is shown in Figure 3.2.

The signal from the PMT is recorded by a transient digitizer (Licel) with a sampling rate of 20 MS/s, which limits the range resolution to 7.5 m, while the recording length limits the maximum distance to 10 km, which vertically covers most troposphere and can even reach the stratosphere, depending on the monitoring location and weather conditions. The start of the recording is triggered by a TTL signal from the Nd:YAG laser before each pulse, with a tunable delay applied. The recorded LIDAR curves are read out by a program developed using LabView graphic language, averaged within a certain (controllable) period of time, and saved as one measurement onto the harddisk. The same program controls a mechanical chopper to block the laser beam after every certain numbers of measurements and records the background of the sun- and sky-radiation, which will be subtracted from the measured raw curves.

The mobile LIDAR system is enclosed in a laboratory enclosure on a Volvo truck (Volvo, F6 Turbo). The environmental temperature and humidity are well controlled through air-conditioning systems. A motor generator (KraftProdukt AB, P45P1) with a power of 40 kW is arranged as an 2-ton trailer, which extremely enhances the mobile ability of the LIDAR system when running in rural areas.

### 3.1.3 Measurements and data analysis

#### Raw data and retrieval

In the spring of 2009, the mobile LIDAR system was parked at the Vavihill background air monitoring station located in the south of Sweden, and vertical aerosol sounding were performed. The site is far from industry and heavy traffic, thus the amount of locally produced anthropogenic particles is expected to be low. For calibration, the back-scattering and extinction coefficients of the aerosols close to the ground are measured by a nephelometer. During the four days (April 6th–9th, 2009) of the measurement campaign, there was no extended time period of perfectly clear weather; only shorter clear periods occurred.

Figure 3.3 illustrates a flow chart used to retrieve the extinction coefficient from the raw LIDAR signal. The system constant  $K$  in Equation (3.1) is found to be invalid at close range, where the

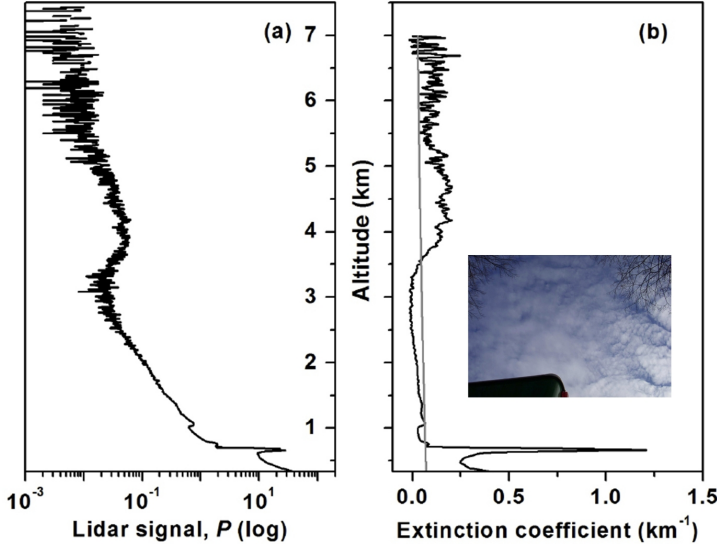


**Figure 3.5.** The raw LIDAR signal (a) and the retrieved extinction coefficient (b) on 16:02, April 8, 2009. The inset shows a photography taken by a vertically-looking camera at the site.

telescope collecting efficiency becomes low. The function of  $K$  corresponding to range  $R$ , can be calibrated from a horizontal measurement of aerosols, which is regarded to be symmetrically distributed. The calibrated curve for our LIDAR system is shown in Figure 3.4(a). For ranges larger than 700 m, a constant value is used while in the ‘blind’ area, a linear decay is assumed. Such a curve is calibrated from the raw LIDAR signal before further steps of calculations.

The extinction coefficient  $\alpha_m$ , backscattering coefficient  $\beta_m$  and their ratio  $S_m$  corresponding to the part of air molecules in the atmosphere are available from literature such as [66, 67, 69]. Figure 3.4(b) shows that  $\alpha_m$  exponentially decreases with the altitude, due to the decay of the atmospheric pressure [67]. These parameters are required when using Equation (3.4) to calculate the extinction coefficient,  $\alpha_a$ , corresponding to the aerosol part. From the nephelometer in the background-monitoring station, the extinction-backscattering ratio,  $S_a \approx 8$ , of close-ground aerosols is measured, and used as a constant value in the calculation.

In the calculation, the reference distance is set at a far distance (7 km), which is with higher stability compared with a setting at a close range [65]. The extinction coefficient at the reference distance is adjusted until the calculated value,  $\alpha_a(0)$ , at the short range gets close to the value ( $\alpha_N$ ) measured by the nephelometer on the ground.

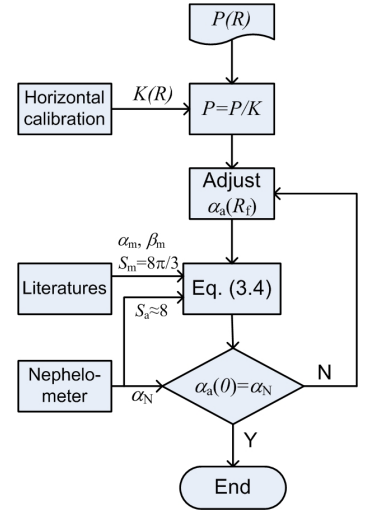


**Figure 3.3.** A schematic flow chart for retrieving the extinction coefficient.

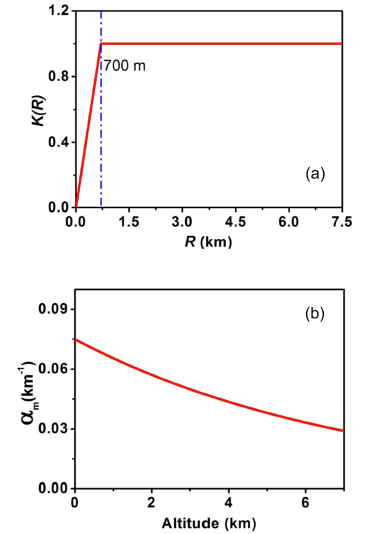


**Figure 3.4.** (a) Systemic coefficient  $K$  shows the blind area of the telescope; (b) Extinction coefficient of air molecules in vertical atmosphere.





**Figure 3.6.** The vehicle-based LIDAR was parked at Vavihill, Sweden (top) and the Zijingang Campus, China (bottom) [Paper III].

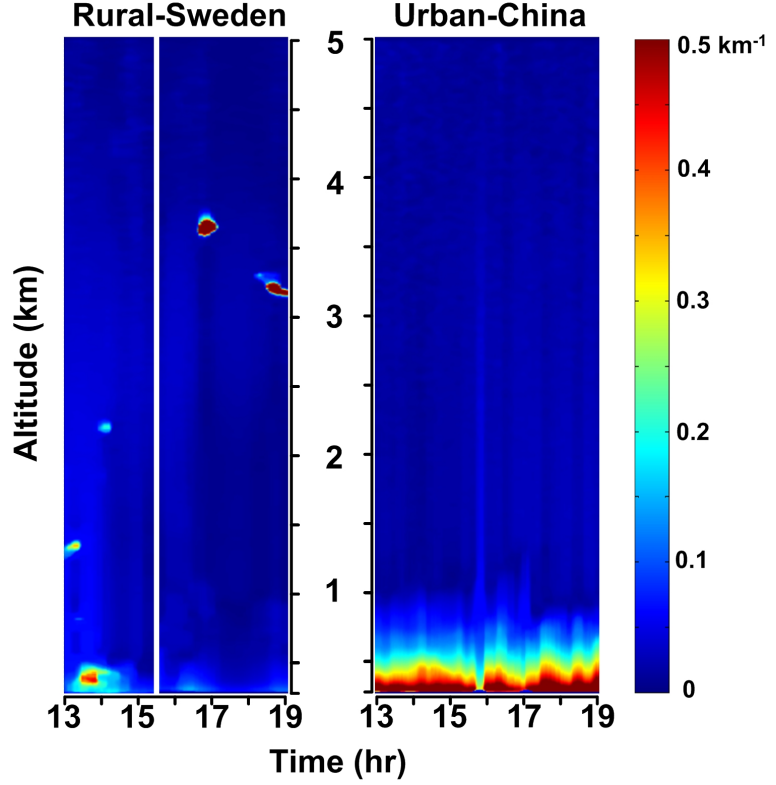


**Figure 3.7.** The aerosol extinction coefficient calculated for the time period between 13:00 and 19:00 in urban China and in rural Sweden.

One example of using the above retrieval algorithm is shown in Figure 3.5. (a) shows a raw LIDAR curve measured on 16:02, April 8, 2009. This curve is taken for demonstration since rich atmospheric structures can be seen at different ranges. The extinction coefficient of aerosols (dark curve) is retrieved from the raw data and shown in (b), together with the coefficient of air molecules (gray curve) for comparison. A thin layer of dense cloud can be seen at an altitude around several hundred meters. Higher up, a layer of haze from 3 to 5 km is observed by the LIDAR.

### Comparative study

In the autumn of 2009, the LIDAR system was deployed to China for environmental monitoring, as part of a Sino-Swedish collaboration project. The vehicle was parked in Zijingang Campus of Zhejiang University (Hangzhou) and the vertical measurements were carried out in days from 9th to 22th, of November, 2009.

Hangzhou is a major city in China, with population around 9 million, abundant traffic, and some industry emission. The weather stayed clear during the measurements

Since exactly the same LIDAR system was employed in the measurements of vertical distribution of atmospheric aerosols at two sites with completely different situations, the results from the measurements are possible to compare and the anthropogenic pollution can thus be revealed. The data in the same time period, 13:00 to 19:00, in the afternoon, on 8th of April at Vavihill Sweden, and on 22nd of November in China, are analyzed and presented in Figure 3.7. Generally, the same retrieval method in Figure 3.3 is applied, but for the Chinese data, the loop for optimization is neglected since no nephelometer data are available close to the ground. Instead, an average extinction coefficient at 5 km ( $\alpha_a(5 \text{ km}) = 0.002 \text{ km}^{-1}$ ) obtained from Vavihill measurements is used as a reference value for Chinese measurements, based on the assumption that the aerosol density is very low, and the stable scattering from air molecules dominates in high atmosphere.

From Figure 3.7, it can be obviously seen that the aerosol density (extinction coefficient) is much higher in the atmosphere above an urban environment, especially at the close range. It reveals that the aerosol pollution is of local origin.

## 3.2 Differential absorption LIDAR (DIAL)

### 3.2.1 DIAL equation and solution

In order to measure the concentration of trace pollutants in the atmosphere, the resonance absorption due to the specific molecules is utilized in the differential absorption LIDAR (DIAL) technique, similar as in long-path-absorption methods like DOAS. However, DIAL does not require a retroreflector, since distributed aerosols/molecules are reflectors everywhere. The integrated absorption from the light source to any of such reflectors are measured along the LIDAR path, and the concentration information can thus be deduced by a differential algorithm. Detailed theoretical analysis is discussed as follows.

Modified from Equation (3.1) that describes elastic LIDAR, the DIAL equation is expressed as

$$P(\lambda, R) = K(\lambda, R)\beta(\lambda, R) \times \exp\left\{-2 \int_0^R [\alpha(\lambda, r) + \sigma(\lambda)N(r)]dr\right\}/R^2. \quad (3.6)$$

Compared with Equation (3.1), one can find the addition of the absorption term for the operating wavelength ( $\lambda$ ) in Equation (3.6). Except the scattering-induced attenuation  $\alpha(\lambda, r)$ ,  $\sigma(\lambda)N(r)$  is

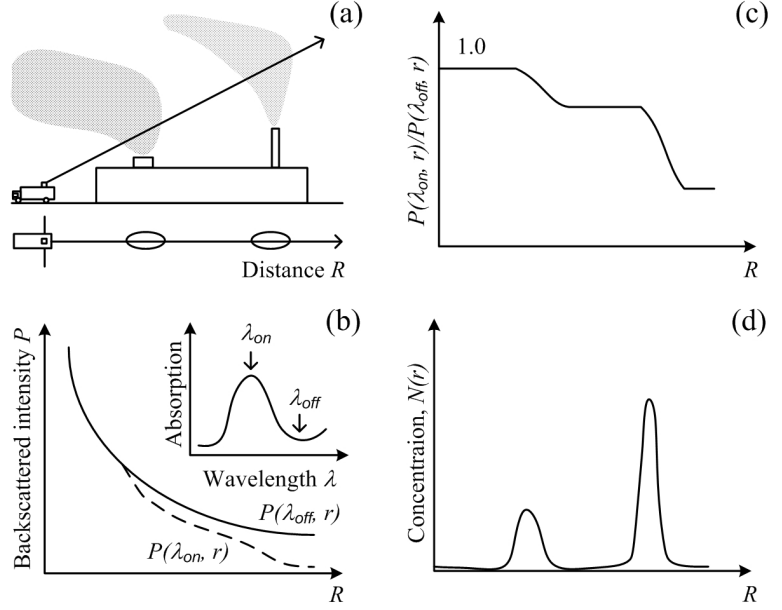


**Figure 3.8.** Illustration of DIAL principle [70].

added as an extra extinction term, due to the resonance absorption. Here,  $\sigma(\lambda)$  indicates the absorption cross-section and  $N(r)$  is the concentration of the trace pollutant.

Using  $\lambda_{on}$  and  $\lambda_{off}$ , indicating the wavelengths on and off the resonance absorption peak, the ratio between the on- and off-LIDAR curves is calculated as,

$$\frac{P(\lambda_{on}, R)}{P(\lambda_{off}, R)} = \frac{K(\lambda_{on}, R)}{K(\lambda_{off}, R)} \cdot \frac{\beta(\lambda_{on}, R)}{\beta(\lambda_{off}, R)} \times \exp\left\{-2 \int_0^R [(\alpha(\lambda_{on}, r) - \alpha(\lambda_{off}, r)) + (\sigma(\lambda_{on}) - \sigma(\lambda_{off}))N(r)]dr\right\}. \quad (3.7)$$

$K(\lambda, R)$  is a systemic parameter that is related to the laser energy, effective receiver area, detector sensitivity, etc., but not sensitive to the wavelength switching, i.e.,  $K(\lambda_{on}, R) \simeq K(\lambda_{off}, R)$ . It is worthwhile mentioning that  $K(\lambda, R)$  is canceled even if it is an unknown function of  $R$ , while in Equation (3.1) for elastic LIDAR,  $K(R)$  is preferred to be a constant, or a least a well known function, so that the LIDAR curve can be calibrated for aerosol analysis. Using this advantage, the sensitivity of a DIAL system can be modulated in time/spatial domain, in order to suppress the strong

signal from short range while enhancing the weak signal from far distance. Similarly, since the absorption lines of trace gases are relatively sharp compared with the broad spectral features of scattering events, the effect of the wavelength switching on the scattering coefficient can be ignored. This is especially true if the switching is fast enough so that the aerosol distribution can be treated as static. With  $\beta(\lambda_{on}, R) \simeq \beta(\lambda_{off}, R)$ ,  $\alpha(\lambda_{on}, R) \simeq \alpha(\lambda_{off}, R)$ , and  $K(\lambda_{on}, R) \simeq K(\lambda_{off}, R)$ , Equation (3.7) can be simplified as,

$$\frac{P(\lambda_{on}, R)}{P(\lambda_{off}, R)} = \exp\left\{-2 \int_0^R [\Delta\sigma \cdot N(r)] dr\right\}, \quad (3.8)$$

where  $\Delta\sigma = \sigma(\lambda_{on}) - \sigma(\lambda_{off})$  is the differential absorption cross-section. With the pollutant absorption spectrum well known, the range-resolved concentration information can be deduced using a differential algorithm,

$$N(R) = -\frac{1}{2\Delta\sigma} \frac{d}{dR} \ln \frac{P(\lambda_{on}, R)}{P(\lambda_{off}, R)}. \quad (3.9)$$

The working principle of the DIAL technique described above is illustrated in Figure 3.8.

### 3.2.2 DIAL system

As shown in Figure 3.9, the DIAL system shares the same transmitting- and receiving optics with the elastic LIDAR system. The light source, however, is an optical parametric oscillator (OPO; SpectraPhysics, MOPO-730), which is pumped by the third harmonic frequency of a single-mode Nd:YAG laser. The OPO system is of two-stage design. The first stage, called master oscillator, controls the linewidth of the oscillation to be as narrow as  $0.2 \text{ cm}^{-1}$ , through constructing an external cavity containing a Type-I BBO crystal, and a grating for wavelength selection. The seeding light from the Master Oscillator is then amplified by the second stage, called Power Oscillator. The emission can be tuned from 400 nm to 700 nm for the signal emission, and from 720 nm to 2000 nm for the idler emission, and extended to 200 nm through frequency doubling. The wavelength tuning mechanics were originally stepper-motor driven but modified later by installing piezoelectric transducer for speed enhancement. The speed of switching between on- and off-wavelength matches the repetition rate of the laser system, 20 Hz. For wavelength and linewidth monitoring, part of the signal emission is measured by a high-resolution wavemeter (Burleigh, WA-4500). The scanning optics, which is protected by a dome, can be hoisted up to the roof top, and scan the laser beam 360 degree horizontally and from -5 to 75 degree vertically. A three-dimension distribution of trace pollutants are thus possible to be mapped out. Vertical (90 degree) measurements

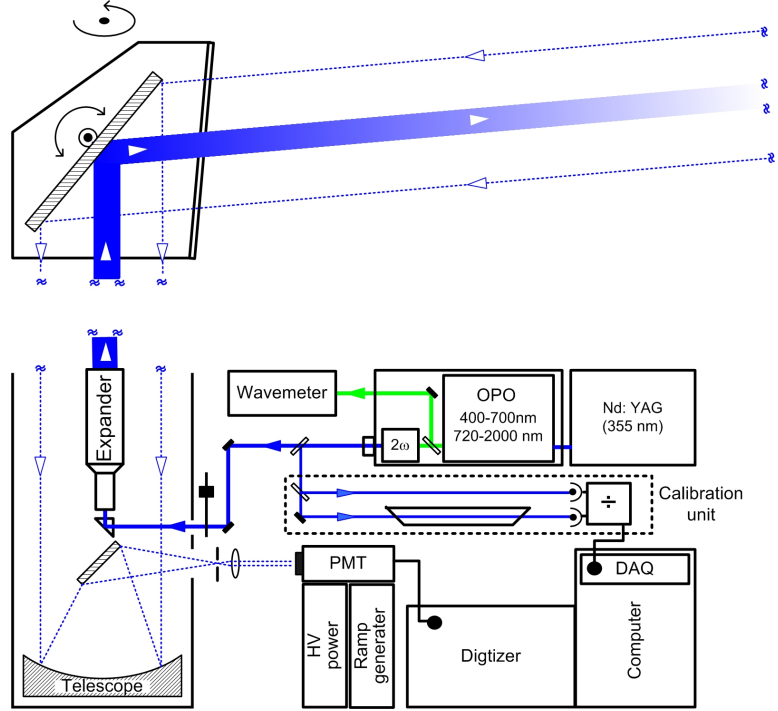


**Figure 3.9.** *The schematic diagram of the DIAL system.*

are also possible by removing the dome as done in Section 3.1 for vertical aerosol analysis. The same PMT tube for elastic LIDAR is used to detect the back-scattered signal. Except a constant negative high voltage that is suitably divided and applied on different dynodes of the PMT, a ramped voltage, from 0 to -25 volt, is added extra on certain dynodes, in order to induce a ramped modulation on the sensitivity of the PMT and suppress the strong close-range signal. The amplitude, slope, and start time of the ramping are tunable according to realities of measurements. The transient digitizer reads out the signal and transfers it into the hard disk of the computer, which controls the chopper for background measurements after saving 8 ‘on’ and 8 ‘off’ LIDAR curves, as one cycle. Many cycles of on- and off-curves are averaged after removing the background components, in order to get better signal-to-noise ratio (SNR) in their ratio curve. Meanwhile, 4 % of the emission from the OPO is coupled into a calibration unit. The absorption of a gas cell with well-known concentration is measured in a differential way. The results are recorded also by the computer through a data acquisition (DAQ) system, and was used later to calibrate the differential cross-section ( $\Delta\sigma$  in Equation (3.9)). The trigger

| Isotope | Abundance | Frequency ( $\text{cm}^{-1}$ ) | $F_g$ | $F_e$ |
|---------|-----------|--------------------------------|-------|-------|
| 198     | 10.10%    | 39412.4603                     | 0     | 1     |
| 199A    | 17.0%     | 39411.9463                     | 1/2   | 1/2   |
| 199B    |           | 39412.6847                     | 1/2   | 3/2   |
| 200     | 23.1%     | 39412.3000                     | 0     | 1     |
| 201a    | 13.2%     | 39411.9713                     | 3/2   | 5/2   |
| 201b    |           | 39412.4377                     | 3/2   | 3/2   |
| 201c    |           | 39412.6895                     | 3/2   | 1/2   |
| 202     | 29.65%    | 39412.1233                     | 0     | 1     |
| 204     | 6.85%     | 39411.9495                     | 0     | 1     |

Table 3.1: Isotopic abundance and line positions for atomic mercury isotopes used in theoretical absorption calculations. Total angular momentum quantum numbers for the ground ( $F_g$ ) and excited ( $F_e$ ) states are also given [72].

signal from the Nd:YAG laser is distributed to slave equipments through two multiple-channel delay generators (Stanford Research System), which, however, are not presented in Figure 3.9.

### 3.2.3 Pollutant measurements in the atmosphere

As mentioned, the Lund University mobile LIDAR system was deployed to China for environmental monitoring. With the help of the DIAL system described above, the vertical distribution of the atomic mercury and nitrogen monoxide in the atmosphere above a major city was measured, in November 2009. Technical details and experimental results are given in the following text.

#### Atomic mercury

##### *Absorption spectrum, calibration, and $O_2$ interference*

One strong atomic transition of mercury (Hg) is at about 254 nm. The line consists of several isotopic and hyperfine structure components, as mapped out at high spectral resolution, e.g. in [71]. Isotopic abundances and line positions are listed in Table 3.1. According to the theory described in e.g., [72], the absorption spectrum is calculated and shown in Figure 3.10. The spectrum of each isotopic component is also given for comparison. In the calculation, the environmental pressure and temperature are set to be 1 standard atmosphere and 296 K, respectively. One can see that these isotopic components merge into a broadened structure with a half-width of about 0.005 nm.

Compared with such a narrow absorption bandwidth, the linewidth of the light source (OPO; regularly  $0.2 \text{ cm}^{-1}$ ) is not ignorable. The broadening effect is simulated by convoluting the

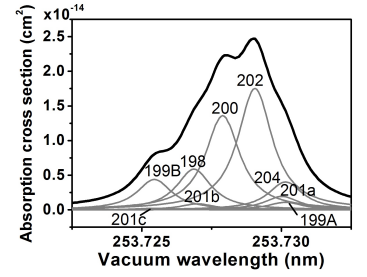


Figure 3.10. The calculated absorption spectrum of mercury with isotopic components shown as gray curves.

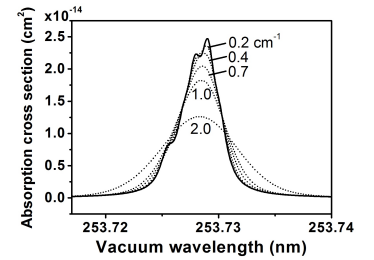
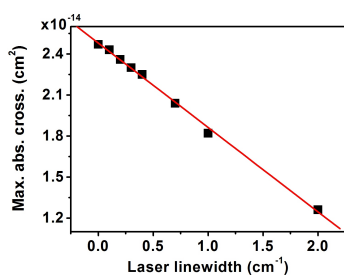
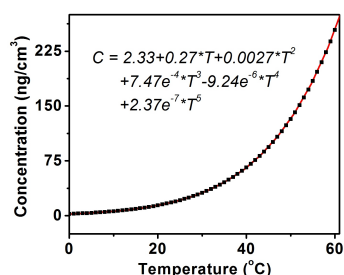


Figure 3.11. The simulated spectral broadening for an increasing laser linewidth.



**Figure 3.12.** Maximum absorption cross section decreases as the laser linewidth becomes broader.



**Figure 3.13.** Concentration of saturated Hg vapor v.s. environmental temperature [73].

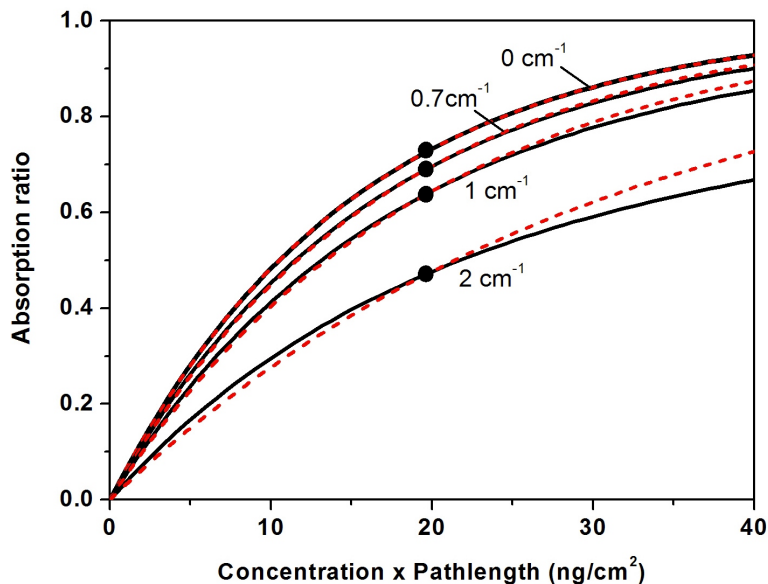


**Figure 3.14.** The comparison between Beer-Lambert law (dashed curves) and real absorption curves (solid curves) in the condition of different laser linewidth.

absorption spectrum shown in Figure 3.10 with a Gaussian function that describes the laser line shape. Figure 3.11 shows the situation when the laser linewidth is set to be different values. The maximum value of the absorption cross section decreases obviously as the laser linewidth becomes broader, as shown in Figure 3.12. Unexpected broadening of the laser linewidth will induce an under-estimation during the measurements.

To compensate such an uncertainty induced by the light source, the absorption ratio of a gas cell with well-known concentration is used for calibration. A drop of liquid mercury is sealed inside a quartz cell with a pressure of one atmosphere. The saturated vapor pressure of the mercury only depends on the temperature, following the relationship as shown in Figure 3.13. For instance, when a 9.7 mm-long cell is in a 25 °C environment, the product of the concentration and the path length is 20.5 ng/cm². The absorption of the gas cell will be measured (calculated here for demonstration) to be different in case of different laser linewidths, and shown as solid marks in Figure 3.14, where the calibration method is illustrated. Using the Beer-Lambert law, dashed curves, showing the relationship between the concentration and absorption, are calculated to pass through these marks. The concentration of the atmospheric mercury can thus be estimated with the absorption

being measured.

In order to test the validity of the Beer-Lambert law in the calibration, the real relationship between the Hg concentration and the absorption ratio is calculated by considering the laser linewidth in the simulation, as illustrated in Figure 3.11. In Figure 3.14, solid curves are plotted to compare with the Beer-Lambert curves. One can see that the Beer-Lambert law is a good approximation when the laser linewidth is less than  $1\text{ cm}^{-1}$ , which is not a problem when the DIAL system works in normal condition. However, the increase in the estimated error should be kept in mind when the performance of the OPO system becomes degraded.

The weak absorption lines of the molecular oxygen ( $\text{O}_2$ ) at both sides of the Hg lines were earlier indicated in [74]. Since no detailed description about these forbidden transitions was available in the literature, their interference on Hg measurements were hard to calculate and comment at that time. Fortunately, since the dye laser system used in [74] was with narrow linewidth and stable performance, the interference from the  $\text{O}_2$  in the air can be well avoided by carefully choosing ‘on’ and ‘off’ wavelengths.

As indicated in [74], the oxygen lines as measured with the dye laser are considerably narrower than the mercury line. Therefore, the potential influence of oxygen on mercury monitoring will be dependent on the laser linewidth. Interference studies are important, especially since the OPO used has a finite linewidth. As mentioned above, the typical linewidth of emission from the OPO is around  $0.2\text{ cm}^{-1}$ . However, in a long-term running (e.g. diurnal measurement), the degradation of the system and the drift of the central wavelength can possibly make the effective linewidth considerably worse.

With the oxygen data available in the UV range in a recently updated HITRAN database [75], it is possible to investigate the interference of oxygen on the atmospheric mercury monitoring through calculation. Figure 3.15 illustrates an example when the laser linewidth is  $1.5\text{ cm}^{-1}$ . One can see that the left wing of the broadened  $\text{O}_2$  spectrum at longer wavelength overlaps with the absorption spectrum of Hg (set as  $7\text{ ng/m}^3$  for demonstration). If the on- and off-wavelengths are set at the indicated positions ( $253.728\text{ nm}$  and  $253.745\text{ nm}$ ), the contribution of such a residual absorption is calculated to be  $1.75\text{ ng}$  of spurious Hg, which should be subtracted in the measurements. The spurious concentration is calculated for different laser linewidths and is shown in Figure 3.16. Obviously, such an interference is not a problem when measurements are carried out at locations with high concentration [76], but is not ignorable when measuring low concentrations, e.g. background Hg in the atmosphere. The correction can be done with the help from the calibration unit, where the effective absorption cross section of Hg in the gas cell is measured. From the curve shown in Figure 3.12, the linewidth of the laser system

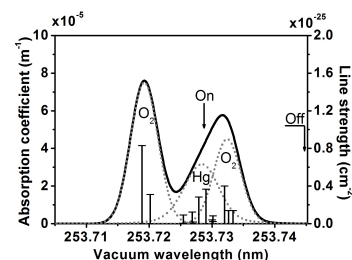


**Figure 3.15.** The calculated absorption spectrum (solid dark line) of  $\text{O}_2$  (21%) and Hg ( $7\text{ ng/m}^3$ ) in the atmosphere. The dashed lines respectively show the separated spectra, correlated to the absorption lines (the line strength of Hg is scaled by  $10^{-25}$ ). (Adapted from Paper I.)

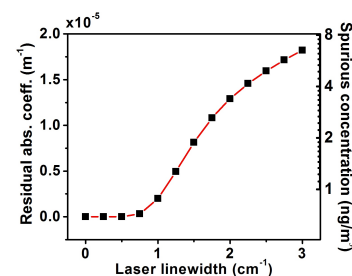


**Figure 3.16.** Calculated residual absorption coefficient/spurious concentration induced by  $\text{O}_2$  at wavelength ‘on’, adapted from Paper I.



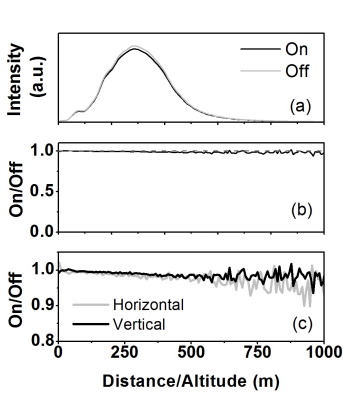


**Figure 3.17.** (a) LIDAR curves for on- and off-resonance wavelengths; (b) the DIAL curve; (c) comparison between the horizontal and the vertical measurements [Paper I].

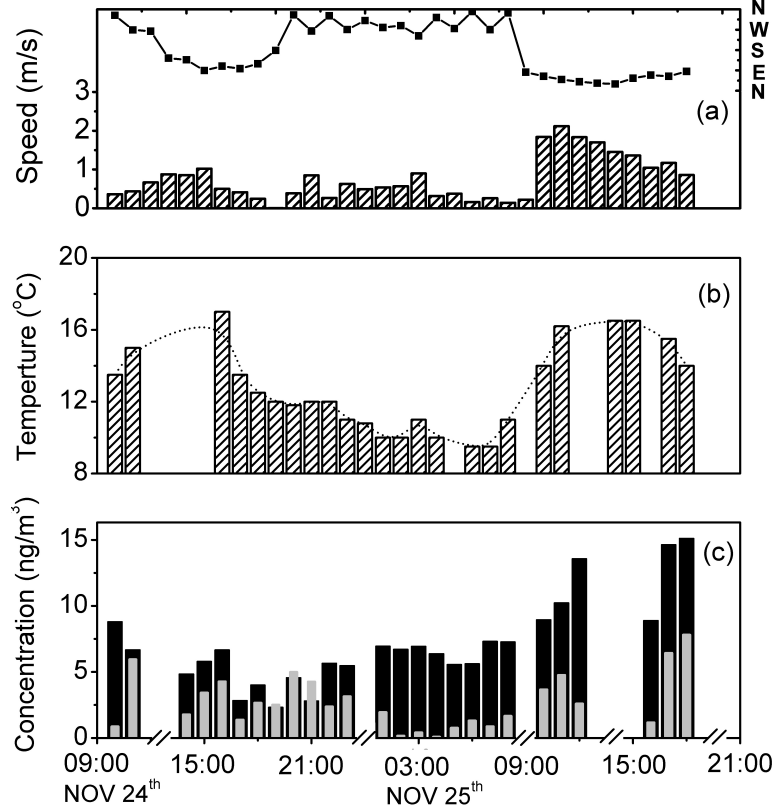


**Figure 3.18.** The measured wind speed/direction (a), and ground temperature (b) during the diurnal Hg monitoring. (c) The average concentration of Hg in low (dark) and high (gray) layers of atmosphere [Paper I].

can be estimated and then the spurious concentration is known from Figure 3.16, and subtracted later.

#### *Hg sounding, diurnal variation, and washout effect*

Vertical Hg sounding was performed during (parts of) 5 days in November 2009 in China, and results have been published in Paper I. Figure 3.17(a) shows a pair of typical LIDAR curves by setting the on- and off-resonance wavelengths at 253.728 nm and 253.745 nm, respectively, when the laser pulse energy was about 6 mJ. Since ramping voltage was applied on the PMT, the signal at close range was obviously suppressed. As introduced in Section 3.2.1, such an asymmetric responsivity of the detector is canceled when dividing the on- and off-curves. The on/off ratio

is shown in Figure 3.17(b). From the slope, the Hg concentration can be evaluated by the calibration method described above, and applying correction for O<sub>2</sub> interference, since very low concentration (few ng/m<sup>3</sup>) is expected for background Hg level in the atmosphere. Although the total absorption for a range of 1 km is a few percent or less, some range-resolved concentration information is still possible to be retrieved. By comparing the ratio curves corresponding to vertical and horizontal measurements in Figure 3.17(c), one can clearly see that the slope of the vertical curve decreases, indicating lower Hg concentration at longer distance (higher altitude). In contrast, for the horizontal one, the slope remains mainly constant, indicating that the concentration of Hg at the same altitude is stable.

Therefore, the concentrations of Hg were evaluated by dividing the vertical atmosphere into two layers, i.e. the lower one, from 80 to 380 m, and the higher one, from 380 to 770 m, respectively. A 36-hour continuous measurement was carried out and the results are shown in Figure 3.18, together with weather parameters. Obviously, lower concentration were found in higher atmosphere, since Hg atoms are much heavier than air molecules. One can also notice that low concentrations appear during the early morning. This seems to be related to low atmospheric temperature, and the north-west wind mostly from rural areas, by correlating to the weather parameters.

The removal of atmospheric Hg by rain fall was observed. Figure 3.19 shows the comparison of concentration in the low atmosphere between measurements on the 14th and 19th of December 2009. The results were averaged during the same time section on both days. The rain started on 13th and the weather turned to be clear after 16th. One can see that in rainy weather condition, an unusually low concentration, 2 ng/m<sup>3</sup> (equal to the background level on the Atlantic), was observed in a Megacity. However, the concentration returned to around 10 ng/m<sup>3</sup>, after few days of clear weather, although the temperature became even lower. Usually, the wash-out effect on atmospheric Hg is regarded to be not as obvious as those water-soluble pollutants such as SO<sub>2</sub> and NO<sub>2</sub>. Still, some literature, such as [77], has discussed such issues by, e.g., measuring the concentration of mercury in rainwater in the time domain. Here, instead, we demonstrated it by using a LIDAR.

### Nitrogen monoxide

The LIDAR monitoring of atmospheric nitrogen monoxide (NO) was firstly demonstrated by Menyuk et al. [78] and by Aldén et al. [79], in 1980 and 1982, for the IR and UV regions, respectively. Later, Kölsch *et al.* realized simultaneous LIDAR monitoring of NO and NO<sub>2</sub>, based on the connection of the 450-nm absorption band of NO<sub>2</sub> and the 227-nm absorption band of NO reachable

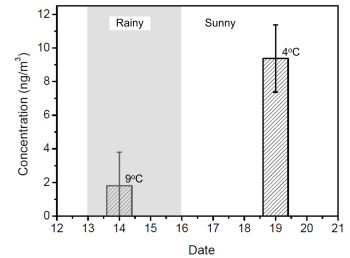


**Figure 3.19.** The washout effect of rain fall on the concentration of atmospheric mercury [Paper I].

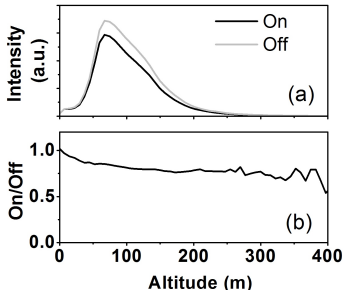


**Figure 3.20.** (a) On- and off-resonance curves at the preferred wavelength pair, and (b) the DIAL curve

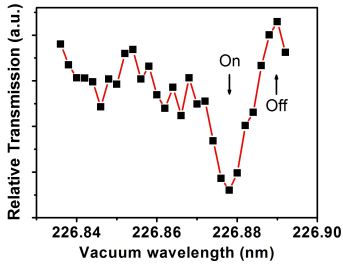


**Figure 3.21.** The scanned transmission spectrum of NO.

by frequency doubling [80, 81]. First NO measurement using a solid state laser system can be referred to [82]. In our work, the vertical LIDAR sounding for NO pollution was, for the first time, performed in China, using an OPO transmitter.

The vertical NO sounding was performed on November 25-26, 2009. Since we chose the absorption band around 227 nm and such deep-UV radiation cannot penetrate to high altitude due to the heavy attenuation by strong scattering (especially in the atmosphere of a Chinese Megacity), the measurement range was limited to 450 m. However, good range resolution was realized because of the substantial absorption signal.

#### *NO sounding and absorption spectrum*

Learning from previous NO LIDAR measurements in, e.g. [83], the on- and off-wavelengths were selected to be 226.878 nm and 226.890 nm, respectively. The LIDAR curves and their ratio are shown in Figure 3.20. Compared with Hg measurement, the absorption is much stronger although the LIDAR signal attenuates to zero after 450 m. Unlike in the Hg sounding, reference-cell calibration is invalid for NO measurement, since NO is a reactive gas and cannot be kept stable in the cell. Therefore, the absorption cross-section, which depends on the laser line-width, must be known for the evaluation of range-resolved concentrations. In order to quantify the effective cross-section when using the OPO system, the ‘off’ wavelength is fixed at 226.890 nm while the ‘on’ wavelength is scanned from 226.890 nm to 226.835 nm with step of 0.001 nm and 50 cycles are averaged for each wavelength pair. By integrating the absorption from 50 to 300 m, an absorption spectrum is produced as shown in Figure 3.21. Arrows indicate the preferred wavelength pair. By convoluting this spectrum with a database spectrum, e.g. from [83], which was obtained by using a dye laser with narrower line-width, the effective differential cross-section for the preferred wavelength pair can be deduced as  $(5.2 \pm 1.0) \times 10^{-22} \text{ m}^2$ .

#### *Diurnal NO variations*

Using the effective differential cross-section deduced above, the range-resolved concentration of NO can be evaluated from the DIAL measurements, which were performed for 26-hours continuously. The results are shown in Figure 3.22 together with weather data. In the spatial domain, one can clearly see that the concentration is much higher in atmosphere lower than 100 m. This indicates that the NO is vehicle-generated locally. In the time domain, unexpectedly, the highest concentration appears at midnight, when the local traffic should have reduced compared with in day time. The observations might be related to the sun radiation, which is an important factor for the complex atmospheric chemistry of NO, as is ozone, hydrocarbons, etc.

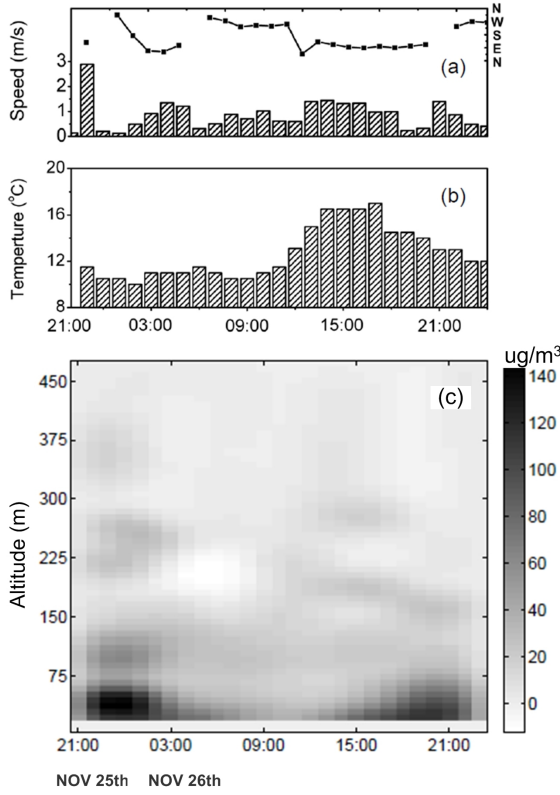


**Figure 3.22.** The measured wind speed/direction (a), and ground temperature (b) during the diurnal NO monitoring. (c) The variation of NO during the 24-hr cycle.

### 3.2.4 Gas analysis in multi-scattering media

#### Working principle

The LIDAR equation (Equation (3.1)) is based on the assumption of single-scattering condition; however, LIDAR techniques can also be used to analyze multi-scattering media such as fogs and clouds [84]. In short-range measurements, a similar technique is used to evaluate the effective path length in scattering media such as bio-tissues [85–87] and tablets [88]. In contrast to the broad-band spectral properties of liquids or solids, the free gases in pores throughout the scattering solid material present extremely sharp structures in absorption spectra. By employing single-mode diode lasers with high spectral resolution, the gases in different materials including wood, polystyrene foam, food, fruits, pharmaceutical tablets, or human air-filled sinus cavities [53–58] have been

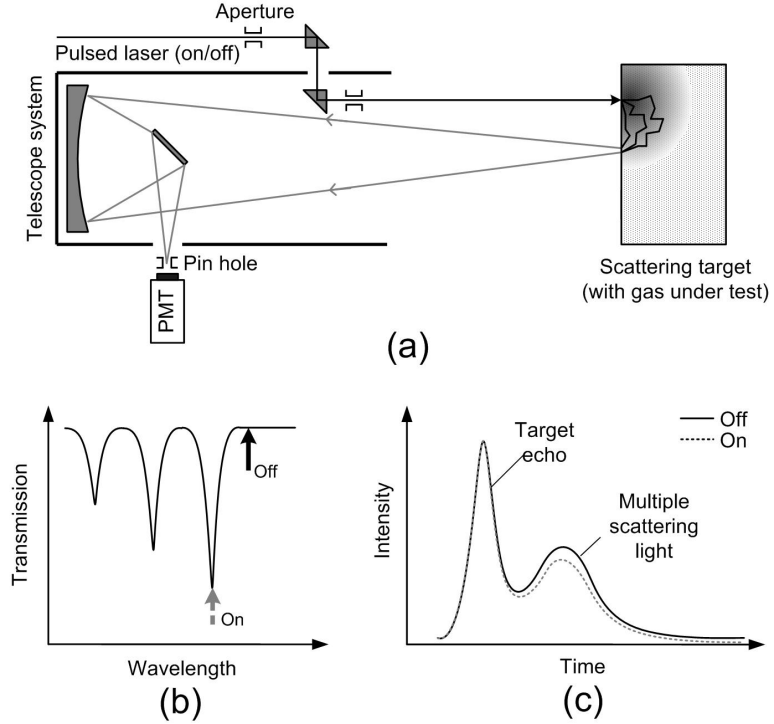


**Figure 3.23.** The working principle of the DIAL technique for gas analysis in multi-scattering media: (a) schematic diagram of the system; (b) switching between on and off can be realized by finely tuning the laser wavelength across an absorption dip of the gas under test; (c) the difference between the curves corresponding to on and off wavelengths reveals the presence of the gas [Paper II].

measured. Such a technique is called GAs in Scattering Media Absorption Spectroscopy (GASMAS) and will be discussed in detail in Section 4.3. In order to realize high sensitivity and high resolution in the measurements, the diode laser is operated in a CW mode and wavelength modulation is applied.

Combining the DIAL technique and the GASMAS principle, a remote version of GASMAS is proposed and published in Paper II. The working principle of the technique, illustrated in Figure 3.23, can be generally described as follows. A pulsed laser with narrow line-width is employed as the light source. Part of the photons that impinge on the target are reflected as an ‘echo’, and the other part penetrates and is heavily scattered inside the material. After having visited deeper layers of the target, some of the scattered photons appear at the surface again with a distance from the injection point, and can be collected by a telescope system aiming at the observation point. The signal is further recorded by a sen-

sitive detector (e.g. a PMT) in the time domain, as in a LIDAR measurement. A strong echo, due to the surface reflection, followed by an extended tail, due to the multiple scattering, can be expected in the recorded curve. By carefully selecting the on- and off-wavelength according to the absorption spectrum of the gas present in the pores of the target, the differential absorption will be found in the tail, where photons have experienced a long path length in the scattering medium. Using the same principle of DIAL, the slope of the ratio curve will reveal the information of gas concentration.

### Experiments and results

A tunable dye laser is an ideal light-source candidate for such a technique, since the laser can run in the pulsed mode while keeping a high spectral resolution and wavelength tunability. In the experiments, a pulsed dye laser pumped by the second harmonic output of a Nd:YAG laser was employed. The pulse width of the pump laser was compressed into around 2 ns by backward stimulated Brillouin scattering in water, in order to realize a high time/spatial resolution in measurements. Detailed information of the laser system can be found in Paper II. The detection system was specially designed to suppress the strong echo, presented in Figure 3.23(c), due to the direct surface reflection. Firstly, a 4 mm pin hole was set at the focus point of the telescope (with a diameter of 25 cm and a focal length of 1 m), which was 6 m away from the target. Therefore the field-of-view of the telescope is limited to a region with diameter of 20 mm on the target, and such a observation region kept a distance away from the injection region, where strong direct reflection occurs. Secondly, apertures were applied to clean the halo of the well-collimated laser beam, ensuring that the laser pulse only illuminates the defined spot on the target. By using the above methods, most echo was suppressed, and the multiple-scattering tail can show up.

Proof-of-principle experiments were carried out in the laboratory. Polystyrene foam and fresh snow were tested as scattering samples, and in both cases, clear extended tails in time domain were observed due to massive scattering in the media. Details are described in Paper II. The oxygen gas in polystyrene foam was analyzed by measuring the differential absorption at the R9Q10 line at 760.654 nm. The dye LC7710 was employed to run the dye laser at this wavelength. Figure 3.24(a) shows the on- and off-LIDAR curves, and the differential absorption can be seen in the tail region, since the photons have visited deep layers of the polystyrene foam sample containing free oxygen gases in pores. An obvious echo was still observed earlier than the tail, due to the imperfection of the optics. The slope of the on/off ratio keeps on constant (see Figure 3.24(b) ), since oxygen distributed uniformly

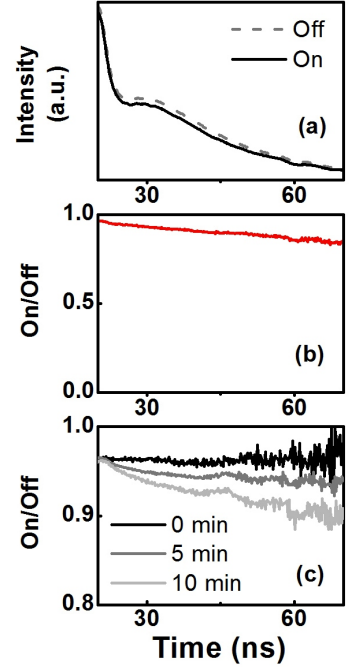


**Figure 3.24.** Experimental results on analysis of the oxygen concentration in polystyrene foam: (a) the difference between pulse curves corresponding to on and off; (b) the ratio of on and off curves reveal the existence of the oxygen in the polystyrene; (c) the slope of the on/off curve increases with time when a nitrogen filled polystyrene is exposed to the air. (Adapted from Paper II.)

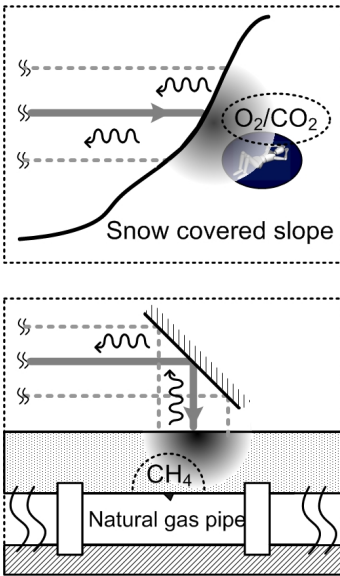


**Figure 3.25.** Schematic diagram of potential applications, e.g., localization of snow-avalanche victims and inspecting possible methane leakage from a snow-covered natural gas pipeline, adapted from Paper II.

in the scattering medium. A gas exchange experiment was also performed. A block of polystyrene foam was sealed over night in a plastic bag filled with nitrogen, which penetrates into the sample and replaces the initially contained air gas. On the second day, measurements were performed immediately after the block was extracted. The experimental results are shown in Figure 3.24(c), from which one can see that the slope of the ratio curve is close to zero at the beginning, indicating no oxygen existing in the sample. However, later in measurements at 5 and 10 min, the slope increases obviously, indicating the reinvasion of the oxygen contained in the external atmosphere into the polystyrene foam.

### Application outlook

Although only proof-of-principle experiments were carried out, unique applications of the DIAL technique used for gas analysis in scattering media can be expected. Two examples are schematically shown in Figure 3.25. In both cases, snow is the scattering medium, which has been tested in our early experiments (see Paper II). One potential application is localization of a snow-avalanche victim, by detecting the abnormal high concentration of  $\text{CO}_2$ , exhaled by the victim, or the reduction of  $\text{O}_2$ , which is consumed. A further application, inspection of the methane leakage from the gas pipe covered snow, is illustrated at the bottom of the figure. Considering that the methane may be trapped by and accumulated in the local snow, even a small leakage would be possible to detect. The absorption lines at  $1.35 \mu\text{m}$  of methane should be compatible with the optical properties of snow.

## 3.3 Fluorescence LIDAR

### 3.3.1 Laser-induced fluorescence (LIF)

Fluorescence is a physical phenomenon of a material that absorbs radiation at short wavelength and yields emission at longer wavelength. The principle is illustrated in Figure 3.26 regarding energy levels and the basic absorption and emission processes. Different from free atoms and molecules, solids and liquids exhibit broad absorption/emission spectra because of strong intermolecular interactions. By electronic excitation, visible or UV photons can be absorbed by the molecules of the target, with promotion of an outer electron to a higher orbit. Each energy level corresponding to a particular electron arrangement has a vibrational structure, while the rotational structure, typically for free molecules, is suppressed by the intermolecular interactions. In complex molecules, there is a large number of vibrational levels.

In contrast to the situation employing a wavelength tunable laser for spectral scans in, e.g. Chapter 4, a fixed frequency laser

can be used as excitation, provided that the photon energy falls within the broad excitation band. Following the excitation, there is a very fast (several ps) radiationless relaxation down to the lowest substate, where the molecules remain for a typical excited-state fluorescence lifetime, which is of the order of some nanoseconds. The decay can then occur to different sublevels of the ground state giving rise to a distribution of fluorescence light, which reflects the lower-state level distribution. Because of the radiationless relaxation, the fluorescence distribution is independent on the exact excitation wavelength. The fluorescence spectrum is a finger print that can be used for recognizing the target material.

Actually, if the wavelength for detection is fixed while the excitation wavelength is scanned instead, an excitation spectrum can also be recorded. Both the fluorescence and excitation spectra can provide information for material recognition and become two important methods for laser-induced fluorescence (LIF). Except the spectral information, the lifetime of the fluorescence action is also characteristic. Many LIF techniques are discussed in a number of monographs and reviews [89–91].

### 3.3.2 Remote LIF

#### General considerations

Laser-induced fluorescence (LIF) has been widely used in biological marking [23], in medical application such as tissue diagnostics [92], and in quantitative measurement of concentrations in fields like combustion, plasma, spray and flow phenomena [93]. However, most LIF equipments are designed for contact/short-distance measurements.

In some other applications, fluorescence recording from remote targets at larger distances is especially attractive. For instance, the historical monuments can be optically diagnosed through remote LIF spectroscopy [38]. Surface degrading due to the action of weather, air pollutants and the invasion of biodeteriogens, is possible to be revealed from the fluorescence signature, although not obvious for visual observation. Such applications have been demonstrated at the Lund Cathedral, Sweden and the Roman Coliseum, Italy, with a mobile LIF system parked 60 m away. By scanning the laser beam, 2-D false color images with each pixel containing the fluorescence information are produced to indicate the abnormal areas, e.g., presenting biodeteriogens. Such remote, non-intrusive, scannable techniques are also very effective for vegetation monitoring [94] and water-quality measurement, since complicated sampling processes are avoided. Fluorescence monitoring can provide additional information to satellite- and air-borne reflectance remote sensing to recognize vegetation types, while the water quality can be evaluated from the specific fluorescence signa-

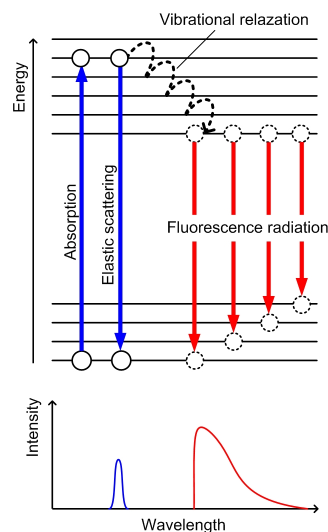


**Figure 3.26.** Schematic molecular energy level diagram and absorption and emission/fluorescence processes in condensed matters. The resulting spectrum is shown in the lower part.



tures corresponding to dissolved organic matter (DOM), oil spills, and phytoplankton.

In addition to measuring the fluorescence signal from a single fixed target, remote LIF can also realize range-resolved measurements. This fluorescence LIDAR variety is useful in assessing phenomena in addition to those relying on elastic backscattering from aerosols. Due to the existence of meteorite-generated alkali atoms and iron ions, resonance fluorescence LIDAR is a unique technique to monitor wind and temperature conditions in the middle and high atmosphere. The Doppler effect makes the fluorescence spectra of these metal atoms/ions broaden at high temperature and shift with the wind speed and direction.

Compared to aerosols, air molecules, and metal atoms/ions in the atmosphere, insects and birds are much larger ‘flying particles’ to be monitored by a fluorescence LIDAR system. The fluorescence signals are noticed to be able to classify their species and sexes. As biomarkers, the movements and migration status of insects and birds are very important to ecological studies. Fluorescence LIDAR provides a new approach for such monitoring.

### **Instrumentation**

A fluorescence LIDAR system consists of, like the elastic LIDAR and the DIAL systems introduced above, a laser transmitter, receiving telescope, and detection system. Figure 3.27 shows a schematic diagram of key components of a fluorescence LIDAR. The UV light source for excitation is the 355 nm and 266 nm radiation from the Nd:YAG laser, or the double frequency of the signal emission from the OPO system. The fluorescence LIDAR shares the same expander, scanning mirror and the telescope system with the elastic LIDAR and the DIAL systems. Two independent detection systems are employed for fluorescence analysis. A metal mirror fixed on a specific mechanical device can be inserted into the light path to switch the collected light between different detection parts, as shown in Figure 3.28.

As shown in Figure 3.27, without the switch mirror, the collected light is distributed by several mirrors and filters, and then detected by three photomultiplier tubes (PMTs). The elastic scattering from the target is selected by a laser mirror and detected by PMT-1, and the fluorescence signal is divided by a dichroic filter into two wavelength bands, i.e., blue (400-500 nm) and yellow (500-750 nm), and measured by PMT-3 and PMT-2, respectively. The time-resolved curves from the three PMTs are recorded by a high speed oscilloscope which samples every 8 ns. The repetition rate of the system is 10 Hz. A detail description of the three-PMT system can be found in Paper V.

With the switching mirror inserted, the light is instead coupled into a 1-mm-thick fiber, which guides the light into a optical

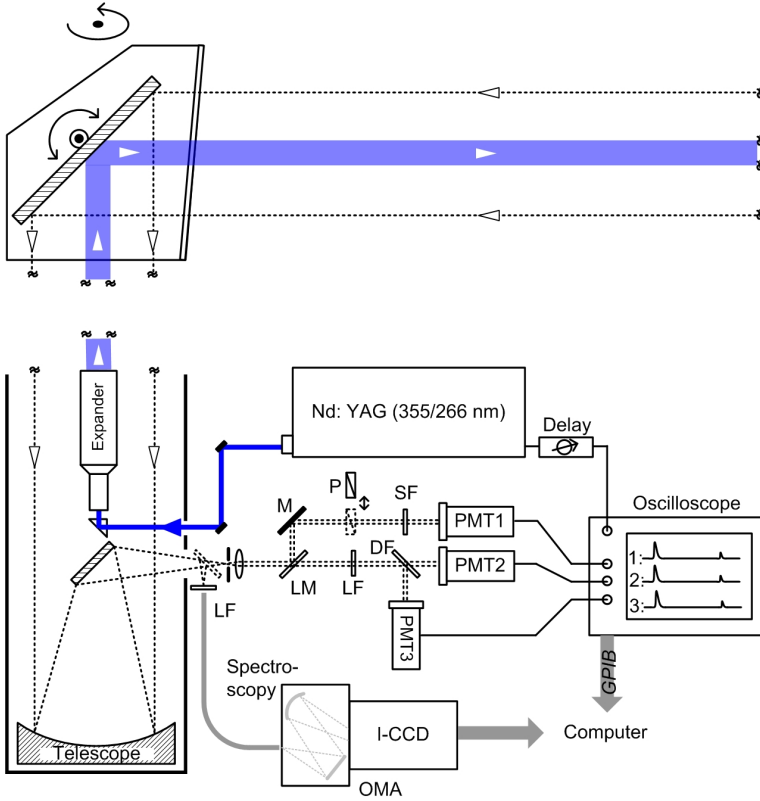


**Figure 3.27.** Key equipment/components of the fluorescence LIDAR. LM: laser mirror; P: polarizer; SF: short-pass filter; DF: dichroic filter; LF: long-pass filter.

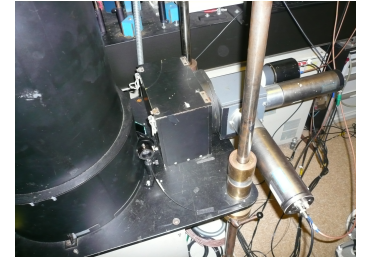


**Figure 3.28.** Detection part of the fluorescence LIDAR.

multi-channel analyzer (OMA). The OMA system consists of a grating-based spectrometer and an intensified CCD (I-CCD). The wavelength range of the spectroscopy is from 300 nm to 800 nm. The dispersed spectrum is amplified and detected by the I-CCD, which can be electronically gated on the nanosecond time scale. The sky background light can thus be suppressed during daytime measurements. Usually a long-pass filter is employed before the OMA to suppress the strong backscattering of the elastic light.

### 3.3.3 Ecological studies

#### Water monitoring

As an important part of the ecological research, hydrological monitoring using ship- or airborne LIDAR systems have been performed for a long time. Initial work was much focused on laser

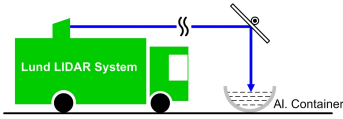


**Figure 3.29.** A schematic diagram illustrates how the LIDAR bus measures fluorescence from remote water samples.

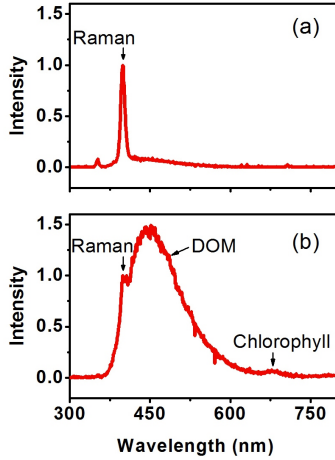


**Figure 3.30.** Fluorescence comparison between drinking water (a) and lake water (b)

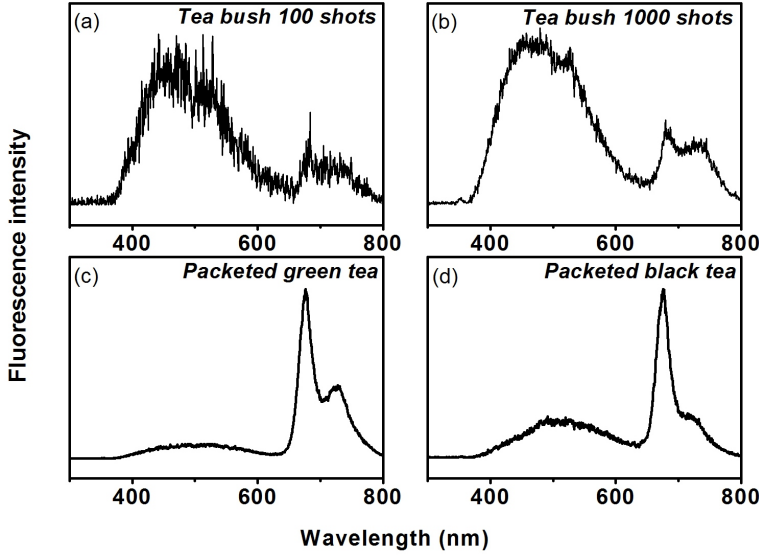
bathymetry [95] directly towards shallow water depth measurements using elastic backscattering. Fluorescence measurements, in addition, are later demonstrated to be able to supply more information to evaluate water quality. As an example, Figure 3.29 schematically shows how the mobile LIDAR system is used to analyze the fluorescence signatures from remote water samples, with a distance of about 50 m. The fluorescence LIDAR facilities described above are contained in the truck cabinet, and the excitation laser beam is turned by an extra plane mirror and illuminates the water samples, which in real applications, can be natural water resources like rivers, lakes and oceans. Here, an aluminum container is used to avoid interfering fluorescence. The fluorescence signal is coupled back to the bus and analyzed by the OMA system.

Figure 3.30 shows two fluorescence curves corresponding to two different water samples when the excitation light is at 355 nm. The measurements were performed at the Zijingang Campus of Zhejiang University in Hangzhou. The Raman scattering, with a Stokes shift of about  $3400\text{ cm}^{-1}$  for the O-H stretch vibration mode of  $\text{H}_2\text{O}$ , can be seen from both water samples. Such a Raman peak at 404 nm can be used for normalization of the fluorescence spectrum. The broadband fluorescence signal peaking at blue-green wavelengths from the lake water is related to the dissolved organic matter (DOM), which has very low concentration in the drinking water, and hence is absent in the spectrum in (a). The weak but clear peak at around 690 nm presenting in (b) is due to the chlorophyll, which is present in all algae.

Information of this kind can even be obtained in a range-resolved way, by simply setting the detecting gate on the OMA with different delays. From range-resolved signals of DOM and chlorophyll, the water quality at different depths can be evaluated [96]. And since the Stokes shift is temperature-related, the Raman signal has been used to deduce temperature information at different water depths [97].

### **Vegetation monitoring**

Vegetation is a main object of air- and satellite-borne remote sensing. Passive optical remote sensing recognizes vegetation types using the absorptive/reflective properties of leaves. Laser-induced fluorescence can supply additional information to find minor differences among different vegetation types. In Figure 3.31, (a) and (b) show remote LIF spectra of a tea bush (Long Jin type, Hangzhou, China) located at a distance of 50 m, compared with those of packeted teas ((c) and (d)) that were measured inside the LIDAR laboratory using basically the same excitation laser and spectrometry (OMA system). From (a) and (b), one can see that 100 shots averaged signal within 5 s clearly shows the fluorescence properties, and the signal-to-noise ratio (SNR) improves after 1000 shots of



**Figure 3.31.** Fluorescence spectra of fresh tea bush (a) and (b), and packeted teas (c) and (d). (a) and (b) are measured with the target located 50 m away, while (c) and (d) are measured in the laboratory.

average within 50 s, which is principally non-limiting for such static targets. At wavelength 690 nm and 735 nm, two fluorescence peaks are related to chlorophyll. The peaks grow as the concentration of the chlorophyll in the leaves increases, but since the 690 nm peak occurs at a wavelength where chlorophyll absorbs, the intensity of this peak will be suppressed if the concentration increases further. Therefore, the ratio between the two peaks can be used to deduce the chlorophyll concentration. The packeted teas present higher intensity at 690 nm since the chlorophyll were partly destroyed during the drying treatment, and black tea contains less chlorophyll than green tea, as would be expected. The fluorescence peak in the blue-green wavelengths is due to the accessory pigments and the leaf wax, which is also largely removed during the tea-fabrication process. Furthermore, studies [98] show that environmental stress can influence the shape of the fluorescence spectrum that provides complementary information to data obtained in reflectance measurements using, e.g. passive optical remote sensing methods.

### Insect monitoring

The movements and migration status of insects are of great importance for understanding, e.g., biological topics like genetic spread, and environmental topics like global warming. One most common

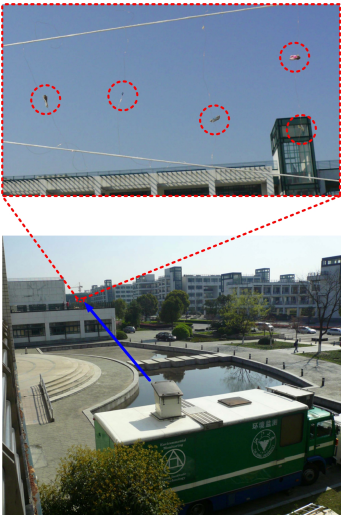


**Figure 3.32.** Test-range experiments of fluorescence recording on insects (Hangzhou, China).

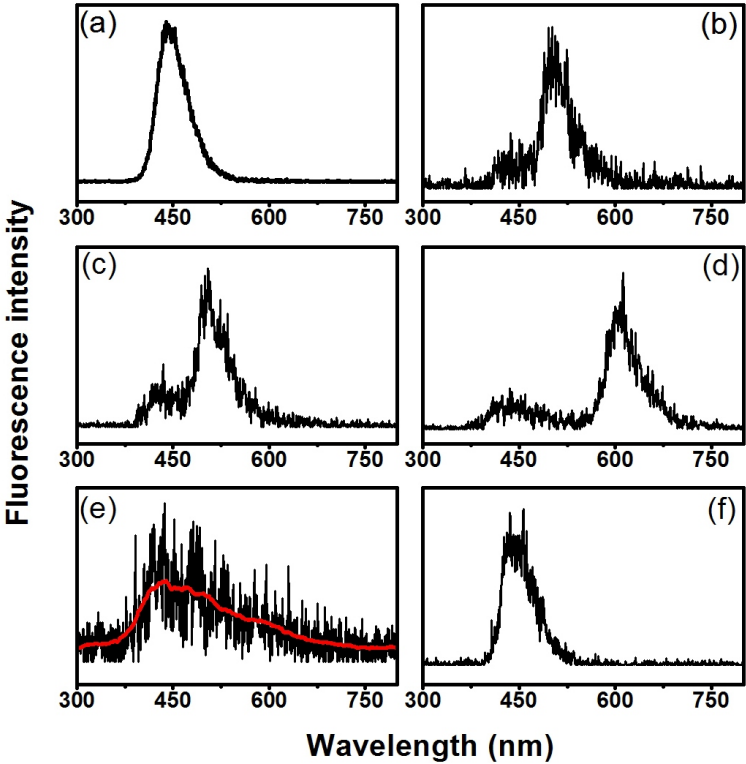


**Figure 3.33.** Fluorescence spectra of moths, *Spodoptera Litura*, marked with blue (a), green (b), yellow (c), red (d) dyes, and without any marking (e). (f) shows the signal corresponding to moth, *Nilaparvata Lugens*, marked with blue. (Adapted from [19]).

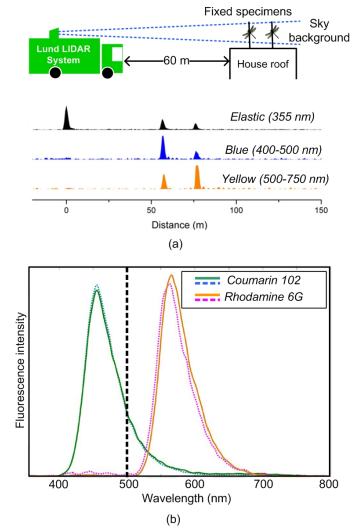
method now used by biologists is to release dye-marked groups into a natural environment and later to collect the marked individuals at another population after a period of time. Obviously it is time-consuming and low efficient. A fluorescence LIDAR provides an opportunity to analyze the live flying insects in a remote way requiring no collecting action, by setting the laser beam in the open air where insects appear frequently or on the way that the migrating insects must pass through. The spatial scanning and range resolving abilities of the LIDAR system can help to map out the distribution of insects in wide spaces.

Figure 3.32 shows a test-range experiment for remote insect measurements. The insect samples are fixed by thin, non-fluorescing metal wires and attached on a building roof 50 m away. Fluorescence curves are measured by the OMA with excitation laser at 355 nm, and shown in Figure 3.33. (a) to (d) show the signals from a type of moth, *Spodoptera Litura* (with individual

size of about  $5 \times 5 \text{ mm}^2$ ) which are dusted with dyes of Comet Blue, Stellar Green, Lunar Yellow, and Nova Red, respectively. These dye powders are from Swada Inc., regularly used by biologists for dispersal and mating studies (see, e.g. [23]), and have been tested to not harm the insects. Clearly the fluorescence signatures corresponding to different dyes are presented at correct wavelength ranges, indicating that many insect types can be coded by dyes/dye-combinations and easily recognized by the fluorescence LIDAR. Moreover, even the auto-fluorescence of the insects, at the blue-green wavelength range, can be seen by the sensitive detection system. They are partly presented in (b), (c), (d), and especially in (e), where an insect without dye dusting is measured. The auto-fluorescence signatures contain sufficient information to recognize species for some insects. For instance, we have reported in Paper IV that the sexes of damselflies can be distinguished using their auto-fluorescence signals. Figure (f) shows the validity of the technique to small insects. The signal of a small moth (*Nilaparvata lugens*) with size of about  $1 \times 3 \text{ mm}^2$ , which is dusted by blue dye, is clearly shown.

Different from static targets such as water or vegetation, signal averaging is not realistic for flying insects in field experiments. The detection system has to be sensitive enough to obtain information within a single laser pulse. Therefore, the three-PMT system described above is employed together with the light distributing scheme that consists of several mirrors and filters. In addition, the PMTs record reflection signals in the time domain and hence can realize range-resolved measurements. The top of Figure 3.34(a) shows such a demonstration at the test distance of 60 m, in Lund, Sweden. Two dead damselflies marked with different dyes (Coumarin 102 and Rhodamine 6G) were placed with 20 m separation in the laser path. The single-pulse reflection that bursts from the damselflies were then recorded by the three-PMT systems, as shown at the bottom of Figure 3.34(a). Obviously, the intensity (ratio) of the two fluorescence bands are different for the damselfly positioned at a closer distance, which is marked by Coumarin 102, a bluish dye, and the other one at a larger distance, marked by Rhodamine 6G, which is reddish. The fluorescence spectra of these two dyes for 355-nm excitation are shown in (b), with the cut-off wavelength of the dichroic beam splitter marked with a dashed line. The above tests indicate that the fluorescence signature from a single LIDAR pulse is sufficient to distinguish damselflies marked with different dyes, which is encouraging for studying flying damselflies in their natural habitats.

Based on the above techniques, the Lund mobile LIDAR system performed insect measurements at the Klingavalsån river, Veberöd (5538' N, 1329' E), in southern Sweden, during two weeks (June, 1-7 and 24-30, 2009). Three geometrical arrangement close over the river surface were set up and the damselflies in the laser beam were



**Figure 3.34.** (a) Setup for test-range measurements, and corresponding range-resolved signals of the three channels, from two serially-placed damselflies marked with different dyes (Coumarin 102 and Rhodamine 6G) [Paper V]. (b) The fluorescence spectra of the two dyes used in the test, with excitation wavelength at 355 nm. The dashed line indicates the cutoff wavelength of the dichroic beam splitter [Paper IV].



**Figure 3.35.** Some bird samples

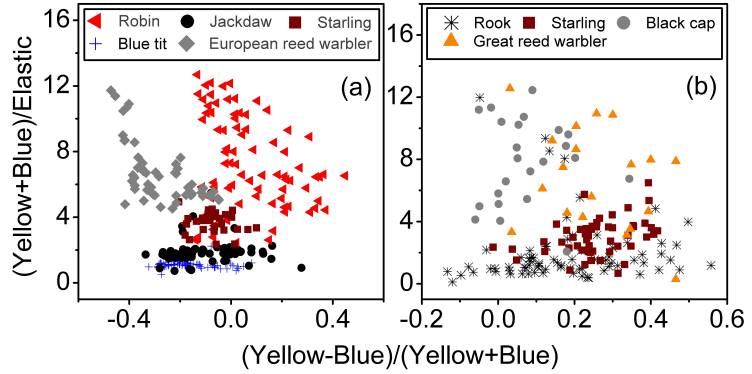


**Figure 3.36.** The scatter plots show possibilities of bird-species classification using fluorescence LIDAR, with excitation wavelength at 355 nm (a) and 266 nm (b), respectively [Paper VI].

measured and counted. Histograms of distribution in time scale and spatial scale were obtained based on a large amount of data. Particularly, groups of damselflies that were captured from other populations and dusted with different dye powders were released to the local environment, and measured continually in later days. Their performance are greatly interesting and have induced many discussion from the collaborating biologists. The research work is published in Paper V.

### Bird monitoring

During the Swedish campaign of measuring insects in the natural field, the fluorescence signals of flying starlings (*Sturnus vulgaris*) were recorded unintentionally. Considering the difficulties of observing birds during night time, which, however, is a perfect condition for fluorescence LIDAR, we realized and demonstrated that remote classification of migrating birds could be an ideal application of the technique.

To explore such a feasibility, 26 bird samples (partly shown in Figure 3.35) from the Lund University Zoological Museum were moved in and out of the light beam to simulate flying birds. Figure 3.36 presents the scatter plots using signal intensities of the three channels, with 355 and 266 nm excitations, respectively. Auto-fluorescence from the different feathers is believed to contain enough information for distinguishing. Here, the x-axis corresponds to the color of the fluorescence; redder signal turns up to the right and bluer to the left. The y-axis corresponds to the strength of the fluorescence compared to the elastic signal. Each analyzed echo is shown as a small marking and since the specific

bird species are known in this experiment, they are given a particular appearance. If a good separation is seen between species in the plot, different kinds should be discernable with the help of their fluorescence.

355 nm illumination was used in the first feasibility test in the field due to the reason that the flying starlings were recorded with this wavelength. Since birds have a UV-vision band in this region, 266 nm light is a preferred wavelength for eye safety reason of the birds. The tests at 266 nm on the museum samples were performed at the docking position of the LIDAR system in Lund. The separation of the bird species in the case of 266 nm illumination is not very prominent, mainly due to a temporarily poor performance of the laser system. The results in the case of 355 nm illumination are, however, much better and demonstrate the method potential.

A full scale field experiment at the Kullaberg National Reserve has been performed. 266 nm excitation was employed and a third fluorescence channel was added for increased discrimination [99].





---

# TUNABLE DIODE LASER ABSORPTION SPECTROSCOPY

---

Tunable diode laser absorption spectroscopy (TDLAS) has been proven to be a very successful tool for gas analysis [44–47]. Most practices of such a technique are carried out for trace gas measurements in free space. One typical operational mode is as shown in the top right of Figure 2.6 in Section 2.2. The integrated absorption along the light path is measured, and principally, air sampling is not required during the operation. Sensitivity, which determines the minimal detectable signal, is a key goal to consider when developing a TDLAS method. By modulating the diode laser through the applied driving current, the noise level at the detector can be dramatically suppressed at high frequency and a minimal detectable absorption as low as  $10^{-7}$  can be realized [46]. TDLAS is thus a sensitive remote technique that can accurately quantify trace-gases/pollutants in the atmosphere.

In Section 4.2 of this chapter, we propose a new method to suppress the detector noise and improve the sensitivity of TDLAS in contrast to modulation techniques. A balanced interferometer is constructed to produce a zero-level background, on which a increasing signal corresponding to the absorption information is detected. Similar to other zero-background spectroscopic techniques such as laser-induced fluorescence spectroscopy [48] and photoacoustic spectroscopy [50], high sensitivity can be expected from proof-of-principle experiments carried out in the laboratory. In addition, the complementary improvements of the technique in real-world applications are considered and discussed with experimental demonstrations and theoretical analysis. Related techniques and research results are published in Papers **VII** and **VIII**.

Further, in Section 4.3, the TDLAS technique is extended to analyze free gases contained in porous scattering media; called GAs

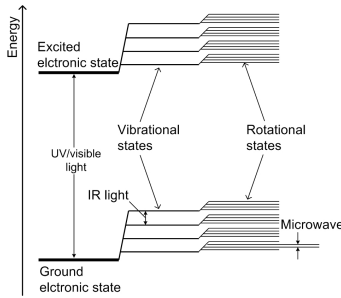


**Figure 4.1.** Schematic molecular energy level diagram with electronic, vibrational and rotational levels, adapted from [33]

in Scattering Media Absorption Spectroscopy (GASMAS). Studied samples of the technique include polystyrene foam, wood, fruit, and even human sinus cavities [53–58]. In this chapter, measurements of the concentration variation of oxygen and water vapor in sealed food packages are described. Obvious difference can be found after exposing the food to ambient environment by performing perforations on the packages. The research proves that GASMAS can be an ideal technique for food monitoring without destroying the packages. Such applications are published in Paper IX; while Paper X reported another application, clinical monitoring, of the GASMAS technique.

In GASMAS measurements, the absorption signal is enhanced by the massive scattering, which increases the effective absorption path length dramatically. However, on the other hand, the propagating paths of photons are not as defined as in free-space measurements. A reference gas with well-known concentration is required to be measured in order to compensate the absorption length and deduce the concentration of another gas under test. Or otherwise, a LIDAR technique could apply simultaneously to gather diffusive scattering and pathlength information. Instead of using pulsed light, we demonstrate that a wavelength-modulated diode laser can realize the same function using a heterodyne technique. The combination of the technique with GASMAS measurements is discussed at the end of this chapter. Such a heterodyne technique is published in Paper XI.

## 4.1 Background knowledge

### 4.1.1 Gas absorption spectrum

When the electromagnetic radiation passes through a material, the frequency that fits the gaps between certain energy levels of the molecule (see Figure 4.1) will be absorbed, by exciting the electrons at the lower energy level to a higher one. The absorption spectra consist of discrete lines containing information of molecular structures. As illustrated in Figure 4.1, the energy gaps between two electronic, vibrational and rotational states correspond to UV-visible light, IR light, and microwave, respectively.

Different from solid/liquid molecules, which present broad-band absorption spectra due to interaction among the molecules, the spectra of free-gas molecules, however, are constituted by many narrow absorption lines, corresponding to the possible energy transitions. As an example, the absorption spectrum of gaseous oxygen at around 760 nm is shown in the top of Figure 4.2. In the lower part of the figure, one specific absorption line, R11R11, is plotted considering different broadening mechanisms, mainly for two reasons. One is called thermal Doppler broadening which is due to the random movements of the molecules depending on temper-

ature. This broadening effect is described by a Gaussian profile. The other is called pressure broadening due to the collisions between gas molecules and is described by a Lorentzian profile. The combination of these two effects can be calculated by convolution into a Voigt function. With the environmental pressure and temperature of 1 standard atmosphere and 296 K, the pressure broadening dominates over the Doppler one. The integrated absorption intensity across the absorption line is proportional to the product of the concentration of the gas and the optical path length, through the Beer-Lambert law.

#### 4.1.2 Diode laser

A diode laser is based on semiconductor materials and the physics behind is quite different from other laser types. The voltage applied on the strongly doped p- and n-semiconductor materials forces the electrons as well as holes into a transition region between them. The recombination of the electrons and the holes induces stimulated light emission, with photons oscillating in a cavity formed by the polished surfaces between the semiconductor and the air.

The diode laser is a type of compact, cost-effective light source, and has been widely applied in for instance CD player, laser pointers and bar code readers. These diode lasers are based on  $\text{Al}_x\text{Ga}_y\text{As}$  material, and the wavelength is around 800 nm at room temperature. Recently, with the fast development of semiconductor materials, the lasing wavelength of diode lasers can (non-continually) cover the wavelength range from deep UV (around 300 nm) to IR (several tens of micrometer). It is also possible to operate diode lasers in a single longitudinal mode, by employing periodical structures, such as a diffraction grating, for mode selection. Distributed feedback (DFB) lasers, vertical-cavity surface-emitting lasers (VCSELs) [100, 101] and quantum cascade lasers (QCLs) [102–104] are especially interesting for spectroscopic applications due to their narrow line-width and wavelength tunability. Coarse tuning is performed by thermo-electric changes of the junction temperature, which alters the band gap and index of refraction, while swift scanning over small spectral region is achieved by current ramping.

The diode laser is an ideal light source for remote sensing. Firstly, the diode laser does not need calibration and maintenance during the long term of running. Secondly, the energy efficiency of diode lasers is extremely high and battery-operation is possible for measurements carried out, e.g., in field work. Thirdly, the driving and temperature controlling electronics for diode lasers are relatively simple. Fourthly, dependable measurements are possible without complicated optical alignments.

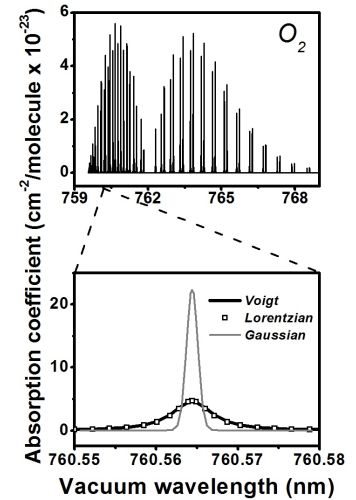


**Figure 4.2.** Top: the absorption spectrum of oxygen at wavelength of 760 nm. Bottom: calculated absorption line (R11R11) with different broadening mechanisms, when the environmental pressure and temperature is 1 atmosphere and 296 K, respectively.

### 4.1.3 Sensitivity

Tunable diode laser absorption spectroscopy (TDLAS) has been proven to be very successful for gas analysis and especially for trace gas measurements in the atmosphere [44–47], where the minimum detectable signal is required to be as low as  $10^{-6}$  or  $10^{-7}$ . The signal-to-noise ratio (SNR) of a TDLAS, which determines the minimum detectable signal, can be generally expressed as

$$SNR = \frac{kI}{\sqrt{(N_s I)^2 + (\beta \sqrt{I})^2 + N_t^2}} \quad (4.1)$$

$I$  is the intensity of light arriving at the detector and  $k$  describes the absorption signal.  $N_s I$ ,  $\beta \sqrt{I}$ , and  $N_t$  are the laser source noise, the detector quantum noise and the detector thermal noise, respectively.

Equation (4.1) can be improved by increasing the signal intensity in the numerator, or decreasing the noise terms in the denominator. For instance, White cells or ring-down cavities largely increase the optical path length and can thus enhance the absorption signal ( $k$ ) and improve the SNR efficiently. On the other hand, since the noise term  $N_s I$ , which dominates at low frequency, can be suppressed efficiently by going to high frequencies ( $N_s I \propto 1/f$ ), modulation methods are effective to improve the SNR of a TDLAS. Wavelength modulation and frequency modulation are two typical ways for suppressing the laser source noise to be less than the quantum noise, and quantum limited measurements can thus be realized [46]. The advantage of a quantum limited measurement is that the SNR can be continually improved by increasing the light intensity  $I$ . Combining external-cavity-enhancement technique and modulation techniques, sensitivity as high as  $10^{-12}$  is in principle feasible for noise-immune cavity enhanced optical heterodyne molecular spectroscopy (NICE-OHMS) [47].

In the following text, the wavelength modulation technique is utilized in Section 4.3, and will be discussed in details, while in Section 4.2, a method operating the TDLAS on a zero-background is proposed and proven to be able to improve the systemic SNR in another way.

## 4.2 Zero-background TDLAS

### 4.2.1 Working principle

Several zero-background spectroscopic techniques can be mentioned before we discuss the zero-background TDLAS. Laser-induced fluorescence (LIF) spectroscopy produces a signal when the laser frequency is tuned to the molecular absorption line. This

technique is sensitive enough to track a single ion or atom [48, 49]. Similarly, in photo-acoustic spectroscopy, the acoustic signal appears when the laser wavelength matches an absorption line to excite the molecules [50]. Another prominent example is polarization spectroscopy [51], where a crossed polarizer placed in front of the detector will normally block out the linearly polarized laser light background. Only at the line center the polarization plane is rotated by the polarized sample and a signal occurs from zero-background providing a higher sensitivity compared with standard saturation spectroscopy [105]. In the above techniques, a spectroscopic signal ( $I_s$ ) rises from a zero or low background. The SNR of such zero-background techniques is described by

$$SNR = \frac{I_s}{\sqrt{(N_s I_s)^2 + (\beta \sqrt{I_s})^2 + N_t^2}} \quad (4.2)$$

Here, a high SNR can still be obtained even if  $N_s I_s$  ( $N_s \ll 1$ ) dominates in the absence of high-frequency modulation. Most importantly, the small quantity  $I_s$  now replaces the large quantity  $I$  in Equation (4.1) when measuring small signals. This explains why zero-background spectroscopies are usually with high sensitivities.

Getting inspired from excellent performances of the above spectroscopic techniques operating on zero background, here we create a background-free signal from the absorption information for normal TDLAS techniques, using a method different from those discussed above. As shown in Figure 4.3(a), a fiber-optic Michelson interferometer is employed in a destructive interference mode to form a zero output intensity, which constitutes the background at the detector for the spectroscopic signal to be recorded. It is worthwhile noting that fiber-optics is not necessary for the proposed technique, thus making it also suitable in the IR region, where fibers are not readily available. When the optical path difference (OPD) of the two arms is adjusted to zero, and the polarization states and the light intensities of both arms are adjusted to be the same, the light intensity will be very low at the detector in the absence of gas absorption. When the gas absorption occurs in one arm, such a balance is perturbed and a non-zero signal ( $I_s$ ) is detected by the detector,

$$I_s = \frac{1}{4}P(1 - k\sqrt{1 - A})^2 \approx \frac{1}{4}P(\frac{1}{4}k^2 A^2 + k\delta A + \delta^2) \quad (4.3)$$

Here  $P$  is the laser power,  $A$  is the gas absorption,  $k$  ( $0 < k < 1$ ) is a balance factor for intensities of the two interfering light beams, and the unbalance factor  $\delta$  is defined as  $\delta = 1 - k$ . It is worthwhile noting that  $\delta$  has an amplification function similar to the bias angle  $\theta$  in a polarization spectroscopy [51]. A non-zero  $\delta$

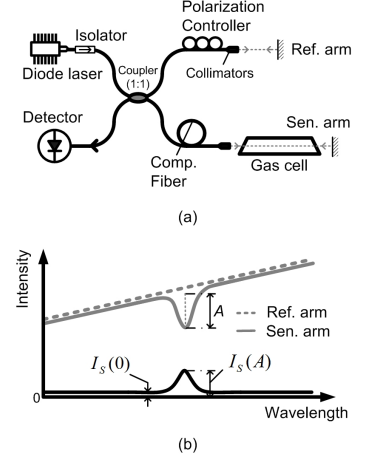


**Figure 4.3.** (a). Schematic diagram of zero-background TDLAS; (b) the principle for forming the zero background, adapted from Paper VII.

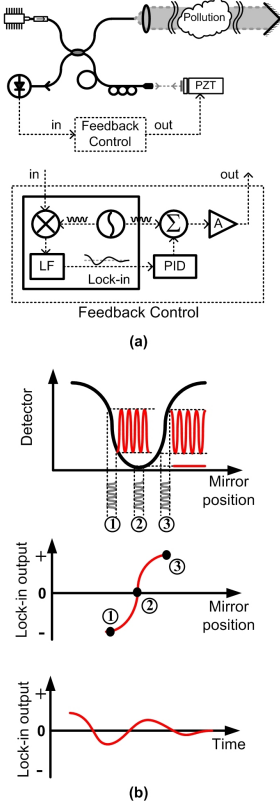


**Figure 4.4.** (a) The schematic diagram of the feed-back control on the interferometric phase, and (b) illustration of the working principle, adapted from Paper VIII.

improves the responsivity of measurement (see the second term of Equation (4.3)); however, degrades the systemic SNR since a higher-level background appears at the detector. Detailed theoretical analysis has been performed and calculation results can be found in Paper VII. Further, proof-of-principle experiments on methane have also been carried out to investigate the performances of such a zero-background TDLAS. As believed, the SNR can be much improved comparing to a conventional TDLAS, where the absorption signal is measured on a huge light intensity background.

## 4.2.2 Real-world application considerations

### Destructive interference

As discussed above, one key property of the zero-background TDLAS is that the interferometer works in a destructive mode, which produces a zero/very low background. However, such a magic status is very hard to passively keep, especially in real-world remote applications, where the sensing arm integrates a long-path of absorption; e.g., in differential optical absorption spectroscopy (DOAS). The turbulence of the atmosphere or the temperature-induced variation in the refractive index, as well as the mechanical instability, can easily turn the destructive interference into a constructive one, by changing the optical path lengths of the interfering arms with half wavelength. Therefore a close-loop controlling design on the mirror position in at least one arm is necessary to actively compensate the instabilities described above.

The proportional-integral-derivative (PID) controller is known to be the most commonly used feedback controller, which can swiftly adjust the target output to the setting point without knowing the underlying process. Such a function can be realized in either hardware fashion or software fashion, and the cost is low due to the mass production of general electronic devices. For the above reasons, we choose a PID controller as the key component in our close-loop controlling scheme. We realized that the interference signal at the detector can not directly work as the feedback for the PID, since the aim is to optimize the light intensity at the detector to be lowest as realizing the destructive interference, while the PID controller, if the sign of parameter I stays the same, principally can work only when the response function performs in one direction.

To solve this problem, Figure 4.4(a) shows a design containing a lock-in scheme. The output signal from the PID controls the horizontal position of the mirror through a piezo-electric transducer (PZT), after being amplified by a PZT driver. A perturbation signal from the oscillator of a lock-in amplifier is superimposed onto the controlling signal, and the responses of the interferometer can be seen from the top of Figure 4.4(b) at different mirror positions.

When the mirror position is controlled at the destructively interferometric position (2), the oscillating part of the detected light is very low, while when the mirror moves towards both sides (position 1 and 3), the oscillation increases in intensity but with phases different by 180 degree, which decides the sign of the signal output from the lock-in amplifier, as shown in the middle of Figure 4.4(b). Such a signal feeds back to the PID, where the target function is set to be zero, and the controller will automatically adjust the mirror to position 2, where the destructive interference is realized.

The feedback controlling system shown in Figure 4.4 was constructed, and good performance was obtained. A lock-in amplifier (EG&G\PARC, 5209) containing an internal oscillator was employed, and the frequency of the perturbational signal (sinusoidal waveform) was set to be 9 kHz. The PID controller is from Stanford Research System Inc. (SRS, SIM960), with a bandwidth of 40 kHz, which is sufficiently fast for compensating environmental instability (usually less than 1 kHz). The PZT driver (Thorlabs, MDT690) can transfer the controlling signal (0-10 V) into a driving voltage (0-150 V). The obvious difference of the light intensity at the detector between situations with and without feedback controlling is shown in Figure 4.5, where the curve is normalized to the maximum value. From 350 s to 550 s, when the control is applied, the destructive interference is stably maintained with the light intensity at the detector being lower than 0.5% of the maximum light intensity when constructive interference is achieved, in the time period when no control is applied. From the bottom figure, where the details of the curve from 400 s to 500 s are shown, the residual light intensity, ca. 0.43%, can be seen due to the non-zero unbalance factor in a real world. The fluctuation of the curve is better than 0.025%, which shows the success of the controlling system.

### Unbalance factor

From Fig. 2. of Paper VII and Equation (4.3) we noticed the signal intensity is amplified by the unbalance factor of the interferometer, which indicates, on the other hand, any minor variation of the interfering structure can induce an obvious instability on the result. In measurements, as generally understood, the intensity difference between the signal peak ( $I_s(A)$ , corresponding to the absorption dip; see Figure 4.3) and the background ( $I_s(0)$ , where the absorption is zero) is used to estimate the absorption induced by the gas. However, as can be seen from the curves shown in Fig. 2. of Paper VII, the problem originates from the dependence of the responsivity on the unbalance factor. The same external absorption induces a higher signal with a larger unbalance factor. The structure degrading in the sensing arm will make an over-estimate of the pollutant concentration. It is especially serious when the external

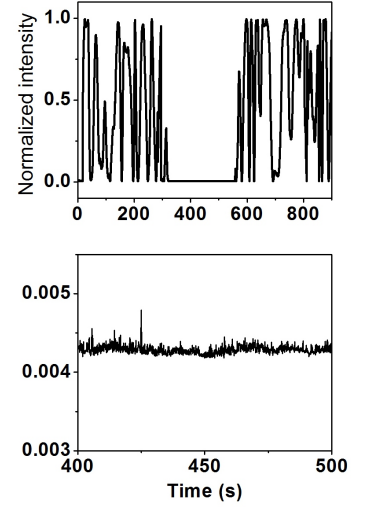


**Figure 4.5.** The demonstration of the performance of our feedback controller. The bottom figure shows details of the curve when the feedback controlling is applied and the destructive interference is stabilized. (Adapted from Paper VIII.)



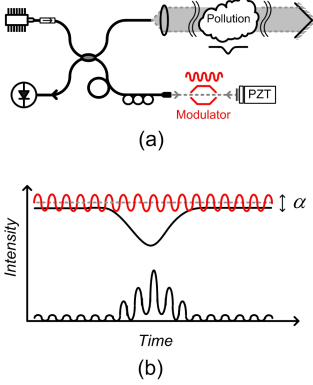


**Figure 4.6.** (a) The schematic diagram and (b) the principle illustration of the modulation version of the zero-background DLAS

absorption ratio is small. For instance, when the absorption under test is 0.001, a degrading of  $\delta$  from 0.001 to 0.002 could induce a factor 1.8 of increase in the signal. It is almost impossible to avoid such minor degrading in real-world applications, especially for remote cases. Either instability of mechanics or dust and dirt on optics can easily destroy the measurements in absence of frequent calibrations. Therefore a different method for signal extraction is required.

We realize that, if the unbalance factor is artificially modulated at a certain frequency, with a stable amplitude, the absorption signal will appear at the modulation frequency and be amplified by the modulation amplitude instead. The variation of the unbalanced factor induced by the structure natural degrading will show ignorable influence at the modulation frequency. Importantly, if the modulation amplitude is controlled to be reasonably small, a close-to-zero background can still be kept. Modulation can further suppress the noise by going to high frequency, but it is not discussed here.

Figure 4.6 shows one possible scheme to realize the above technique. A modulator that can accurately control the modulation amplitude ( $\alpha$ ) is inserted in the reference beam. Therefore the light intensity  $I_s$  at the detector is consequently modified as,

$$I_s = \frac{1}{4} P (\sqrt{1 + \alpha \cdot \cos(2\pi f t)} - k \sqrt{1 - A})^2, \quad (4.4)$$

where  $f$  is the modulation frequency and  $\alpha (\alpha \ll 1)$  is the amplitude. The signal at the modulation frequency can be approximately expressed as

$$I_s^f(A) - I_s^f(0) \approx \frac{1}{4} P \left[ \frac{1}{4} \alpha k A + O(A^2) \right] \quad (4.5)$$

Comparing Equation (4.5) with Equation (4.3), the amplification coefficient is changed from the unbalanced factor  $\delta$  to a stable modulation amplitude  $\alpha$ . The modulation-version system is thus expected to be more stable than the non-modulated one. From Equation (4.5), one can calculate that when the unbalance factor degrades from 0.001 to 0.002 (balance factor from 0.999 to 0.998), the signal only changes 0.1%.

### 4.3 Gas in scattering media absorption spectroscopy

#### 4.3.1 Principle and technique

The TDLAS is well known for gas tracing in free space, but is new for measurements of gases contained in turbid scattering media. Lund University has demonstrated it feasible by analyzing the

weak light that leaks from the sample after massive scattering [52]. Figure 4.7(a) shows two possible arrangements of transmission and reflection modes, depending on the scattering material and practical measurement conditions. The spectrum of the diffused light consists of a broad background due to the solid/liquid attenuation and sharp structures due to the gas-molecule absorption. From such fingerprints, the gas types can be recognized and the concentration can be evaluated from the absorption intensity. The technique is therefore named GAs in Scattering Media Absorption Spectroscopy (GASMAS).

Oxygen and water vapor are two typical gases measured in scattering media. Oxygen is present with 21 % in natural air while the saturated water vapor pressure only depends on the temperature in a sealed environment, which is usually valid for GASMAS applications. Through studying the concentration of them, the activity of the isolated local environment as well as its interchange with the external atmosphere can be well understood. Oxygen and water vapor are measured at wavelengths of 760 nm and 935 nm, respectively, for many practical reasons. Firstly, diode lasers with sufficiently narrow linewidth are commercially available at these wavelengths. Secondly, scattering media under test, which are frequently bio-materials, present a transparency window considering the absorption of haemoglobin at wavelength shorter than about 630 nm, and of liquid water at wavelength longer than 1.4  $\mu\text{m}$ . Thirdly, sensitive detectors, including PMTs and semiconductor photodiodes, are available for the wavelengths.

Due to the weak absorption of both gases at the indicated wavelengths, modulation of the light source is necessary to enhance the system sensitivity. Wavelength modulation is a well-developed tool for TDLAS by sinusoidal modulating the laser wavelength during the linear scan, and detecting at harmonics of the modulation frequency (the second harmonic,  $2f$ , is a common choice). A portable system for gas analysis in different scattering media has been developed at Lund University and measurements have been carried out on various porous materials including polystyrene foam, wood, pharmaceutical tablets, human sinus cavities and packaged food. Food package monitoring based on GASMAS technique is particularly discussed in this section, as an important part of the environmental monitoring from general understanding.

It is worthwhile mentioning that the effective path length of the scattered light is not defined in the GASMAS technique and the absolute concentration of the gas is hard to extract using the Beer-Lambert law. Nevertheless, it is possible to know the concentration of the oxygen if the water vapor, the concentration of which is well known from the temperature in the sealed environment, works as a reference gas to calibrate the scattering path length that is assumed to be close/related at the two wavelengths. As described in Section 3.2.4, the LIDAR technique can accurately

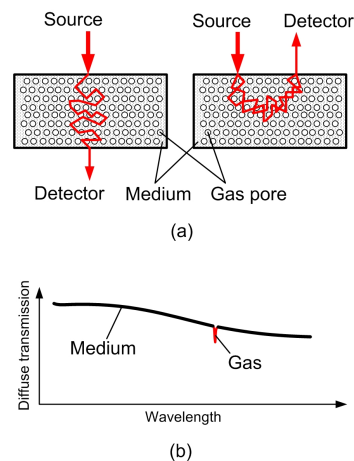


**Figure 4.7.** Working principle of the GASMAS technique: (a) the schematic diagram and (b) the diffuse transmission spectrum

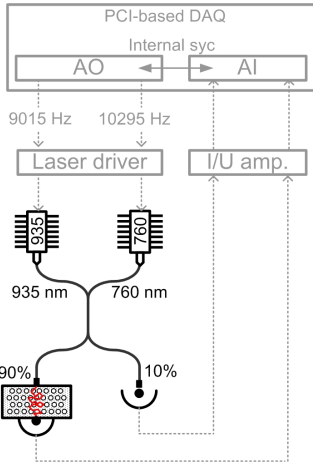


**Figure 4.8.** Experimental arrangement of the GASMAS technique

define the effective pathlength of photons that diffuse in scattering media. Although diode lasers can hardly be pulsed with high energy, it is still possible to obtain the photon distribution in the time domain, by statistically counting the delays of single photons captured by a sensitive PMT [106, 107]. In Section 4.3.3, differently, we demonstrated that the diffuse path of light in scattering media can also be assessed in the frequency domain, by linearly modulating the laser wavelength, which is very simple for a diode laser. With pathlength information obtained by such techniques, the absolute concentration of the gas contained in scattering medium can be measured.

The GASMAS system developed by the Lund research group is a fiber-based dual-beam system based on coherent sampling and digital wavelength modulation spectroscopy (dWMS). A schematic of the instrumentation is given in Figure 4.8. Two pigtailed DFB diode lasers (Nanoplus, Germany) are employed for oxygen and water vapor detection, by running at wavelengths of 760.445 nm and 935.686 nm, respectively. Through a 1:1 fiber coupler, the two laser beams merge into one, which is later split by a second coupler into 90%, as the sample arm, and 10%, as the reference arm, respectively. The scattering medium is placed in the sample arm for gas analysis; while in the reference arm, the fiber end is very close to the detector so that only the interference pattern originating from optical components can be measured, without containing any gas absorption signal. The detectors are two photodiodes (S3590-01, Hamamatsu), and the detected signals are amplified by two current-voltage amplifiers (DLPCA-200, FEMTO Messtechnik, Germany) and recorded at the analog input terminations of a PCI-board DAQ equipment. The analog outputs of the same board are used to generate the modulation waveforms for both lasers, through two diode laser drivers (06DLD103, Melles Griot). The modulation waveforms consist of a 5-Hz triangle waveform and a sinusoidal waveform with frequency of 9015 and 10295 Hz, respectively, for the oxygen and water vapor lasers. In this way, the signals corresponding to the two gases can be distinguished in the frequency domain. More details of the system are described in Paper X.

An example of acquired raw data from the sample arm,  $u_s(t)$ , and its corresponding Fourier spectrum are shown in Figure 4.9. One can see that the  $1f$  components are dominated by residual amplitude modulation (RAM) of the diode lasers, while the  $2f$  harmonic signals are used in detection for baseline-free property and good SNR. In contrast to conventional WMS, where a lock-in amplifier is used to monitor a single frequency channel, dWDM simulates the lock-in function in a digital way. As introduced in [108], the  $2f$  harmonic signal in the frequency domain is filtered out by a bandpass filter, down converted to zero frequency, and transferred into the time domain again through an inverse

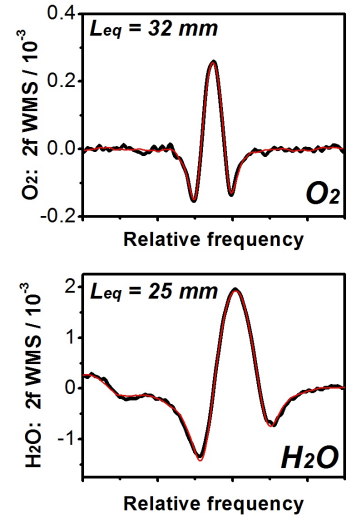
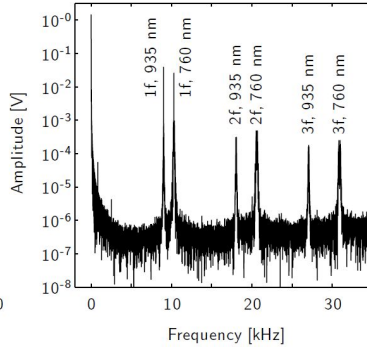
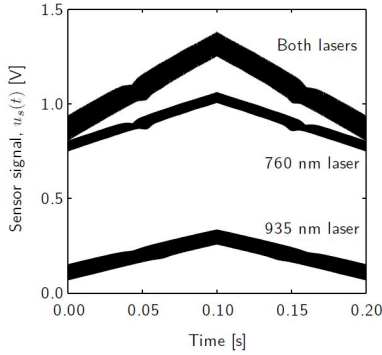


**Figure 4.9.** Raw data exemplified by a measurement on a 1000 mm path through ambient air. Two lasers contribute to the detected signal, and the individual contributions and their sum is shown in (left). A single-sided amplitude spectrum of the full signal (both lasers) is given in (right), showing 1-3 f WMS components due to interactions with absorption features [Paper X].

**Figure 4.10.** Background-removed 2f WMS signals (black curves) and their fitting with ‘standard’ signals (red curves) obtained from e.g., the measurement shown in Figure 4.9, adapted from Paper X.

Fourier transformation. Typical 2f WMS signals are, for instance, shown in Figure 4.10. In case when the absorption signal is weak, the interference pattern induced by the fiber devices etc. can degrade the SNR, and make the measurement impossible. For this practical reason, the signal from the reference arm, which does not include any gas absorption but only shows the interference pattern, is recorded simultaneously. After removal of such a background, the signal of the sample arm, shown as black curves in Figure 4.10, is used to fit a ‘standard’ WMS signal (shown as red curves) which is recorded for a strong and well-known absorption beforehand, e.g., from the measurement shown in Figure 4.9. Using a specific fitting algorithm, the absorption signal is deduced as equivalent pathlength ( $L_{eq}$ ). Details of the above-mentioned signal process method can be found in [109]. For even better SNR, which is required in, e.g., clinical studies, a much more comprehensive and effective algorithm is proposed in Paper X, by considering both real and imaginary parts in Fourier transformations.

### 4.3.2 Food monitoring

Using the above described instrumentation, both oxygen and water vapor are measured in scattering food samples including packaged minced meat, packaged bake-off bread and milk cartons, and the equivalent pathlengths of them are evaluated.

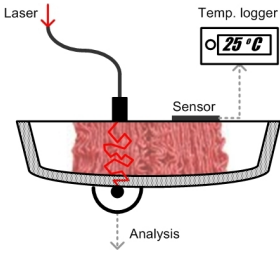


**Figure 4.11.** Geometrical arrangement in minced-meat measurements

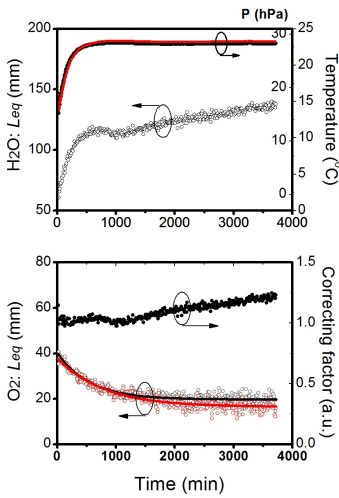


**Figure 4.12.** Experimental results from the minced-meat measurement, adapted from Paper IX

### Minced meat

As shown in Figure 4.11, a meat package purchased in a local grocery store was measured over three days in the laboratory by the GASMAS technique described above. The minced meat was packaged in a tray of polystyrene foam, and covered by a transparent plastic film. The fiber-coupled laser light was injected through the plastic film, and the light passing through the meat and the tray was detected by the photodiode. In the data analysis process, the dWMS signal was averaged within 1 minute for each measurement, which was performed every 10 minutes. Since the meat package was frozen before putting to a room-temperature environment, its temperature was monitored with a temperature logger (Picotechnology TH-03) during the measurement. In the experiment, we noticed that the temperature measured on top of the minced meat sample correlated with the one measured inside the meat, only with an offset as a difference. Therefore, the temperature inside the meat principally can be known by just measuring the top temperature, without invasion into the package.

The top of Figure 4.12 shows the obtained  $L_{eq}$  values (dark circle marks) of water vapor in a minced meat package over time. The temperature measured inside a similar package is shown as dark curve in the figure, and the corresponding partial pressure is calculated through the Arden Buck equation [110] and presented in red, since the relative humidity is expected to be 100% in the closed volume. The sharp increase of the GASMAS signal at the beginning can be seen to originate from the temperature-dependence of the water vapor signal. In later measurement stages, the difference becomes obvious between the stable water vapor pressure (deduced from the temperature) and the slightly-increasing signal. This is attributed to the variation of the photon diffusing path, induced by the geometrical instability in the long term measurement. However, such a variation can be quantified by dividing the GASMAS curve over the pressure curve, see dark solid marks in bottom of Figure 4.12, and used for correction purpose in the oxygen measurement.

The  $L_{eq}$  value of molecular oxygen in the minced meat package over time is presented as dark circles marks at the bottom of Figure 4.12. The data applied with path-variation correction are shown as red circles. From their exponential fits (dark and red curves, respectively), the correction effect can be clearly seen. With the path-variation removed, the red curve, as believed, presents the oxygen concentration in the package with better accuracy. The decrease of the curve over time, is interpreted as the minced meat consuming ambient oxygen by oxidation.

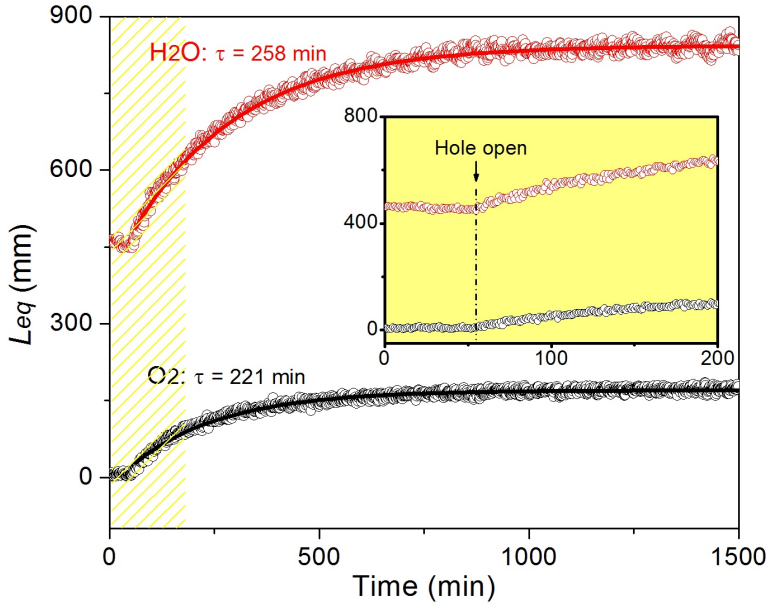


**Figure 4.13.** Experimental results from the bake-off bread measurement. Circle marks show the 1-min averaged signals of water vapor (red) and oxygen (black), respectively. Exponential fits after the puncture are presented as solid curves. The inset shows the immediate change of the signals when the puncture happens. (Adapted from Paper IX.)

### Bake-off bread

A plastic package containing eight buns of bake-off bread in a modified oxygen-free atmosphere was measured for 25 hours. The light was injected through the plastic film into one bun, and detected in a transmission mode at the other side of the package. Differently from the minced meat, the package of bake-off bread was all the time at room temperature. After around one hour of measurement, a hole of about 1 cm in diameter was made in the package, resulting in air flowing into the package. The signal was measured for 24 further hours, with each measurement proceeding for 1 minute for average. The time-signal curve can be further (off-line) smoothed by averaging, e.g., 10 adjacent points over time of 10 minutes.

Experimental results for the bake-off bread are shown in Figure 4.13. At the dash dotted line in the inset, a hole of about 1 cm was made in the package. The very low values of oxygen before the puncture show the absence of such a gas, since the tight package stopped the penetration of external air. At puncture, an immediate change was observed for both oxygen and water vapor, since a path to the external atmosphere was open. The increase of the water vapor signal shows that a 100% relative humidity was



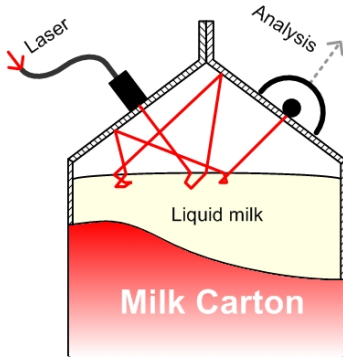


**Figure 4.14.** Geometrical arrangement in the milk-carton measurement

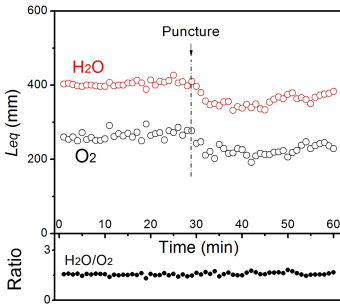


**Figure 4.15.** Experimental results from the milk-carton measurement, adapted from Paper IX

not present in the non-perforated package due to lack of water, not allowing saturation. However, water vapor was present in the non-perforated package since an initial value of 450 mm was measured. The time constant of the diffusion of molecular oxygen and water vapor into the bread bun was  $\tau=211$  min and  $\tau=258$  min, respectively, using an exponential fit.

### Milk carton

As shown in Figure 4.14, even the headspace of a milk container, made of white and red paper of 0.5 mm thickness, can be monitored by a GASMAS technique. The laser light was injected through one paper surface and detected at the opposite surface. As indicated in the figure, multiple passages of the laser beam due to the scattering result in a larger signal than corresponding to the physical geometry. In the total 60 minutes of the measurement, a small hole of about 2 mm diameter was open at around 30 minutes.

Results for water vapor and molecular oxygen from the measurements over time are shown in Figure 4.15. As the package is perforated an offset in the water vapor and oxygen signal is seen. Under the perforating process small displacements of the detector and injecting fiber are noted, which can provide an explanation for the offset. Small displacements of especially the injecting fiber can give effects on the path length of the detected light. The ratio of the oxygen and water vapor signals is presented and keeps stable over the whole investigation. A 100% relative humidity is expected since the large wet surface fully moisturises the gas in the head space in spite of the ventilation. The stable ratio suggests that the oxygen concentration in the headspace in the milk carton was the same as in the ambient air.

### 4.3.3 Path-length assessment

As indicated in the above descriptions, one advantage of the GASMAS technique originates from the massive scattering, which extends the effective absorption pathlength as a White cell does, while, on the other hand, such an extension is not defined and depends considerably on the scattering medium, and the geometrical arrangement of the illumination and the detection. A slight perturbation during the measurement could change the light propagating path in the medium and hence influence the experimental results. Such effects have shown up in the measurements on the minced meat and the milk carton in the above subsection. In both cases, the saturated water vapor is used as a reference gas for pathlength calibration, which is rough since the scattering paths of these two widely-separated wavelengths (760 nm and 935 nm) are not exactly the same.

To solve the problem, the path-length of photon propagating in scattering media is required to be evaluated. A straightforward method is a LIDAR-fashion technique, where the sample is illuminated with short-pulse light, and the photons that appear at the detector are counted by time of flight, as shown in Figure 4.16. The extended tail in the recorded curve is due to the scattering events, and can be used to evaluate the average pathlength of photons that propagate through the sample. Such techniques have been reported in [53], to supply pathlength information for GASMAS measurements, and discussed in Section 3.2.4 and Paper **II**, as well, for gas analysis combining the differential absorption technique. The above-mentioned equipments employ Q-switched high-power solid-state lasers, but considering the cost and convenience of operation, diode lasers clearly have great advantages. For instance, the path-length evaluation and the GASMAS measurements are possible to be combined into one instrumentation employing the same light source and detector. Diode lasers can work in pulsed mode with extremely high repetition rate although each pulse energy is relatively weak. Thus, transient digitizer techniques cannot be used for capturing time-resolved signals. Instead, a technique called time-correlated single photon counting (TCSPC) [106, 107] is frequently employed to generate a histogram of arrival times of individual photons at the detector, a PMT which is cooled down to reduce dark current counts. Fast electronics matching the pulse width of the laser source are required.

Another method to utilize diode lasers for path-length analysis in scattering media is called the frequency modulation continuous wave (FMCW) method, and has been presented in Paper **XI**. The idea is inspired from the application of the FMCW technique on range finding in free space [111] or fiber network [112], where single scattering is frequently assumed. We show that the extension to multiple scattering is straightforward by illustrating the schematic diagram and the working principle in Figure 4.17 and Figure 4.18.

As in the conventional FMCW technique, the frequency of the laser source is linearly modulated with, e.g., a triangular waveform. The modulated light is then separated into two beams, a reference beam and a probe beam. The reference beam passes through a well-known distance while the probe beam passes through an unknown optical path length. Both beams arrive at the same detector and interfere with each other. A beat frequency ( $f_b$ ) proportional to the time delay ( $\tau$ ) between these two beams will be induced in the detected signal (see Figure 4.18(b)). This specific frequency can be used to deduce the path length of the probe beam. In the case when the probe beam passes through a multiple scattering medium, the path lengths of the photons will show a distribution with an extended tail indicating the scattering information, in the frequency domain. With detailed theoretical analysis of the technique given in Paper **XI**, two conclusions can be drawn. Firstly,

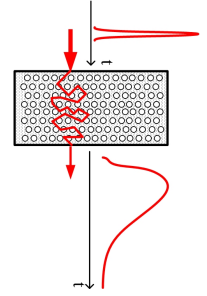


**Figure 4.16.** Pulsed light extends after propagating through a scattering medium.



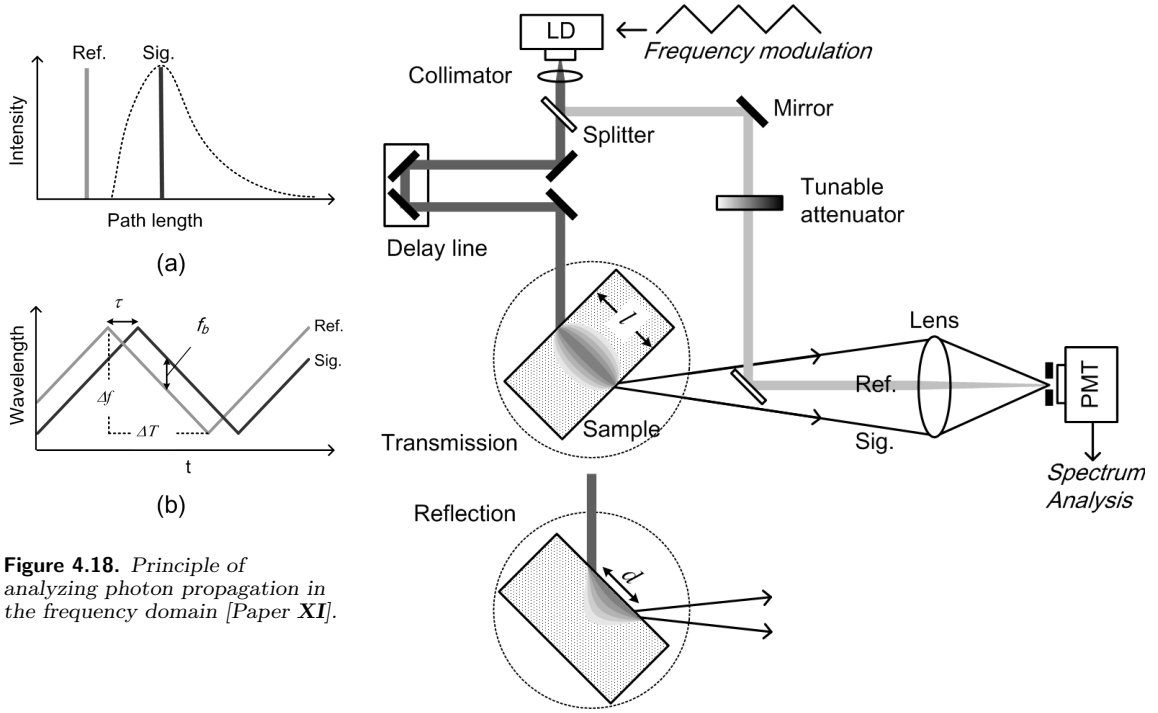


**Figure 4.18.** Principle of analyzing photon propagation in the frequency domain [Paper XI].

**Figure 4.17.** Schematic diagram of the FMCW technique for path-length assessment in scattering media [Paper XI].

the measuring range is limited by the coherent length of the laser source due to the interference basis of the method. Second, the minimal resolvable optical path length ( $R$ ) is determined by the frequency range of the modulation ( $\Delta f$ ) through  $R \approx c/\Delta f$ , where  $c$  is the speed of light in vacuum.

For demonstration, an experimental system was built according to Figure 4.17, with details described in Paper XI. Generally, a DFB diode laser, operating in a single longitudinal mode, was employed as the light source. By ramping the driving current (and hence the wavelength of the diode) with a triangular waveform, the optical pathlength information of photons passing through scattering sample can be analyzed in the spectrum of the signal recorded by the detector (PMT in the figure). When the driving current is ramped with a 10 Hz triangle waveform, and the tunable range of frequency of the diode is around 40 GHz, the spectral performance at the detector is about 3 kHz corresponding to 1 m of optical path length. The range resolution, according to  $R \approx c/\Delta f$ , can be as high as 0.75 cm, however, degrades to around 3 cm in experimental tests due to Doppler broadening induced by mechanical instabil-

ities. Compared with LIDAR-fashion techniques, which evaluate the optical pathlength in the time domain and require extremely short laser pulse and fast detection electronics, the advantage of the FMCW technique is obvious.

With the developed experimental setup, measurements were performed on different samples including a piece of normal printing paper (white, 100  $\mu\text{m}$  thick), a tissue phantom (a 10 mm thick sample of gelatin containing ink as absorber,  $\mu'_s = 6.9 \text{ cm}^{-1}$  and  $\mu_a = 0.3 \text{ cm}^{-1}$ ), and polystyrene foam (11 mm thick,  $\mu'_s$  is ca.  $30 \text{ cm}^{-1}$  and  $\mu_a$  is ca.  $0.001 \text{ cm}^{-1}$ , respectively). Obvious differences can be seen in Figure 4.19. The thin white paper presents a narrow curve, which is limited by the systemic resolution 3 cm. In the tissue and the polystyrene foam, an extended tail, due to the multiple scattering, can be clearly seen. And as expected, the polystyrene foam presents stronger scattering than the tissue. As indicated in Figure 4.17, samples can be measured in both transmission and reflection modes. Measurements were also performed on polystyrene foam with different thicknesses (see  $l$  in Figure 4.17) in the transmission mode, as well as in the reflection mode, where the illumination-observation distance ( $d$ ) was adjusted. Encouraging results were obtained and have been published in Paper **XI**.

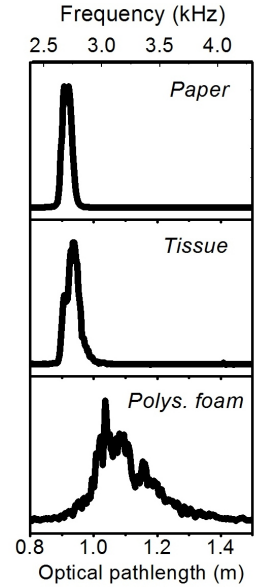


**Figure 4.19.** Spectral responses for different samples. Curves are normalized to the maximum values [Paper **XI**].



---

# FIBER-OPTIC SENSORS

---

Fiber-optic sensors, based on the optical fiber itself or other sensitive fiber devices, constitute an important division of sensor technology. It has been developed for half a century since the perfection of communication fibers in 1960s, by Charles K. Kao, who later won the 2009 Nobel Prize in Physics for his contributions. Specific advantages of fiber-optic sensors over others can be mentioned. For instance, fiber-optic sensors are electronically passive in measurements and with good immunity to electromagnetic interference (EMI). Many units of them are possible to be connected with communication fibers, and a sensor network with high geometrical flexibility can be formed. A single communication fiber is able to lead out all the sensing information from the sensor network, and the signal of each sensor unit can be detected and analyzed remotely. With such advantages, arrays of fiber-optic sensors are employed for remote temperature and strain monitoring in structures such as buildings, bridges, tunnels, etc. In this chapter, we will particularly discuss the fiber-optic sensor used for methane monitoring, which is critical for occupational safety in, e.g. coal mines, especially in Third World countries like China.

In Section 5.1, a very important candidate for fiber-optic sensor, the fiber Bragg grating (FBG), is introduced. The working principle of FBG sensors, and some interrogation schemes for such sensors are described. Further, in Section 5.2, a novel FBG-based methane sensor is proposed. A type of catalyst is employed to transfer information on the methane content in ambient air into heat, which is measured by the sensitive FBG device. The wavelength shift of the sensing FBG is later read out through a reference FBG, and high sensitivity (with minimal detectable signal of 64 ppm) is realized. Last but not the least, in Section 5.3, a low-coherence multiplexing scheme is applied on sensors with such double-grating structures, so that multiple methane sensors are

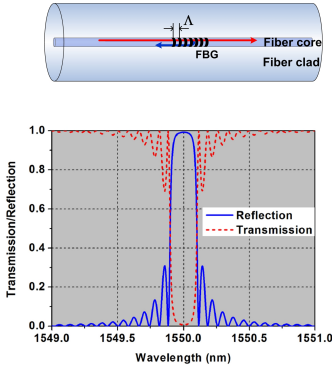


**Figure 5.1.** Schematic diagram (top) and spectral responses (bottom) of a typical FBG

possible to be connected into one network that shares a common light source and detection system.

## 5.1 Fiber Bragg Grating (FBG)

### 5.1.1 Basics of FBG

Generally speaking, the fiber Bragg grating (FBG) is a periodic modulation of refractive index in the fiber core. Similar to a conventional diffraction grating, where the light with certain frequency (color) diffracts at a certain angle according to the grating equation, the Bragg grating in a single-mode fiber couples a narrow band of propagating light back into the counter-propagating direction, matching the resonance condition,

$$\lambda_R = 2 \times n_{eff} \cdot \Lambda \quad (5.1)$$

where  $\lambda_R$  is the resonant wavelength indicating the central frequency of the reflection spectrum,  $n_{eff}$  is the effective refractive index of the fundamental guided mode in the fiber core, and  $\Lambda$  is the grating period. In contrast to the reflection spectrum, an attenuation dip presents in the transmission. The typical reflection and transmission spectra at the communication wavelength 1550 nm are shown at the bottom of Figure 5.1. According to Equation (5.1), the period of the grating can be estimated to be about 500 nm, by knowing that  $n_{eff}$  is about 1.5 for the fiber-core material,  $\text{SiO}_2$ . Therefore the FBG is principally a nano-structure. Like the resolution of a diffraction grating, the width of the reflection band of the FBG is determined by the grating period number. For a grating with a length of 1 cm, the typical value is 0.1 nm.

An FBG is a narrow-band fiber mirror very useful for constructing fiber lasers and also passive components such as fiber etalons [113–115]. Meanwhile, FBG is also a filter with central wavelength tunable; both the grating period and the refractive index depend on the environmental temperature and the strain applied on the fiber. Such fiber filters are massively used now for uploading or downloading certain signal channels at specific wavelengths, in wavelength domain multiplexing schemes of fiber-optic communication [116, 117]. Another very important application of FBGs is constructing fiber sensors, which will be discussed in detail in the next subsection.

The first FBG was unintentionally fabricated by the Canadian scientist K.O. Hill in 1978 [61], when studying the nonlinear effect of a communication fiber. The 488 nm radiation from an Argon-ion laser was coupled into the fiber from one end, and interfered with the light reflected from the other end surface. After long-term exposure, the interference pattern induced a periodic change in the refractive index of the fiber core, i.e., the first FBG in the

world was created. Later, researchers found that the fabrication efficiency can be much improved by exposing UV light on the side of photosensitive fibers, where the core material is doped with Be and Ge, or treated in an environment with a high pressure (100 atmosphere) of hydrogen and high temperature (100 °C) [118]. The interference pattern can be produced by using two interfering laser beams with good coherence (like making a hologram) [119], or simply by employing a phase mask, as shown in Figure 5.2 [120, 121]. The phase mask is designed to suppress the zeroth order of the diffraction while enhancing the positive and negative first orders, the interference of which produces a periodic distribution of the light intensity on the fiber side, and the FBG can be formed in the fiber core. Clearly, the phase-mask technique achieves a dependable and repeatable way in fabrication, particularly since moderate requirements on light coherence allow robust and cost-effective pulsed excimer UV laser to be employed for fabrication. Therefore, the invention of the phase-mask technique made mass production possible and considerably promoted the FBG industry in the 1990s.

In Zhejiang University of China, the development of an automatic FBG fabricating system, shown in Figure 5.3, has been started by the author and his colleagues in 2003. Basically, a pulsed KrF excimer laser (248 nm; Tuilaser, Germany) is used as the light source, which can be well adjusted and focused on the fiber side, through some optics and a phase mask. A linear stage (Newport, USA) driven by a stepper motor, carries optical devices and can accurately position the laser beam along the fiber radial direction. An optical spectrum analyzer (OSA; ANDO AQ6317, Japan) was used to monitor the spectral performance while the grating grows. It is worthwhile mentioning that the laser and the step motor are well synchronized by a program, and repeatable fabrication can be realized by simply clicking one button on the software. The photosensitive fiber used in fabrication includes commercially available Be/Ge doped fiber (Fibercore, UK), or SMF-28 fiber (Corning, USA) which is treated with high-pressure and high-temperature hydrogen in a home-made container.

### 5.1.2 FBG sensors

FBG has proved to be very successful for fiber-optic sensing. As a single-point sensor, the resonant wavelength of a FBG is sensitive to the variation of the environmental temperature and the strain applied on the fiber, through Equation (5.1). The strain response arises due to both the physical elongation of the sensor (and corresponding fractional change in grating period,  $\Lambda$ ), and the change in fiber index,  $n_{eff}$ , due to photoelastic effects, whereas the thermal response arises due to the inherent thermal expansion of the fiber material and the temperature dependence of the refractive index.

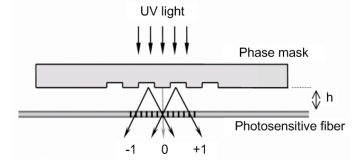


**Figure 5.2.** The phase-mask technique for FBG fabrication



**Figure 5.3.** The FBG fabrication system at Zhejiang University.

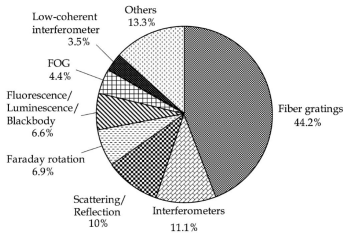


**Figure 5.4.** Distribution of OFS-15 papers according to technologies, adapted from [122].

For single mode fibers operating at communication wavelengths, typical responsivities of a FBG sensor to strain and temperature are around  $1 \text{ pm}/\mu\epsilon$  and  $10 \text{ pm}/^\circ\text{C}$ , respectively. The temperature and strain information can be known by measuring the wavelength shift of the reflection spectrum of a FBG sensor. Use of wavelength detection gains the immunity of the signal to the light-intensity variation because of an unstable light source etc.

The statistics (Figure 5.4) of the 15th Optical Fiber Sensor Conference (Portland, USA, 2002) shows that research interests were specially paid on fiber gratings. When conventional electro-mechanical sensor systems slow down the market penetration of other fiber-optic sensors, the FBG sensors that have all the advantages attributed to fiber-optic sensors, however, win more success because of ease in realizing (quasi-) distributed sensing by employing wavelength coding. Many FBG sensors with different resonant wavelengths can be serially connected within one single fiber, and their signals can be collected, separated and analyzed in a central office remotely, by employing suitable interrogation and multiplexing schemes. Such FBG sensor arrays have been applied in, e.g., concrete structure monitoring in large-scale civil projects like bridges [123–127], stress monitoring on bodies of aircrafts and marine vehicles [128, 129], depth measurements [130] in streams, rivers, and reservoirs for flood control.

### 5.1.3 Interrogation schemes

In an FBG sensing system, the interrogation scheme is sometimes even more critical than sensors. Frequently, the interrogator decides the systematic performances such as sensitivity, dynamic range, multiplexing ability, etc. Different kinds of interrogation schemes for FBG sensor (arrays) are reviewed in the literature [62].

Since the physical quantities are measured through the wavelength shift of the reflection spectrum of the FBG, the interrogation schemes are principally spectroscopic techniques that quantifies such shifts. For instance, optical-grating-based spectrometers (where a CCD is usually employed for detecting the diffracted spectrum) or monochromator (where the spectrum is scanned by rotating the grating and a single detector is used) are two straightforward and effective tools to interrogate an array of wavelength-coded FBG sensors [131]. Similarly, the spectrum can also be scanned by using a tunable light source with narrow line-width [132, 133]. Or otherwise, a narrow-band tunable filter can be used for scanning instead, when a broadband light source is employed [134]. By using a standard Fabry-Pérot etalon for wavelength calibration, the above two scanning methods have become the most commercialized schemes. In contrast to scanning the reflection spectrum point by point, a Fourier transform spectrometer scans one arm of the Michelson interferometer and recovers the

spectral information from the interference pattern. Such a technique has also been proved valid for FBG array interrogation [135], and the spectral resolution (or the system sensitivity) can be high if the scanning range is sufficiently large.

The choice of a specific interrogator depends on the requirements from real applications. Main considerations include the minimal detectable signal and the dynamic range of each single sensor, the multiplexing number of sensors, and the scanning speed of the system, etc. In Figure 5.5, an interrogation scheme with high sensitivity but limited dynamic range is presented. Somewhat different from the above-mentioned schemes based on spectral scan, here, an extra reference FBG (that is placed in a stable environment) is employed to read out the wavelength shift of the sensing FBG. When the reflection spectra of both gratings overlap perfectly, the light presents a maximum intensity at the detector, after being reflected twice by the two gratings. Any spectral mismatch will induce a decay in the detected signal, and the wavelength shift of the sensing grating can thus be measured. Such a simple passive interrogation scheme was firstly published in [136], and has been applied widely. Thanks to the narrow bandwidth (shape spectral slope) of both gratings, the responsivity of such a scheme is extremely high (see, e.g.,  $\text{CH}_4$  measurements in Section 5.2), but as a penalty, the dynamic range is limited. To improve this, the reference grating can be attached on a piezo-electric transducer (PZT), which is controlled by a servo circuit that always actively adjusts the reference grating matching the sensor grating. Through the voltage applied on the PZT, the shift of the sensor grating can be read out. In this way shifting the spectrum of the reference grating following that of the sensor grating, the dynamic measurement range is improved; however, the response speed of the system is much decreased. Such a reference-grating interrogation scheme can be extended for many FBG sensors, simply by employing multiple reference gratings in parallel.

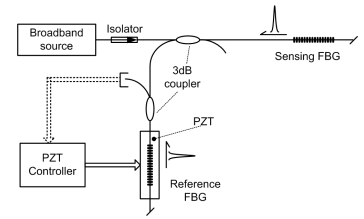


**Figure 5.5.** The schematic diagram of a basic unit of the reference-grating interrogation scheme, adapted from [136]

## 5.2 FBG methane sensor

Methane is a very dangerous gas in coal mines. Occasionally, huge amounts of methane are produced and blast out during the mining operation. The risk of explosion becomes high if the concentration of methane increases above 5% in the local atmosphere. According to statistics, methane-induced explosion is responsible for 95% of coal-mine accidents in China, although according to Chinese law, all mining action must stop and all working staff must leave as long as the methane concentration is above 2%. Without any doubt, it is of great importance to develop a sensor system that can monitor many locations in a coal mine simultaneously, map out the gas diffusion in tunnels, evaluate the danger of accidents, and



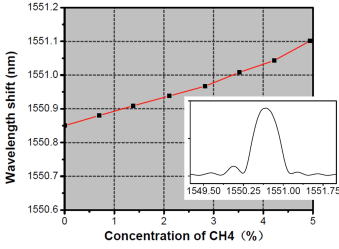


**Figure 5.6.** The reflection spectrum of the FBG shifts towards longer wavelengths as the methane concentration increases. The inset shows the reflection spectrum at room temperature. (Adapted from Paper XII.)

plan evacuation strategies. However, the conventional equipment in Chinese coal mines is a single-point methane meter carried by each staff member, who sometimes finds it is already too late when he/she reads a dangerous concentration. A global sensor network that covers the whole mining area has not been established yet.

### 5.2.1 Methane transducer

The above-mentioned single-point methane meter is based on a type of catalyst (see, e.g. [137]). When the catalyst is warmed up to a certain temperature by applying a current of several hundred mA, it can transfer the methane information into heat, which is then read out by a thermistor through a Wheatstone bridge circuit. Such an electronic methane meter has been successfully commercialized. The minimal detectable signal is about 0.1% within the measurement range of 10%. One main disadvantage of such a methane meter is that the electronic signal could be considerably disturbed by strong EMI from mining machines, when directly read out or through long-distance communication. Therefore, a sensor network is not easy to build.

Considering the advantages of FBG regarding EMI immunity, and in remote/distributed sensing, a FBG methane sensor is developed. The same catalyst with warming-up circuit is still employed. Differently, we utilize a FBG, instead of the thermistor, to read out the temperature information. The grating is fabricated by the system shown in Figure 5.3 using the phase-mask technique. The reflection spectrum is shown in the inset of Figure 5.6. Through some mechanical designs, the grating, attached closely to the catalyst, is packaged into a compact sensor head (see Figure 5.7). In order to test its performance, the sensor head is placed in a gas cell filled with well-mixed gas of CH<sub>4</sub> and air. The ratio between them are accurately controlled through high-accuracy flow meters. Meanwhile, a spectral analyzer (OSA) measures the reflection spectrum in real time when the methane concentration increases from 0 to 5%. Figure 5.6 records the obvious shift of the spectrum, since the local temperature around the FBG increases when the catalyst transforms the methane into heat. A slope of 0.051 nm/1% can be found from the figure, and a minimal detectable signal of 0.39% can be realized using such a spectral analyzer with a resolution of 0.02 nm.

### 5.2.2 Reference-FBG interrogation

In order to improve the systematic sensitivity (at least better than 0.1%), and considering the measurement range is not broad (less than 5%), the reference-grating interrogation scheme described above is an ideal method. Figure 5.7 shows the experimental setup that demonstrates the capability of such a scheme. The light-

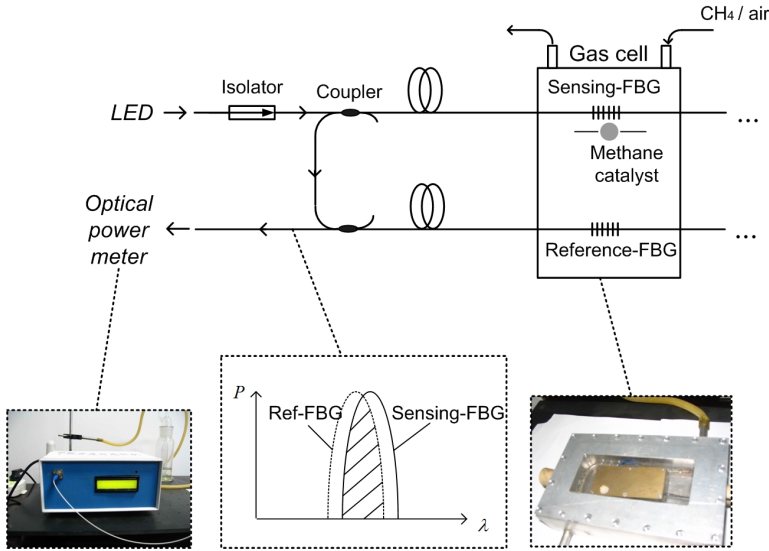


**Figure 5.7.** The schematic diagram of the reference-grating interrogation system for the FBG methane sensor

emitting diode (LED) is a type of inexpensive light source with bandwidth broader than diode lasers. It has found many specific applications in field of optical sensing and measurement, with one example shown in Paper XV. Here a pigtailed LED with central wavelength at around 1550 nm works as a broadband light source. The broadband light passes through an optical isolator (avoiding reflected light back to the light source), a 3-dB fiber coupler, and a long section of communication fiber, before arriving at the sensing FBG. The reflected narrow-band light is coupled to the reference grating and reflected for the second time. The twice reflected light is then detected by a home-made power meter. Basically it is a photodiode with the signal amplified by two stages of amplification circuits. As illustrated in the middle inset of the figure, the reflection spectra of the sensing- and reference gratings are well matched, while the methane in the ambient air will induce a wavelength shift for the sensing grating, which is set close to the catalyst, but not for the reference grating, which is isolated. Such a spectral mismatch will induce an intensity decay at the detector and can thus be measured.

The experimental results are shown in Figure 5.8. When the methane concentration in the gas cell increases from 0 to 6%, the signal at the detector decays with an average slope of  $-0.783 \text{ V}/1\%$ . The top of the figure reveals that such a decay is due to the spectral mismatch between the sensing- and reference gratings, as expected.

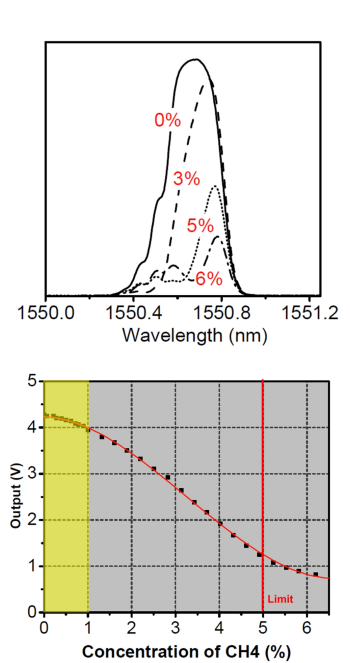


**Figure 5.8.** The spectral (top) and the light-intensity (bottom) responses at the power meter, as the methane concentration increases from 0 to 6%. (Adapted from Paper XII.)

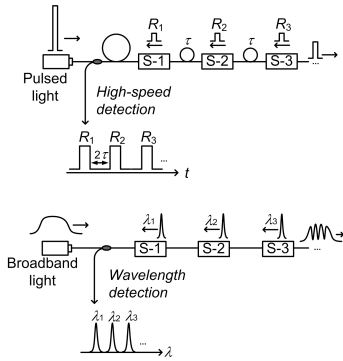


**Figure 5.9.** Illustrations of time domain multiplexing (top) and wavelength domain multiplexing (bottom)

In the experiment, the system is tested to be able to measure a minimal concentration of 64 ppm, which is an improvement of about 60 times compared with using the spectral analyzer, OSA, which basically is a optical-grating-based monochromator.

It is worthwhile particularly mentioning that the reference-grating scheme is inherently immune to the environmental temperature variation. When environmental temperature changes, the spectra of both gratings shift together and the mismatch will not increase, neither the signal at the detector. A stability better than 0.013% of the output voltage from the power meter has been achieved in the situation of increasing the ambient temperature from 30 °C to 60 °C.

### 5.3 Multiplexing schemes

As the key technique for a fiber-optic sensor network, a multiplexing scheme distributes the light energy of the common source among many sensors, and distinguishes their signals at a common termination as well. Two basic schemes, time-division multiplexing (TDM) and wavelength-division multiplexing (WDM), can be mentioned, with their working principles illustrated at the top and bottom of Figure 5.9, respectively. A short-pulsed light source is required in a TDM scheme, which records the reflected light signals in the time domain by employing a high-speed detector. The signals, from the serially connected sensors (S-1, S-2 and S-3), are separated due to the delay lines (sections of fiber) inserted in between. Except for such a quasi-distributed geometry of the sensor network, TDM scheme has also been successfully applied on distributed sensing schemes such as Raman/Brillouin fiber sensors [138, 139]. In later cases, a normal communication fiber works as a distributed sensor, and similar with the LIDAR technique, the Raman/Brillouin backscattering from the fiber is recorded by time of flight. The temperature and strain information contained in the Raman/Brillouin signals, are thus measured along the sensing fiber. The range resolution is limited by the pulse width of the light source and the response speed of the detection system.

The bottom of Figure 5.9 shows a WDM scheme, which separates the sensor signal in the spectral domain. Here broadband light is required for providing sufficient multiplexing ability. Each sensor in the network occupies a certain narrow band of the total spectrum, and their signals can thus been distinguished at the detection termination where the total spectrum is analyzed. Such a method is specially suitable for FBG sensors, the reflection spectra of which are narrow-band, and the resonance wavelengths can be designed by simply changing the grating period.

### 5.3.1 Low-coherence multiplexing

Different from the TDM and WDM schemes described above, there exists another group of techniques that can multiplex interferometric sensors into a network. As illustrated in Figure 5.10, a low-coherence light source is utilized, and the light energy is distributed by fiber couplers (splitters) into parallel-arranged sensors based on fiber-optic interferometers (Mach-Zehnder interferometers in the figure). These interferometers have different lengths in the two interfering arms. The difference is designed to be larger than the coherent length of the light source and with a specific value for each individual sensor. The light beams passing through the two arms of the interferometer cannot interfere until the optical pathlength difference (OPD) is compensated by an extra interferometer (Michelson interferometer in the figure) with the length of one arm scannable. The detector can record an interferometric pattern only when the mirror moves horizontally to certain positions where the OPDs of individual sensors are compensated. In this way, the signals corresponding to the sensors containing different OPDs can be distinguished. Compared with TDM and WDM techniques, low-coherence multiplexing does not need complex high-speed detection or spectral analysis. The multiplexed signals are separated by simply employing mechanical scans, and the requirements for the detection system are intermediate. However, on the other hand, such a mechanical-scan-based method is not valid in applications, e.g., for measuring vibration, where fast response speed is needed.

Initially, the low-coherence multiplexing schemes were applied for sensors that were constructed as interferometers by just using fibers [140–142]. The sensing signal was interrogated as the shift of the low-coherent interference pattern, because of the radial extension of one arm of the interferometer, due to the external influence applied. No spectral information is considered in such applications. Recently, low-coherence multiplexing has been extensively studied at Zhejiang University to be applied on fiber gratings, which can allow compact in-fiber interferometers and also contain rich spectral information [143–149]. For instance, both TDM and WDM methods are not valid for long period fiber gratings (LPGs), another type of sensitive sensors, which present broad transmission spectrum but no reflection. Low-coherence multiplexing instead works by constructing a pair of LPGs into an in-fiber Michelson interferometer [143–145]. Similarly, pairs of FBGs can form Fabry-Pérot interferometers, and they are possible to construct a sensor network multiplexed by low coherence techniques [147–149]. Particularly, the spectral information of gratings is focused in interrogation in contrast to conventional low-coherence multiplexing techniques.

Figure 5.11 shows the schematic diagram of the low-

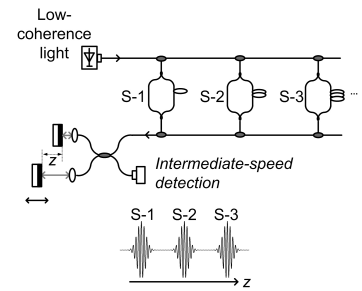


**Figure 5.10.** Illustration of low-coherence multiplexing

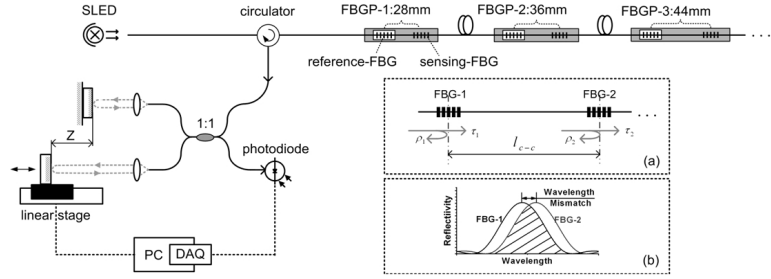


**Figure 5.11.** Low-coherence multiplexing scheme for FBG sensors. In-sets (a) and (b) show the Fabry-Pérot interferometer formed by a pair of FBGs and its working principle, respectively [Paper XIII].

coherence multiplexing applied for FBG sensors, as adapted from Paper XIII. As illustrated in the inset (a), a pair of identical FBGs forms an Fabry-Pérot interferometer, and the OPD between the light beams reflected by the first and the second grating (FBG-1 and FBG-2) is proportional to the center-to-center distance ( $l_{c-c}$ ) between the two gratings. These two light beams can interfere with each other when their OPD is compensated by another scannable Michelson interferometer to be less than the coherent length of the light source (a Superluminescent LED, SLED, here employed), and the interference pattern appears at the detector. By setting the grating gap in each FBG pair (FBGP) to be different, the interference patterns of many serially-connected FBGPs can be separated in one scan of the Michelson interferometer.

In each FBGP sensor, FBG-1 works as a reference grating and FBG-2 is a sensing grating. As shown in the inset (b), when FBG-2 is exposed to the environment under test while FBG-1 is isolated, the induced spectral mismatch will dramatically decrease the visibility of the interference pattern, and thus be measured. Here, the idea of the reference-grating interrogation is applied again, and the good performance discussed above is kept. Details can be found in Paper XIII, where the technique is analyzed in both theoretical and experimental terms.

### 5.3.2 Multiplexing of methane sensors

In Section 5.2.2, the spectral mismatch between two FBGs is used for indicating the methane concentration, and in Section 5.3.1, the low-coherence technique has been introduced to multiplex pairs of FBGs, the spectral mismatch of which can be measured from the intensity of the interference pattern. Therefore, it is natural to combine the two techniques to realize the multiplexing of methane sensors. In order to place the two gratings conveniently, a specific

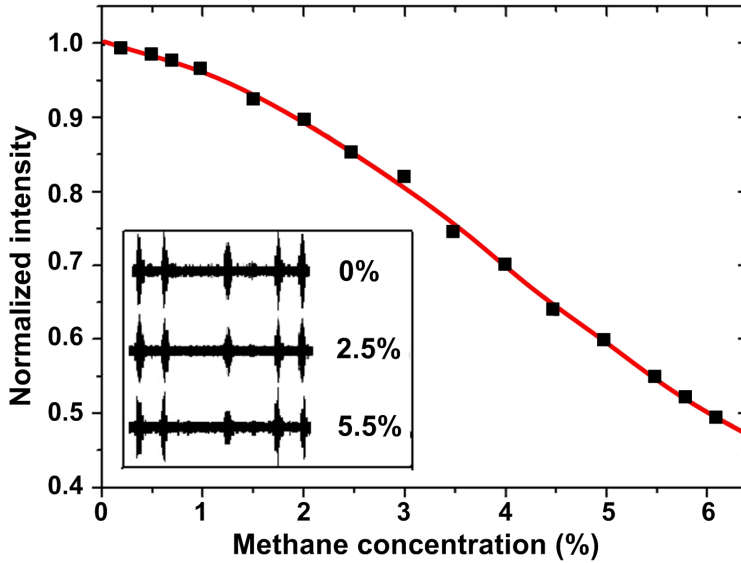


**Figure 5.13.** The intensity of the interference pattern corresponding to the third sensor decreases as the concentration of methane increases. The inset shows the evolution of interference pattern of five multiplexed sensors.

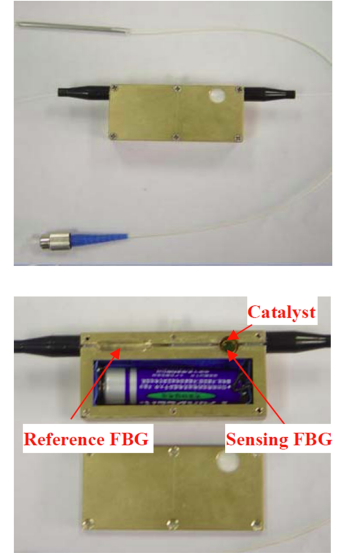


**Figure 5.12.** Methane sensor-head designed for low-coherence multiplexing.

sensor head is designed as shown in Figure 5.12. The sensing FBG locates close to the catalyst, which can transfer the methane information into heat, while the reference FBG is placed away from the catalyst. The gap between the two gratings, as a label for distinguishing among sensors, is set to be different for different units. A 1.5-V battery is installed in the sensor head for powering the catalyst. The battery can be replaced in real applications by a constant voltage cable that is arranged parallel to the optical fiber.

Five such sensor heads were fabricated and connected in series to simulate a distributed sensor network. The same low-coherence multiplexing scheme as shown in Figure 5.11 is used to distinguish and interrogate signals from different sensors. Since the grating gap is designed to be different for each sensor, the interference signal appears at different scanning positions, as can be seen in the inset of Figure 5.13. To test the sensing performance, the sensor corresponding to the third interference pattern was placed into a sealed cell with methane, while the others were kept in an environment without background methane. By increasing the concentration of methane in the cell, the intensity of the third interference pattern decreases obviously in a similar tendency as shown in Figure 5.8. The above results indicate that the methane

sensor in such a low-coherence multiplexing scheme keeps the same operation principle as in a reference-grating interrogation scheme, and the high sensitivity can thus be maintained. From the inset of Figure 5.13, one can also see that the intensities of the interference patterns of the other sensors keep stable, since they were kept in an environment without ambient methane.

---

# FUTURE WORK

---

This thesis covers a broad scale of techniques and applications regarding laser remote sensing for environmental monitoring. However, due to the limitation of time and energy of the author in the Ph.D. program, several ideas have arisen but not been performed, and some have been demonstrated but still require further studies. For future investigations three of them are proposed.

## Multiple-wavelength LIDAR for aerosol analysis

To achieve optical properties and size distributions of atmospheric aerosols, a LIDAR system with several wavelengths can be employed. For instance, the radiation ( $1.06\text{ }\mu\text{m}$ ) of a Nd:YAG laser and its second and third harmonic frequencies (532 nm and 355 nm) become a typical three-wavelength LIDAR transmitter. The ability of such a technique is limited by wavelength number, which is typically three or four. For instance, the size distribution of aerosols has to be assumed into some specific models with a few parameters that can be recovered from the limited spectral information.

One transmitter described in Chapter 3 of the thesis is a tunable OPO system, with wavelength range covering from 200 nm to  $2\text{ }\mu\text{m}$ . Principally, there is no spectral limitation to employ such a light source for multiple-wavelength aerosol analysis, and no doubt, richer optical properties and more detailed size information of aerosols can be retrieved due to the increased spectral bands.

## Combination of LIDAR and GASMAS techniques

The combination of LIDAR and GASMAS techniques has been demonstrated in two ways as described in Sections 3.2.4 and 4.3.3, respectively. In Section 3.2.4, the differential absorption LIDAR



---

(DIAL) technique is used for gas analysis in multiple-scattering media, and in Section 4.3.3, range-resolved techniques, e.g., a FMCW method, are proposed to define path lengths in GASMAS measurements.

Both techniques can measure gases in the pores of a scattering medium, but have different application potentials. The DIAL technique can map out the gas distribution in a scattering medium; while the GASMAS technique measures the integrated absorption along the multiple-scattering path with a higher sensitivity, and the range-resolved technique only assists to obtain the information of the scattering pathlength. Therefore, the DIAL technique is proposed for localization of abnormal gas concentration, qualitatively, e.g., for detecting of the methane leakage from a snow-covered gas pipe; while the GASMAS is more suitable for quantitative gas concentration measurement, where the gas is assumed to distribute uniformly throughout the medium.

In this thesis, the DIAL technique has been demonstrated for oxygen measurements in a block of polystyrene foam, and two possible applications have been proposed but without further test. Clearly, more studies are required to make such a technique realistic in real-world applications. In contrast, the GASMAS technique is more mature after many years of development in the Lund research group. The demonstration of the FMCW technique for multiple-scattering media analysis has also been successfully carried out and encouraging results have been obtained. However, the combination of the FMCW and GASMAS technique has not been performed, although many advantages of such a hybrid can be expected and have been discussed in the end of Section 4.3.3. Further research work is therefore strongly encouraged.

### **Improvement of the zero-background TDLAS**

The zero-background TDLAS clearly stays on a early research stage. Although only proof-of-principle experiments were carried out, the potential of such a technique for SNR enhancement can be seen. Two considerations for real-world applications are proposed in the thesis. A close-loop phase controller has also been developed to stabilize the zero background. Further, an intensity modulation method has been proposed to make the measurements more stable and theoretical analysis has been performed. More experimental tests are needed to support the feasibility of such a technique.

This technique is still under development in the Lund group, and hopefully, encouraging results will be published in near future.

# COMMENTS ON THE PAPERS

---

## **I Vertical lidar sounding of atomic mercury and nitric oxide in a major Chinese city**

*Z.G. Guan, P. Lundin, L. Mei, G. Somesfalean, S. Svanberg*

This paper reports the vertical DIAL measurements performed in a major city in China. Two types of atmospheric pollutants, atomic mercury and nitrogen monoxide, were measured. This work is part of a Sino-Swedish collaboration project, and is probably the first of its kind in China for these gases.

I performed most experiments, with supervision from Svanberg, and help from the other coauthors. I was the responsible person for the mobile LIDAR laboratory during the measurement. The DIAL facility was adjusted to fit the measurement, and the system control and recording programs were modified by me as well. In addition, I also did all data analysis, plotted all figures, and strongly contributed to the manuscript.

## **II Gas analysis within remote porous targets using LIDAR multi-scatter techniques**

*Z.G. Guan, M. Lewander, R. Grönlund, H. Lundberg, S. Svanberg*

This paper reports the potential and feasibility of the DIAL technique for gas analysis in massive scattering media. The gas exchange occurring in a block of polystyrene foam was monitored. Snow, as a natural scattering material, was also tested, by considering the specific applications in, e.g., localization of snow-avalanche victims and inspection of methane leakage of a gas pipe covered by snow.

I was the responsible person of the experiment, with laboratory work together with Lewander and Lundberg, and hard-core supervision from Svanberg. I was involved in all measurements, did all data analysis, prepared all figures, and contributed in drafting the manuscript.

### III Aerosol sounding at a rural Swedish area and in a major Chinese city - A comparative study with the Lund lidar system

*P. Lundin, Z.G. Guan, L. Mei, G. Somesfalean, E. Swietlicki, S. Svanberg*

This paper reports on a comparative study on vertical distributions of atmospheric aerosols at a rural Swedish area and in a major Chinese city, by using a same mobile LIDAR system. The anthropogenic pollution in the city was clearly revealed. The work is also included in the Sino-Swedish collaboration project.

I performed most experiments in the measurement in Sweden, with supervision from Svanberg, and help from Lundin. A program for automatic data recording was developed by me. While in China, Lundin performed the measurements with the same program, and I assisted as the responsible LIDAR operator. I also contributed in the discussion of data analysis and in manuscript drafting.

### IV Insect monitoring with fluorescence lidar techniques: feasibility study

*M. Brydegaard, Z.G. Guan, M. Wellenreuther, S. Svanberg*

This paper reports, for the first time, the application of the fluorescence LIDAR on insect monitoring. The feasibility of the technique was tested by setting the targets at a distance of 60 m, and encouraging results were obtained.

My role in this work was again the key LIDAR operator, and I have taken part in all LIDAR measurements. I also highly contributed in data analysis, figure plotting and manuscript preparation.

### V Insect monitoring with fluorescence lidar techniques: field experiments

*Z.G. Guan, M. Brydegaard, P. Lundin, M. Wellenreuther, A. Runemark, E.I. Svensson, S. Svanberg*

This paper reports the two weeks of field experiments on damselfly monitoring using fluorescence LIDAR techniques. The feasibility of the technique in a natural environment was tested and interesting measurement results inspiring biological discussions were obtained.

I was involved in all the experiments, as the key LIDAR operator. My contributions include the participation in the system modification, the program development, and the analysis of most data. I prepared most figures and drafted most at the manuscript.

**VI Feasibility study: fluorescence lidar for remote bird classification**

*M. Brydegaard, P. Lundin, Z.G. Guan, A. Runemark, S. Åkesson, S. Svanberg*

This paper reports, for the first time, the feasibility of the fluorescence LIDAR to classify bird species in a remote way. 26 bird samples of 12 species were tested and promising results were obtained.

As the key LIDAR operator, I performed all the LIDAR measurements together with Brydegaard and Lundin. The same recording program, developed by me, for the damselfly monitoring was used. I also highly contributed in figure preparation and manuscript drafting.

**VII Quasi zero-background tunable diode laser absorption spectroscopy employing a balanced Michelson interferometer**

*Z.G. Guan, M. Lewander, S. Svanberg*

This paper, for the first time, presents a technique to operate the tunable diode laser absorption spectroscopy (TDLAS) on a zero-background. The signal-to-noise ratio of the technique is improved compared with a conventional TDLAS.

I planned, set up and performed all the experiments, with most useful discussions with Lewander and Svanberg. I plotted all the figures and drafted most at the manuscript.

**VIII Active feed-back regulation of a Michelson interferometer to achieve zero-background absorption measurements**

*P. Lundin, Z.G. Guan, S. Svanberg*

This manuscript reports the work following that of Paper VII. A phase controlling scheme based on PID and lock-in techniques was applied to optimize the interferometer operating in a destructive mode, and hence the zero background can be kept stable in long term. In this way, the performance of the zero-background TDLAS is expected to improve considerably.

In this work, I planned the experiments with discussions with Lundin and Svanberg, while Lundin is the main person performing experiments and simulations with assistance from me. I contributed in designing the phase controller by offering the key idea and in other technical ways.

**IX Food monitoring based on diode laser gas spectroscopy**

*M. Lewander, Z.G. Guan, L. Persson, A. Olsson, S. Svanberg*

This paper reports the GASMAS technique applied for food package monitoring. Measured samples include a package of minced meat, a plastic bag of bake-off bread, and a milk carton.

In this work, I helped to improve the performance of the GASMAS system, and I also took active part in the experiment, offering assistance to set up the measurement platform. I contributed in discussions of data analysis and manuscript drafting.

**X Clinical system for non-invasive *in situ* monitoring of gases in the human paranasal sinuses**

*M. Lewander, Z.G. Guan, K. Svanberg, S. Svanberg, T. Svensson*

This paper publishes the improvement of the Lund GASMAS system with sensitivity largely enhanced, and its clinical application in measurements of human paranasal sinuses.

I assisted in the work of hardware and program improvement, and took an active part in the clinical measurements, as a system operator. I also contributed in discussions for manuscript drafting.

**XI Assessment of photon migration in scattering media using heterodyning techniques with a frequency modulated diode laser**

*Z.G. Guan, P. Lundin, S. Svanberg*

This paper, for the first time, presents a technique to assess the photon migration in massively scattering media by using a frequency modulated diode laser. The technique has advantages over other existing techniques and can realize a straight-forward combination with GASMAS techniques.

I planned, set up and performed all the experiments, with dependable assistance from Lundin and most helpful discussion from Svanberg. I also did all data analysis, prepared all figures and drafted most of the manuscript.

**XII An optical sensing system for the concentration of methane based on fiber Bragg gratings**

*B. Zhou, G. Liu, Z.G. Guan, S. He*

This paper proposed a novel methane sensor based on fiber Bragg gratings (FBGs). Such cost-effective sensors are of ease to realize remote and distributed sensing, and very suitable for safety monitoring in Chinese coal mines threatened by methane-originated accidents. For this reason, the paper was published in a Chinese journal.

In the early stage of the work, I drew the idea, planned the experiments, and tested the feasibility of the method. The FBGs were fabricated by a system which I in a very substantial way developed earlier with other researchers. Later Zhou and Liu performed the measurements with assistance and advice from me. I was responsible during the whole project, and also the corresponding author of the paper, which was mostly drafted by me.

**XIII Coherence multiplexing of distributed sensors based on pairs of fiber Bragg gratings of low reflectivity**

*Z.G. Guan, D. Chen, S. He*

In this paper, a coherence multiplexing technique is published to multiplex and interrogate fiber-optic sensors based on pairs of FBG. These dual-grating units can be modified into methane sensors, and the coherence technique can thus solve the multiplexing problem of many such units likewise.

With the idea generated by me, I planned, set up and performed the experiments, while Chen did the simulation. I also did most data analysis, plotted all figures and drafted the first version of the manuscript, which was improved later by Prof. He.



# ACKNOWLEDGEMENTS

---

This thesis would not be possible without helps from a number of people, and I would like to sincerely thank them.

First of all, I am heartily grateful to the main supervisor of the thesis, Prof. Sune Svanberg, for his guidance, encouragement, and support, from the initial to the final level within the Ph.D. program. His true scientific spirit, rich experiences, and diligent working attitude will benefit me for the rest of life.

The same gratitude goes to co-supervisors, Prof. Stefan Andersson-Engels and Dr. Gabriel Somefalean. Thanks, Stefan, for your advice, and the excellent course Medical Optics. Thanks, Gabriel, for helpful discussion, and the importance of smoothing the collaboration between Lund (Sweden) and Zhejiang (China).

I would like to express special appreciation to other Ph.D candidates in the research group. They are Mikkel Brydegaard, Märta Lewander, and Patrik Lundin. I thank them for leaving me the best working experience and for providing the most friendly atmosphere. Deep thanks are also given to earlier colleagues, Drs Rasmus Grönlund and Tomas Svensson, for their most helpful advice and valuable discussions.

Everyone at the Atomic Physics Division has offered direct or indirect help and therefore I thank all of them. In particular, I would like to show my gratitude to Prof. Claes-Göran Wahlström, head of the division, for his leadership and general organization, Minna Ramkull, for her working efficiency and service spirit, Dr. Anders Persson and Dr. Hans Lundberg, for their knowledgeable advice and laboratory assistance, and Bertil Hermansson, for his electronics and IT help.

Furthermore, I would like to thank people who contributed a lot in the collaborations: Prof. Erik Swietlicki, for helping organizing aerosol measurements at Vavihill and for offering reference data; Profs Christer Löfstedt, Erik Svensson and Susanne Åkesson, Dr. Maren Wellenreuther, and Anna Runemark, for their hard work in biological measurements and helpful discussion. In addition, I am grateful to our Chinese collaborators in the Sino-Swedish project. They are Prof. Sailing He, Dr. Chunsheng Yan, Liang



Mei, Binhao Wang and Haojiang Zhou. Their contributions were extremely valuable. I am especially grateful to Prof. Sailing He, for being the supervisor for my earlier scientific work in China.

I can never forget the great friendships that I met at Lund. Apart from the kind colleagues mentioned above, I appreciate very much the relationship with Sune Svanberg's family, for taking care of me as a member. I also thank those Chinese families (He, Liu, Xie, Yan, etc), for spending happy time with them.

All words fail to express my appreciation to Grace Lv, my beloved wife, who always makes life full of joy. Her love, forever confidence and trust was a great support for me to complete this thesis. Equally important support comes from my parents, who brought me up and I can never thank them enough for their efforts and love, and from my parents in law, who accepted me as a family member.

# REFERENCES

---

- [1]. <http://tcgffoodsafety.com>.
- [2]. <http://ww2.iirme.com/oh/>.
- [3]. <http://www.epa.gov/OCEPAterms/pterm.html>.
- [4]. Aerosols. *United States National Institute for Occupational Safety and Health*, Retrieved 2008-03-15.
- [5]. S. Bauman, P. D. Houmire, and J. W. Nelson. Cascade impactor aerosol samples from PIXE and PESA analyses. *Nuclear Instruments and Methods*, 181(1-3):499–502, 1981.
- [6]. A. Soutar, M. Watt, J. W. Cherrie, and A. Seaton. Comparison between a personal PM<sub>10</sub> sampling head and the tapered element oscillating microbalance (TEOM) system. *Atmospheric Environment*, 33(27):4373–4377, 1999.
- [7]. A. J. Armendariz and D. Leith. Concentration measurement and counting efficiency for the aerodynamic particle sizer 3320. *Journal of Aerosol Science*, 33(1):133–148, 2002.
- [8]. C. Sioutas, E. Abt, J. M. Wolfson, and P. Koutrakis. Evaluation of the measurement performance of the scanning mobility particle sizer and aerodynamic particle sizer. *Aerosol Science and Technology*, 30(1):84–92, 1999.
- [9]. Special Issue, Water Air and Soil Pollution. In *Proceedings of the Eighth International Conference on Mercury as a Global Pollutant*, Guizhou, China, June 7-12, 2009.
- [10]. R. K. Monson. Volatile organic compound emissions from terrestrial ecosystems: A primary biological control over atmospheric chemistry. *Israel Journal of Chemistry*, 42(1):29–42, 2002.
- [11]. P. Forster, V. Ramaswamy, P. Artaxo, T. Berntsen, R. Betts, D.W. Fahey, J. Haywood, J. Lean, D.C. Lowe, G. Myhre, J. Nganga, R. Prinn, G. Raga, M. Schulz, and R. Van Dorland. Changes in atmospheric constituents and in radiative forcing. In S. Solomon, D. Qin, M. Manning, Z. Chen, M. Marquis, K.B. Averyt, M. Tignor, and H.L. Miller, editors, *Climate Change 2007: The Physical Science Basis. Contribution of Working Group I to the Fourth Assessment Report of the Intergovernmental Panel on Climate Change*. Cambridge University Press, Cambridge, United Kingdom and New York, NY, USA, 2007.
- [12]. H. Okabe, P. L. Splitsto, and J. J. Ball. Ambient and source SO<sub>2</sub> detector based on fluorescence method. *Journal of the Air Pollution Control Association*, 23(6):514–516, 1973.
- [13]. R. S. Braman, M. A. Delacanter, and X. H. Qing. Sequential, selective hollow tube preconcentration and chemiluminescence analysis system for nitrogen-oxide compounds in air. *Analytical Chemistry*, 58(7):1537–1541, 1986.

- [14]. J. G. Goode, R. J. Yokelson, D. E. Ward, R. A. Susott, R. E. Babbitt, M. A. Davies, and W. M. Hao. Measurements of excess  $O_3$ ,  $CO_2$ ,  $CO$ ,  $CH_4$ ,  $C_2H_4$ ,  $C_2H_2$ ,  $HCN$ ,  $NO$ ,  $NH_3$ ,  $HCOOH$ ,  $CH_3COOH$ ,  $HCHO$ , and  $CH_3OH$  in 1997 Alaskan biomass burning plumes by airborne Fourier transform infrared spectroscopy (AFTIR). *Journal of Geophysical Research-Atmospheres*, 105(D17):22147–22166, 2000.
- [15]. H. Edner, A. Sunesson, S. Svanberg, L. Uneus, and S. Wallin. Differential optical-absorption spectroscopy system used for atmospheric mercury monitoring. *Applied Optics*, 25(3):403–409, 1986.
- [16]. H. Edner, P. Ragnarson, S. Spannare, and S. Svanberg. Differential optical-absorption spectroscopy (DOAS) system for urban atmospheric pollution monitoring. *Applied Optics*, 32(3):327–333, 1993.
- [17]. J. Sandsten, H. Edner, and S. Svanberg. Gas imaging by infrared gas-correlation spectrometry. *Optics Letters*, 21(23):1945–1947, 1996.
- [18]. J. Sandsten, P. Wiebring, H. Edner, and S. Svanberg. Real-time gas-correlation imaging employing thermal background radiation. *Optics Express*, 6(4):92–103, 2000.
- [19]. L. Mei, Z. G. Guan, J. Lv, C. Löstedt, H.J. Zhou, F.J. Chen, Z.R. Zhu, J.A. Cheng, S. Svanberg, and G. Somesfalean. Agricultural pest monitoring with fluorescence LIDAR techniques: feasibility study. *manuscript in preparation*, 2010.
- [20]. M. Campero, F. Ollevier, and R. Stoks. Ecological relevance and sensitivity depending on the exposure time for two biomarkers. *Environmental Toxicology*, 22(6):572–581, 2007.
- [21]. R. Hickling, D. B. Roy, J. K. Hill, and C. D. Thomas. A northward shift of range margins in British Odonata. *Global Change Biology*, 11(3):502–506, 2005.
- [22]. T. J. Case and M. L. Taper. Interspecific competition, environmental gradients, gene flow, and the coevolution of species’ borders. *American Naturalist*, 155(5):583–605, 2000.
- [23]. M. Joron and P. M. Brakefield. Captivity masks inbreeding effects on male mating success in butterflies. *Nature*, 424(6945):191–194, 2003.
- [24]. J. A. Shaw, N. L. Seldomridge, D. L. Dunkle, P. W. Nugent, L. H. Spangler, J. J. Bromenshenk, C. B. Henderson, J. H. Churnside, and J. J. Wilson. Polarization lidar measurements of honey bees in flight for locating land mines. *Optics Express*, 13(15):5853–5863, 2005.
- [25]. K. S. Repasky, J. A. Shaw, R. Scheppele, C. Melton, J. L. Carsten, and L. H. Spangler. Optical detection of honeybees by use of wing-beat modulation of scattered laser light for locating explosives and land mines. *Applied Optics*, 45(8):1839–1843, 2006.
- [26]. T. Alerstam and Å. Lindström. Optimal bird migration: the relative importance of time, energy and safety. In E. Gwinner, editor, *Bird Migration: Physiology and Ecophysiology*, pages 331–351. Springer-Verlag, Berlin, Heidelberg, 1990.
- [27]. T. Alerstam, A. Hedenström, and S. Åkesson. Long-distance migration: evolution and determinants. *Oikos*, 103(2):247–260, 2003.
- [28]. B. Olsen, V. J. Munster, A. Wallensten, J. Waldenström, Adme Osterhaus, and R. A. M. Fouchier. Global patterns of influenza A virus in wild birds. *Science*, 312(5772):384–388, 2006.
- [29]. S. Zehnder, S. kesson, F. Liechti, and B. Bruderer. Seasonal and diurnal patterns of nocturnal bird migration at Falsterbo, south Sweden. *J. Avian Biol.*, 32:239–248, 2001.
- [30]. P. Kerlinger and F. R. Moore. Atmospheric structure and avian migration. In R. F. Johnston, editor, *Current Ornithology*, volume 6, pages 109–142. Plenum Press, New York, 1989.

- 
- [31]. A. Lindström. The role of predation risk in stopover habitat selection in migrating bramblings, *Fringilla montifringilla*. *Behavioral Ecology*, 1(2):102–106, 1990.
- [32]. L. Cocola, M. Fedel, and G. Tondello. A new device for the measurement of gaseous oxygen in closed containers. In *Proceedings of the 3rd International Multi-conference on Engineering and Technological Innovation (IMETI 2010)*, Orlando, 2010.
- [33]. S. Svanberg. *Atomic and molecular spectroscopy*. Springer, Berlin, 4th edition, 2004.
- [34]. N. Takeuchi. Elastic lidar Measurement of the troposphere. In T. Fujii and T. Fukuchi, editors, *Laser remote sensing*, pages 63–122. CRC Press, Boca Raton, 2005.
- [35]. S. W. Henderson, P. Gatt, D. Rees, and R. M. Huffaker. Wind lidar. In T. Fujii and T. Fukuchi, editors, *Laser remote sensing*, pages 469–722. CRC Press, Boca Raton, 2005.
- [36]. X. Chu and G. C. Papen. Resonance fluorescence lidar. In T. Fujii and T. Fukuchi, editors, *Laser remote sensing*, pages 179–432. CRC Press, Boca Raton, 2005.
- [37]. S. Svanberg. Fluorescence spectroscopy and imaging of LIDAR targets. In T. Fujii and T. Fukuchi, editors, *Laser remote sensing*, pages 433–468. CRC Press, Boca Raton, 2005.
- [38]. P. Weibring, T. Johansson, H. Edner, S. Svanberg, B. Sundner, V. Raimondi, G. Cecchi, and L. Pantani. Fluorescence lidar imaging of historical monuments. *Applied Optics*, 40(33):6111–6120, 2001.
- [39]. D. Lognoli, G. Cecchi, I. Mochi, L. Pantani, V. Raimondi, R. Chiari, T. Johansson, P. Weibring, H. Edner, and S. Svanberg. Fluorescence lidar imaging of the cathedral and baptistery of Parma. *Applied Physics B-Lasers and Optics*, 76(4):457–465, 2003.
- [40]. B. Calpini and V. Simeonov. Trace gas species detection in the lower atmospheric pollutant to possible air pollution abatement strategies. In T. Fujii and T. Fukuchi, editors, *Laser remote sensing*, pages 123–178. CRC Press, Boca Raton, 2005.
- [41]. J. Kasparian, R. Bourayou, S. Frey, J.C. Luderer, G. Mejean, M. Rodriguez, E. Salmon, H. Wille, J. Yu, J.-P. Wolf, and L. Wöste. Femtosecond white-light lidar. In T. Fujii and T. Fukuchi, editors, *Laser remote sensing*, pages 37–62. CRC Press, Boca Raton, 2005.
- [42]. H. Wille, M. Rodriguez, J. Kasparian, D. Mondelain, J. Yu, A. Mysyrowicz, R. Sauerbrey, J. P. Wolf, and L. Wöste. Teramobile: A mobile femtosecond-terawatt laser and detection system. *European Physical Journal-Applied Physics*, 20(3):183–190, 2002.
- [43]. J. Kasparian, M. Rodriguez, G. Mejean, J. Yu, E. Salmon, H. Wille, R. Bourayou, S. Frey, Y. B. Andre, A. Mysyrowicz, R. Sauerbrey, J. P. Wolf, and L. Wöste. White-light filaments for atmospheric analysis. *Science*, 301(5629):61–64, 2003.
- [44]. H.I. Schiff, G.I. Macay, and J. Bechara. The use of tunable diode laser absorption spectroscopy for atmospheric measurements. In M.W. Sigrist, editor, *Air Monitoring by Spectroscopic Techniques*. Wiley, New York, 1994.
- [45]. P. Werle and F. D’Amato. Field laser applications in industry and research. *Applied Physics B-Lasers and Optics*, 92(3):303–304, 2008.
- [46]. M. Gehrtz, G. C. Bjorklund, and E. A. Whittaker. Quantum-limited laser frequency-modulation spectroscopy. *Journal of the Optical Society of America B-Optical Physics*, 2(9):1510–1526, 1985.
- [47]. J. Ye, L. S. Ma, and J. L. Hall. Ultrasensitive detections in atomic and molecular physics: demonstration in molecular overtone spectroscopy.

- Journal of the Optical Society of America B-Optical Physics*, 15(1):6–15, 1998.
- [48]. W. M. Fairbank, T. W. Hansch, and A. L. Schawlow. Absolute measurement of very low sodium-vapor densities using laser resonance fluorescence. *Journal of the Optical Society of America*, 65(2):199–204, 1975.
- [49]. W. Neuhauser, M. Hohenstatt, P. E. Toschek, and H. Dehmelt. Localized visible  $\text{Ba}^+$  mono-ion oscillator. *Physical Review A*, 22(3):1137–1140, 1980.
- [50]. M.W. Sigrist. Air monitoring by laser photoacoustic spectroscopy. In M.W. Sigrist, editor, *Air Monitoring by Spectroscopic Techniques*. Wiley, New York, 1994.
- [51]. C. Wieman and T. W. Hansch. Doppler-free laser polarization spectroscopy. *Physical Review Letters*, 36(20):1170–1173, 1976.
- [52]. M. Sjöholm, G. Somesfalean, J. Alnis, S. Andersson-Engels, and S. Svanberg. Analysis of gas dispersed in scattering media. *Optics Letters*, 26(1):16–18, 2001.
- [53]. G. Somesfalean, M. Sjöholm, J. Alnis, C. af Klinteberg, S. Andersson-Engels, and S. Svanberg. Concentration measurement of gas embedded in scattering media by employing absorption and time-resolved laser spectroscopy. *Applied Optics*, 41(18):3538–3544, 2002.
- [54]. L. Persson, H. Gao, M. Sjöholm, and S. Svanberg. Diode laser absorption spectroscopy for studies of gas exchange in fruits. *Optics and Lasers in Engineering*, 44(7):687–698, 2006.
- [55]. T. Svensson, L. Persson, M. Andersson, S. Svanberg, S. Andersson-Engels, J. Johansson, and S. Folestad. Noninvasive characterization of pharmaceutical solids by diode laser oxygen spectroscopy. *Applied Spectroscopy*, 61(7):784–786, 2007.
- [56]. M. Andersson, L. Persson, M. Sjöholm, and S. Svanberg. Spectroscopic studies of wood-drying processes. *Optics Express*, 14(8):3641–3653, 2006.
- [57]. L. Persson, K. Svanberg, and S. Svanberg. On the potential of human sinus cavity diagnostics using diode laser gas spectroscopy. *Applied Physics B-Lasers and Optics*, 82(2):313–317, 2006.
- [58]. L. Persson, M. Andersson, M. Cassel-Engquist, K. Svanberg, and S. Svanberg. Gas monitoring in human sinuses using tunable diode laser spectroscopy. *Journal of Biomedical Optics*, 12(5):Article No.: 054001, 2007.
- [59]. M. Lewander, Z. G. Guan, L. Persson, A. Olsson, and S. Svanberg. Food monitoring based on diode laser gas spectroscopy. *Applied Physics B-Lasers and Optics*, 93(2-3):619–625, 2008.
- [60]. M. Lewander, Z. G. Guan, K. Svanberg, S. Svanberg, and T. Svensson. Clinical system for non-invasive in situ monitoring of gases in the human paranasal sinuses. *Optics Express*, 17(13):10849–10863, 2009.
- [61]. K. O. Hill and G. Meltz. Fiber Bragg grating technology fundamentals and overview. *Journal of Lightwave Technology*, 15(8):1263–1276, 1997.
- [62]. A. D. Kersey, M. A. Davis, H. J. Patrick, M. LeBlanc, K. P. Koo, C. G. Askins, M. A. Putnam, and E. J. Friebele. Fiber grating sensors. *Journal of Lightwave Technology*, 15(8):1442–1463, 1997.
- [63]. B. Zhou and Z. G. Guan. Methane concentration monitoring system based on a pair of FBGs. In *AOE 2007: Asia Optical Fiber Communication and Optoelectronic Exposition and Conference, Conference Proceedings*, pages 296–298, Shanghai, 2008. AOE.
- [64]. R.M. Measures. *Laser remote sensing: Fundamental and applications*. Wiley, New York, 1984.

- 
- [65]. J. D. Klett. Stable analytical inversion solution for processing lidar returns. *Applied Optics*, 20(2):211–220, 1981.
- [66]. F. G. Fernald. Analysis of atmospheric lidar observations - some comments. *Applied Optics*, 23(5):652–653, 1984.
- [67]. E. Boeker and R. von Grondelle. *Environmental science: physical principles and applications*. John Wiley and Sons Ltd., 2001.
- [68]. P. Weibring, H. Edner, and S. Svanberg. Versatile mobile lidar system for environmental monitoring. *Applied Optics*, 42(18):3583–3594, 2003.
- [69]. R. Penndorf. Tables of the refractive index for standard air and the Rayleigh scattering coefficient for the spectral region between 0.2 and 20.0  $\mu\text{m}$  and their application to atmospheric optics. *Journal of the Optical Society of America*, 47(2):176–182, 1957.
- [70]. H. Edner, K. Fredriksson, A. Sunesson, S. Svanberg, L. Uneus, and W. Wendt. Mobile remote-sensing system for atmospheric monitoring. *Applied Optics*, 26(19):4330–4338, 1987.
- [71]. J. Alnis, U. Gustafsson, G. Somesfalean, and S. Svanberg. Sum-frequency generation with a blue diode laser for mercury spectroscopy at 254 nm. *Applied Physics Letters*, 76(10):1234–1236, 2000.
- [72]. T. N. Anderson, J. K. Magnuson, and R. P. Lucht. Diode-laser-based sensor for ultraviolet absorption measurements of atomic mercury. *Applied Physics B-Lasers and Optics*, 87(2):341–353, 2007.
- [73]. M. L. Huber, A. Laesecke, and D. G. Friend. Correlation for the vapor pressure of mercury. *Industrial and Engineering Chemistry Research*, 45(21):7351–7361, 2006.
- [74]. H. Edner, G. W. Faris, A. Sunesson, and S. Svanberg. Atmospheric atomic mercury monitoring using differential absorption lidar techniques. *Applied Optics*, 28(5):921–930, 1989.
- [75]. L. S. Rothman, I. E. Gordon, A. Barbe, D. C. Benner, P. E. Bernath, M. Birk, V. Boudon, L. R. Brown, A. Campargue, J. P. Champion, K. Chance, L. H. Coudert, V. Dana, V. M. Devi, S. Fally, J. M. Flaud, R. R. Gamache, A. Goldman, D. Jacquemart, I. Kleiner, N. Lacome, W. J. Lafferty, J. Y. Mandin, S. T. Massie, S. N. Mikhailenko, C. E. Miller, N. Moazzen-Ahmadi, O. V. Naumenko, A. V. Nikitin, J. Orphal, V. I. Perevalov, A. Perrin, A. Predoi-Cross, C. P. Rinsland, M. Rotger, M. Simeckova, M. A. H. Smith, K. Sung, S. A. Tashkun, J. Tennyson, R. A. Toth, A. C. Vandaele, and J. Vander Auwera. The HITRAN 2008 molecular spectroscopic database. *Journal of Quantitative Spectroscopy and Radiative Transfer*, 110(9-10):533–572, 2009.
- [76]. R. Grönlund, M. Sjöholm, P. Weibring, H. Edner, and S. Svanberg. Elemental mercury emissions from chlor-alkali plants measured by lidar techniques. *Atmospheric Environment*, 39(39):7474–7480, 2005.
- [77]. R. Ferrara, B. Maserti, A. Petrosino, and R. Bargagli. Mercury levels in rain and air and the subsequent washout mechanism in a central Italian region. *Atmospheric Environment*, 20(1):125–128, 1986.
- [78]. N. Menyuk, D. K. Killinger, and W. E. Defeo. Remote-sensing of NO using a differential absorption lidar. *Applied Optics*, 19(19):3282–3286, 1980.
- [79]. M. Alden, H. Edner, and S. Svanberg. Laser monitoring of atmospheric NO using ultraviolet differential-absorption techniques. *Optics Letters*, 7(11):543–545, 1982.
- [80]. H. J. Kolsch, P. Rairoux, J. P. Wolf, and L. Wöste. Simultaneous NO and NO<sub>2</sub> DIAL measurement using BBO crystals. *Applied Optics*, 28(11):2052–2056, 1989.
- [81]. H. J. Kolsch, P. Rairoux, J. P. Wolf, and L. Wöste. Comparative-study of nitric-oxide immission in the cities of Lyon, Geneva, and Stuttgart

- using a mobile differential absorption lidar system. *Applied Physics B-Photophysics and Laser Chemistry*, 54(1):89–94, 1992.
- [82]. R. Toriumi, H. Tai, H. Kuze, and N. Takeuchi. Tunable, UV solid-state lidar for measurement of nitric oxide distribution. *Japanese Journal of Applied Physics Part 1-Regular Papers Brief Communications and Review Papers*, 38(11):6372–6378, 1999.
- [83]. H. Edner, A. Sunesson, and S. Svanberg. NO plume mapping by laser-radar techniques. *Optics Letters*, 13(9):704–706, 1988.
- [84]. L. R. Bissonnette and D. L. Hutt. Lidar remote sensing of cloud and fog properties. In P. Fabian, V. Klein, M. Tacke, K. Weber, and C. Werner, editors, *Air Pollution and Visibility Measurements*, volume 2506 of *Proceedings of the Society of Photo-Optical Instrumentation Engineers (SPIE)*, pages 512–523. SPIE - Int Soc Optical Engineering, Bellingham, 1995.
- [85]. *Medical Optical Tomography, Functional Imaging and Monitoring*, volume 11 of *SPIE Institute Series*. SPIE, Bellingham, 1993.
- [86]. T. Vo-Dinh. *Biomedical Photonics Handbook*. CRC Press, Boca Raton, 2003.
- [87]. C. af Klinteberg, A. Pifferi, S. Andersson-Engels, R. Cubeddu, and S. Svanberg. In vivo absorption spectroscopy of tumor sensitizers with femtosecond white light. *Applied Optics*, 44(11):2213–2220, 2005.
- [88]. C. Abrahamsson, T. Svensson, S. Svanberg, S. Andersson-Engels, J. Johansson, and S. Folestad. Time and wavelength resolved spectroscopy of turbid media using light continuum generated in a crystal fiber. *Optics Express*, 12(17):4103–4112, 2004.
- [89]. S. Udenfriend. *Fluorescence assay in biology and medicine*, volume I and II. Academic Press, New York, 1969.
- [90]. *Modern fluorescence spectroscopy*, volume 1 and 2. Plenum, New York, 1976.
- [91]. J. R. Lakowicz. *Principles of fluorescence spectroscopy*. Plenum, New York, 1983.
- [92]. S. Andersson-Engels, A. Elner, J. Johansson, S. E. Karlsson, L. G. Salford, L. G. Stromblad, K. Svanberg, and S. Svanberg. Clinical recording of laser-induced fluorescence spectra for evaluation of tumor demarcation feasibility in selected clinical specialties. *Lasers in Medical Science*, 6(4):415–424, 1991.
- [93]. G. Kychakoff, R. D. Howe, R. K. Hanson, M. C. Drake, R. W. Pitz, M. Lapp, and C. M. Penney. Visualization of turbulent flame fronts with planar laser-induced fluorescence. *Science*, 224(4647):382–384, 1984.
- [94]. H. Edner, J. Johansson, S. Svanberg, and E. Wallinder. Fluorescence lidar multicolor imaging of vegetation. *Applied Optics*, 33(13):2471–2479, 1994.
- [95]. H. H. Kim. Airborne bathymetric charting using pulsed blue-green lasers. *Applied Optics*, 16(1):46–56, 1977.
- [96]. G. Cecchi, M. Bazzani, C. Cuzzi, D. Lognoli, I. Mochi, L. Pantani, V. Raimondi, R. Carla, R. Cappadona, B. Breschi, D. Novelli, Th. Johansson, P. Weibring, H. Edner, and S. Svanberg. Probing the marine environment with fluorescence lidars—comparison of three fluorensors in a field campaign. Technical report, 2003.
- [97]. D. A. Leonard, B. Caputo, and F. E. Hoge. Remote-sensing of subsurface water temperature by Raman-scattering. *Applied Optics*, 18(11):1732–1745, 1979.
- [98]. H. K. Lichtenthaler and U. Rinderle. The role of chlorophyll fluorescence in the detection of stress condition in plants. *Crc Critical Reviews in Analytical Chemistry*, 19:S29–S85, 1988.

- [99]. P. Lundin et al. Field experiment: fluorescence lidar for remote bird classification. 2010, to appear.
- [100]. K. Iga, F. Koyama, and S. Kinoshita. Surface emitting semiconductor-lasers. *IEEE Journal of Quantum Electronics*, 24(9):1845–1855, 1988.
- [101]. M. Grabherr, R. Jager, R. Michalzik, B. Weigl, G. Reiner, and K. J. Ebeling. Efficient single-mode oxide-confined GaAs VCSEL’s emitting in the 850-nm wavelength regime. *IEEE Photonics Technology Letters*, 9(10):1304–1306, 1997.
- [102]. J. Faist, F. Capasso, D. L. Sivco, C. Sirtori, A. L. Hutchinson, and A. Y. Cho. Quantum cascade laser. *Science*, 264(5158):553–556, 1994.
- [103]. F. Capasso, J. Faist, C. Sirtori, and A. Y. Cho. Infrared (4–11  $\mu\text{m}$ ) quantum cascade lasers. *Solid State Communications*, 102(2-3):231–236, 1997.
- [104]. K. Namjou, S. Cai, E. A. Whittaker, J. Faist, C. Gmachl, F. Capasso, D. L. Sivco, and A. Y. Cho. Sensitive absorption spectroscopy with a room-temperature distributed-feedback quantum-cascade laser. *Optics Letters*, 23(3):219–221, 1998.
- [105]. T. W. Hansch, I. S. Shahin, and A. L. Schawlow. High-resolution saturation spectroscopy of sodium D lines with a pulsed tunable dye laser. *Physical Review Letters*, 27(11):971–977, 1971.
- [106]. P. Taroni, A. Torricelli, L. Spinelli, A. Pifferi, F. Arpaia, G. Danesini, and R. Cubeddu. Time-resolved optical mammography between 637 and 985 nm: clinical study on the detection and identification of breast lesions. *Physics in Medicine and Biology*, 50(11):2469–2488, 2005.
- [107]. T. Svensson, S. Andersson-Engels, M. Einarsdottir, and K. Svanberg. In vivo optical characterization of human prostate tissue using near-infrared time-resolved spectroscopy. *Journal of Biomedical Optics*, 12(1):10, 2007.
- [108]. T. Fernholz, H. Teichert, and V. Ebert. Digital, phase-sensitive detection for in situ diode-laser spectroscopy under rapidly changing transmission conditions. *Applied Physics B-Lasers and Optics*, 75(2-3):229–236, 2002.
- [109]. L. Persson, F. Andersson, M. Andersson, and S. Svanberg. Approach to optical interference fringes reduction in diode laser absorption spectroscopy. *Applied Physics B-Lasers and Optics*, 87(3):523–530, 2007.
- [110]. A. L. Buck. New equations for computing vapor-pressure and enhancement factor. *Journal of Applied Meteorology*, 20(12):1527–1532, 1981.
- [111]. A. Dieckmann. FMCW-LIDAR with tubable twin-guide laser-diode. *Electronics Letters*, 30(4):308–309, 1994.
- [112]. D. Uttam and B. Culshaw. Precision time domain reflectometry in optical fiber system using a frequency modulated continuous wave ranging technique. *Journal of Lightwave Technology*, 3(5):971–977, 1985.
- [113]. X. W. Shu, K. Sugden, and K. Byron. Bragg-grating-based all-fiber distributed Gires-Tournois etalons. *Optics Letters*, 28(11):881–883, 2003.
- [114]. X. W. Shu, K. Sugden, and I. Bennion. Dual-direction Gires-Tournois etalon based on a single complex fiber Bragg grating. *Optics Letters*, 31(15):2263–2265, 2006.
- [115]. J. Lumeau, L. B. Glebov, and V. Smirnov. Tunable narrowband filter based on a combination of Fabry-Perot etalon and volume Bragg grating. *Optics Letters*, 31(16):2417–2419, 2006.
- [116]. M. J. Chawki, V. Tholey, E. Delevaque, S. Boj, and E. Gay. Wavelength reuse scheme in a WDM unidirectional ring network using a proper fiber grating add/drop multiplexer. *Electronics Letters*, 31(6):476–477, 1995.
- [117]. A. Carballar, M. A. Muriel, and J. Azana. Fiber grating filter for WDM



- systems: An improved design. *IEEE Photonics Technology Letters*, 11(6):694–696, 1999.
- [118]. P. J. Lemaire, R. M. Atkins, V. Mizrahi, and W. A. Reed. High-pressure H<sub>2</sub> loading as a technique for achieving ultrahigh UV photosensitivity and thermal sensitivity in GeO<sub>2</sub> doped optical fibers. *Electronics Letters*, 29(13):1191–1193, 1993.
- [119]. G. Meltz, W. W. Morey, and W. H. Glenn. Formation of Bragg grating in optical fibers by a transverse holographic method. *Optics Letters*, 14(15):823–825, 1989.
- [120]. K. O. Hill, B. Malo, F. Bilodeau, D. C. Johnson, and J. Albert. Bragg gratings fabricated in monomode photosensitive optical fiber by UV exposure through a phase mask. *Applied Physics Letters*, 62(10):1035–1037, 1993.
- [121]. J. D. Prohaska, E. Snitzer, S. Rishton, and V. Boegli. Magnification of mask fabricated fiber Bragg gratings. *Electronics Letters*, 29(18):1614–1615, 1993.
- [122]. B. Lee. Review of the present status of optical fiber sensors. *Optical Fiber Technology*, 9(2):57–79, 2003.
- [123]. R. Maaskant, T. Alavie, R. M. Measures, G. Tadros, S. H. Rizkalla, and A. Guha-Thakurta. Fiber-optic Bragg grating sensors for bridge monitoring. *Cement and Concrete Composites*, 19(1):21–33, 1997.
- [124]. J. D. Prohaska, E. Snitzer, B. Chen, M. H. Maher, E. G. Nawy, and W. W. Morey. Fiber optic Bragg grating strain sensor in large-scale concrete structures. In R. O. Claus and R. S. Rogowski, editors, *Fiber Optic Smart Structures and Skins V*, volume 1798 of *Proceedings of the Society of Photo-Optical Instrumentation Engineers (SPIE)*, pages 286–294. SPIE - Int Soc Optical Engineering, Bellingham, 1993.
- [125]. C. J. Groves-Kirkby. Optical-fibre strain sensing for structural health and load monitoring. *GEC Journal of Technology*, 15(1):16–26, 1998.
- [126]. W. L. Schulz, E. Udd, J. M. Seim, and G. E. McGill. Advanced fiber grating strain sensor systems for bridges, structures, and highways. In S. C. Liu, editor, *Smart Systems for Bridges, Structures, and Highways*, volume 3325 of *Proceedings of the Society of Photo-Optical Instrumentation Engineers (SPIE)*, pages 212–221. SPIE-Int Soc Optical Engineering, Bellingham, 1998.
- [127]. E. Udd, J. Seim, W. Schulz, R. MacMahon, S. Soltesz, and M. Laylor. Monitoring trucks, cars and joggers on the Horsetail Falls bridge using fiber optic grating strain sensors. In A. G. Mignani and H. C. Lefevre, editors, *14th International Conference on Optical Fiber Sensors*, volume 4185 of *Proceedings of the Society of Photo-Optical Instrumentation Engineers (SPIE)*, pages 872–875. SPIE-Int Soc Optical Engineering, Bellingham, 2000.
- [128]. D. R. Hjelm, L. Bjerkan, S. Neegard, J. S. Rambech, and J. V. Aarsnes. Application of Bragg grating sensors in the characterization of scaled marine vehicle models. *Applied Optics*, 36(1):328–336, 1997.
- [129]. A. Cusano, P. Capoluongo, S. Campopiano, A. Cutolo, M. Giordano, F. Felli, A. Paolozzi, and M. Caponero. Experimental modal analysis of an aircraft model wing by embedded fiber Bragg grating sensors. *IEEE Sensors Journal*, 6(1):67–77, 2006.
- [130]. K. Fukuchi, S. Kojima, Y. Hishida, and A. Hongo. Optical water level sensing systems using fiber Bragg grating. In Y. J. Rao, J. D. Jones, H. Naruse, and R. I. Chen, editors, *Advanced Sensor Systems and Applications*, volume 4920 of *Proceedings of the Society of Photo-Optical Instrumentation Engineers (SPIE)*, pages 54–61. SPIE-Int Soc Optical Engineering, Bellingham, 2002.

- [131]. C. G. Askins, M. A. Putnam, and E. J. Friebele. Instrumentation for interrogating many-element fiber Bragg grating arrays. In W. B. Spillman, editor, *Smart Sensing, Processing, and Instrumentation - Smart Structures and Materials 1995*, volume 2444 of *Proceedings of the Society of Photo-Optical Instrumentation Engineers (SPIE)*, pages 257–266. SPIE - Int Soc Optical Engineering, Bellingham, 1995.
- [132]. S. H. Yun, D. J. Richardson, and B. Y. Kim. Interrogation of fiber grating sensor arrays with a wavelength-swept fiber laser. *Optics Letters*, 23(11):843–845, 1998.
- [133]. M. S. Muller, L. Hoffmann, T. Bodendorfer, F. Hirth, F. Petit, M. P. Plattner, T. C. Buck, and A. W. Koch. Fiber-optic sensor interrogation based on a widely tunable monolithic laser diode. *IEEE Transactions on Instrumentation and Measurement*, 59(3):696–703.
- [134]. A. D. Kersey, T. A. Berkoff, and W. W. Morey. Multiplexed fiber Bragg grating strain-sensor system with a fiber Fabry-Perot wavelength filter. *Optics Letters*, 18(16):1370–1372, 1993.
- [135]. M. A. Davis and A. D. Kersey. Fiber Fourier-transform spectrometer for decoding Bragg grating sensors. In B. Culshaw and J. D. C. Jones, editors, *Tenth International Conference on Optical Fibre Sensors*, volume 2360 of *Proceedings of the Society of Photo-Optical Instrumentation Engineers (SPIE)*, pages 167–170. SPIE - Int Soc Optical Engineering, Bellingham, 1994.
- [136]. G. P. Brady, A. B. L. Ribeiro, D. J. Webb, L. Reekie, J. L. Archambault, and D. A. Jackson. Simple multiplexing scheme for fiber optic grating sensor network. In A. D. Kersey and J. P. Dakin, editors, *Distributed and Multiplexed Fiber Optic Sensors III*, volume 2071 of *Proceedings of the Society of Photo-Optical Instrumentation Engineers (SPIE)*, pages 163–168. SPIE - Int Soc Optical Engineering, Bellingham, 1993.
- [137]. J. C. Kim, H. K. Jun, J. S. Huh, and D. D. Lee. Tin oxide-based methane gas sensor promoted by alumina-supported Pd catalyst. *Sensors and Actuators B-Chemical*, 45(3):271–277, 1997.
- [138]. T. Horiguchi, K. Shimizu, T. Kurashima, M. Tateda, and Y. Koyamada. Development of a distributed sensing technique using Brillouin-scattering. *Journal of Lightwave Technology*, 13(7):1296–1302, 1995.
- [139]. J. P. Dakin, D. J. Pratt, G. W. Bibby, and J. N. Ross. Distributed optical fiber Raman temperature sensor using a semiconductor light-source and detector. *Electronics Letters*, 21(13):569–570, 1985.
- [140]. J. L. Brooks, R. H. Wentworth, R. C. Youngquist, M. Tur, B. Y. Kim, and H. J. Shaw. Coherence multiplexing of fiber-optic interferometric sensor. *Journal of Lightwave Technology*, 3(5):1062–1072, 1985.
- [141]. W. V. Sorin and D. M. Baney. Multiplexed sensing using optical low-coherence reflectometry. *IEEE Photonics Technology Letters*, 7(8):917–919, 1995.
- [142]. L. B. Yuan and J. Yang. Two-loop-based low-coherence multiplexing fiber-optic sensor network with a Michelson optical path demodulator. *Optics Letters*, 30(6):601–603, 2005.
- [143]. Z. G. Guan, A. P. Zhang, M. Jiang, and S. L. He. Low-coherence interrogation scheme for multiplexed sensors based on long-period-grating Mach-Zehnder interferometers. *IEEE Photonics Technology Letters*, 18(5-8):832–834, 2006.
- [144]. A. P. Zhang, Z. G. Guan, and S. L. He. Optical low-coherence reflectometry based on long-period grating Mach-Zehnder interferometers. *Applied Optics*, 45(22):5733–5739, 2006.
- [145]. Z. G. Guan, A. P. Zhang, R. Liao, and S. L. He. Wavelength detection of coherence-multiplexed fiber-optic sensors based on long-period grating

- pairs. *IEEE Sensors Journal*, 7(1-2):36–37, 2007.
- [146]. M. Jiang, Z. G. Guan, and S. He. Multiplexing scheme for self-interfering long-period fiber gratings using a low-coherence reflectometry. *IEEE Sensors Journal*, 7(11-12):1663–1667, 2007.
  - [147]. Z. G. Guan, D. Chen, and S. L. He. Coherence multiplexing of distributed sensors based on pairs of fiber Bragg gratings of low reflectivity. *Journal of Lightwave Technology*, 25(8):2143–2148, 2007.
  - [148]. W. S. Liu, Z. G. Guan, G. R. Liu, C. S. Yan, and S. L. He. Optical low-coherence reflectometry for a distributed sensor array of fiber Bragg gratings. *Sensors and Actuators a-Physical*, 144(1):64–68, 2008.
  - [149]. W. S. Liu and Z. G. Guan. Multiplexing of fiber Bragg grating pairs for sensing based on optical low coherence technology. *Microwave and Optical Technology Letters*, 50(9):2437–2439, 2008.

PAPERS



# PAPER I

## **Vertical lidar sounding of atomic mercury and nitric oxide in a major Chinese city**

Z.G. Guan, P. Lundin, L. Mei, G. Somesfalean, S. Svanberg.

*Applied Physics B* **Published online**, (August 2010).



## Vertical lidar sounding of atomic mercury and nitric oxide in a major Chinese city

Z.G. Guan · P. Lundin · L. Mei · G. Somesfalean · S. Svanberg

Received: 21 April 2010 / Revised version: 24 June 2010  
© Springer-Verlag 2010

**Abstract** Vertical range-resolved measurements of atmospheric pollutants were performed in a major city in southern China, employing a lidar system operating with an optical parametric oscillator transmitter. Recordings of atomic mercury (Hg) and nitric oxide (NO) absorbing in the deep-UV region were taken, yielding concentration profiles only attainable with lidar techniques. In particular, the potential influence of molecular oxygen in low-concentration mercury monitoring was elucidated. Diurnal observations are discussed and presented together with weather parameters.

### 1 Introduction

Air pollution is a major modern problem, which is of great concern on the local level regarding human health, as well as on the global level, where issues related to extended greenhouse effects and ozone depletion are of key importance. Poor air quality in the megacities of the world is affecting an increasing population and remedy measures are being designed. In particular, Chinese authorities emphasize the importance of environmental aspects and enforce regu-

lations regarding industrial and vehicle emissions. To evaluate the effects of these pollution-reduction efforts, powerful air quality measurement techniques are desirable. Point-monitoring devices (see e.g. [1–3]) operating on different principles are available and widely used by environmental protection authorities. Optical remote sensing performed in the free air has many advantages, since wider areas are covered and sampling technique issues are avoided. Among such optical techniques, differential optical absorption spectroscopy (DOAS), gas correlation techniques, tunable diode laser spectroscopy (TDLs), and differential absorption lidar (DIAL) can be mentioned, for which extensive experience exists among the present authors. While the former techniques are all path-integrated concentration measurement methods, the last one [4, 5] has the additional advantage of range resolution. As part of a Sino-Swedish collaboration project, the Lund University mobile lidar system [6] was deployed to China for environmental monitoring. Figure 1 shows a photograph taken when the lidar system and the motor generator were temporarily parked at the Zijingang Campus of Zhejiang University, Hangzhou. The present paper reports on vertical atmospheric sounding in a major city (with population about 7 million) in southern China. Measurements were performed for atomic mercury (Hg) and nitric oxide (NO), two important atmospheric pollutants for which local range-resolved measurements are only possible with the DIAL technique. NO is mainly emitted from road traffic, and the influence of this type of transportation can thus be evaluated. Since atmospheric chemistry processes swiftly convert NO into nitrogen dioxide (NO<sub>2</sub>), its presence ultimately contributes to acidification problems at washout. Mercury is the only pollutant which exists in the air in atomic form (typically 90 percent of the atmospheric mercury is atomic). It is a serious heavy metal pollutant, which

Z.G. Guan (✉) · P. Lundin · G. Somesfalean · S. Svanberg  
Atomic Physics Division, Lund University, P.O. Box 118,  
221 00 Lund, Sweden  
e-mail: [zuguan.guan@fysik.lth.se](mailto:zuguan.guan@fysik.lth.se)  
Fax: +46-46-2224250

Z.G. Guan · L. Mei · G. Somesfalean  
Joint Research Centre of Photonics, Zhejiang University,  
Hangzhou 310058, P.R. China

L. Mei · G. Somesfalean  
Centre for Optical and Electromagnetic Research, Zhejiang  
University, Hangzhou 310058, P.R. China

Published online: 08 August 2010

 Springer



**Fig. 1** The vehicle-based lidar system (green) and the motor generator (white) parked in a temporary position at the Zijingang Campus of Zhejiang University, Hangzhou, China



has its origin in coal combustion, waste incineration, chlor-alkali industries, and mining activities.

Lidar monitoring of NO was first performed by Menyuk et al. [7] and by Aldén et al. [8] in the mid-IR and deep-UV spectral regions, respectively. Mapping of an industrial plume was demonstrated by Edner et al. [9], and Kölsch et al. [10, 11] demonstrated simultaneous lidar monitoring of NO and NO<sub>2</sub> using the spectral coincidence which had been pointed out in Refs. [8, 12]. NO lidar monitoring using a solid-state (Ti:sapphire) laser was described by Toriumi et al. [13]. To our knowledge, the present NO lidar work is the first one using an optical parametric oscillator (OPO) transmitter and the first vertical lidar NO sounding in China.

Mercury lidar techniques were developed by the Lund University group and are described in Refs. [14, 15]. Since then the technique has been used to map out high concentrations of the metal at mercury mines and at chlor-alkali plants [16, 17]. However, range-resolved vertical sounding of low/background mercury concentrations as described in the present paper has not been reported to our knowledge. In particular, an interference problem in low-level mercury lidar monitoring, due to the abundant molecular oxygen, is discussed and solved.

## 2 Lidar system

The mobile lidar system is thoroughly described in Ref. [6]. The transmission dome, normally used for lateral scanning, was removed for vertical transmission without any sealing window between the system and the atmosphere. The main parts of the lidar system are briefly described below. An optical parametric oscillator (OPO) is employed as a transmitter, which is pumped by the third harmonic of an Nd:YAG

laser. The output frequency and the line width of each laser shot could be measured with a pulsed digital wavemeter. The receiving telescope is of Newtonian type and has a diameter of 40 cm. The telescope field of view, normally selected to be about 2 mrad and determined by an iris aperture placed in the focal plane of the telescope, was matched to the divergence of the transmitted beam, set by proper adjustment of a Keplerian telescope. A photomultiplier tube, with ramped amplification to suppress the strong close-range signal, was connected to a transient digitizer, allowing on- and off-resonant lidar transients to be stored and averaged in separate memories. A measurement cycle consisted of interlacing recordings of eight shots on and eight shots off, respectively, the specific absorption line of the species under investigation, followed by one blank/background recording with the laser beam blocked by a chopper for the on- and off-laser settings. Depending on the required signal-to-noise ratio, the number of cycles to be averaged could be selected.

## 3 Measurements and results

### 3.1 Atomic mercury

Mercury occurs normally at low concentrations in the atmosphere; for instance, the Atlantic background is around 2 ng/m<sup>3</sup>. However, urban concentrations can be 10 times higher or more, while concentrations of 1 µg/m<sup>3</sup> occur in direct vicinity of mercury mines and ore smelters. Mercury pollution is extensively studied world wide, especially since the extremely toxic compound methyl mercury is formed over time and causes serious brain damage in humans. Special international conferences devoted to this topic are arranged every third year (see e.g. [18]).

### 3.1.1 Hg sounding and O<sub>2</sub> interference

The atomic transition at about 254 nm was utilized. The line consists of several isotopic and hyperfine structure components, as mapped out at high spectral resolution, e.g. in Ref. [19]. At atmospheric pressure these components merge into a broadened structure with a half-width of about 0.005 nm. In connection with the work reported in Ref. [15], it was observed that there are two unclassified weak absorption lines due to molecular oxygen close to the mercury line. These can cause problems when low concentrations of atmospheric mercury are measured, and especially when the line width of the laser degrades and the central wavelength drifts during a long-term measurement. In the present work, focusing on accurate range-resolved measurements of low-level mercury, a detailed study of the spectral interplay between mercury and molecular oxygen was performed.

Vertical lidar recordings were made at a typical laser pulse energy of 6 mJ, and elastic backscattering for the on- and off-resonance wavelengths of 253.728 and 253.745 nm, respectively, was recorded as shown in Fig. 2a. The initially low backscattering signals are due to the ramping of the photomultiplier voltage, reaching a steady maximum at about 400-m distance. From the slope of the on/off ratio 'DIAL' curve (Fig. 2b), the Hg concentration can be evaluated by referring to a 9.7-mm-thick mercury vapor cell of well-known temperature. Part of the laser output is passed through this cell and the detected signal is normalized to a split-off beam

fraction, directly hitting a further detector. Although the total absorption for a range of 1 km is a few percent or less, it is still possible to retrieve some range-resolved concentration information. Figure 2c compares the ratio curves from vertical and horizontal measurements. The slope of the vertical curve decreases, indicating lower Hg concentration at longer distance (higher altitude), while that of the horizontal one remains mainly constant, indicating that the concentration of Hg at the same altitude is stable. The tendency of mercury to seek lower altitudes has been observed by us in earlier work at chlor-alkali plants.

As indicated in Ref. [15], the oxygen lines as measured with a dye laser are considerably narrower than the mercury line. Therefore, the potential influence of oxygen on mercury monitoring will be dependent on the laser line width. Interference studies are important, especially since the OPO used has a considerably broader line width. As mentioned above, the typical line width of emission from the OPO is around 0.2 cm<sup>-1</sup>. However, in long-term running (e.g. diurnal measurement), the degradation of the system and the drift of the central wavelength can possibly make the effective line width considerably worse.

In order to investigate possible interference of molecular oxygen with the low-level mercury measurements, we performed spectroscopic DIAL measurements, where the 'off' wavelength is fixed at 254.745 nm (here the absorption of oxygen is known to be absent) while the 'on' wavelength is scanned with 0.001-nm increments from 254.742 to 253.712 nm. Fifty cycles were averaged for each wavelength pair and the absorption coefficient was evaluated from the average slope for the range 80 to 400 m. At the same time, the differential absorption spectrum for pure mercury in the reference cell was recorded. Knowing the path length through the cell and the accurate temperature, a reference ppt × m value is obtained, from which the effective line width of the light source can also be deduced. The data averaged over two complete scans performed in the way just described are shown as cross marks in Fig. 3a. Using parameters from the spectral database HITRAN [20] and Ref. [21], the absorption spectra of O<sub>2</sub> and Hg in the scanned range are calculated and convoluted with the laser line shape, a Gaussian function with a line width of 1.5 cm<sup>-1</sup>, which is deduced from scanning the reference cell. An Hg experimental transmission profile through the calibration cell is shown as an inset in Fig. 3a. From the fit it is evaluated that a spurious mercury concentration of 1.75 ng/m<sup>3</sup>, induced by the residual absorption of the O<sub>2</sub> lines, must be subtracted from the data using the optimum wavelength pair indicated in Fig. 3a. We note that, with a constant concentration of 21% for O<sub>2</sub> in ambient air, such residual absorptions/spurious concentrations only depend on the effective laser line width, which can be accurately estimated from the reference cell measurements. The spurious

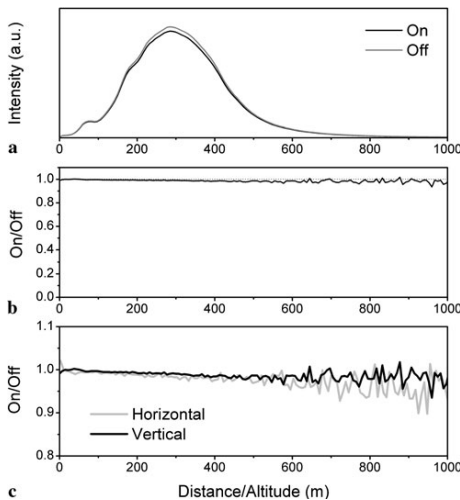
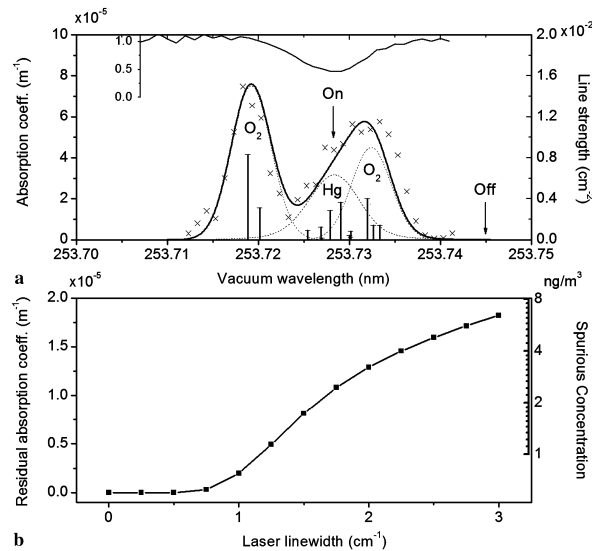


**Fig. 2** (a) DIAL curves for on- and off-resonance wavelengths; (b) the ratio of DIAL curves; (c) comparison between the horizontal and vertical measurements

**Fig. 3** (a) Spectroscopic DIAL data from an 80–400 m range interval. The fit of the calculated absorption spectrum (solid dark line) and the experimental one (cross marks) of O<sub>2</sub> and Hg (7 ng/m<sup>3</sup>) in the atmosphere. The dashed lines respectively show the separated spectra, correlated to the absorption lines (the line strength of Hg is scaled by 10<sup>−25</sup>). The inset curve on top shows the simultaneous experimental recording of the transmission in the mercury cell. (b) Calculated residual absorption coefficient/spurious concentration induced by O<sub>2</sub> at wavelength ‘on’



concentration is calculated for different laser line widths and is shown in Fig. 3b. Clearly, the correction is not ignorable when the Hg concentration is low.

### 3.1.2 Diurnal Hg variations

Vertical atomic mercury soundings were performed during (parts of) five days in November 2009 including a 36-h time series (on 24–25 November 2009). Mercury concentrations averaged from altitude 80 to 380 m, and from 380 to 770 m, respectively, are shown in Fig. 4, together with wind speed and direction, as well as ground temperature. The correction for oxygen interference has been applied according to the above analysis.

From the figure, the following conclusion can be made. The atmosphere at higher altitude generally has lower levels of Hg, which is understandable since Hg atoms are much heavier than air molecules. Further, the low concentration that appears during the early morning seems to be related to low atmospheric temperature, and the north-west wind mostly from rural areas.

### 3.1.3 Washout effect

The washout effect of rain on the atmospheric mercury is discussed in e.g. Ref. [22], by measuring the concentration of mercury in rainwater. We here demonstrate that the washout effect can be seen from the lidar measurement directly. Figure 5 shows the comparison of concentration between measurements on 14th and 19th of December 2009.

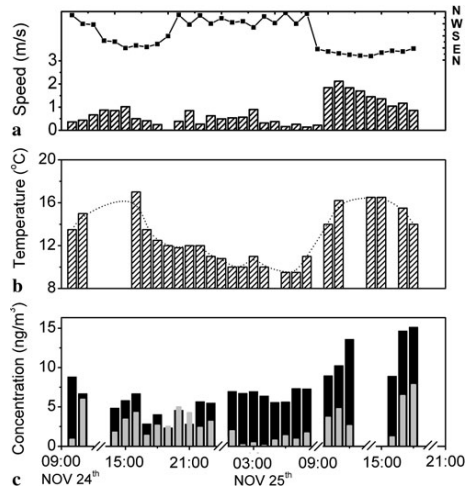


**Fig. 4** The measured wind speed/direction (a) and ground temperature (b) during the diurnal Hg monitoring. (c) The average concentration of Hg in low (dark) and high (gray) atmosphere

The rain started on the 13th and the weather turned to be clear after the 16th. The lower atmospheric layer (80 to 380 m) was measured in the same time period (from 20:00 to 23:00) on 14th and 19th of December. Obviously, the

Vertical lidar sounding of atomic mercury and nitric oxide in a major Chinese city

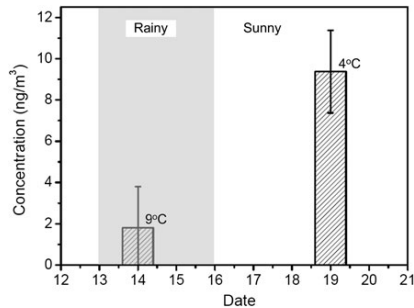


**Fig. 5** The washout effect of rainfall on the concentration of atmospheric mercury

concentration in a rainy weather condition is much lower than that for a clear condition, although the temperature was higher during the recordings in rain.

### 3.2 Nitric oxide

Nitric oxide, which is absorbing at an even shorter wavelength than mercury, is a challenging gas for lidar/optical measurements since the laser beam is heavily attenuated by strong scattering. The preferred wavelength pair for DIAL is 226.878 m and 226.890 nm for the on- and off-wavelengths, respectively.

#### 3.2.1 NO sounding

NO is a quite reactive gas, and thus it is not possible in field experiments to have a reference cell with calibrated gas content for the evaluation of range-resolved concentrations. Since the effective cross sections are line-width dependent, conditions pertaining to the actual measurement situation had to be established. Thus, we again took advantage of the unique multiple-wavelength-pair capability of the Lund University lidar system to differentially scan the region of interest around the NO  $\gamma$ -band close to 226 nm, while recording DIAL curves in the same way as described for the case of Hg above. Examples of on- and off-resonance curves and the DIAL ratio are shown in Fig. 6b and c for the preferred wavelength pair. Although the backscatter signal seems low beyond 300 m on the linear scale of Fig. 6b, the signal is actually strong enough to allow evaluation out to about 450-m distance. The full DIAL scan data, with average differential absorption evaluated from 50 to 300 m, are shown in Fig. 6a. Convoluting the spectrum obtained for atmospheric NO with the higher-resolution calibrated NO spectrum given in Ref. [9], we found that the effective differential absorption cross section  $(5.2 \pm 1.0) \times 10^{-22} \text{ m}^2$  should be used for the preferred wavelength pair.

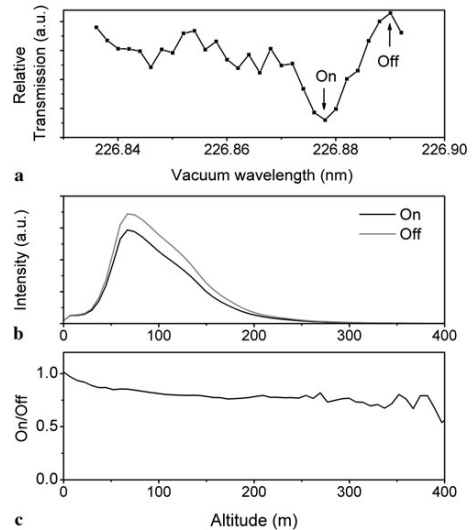


**Fig. 6** (a) The scanned transmission spectrum of NO; (b) on- and off-DIAL curves; (c) the ratio DIAL curve

#### 3.2.2 Diurnal NO variations

Diurnal and range-resolved vertical NO concentrations for 25–26 November 2009 are given in Fig. 7 together with weather data. The NO pollution mainly comes from road traffic, which is strongly reduced at night time. However, the highest concentrations of NO were observed during the night. Atmospheric chemistry for NO is very complex with many interacting factors including ozone, hydrocarbons, and the sunlight. Night fog was observed forming around 11:00 pm and vanished due to the sun irradiation towards 9 am in the morning. The combined atmospheric chemistry factors in interplay with metrology lead to a minimum concentration appearing in the afternoon while the maximum appears towards midnight. Compared to the close-to-ground atmospheric layer, the air at higher altitudes is much cleaner, as expected with NO being vehicle generated.

## 4 Discussion

Our vertical lidar soundings of Hg and NO concentrations show a complex interplay between concentrations and meteorological parameters, and in the case of NO also atmospheric chemistry. The observed vertical gradients could largely be understood. Clearly, systematic measurements under extended times and varying weather conditions,

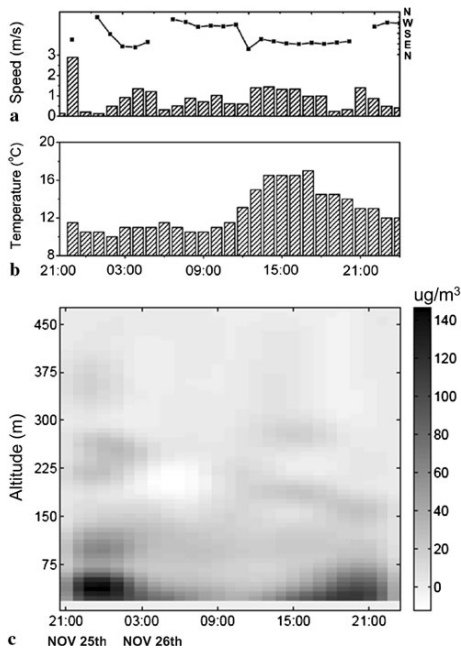


**Fig. 7** The measured wind speed/direction (a) and ground temperature (b) during the diurnal NO monitoring. (c) The variation of NO during the 24-h cycle

and inclusion of ground-based point monitors, would further elucidate the dynamics of the two deep-UV absorbing pollutants—the heavy metal mercury and the vehicle-generated nitric oxide. Our studies suggest that the differential absorption lidar technique for range-resolved pollution monitoring could be an important future possibility in the environmental management of the megacities of China.

**Acknowledgements** This project was supported by the Swedish Research Council through a regular grant and through a SIDA-VR Research Link grant, and also by a Linnaeus grant to the Lund Laser Centre. The authors are very grateful to Sailing He, Jun Hu, Chunsheng Yan, Haojiang Zhou, and Binhao Wang for valuable help and assistance.

## References

1. H. Okabe, P.L. Splitsto, J.J. Ball, J. Air Pollut. Control Assoc. **23**, 514 (1973)
2. R.S. Braman, M.A. Delacanter, X.H. Qing, Anal. Chem. **58**, 1537 (1986)
3. J.G. Goode, R.J. Yokelson, D.E. Ward, R.A. Susott, R.E. Babbitt, M.A. Davies, W.M. Hao, J. Geophys. Res., Atmos. **105**, 22147 (2000)
4. T. Fujii, T. Fukuchi (eds.), *Laser Remote Sensing* (CRC Press, Boca Raton, 2005)
5. S. Svanberg, in *Springer Handbook of Lasers and Optics*, ed. by F. Träger (Springer, Heidelberg, 2007), pp. 1031–1052
6. P. Weibring, H. Edner, S. Svanberg, Appl. Opt. **42**, 3583 (2003)
7. N. Menyuk, D.K. Killinger, W.E. DeFeo, Appl. Opt. **19**, 3282 (1980)
8. M. Aldén, H. Edner, S. Svanberg, Opt. Lett. **7**, 543 (1982)
9. H. Edner, A. Sunesson, S. Svanberg, Opt. Lett. **13**, 704 (1988)
10. H.J. Kölsch, P. Rairoux, J.P. Wolf, L. Wöste, Appl. Opt. **28**, 2052 (1989)
11. H.J. Kölsch, P. Rairoux, J.P. Wolf, L. Wöste, Appl. Phys. B **54**, 89 (1992)
12. Zh. Nickolov, S. Svanberg, Lund Rep. Atomic Physics LRAP-71, Lund Institute of Technology, Lund, Sweden (1986)
13. R. Toriumi, H. Tai, H. Kuze, N. Takeuchi, Jpn. J. Appl. Phys. **38**, 6372 (1999)
14. M. Aldén, H. Edner, S. Svanberg, Opt. Lett. **7**, 221 (1982)
15. H. Edner, G.W. Faris, A. Sunesson, S. Svanberg, Appl. Opt. **28**, 921 (1989)
16. S. Svanberg, Opt. Lasers Eng. **37**, 245 (2002)
17. R. Grönlund, M. Sjöholm, P. Weibring, H. Edner, S. Svanberg, Atmos. Environ. **39**, 7474 (2005)
18. S. Balogh (ed.), Proc. Ninth Int. Conf. Mercury as a Global Pollutant, Guiyang, China. Special Issue, Water Air Soil Pollut., Thorjorn Larssen, and Guangle Qiu, to appear
19. J. Alnis, U. Gustafsson, G. Somesfalean, S. Svanberg, Appl. Phys. Lett. **76**, 1234 (2000)
20. L.S. Rothman, I.E. Gordon, A. Barbe, D.C. Benner, P.F. Bernath, M. Birk, V. Boudon, L.R. Brown, A. Campargue, J.-P. Champion, K. Chance, L.H. Coudert, V. Dana, V.M. Devi, S. Fally, J.-M. Flaud, R.R. Gamache, A. Goldman, D. Jacquemart, I. Kleiner, N. Lacome, W.J. Lafferty, J.-Y. Mandin, S.T. Massie, S.N. Mikhailenko, C.E. Miller, N. Moazzen-Ahmadi, O.V. Naumenko, A.V. Nikitin, J. Orphal, V.I. Perevalov, A. Perrin, A. Predoi-Cross, C.P. Rinsland, M. Rotger, M. Simeckova, M.A.H. Smith, K. Sung, S.A. Tashkun, J. Tennyson, R.A. Toth, A.C. Vandaele, J. Vander Auwera, J. Quant. Spectrosc. Radiat. Transf. **110**, 533 (2009)
21. T.N. Anderson, J.K. Magnuson, R.P. Lucht, Appl. Phys. B **87**, 341 (2007)
22. R. Ferrara, B.E. Maserti, A. Petrosino, R. Bargagli, Atmos. Environ. **20**, 125 (1986)

# PAPER II

## **Gas analysis within remote porous targets using LIDAR multi-scatter techniques**

Z.G. Guan, M. Lewander, R. Grönlund, H. Lundberg, S. Svanberg.  
*Applied Physics B* **93**, 657 - 663 (2008).



## Gas analysis within remote porous targets using LIDAR multi-scatter techniques

Z.G. Guan · M. Lewander · R. Grönlund ·  
H. Lundberg · S. Svanberg

Received: 14 April 2008 / Revised version: 4 July 2008 / Published online: 5 September 2008  
© Springer-Verlag 2008

**Abstract** Light detection and ranging (LIDAR) experiments are normally pursued for range resolved atmospheric gas measurements or for analysis of solid target surfaces using fluorescence of laser-induced breakdown spectroscopy. In contrast, we now demonstrate the monitoring of free gas enclosed in pores of materials, subject to impinging laser radiation, employing the photons emerging back to the surface laterally of the injection point after penetrating the medium in heavy multiple scattering processes. The directly reflected light is blocked by a beam stop. The technique presented is a remote version of the newly introduced gas in scattering media absorption spectroscopy (GASMAS) technique, which so far was pursued with the injection optics and the detector in close contact with the sample. Feasibility measurements of LIDAR-GASMAS on oxygen in polystyrene foam were performed at a distance of 6 m. Multiple-scattering induced delays of the order of 50 ns, which corresponds to 15 m optical path length, were observed. First extensions to a range of 60 m are discussed. Remote observation of gas composition anomalies in snow using differential absorption LIDAR (DIAL) may find application in avalanche victim localization or for leak detection in snow-covered natural gas pipelines. Further, the techniques may be even more useful for short-range, non-intrusive GASMAS measurements, e.g., on packed food products.

**PACS** 42.68.Wt · 07.07.Df

### 1 Introduction

Light detection and ranging (LIDAR) techniques have been proven to be very successful in environmental monitoring of the atmosphere, hydrosphere, or of fixed targets (see, e.g., [1–6]). Normally, LIDAR experiments are of the remote-sensing type and performed over substantial ranges. Atmospheric LIDAR studies can be separated into aerosol monitoring, where the detailed laser tuning is of limited importance, and narrow-band differential absorption LIDAR (DIAL) experiments for gas analysis. By using close-lying on- and off-resonance laser wavelengths for a particular gas, the ratio between the backscattering signals with and without absorption can be used to determine the distribution and concentration of a specific gas in the atmosphere [7]. In environmental monitoring of, e.g., air pollutants, single-scattering is frequently a good assumption. However, multiple-scattering LIDAR is also a well-established method related to fog and cloud conditions (see, e.g., [8]). A similar technique is utilized in short-range time-resolved measurements for strongly scattering media such as tissue [9, 10]. In these measurements, transillumination is frequently employed instead of backscattering methods. By evaluating the effective path length of the light in the scattering medium the concentration of sensitizers in tumors [11] or active components in pharmaceutical tablets [12] can be found using white-light spectroscopy. Such experiments interrogate broad-band spectral structures characteristic of liquids or solids. Recently, we realized that extremely sharp structures due to free gas in pores throughout the scattering solid material are present and can be seen if the spectral resolution of single-mode diode lasers is utilized [13].

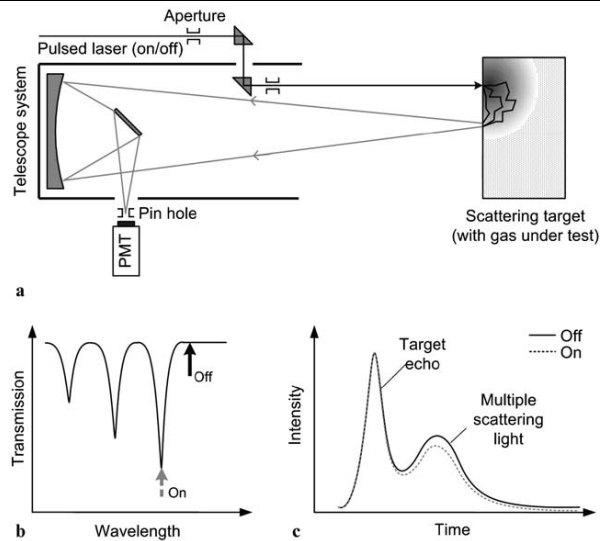
Z.G. Guan · M. Lewander · R. Grönlund · H. Lundberg ·  
S. Svanberg (✉)  
Atomic Physics Division, Lund University, P.O. Box 118, 221 00  
Lund, Sweden  
e-mail: [sune.svanberg@fysik.lth.se](mailto:sune.svanberg@fysik.lth.se)

*Present address:*  
R. Grönlund  
SpectraCure AB, Ideon Research Park, Ole Römers Väg 16,  
223 70 Lund, Sweden



**Fig. 1** The working principle of the technique presented:

(a) schematic diagram of the system; (b) switching between on and off can be realized by finely tuning the laser wavelength across an absorption dip of the gas under test; (c) the difference between the curves corresponding to on and off wavelengths reveals the presence of the gas



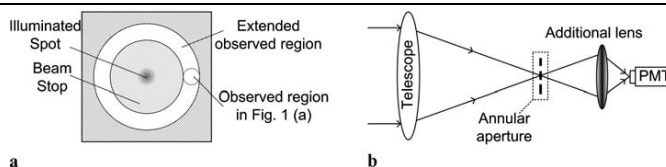
In the applications of such gas in scattering media absorption spectroscopy (GASMAS) to wood, polystyrene foam, food, fruits, pharmaceutical tablets, or human air-filled sinus cavities [14–19], CW lasers are generally used to obtain a high spectral resolution. For pulsed lasers, the resolution is Fourier transform limited making a sufficient temporal and a high spectral resolution hard to attain simultaneously in small samples. The situation is different for larger-scale scenarios.

In the present paper we report the extension of the GASMAS technique to the monitoring of gas in remote porous targets. “Classical” GASMAS [13] is pursued with diode lasers directly coupled to a porous material and with the detector again in direct contact with the multiple-scattering sample. In contrast to the broad absorptive features of the bulk material, the free gas distributed in pores or cavities in the sample gives rise to typically 10,000 times sharper absorption lines than those characteristic of solids. These features can only be observed using techniques developed for atmospheric air-pollution monitoring, as much pursued by the Lund research group. Recently, we realized that remote-sensing GASMAS or LIDAR-GASMAS might be a new LIDAR possibility. A proposal was first put forward in [20]. In contrast to the situation when the light is injected using a probe in contact with the sample, remote light injection in a sample gives rise to a very bright surface reflection. When seen by a remote telescope, this reflection outshines the faint light that has been scattered within the medium. In order to favor the light which has travelled inside the material, an on-

axis aperture stop blocking the surface reflection can be used in the telescope focal plane. We have performed first measurements demonstrating the possibility to remotely monitor gas anomalies in strongly scattering materials, such as snow. We present proof-of-principle DIAL-like measurements to analyze gases in polystyrene foam.

The general principle of the techniques presented is shown in Fig. 1. The photons incident on the target are heavily scattered inside the material. Some of them surface again at a distance from the injection point, after having visited deeper layers of the target. Such photons are collected by a telescope system which is properly aimed and are recorded by a fast and sensitive detector (e.g., a photo-multiplier tube (PMT)). The waveform is digitized in a fast oscilloscope/transient digitizer and is compared with the incident waveform (the transmitted pulse). An echo from the target surface followed by a distribution of delayed photons is expected, the latter having a history of multiple scattering inside the target medium. By finely tuning the laser wavelength to an on- and a close-lying off, reference wavelength, different signal shapes for the delayed photons are expected due to differential absorption for the gas present in the pores of the target; see Figs. 1(b) and 1(c). Like most LIDAR varieties, the presented technique works in a backscattering mode for many practical reasons. On the other hand, the direct surface reflection, the target echo, which is  $\sim 10,000$  times stronger than the scattering light, can easily blind the PMT from seeing any scattering signal if it is not suppressed effectively. Here we use two apertures to clean the halo of

**Fig. 2** Improved imaging system for mobile LIDAR: (a) improved annular aperture; (b) the arrangement of an annular aperture and an additional lens for photon economy reason



the well-collimated laser beam, so that the laser pulse only illuminates a defined spot on the target. The light halo is due to scattering in optical components. A small aperture in a screen at the focal plane of the telescope defines its field of view. By separating the observed spot from the illuminated one, the PMT will in principle only see multiply scattered photons. Due to imperfections an echo from the illuminated spot still will occur; however, by this geometrical arrangement most of the echo can be suppressed.

In a real-world scenario, it is desirable to scan the laser beam and the detection field-of-view in synchronism by using a co-axial LIDAR system with a common folding mirror. This is the arrangement used in the Lund mobile LIDAR system described in [21]. For photon economy reasons, practical measurements would be performed using an annular observation-defining opening aperture in the telescope focal plane as illustrated in Fig. 2. As seen in Fig. 2(a), the detection efficiency is obviously much improved as compared to the case shown in Fig. 1(a). In order to collect the laterally displaced photons on a finite size detector, a lens arrangement, as illustrated in Fig. 2(b), could be used.

## 2 Experimental arrangements

We will now describe the experimental arrangements used in our proof-of-principle experiments performed in the laboratory along the lines illustrated in Fig. 1 and in first outdoor tests with our mobile LIDAR system using the annular aperture arrangement (Fig. 2(a)).

### 2.1 Laboratory setup

In the in-door laboratory experiments, schematically illustrated in Fig. 3(a), we use a wavelength-tunable pulsed laser system based on a dye laser pumped by a Nd:YAG laser (532 nm). The laser pulse (190 mJ, 10 Hz repetition frequency) from the pump has a width of 10 ns and is compressed into  $\sim 2$  ns by backward stimulated Brillouin scattering in water [22]. The wavelength of the system can be tuned from vacuum ultraviolet to near infrared by using different dyes and applying frequency doubling/tripling and Raman shifting techniques. In the present work we operated at 656 nm, 760 nm, and around 330 nm with a line width of about 0.01 nm. The switching (on and off) around 760 nm

was realized by accurately controlling a high-resolution grating in the dye laser.

In order to control the distance  $D$  between the illuminated spot and the observed region on the target (see the inset of Fig. 3(a)), a rotatable prism was employed for scanning the laser beam. Apertures in the optical path can be used to clean the faint halo (due to scattering in optical component) surrounding the well-collimated light. The scattered light emerging from the observed region on the target was collected by a telescope (with a diameter of 25 cm and a focal length of 1 m), set 6 m away, before arriving to a PMT detector (Hamamatsu R2368). A 4 mm pinhole is set at the focal plane of the telescope, corresponding to an observing region with a diameter of 20 mm on the target. With a photodiode (PD), a small amount of light split from the laser beam generated a trigger signal for a fast oscilloscope (Tektronix DPO 7254) used to record the PMT signal.

### 2.2 Mobile LIDAR setup

The Lund mobile LIDAR system used in some initial tests is shown in Fig. 3(b). The system is thoroughly described in [21]. Basically, it is a co-axial system with a roof-top scanning mirror. The transmitter is an Nd:YAG-pumped Optical Parametric Oscillator (OPO) system with wide tunability, augmented by nonlinear wavelength shifting techniques. In our initial experiments we only employed the 355 nm harmonic from the pump laser. The pulse length is about 10 ns. The signal sampling electronics of the system has a modest time resolution and was therefore replaced by a Tektronix TDS220 transient digitizer in the present application. The annular aperture arrangement illustrated in Fig. 2(a) was used. With a central aperture block radius of 5 mm, photons emerging more than 30 cm from the laser impact point on the 60 m distant roof-top target will reach the detector.

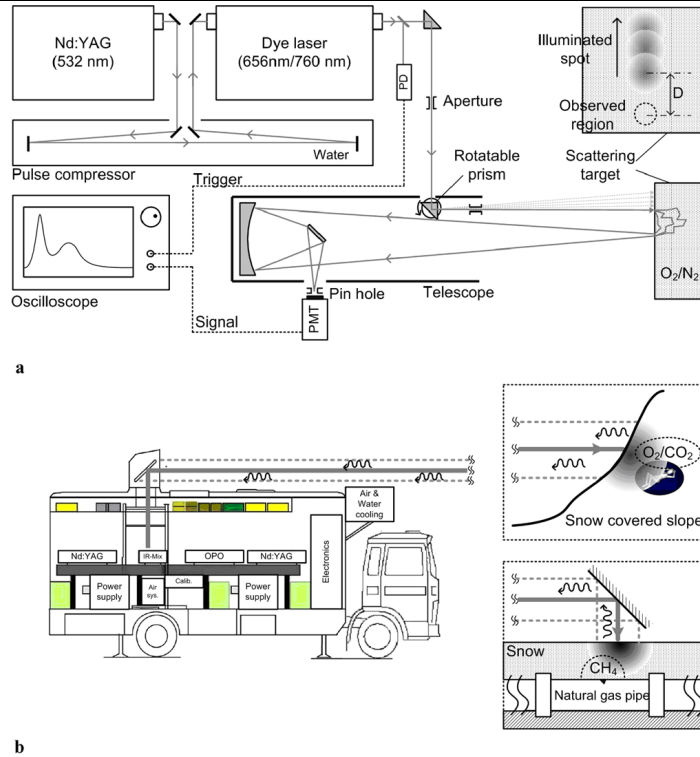
Figure 3(b) also depicts some possible practical applications of the new technique to be discussed later.

## 3 Measurements and results

### 3.1 Surface echo and multiple-scattering recording

We initially used 656 nm laser pulses, employing the laser dye DCM, in laboratory measurements on a 10 cm thick

**Fig. 3** Experimental setups: (a) laboratory setup; (b) mobile LIDAR system and potential applications, e.g., localization of snow-avalanche victims and inspecting possible methane leakage from a snow-covered natural gas pipeline



block of polystyrene foam. Basic time-resolved signals are shown in Fig. 4(a). The shape of the incident laser pulse is shown as the solid grey line, with its peak position set at time 0 corresponding to the time of arrival of the laser pulse at the target. When the distance  $D$  between the illuminating spot and the observed region is set to be 7 cm, the solid black curve is obtained. Clearly it has a tail due to multiple scattered light. Part of the recorded signal can, however, be suspected to be due to a residual, prompt surface echo. To verify this, we cover the observing region on the target by black paper, and a small amount of echo light directly reflected from the illuminating spot is recorded and shown as the dashed grey line. We can clearly see that this echo light has the same shape as the incident pulse but is delayed about 20 ns due to the 6 m distance between the target surface and the PMT. The isolated multiple scattering light (dot-dashed line) can be obtained by subtracting the echo from the composite target signal. The intensities of the echo and the truly scattered light are still comparable, although the echo light has been greatly suppressed by the imaging system. We found that a

major part of the residual echo signal is due to scattering in the telescope mirror surfaces, resulting in light which clearly does not image sharply into the plane of the target-defining telescope aperture.

By prism steering, the laser beam was directed for setting different  $D$  values (see in the inset of Fig. 3(a)). The solid, dot-dashed, dashed, and dotted lines in Fig. 4(b) correspond to truly scattered light when  $D$  is 4, 5.5, 7, and 8.5 cm, respectively. All these curves are obtained with the method used in Fig. 4(a). As  $D$  increases, we can see the delay between the incident light (solid grey line) and the scattered light gradually increase, and the tail due to multiply scattered light becoming longer. This can be understood as due to more extensive scattering with possibilities for photons to penetrate deeper into the polystyrene foam material. We note that scattering delays of 50 ns, corresponding to photon traveling paths of 15 m inside the material are not uncommon.

The same experiments were carried out on a 5 cm thick fresh snow layer. Similar signals are also observed when

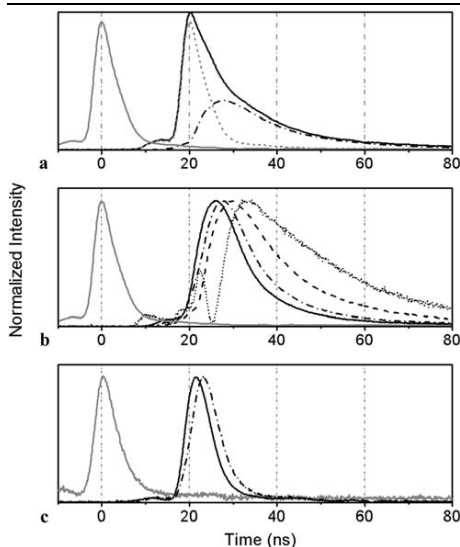


**Fig. 4** Experimental results on measuring multiply scattered and direct echo contributions: (a) the desired isolated scattered light (dot-dashed line) can be obtained by subtracting the direct echo light (dashed grey line) from the recorded temporally expanded pulse (solid dark line); (b) and (c) show the evolution of the multiply scattered light in polystyrene foam and snow, respectively, as  $D$  increases (see text for details)

setting  $D$  to 5 and 10 cm, corresponding to the solid and dot-dashed lines, respectively, in Fig. 4(c). From the figure we can see that the scattering effect of snow is weaker than that of polystyrene foam. However, this result is encouraging, since in a more weakly scattering material, photons can access deeper structures of the target, which is required in real-world applications to be discussed below.

### 3.2 Remote analysis of gas in scattering media

In order to make a proof-of-principle demonstration of the possibility to remotely detect gas and gas anomalies in a porous scattering medium, we used our laboratory setup in experiments with molecular oxygen gas in the polystyrene foam block. The wavelength of the dye laser was tuned to the molecular oxygen A band around 760 nm, now by employing the dye LC7710. Oxygen monitoring in “classical” GASMAS experiments using tunable diode laser has been much pursued [13–19]. The present experiments were performed with differential absorption at the R9Q10 line at 760.654 nm. From Fig. 5(a) a clear difference can be seen between the curves when the laser is at on- and off-resonance wavelengths in recordings for a separation  $D$  of

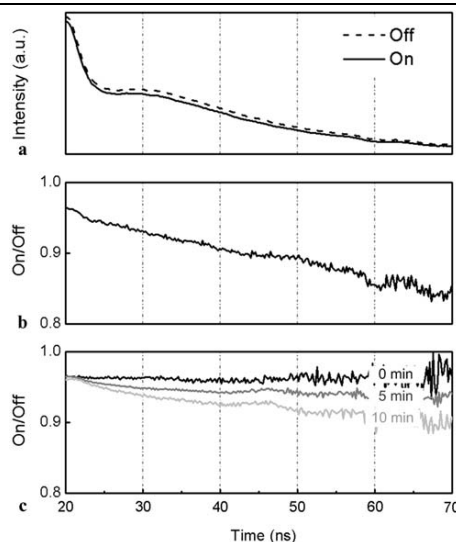
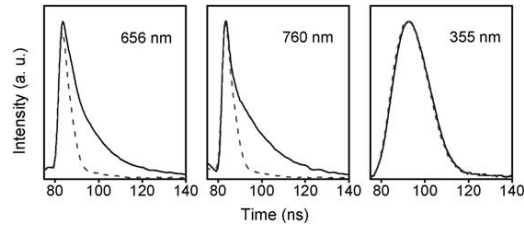


**Fig. 5** Experimental results on analysis of the oxygen concentration in polystyrene foam: (a) the difference between pulse curves corresponding to on and off; (b) the ratio of on and off curves reveal the existence of the oxygen in the polystyrene; (c) the slope of the on/off curve increases with time when a nitrogen filled polystyrene is exposed to the air

7 cm. The ratio of the two curves, the DIAL curve [7], is shown in Fig. 5(b). Clearly, there is a differential absorption effect due to the normal atmospheric oxygen over the measurement path; the influence of this effect can be seen by the ratio not starting at 1.00. The sloping DIAL curve indicates the increasing attenuation of the on-wavelength signal for increasing effective path lengths in the scattering medium and can be used to derive the (uniform) concentration of the gas under investigation [7].

For observing effects of gas concentration anomalies with practical applications in mind, we performed a controlled gas exchange experiment. A block of polystyrene foam was put in a plastic bag, with sealing. The sample was left in this way over night to allow invasion of nitrogen (expulsion of oxygen) in the porous foam. We then extracted the block and immediately performed DIAL measurements. As expected, the slope of the on/off curve is zero at the beginning of the measurement (black curve in Fig. 5(c)) corresponding to the absence of oxygen. The slope of the DIAL curves obtained in measurements at 5 and 10 min obviously increases, due to the reinvasion of oxygen-containing normal air into the polystyrene foam.

**Fig. 6** Comparison between LIDAR-GASMAS signals recorded for 656, 760, and 355 nm in polystyrene foam; the multiple-scattering tail cannot be seen at 355 nm due to strong bulk medium absorption at this wavelength in combination with a lower temporal resolution available in the mobile lidar system



### 3.3 Scattering signal comparison for different wavelengths

Since the scattering and absorption coefficients of a material strongly depend on the wavelength of the light, it is important to find a proper wavelength to analyze a specific gas in a specific scattering material. Taking polystyrene foam for example, we compare results for three different wavelengths in Fig. 6. The data corresponding to 656 and 760 nm are obtained with the laboratory setup. We can see that both of them have obvious tails due to scattering, compared with the incident laser pulses (dashed curves). However, if looking in detail at the data, a slight difference can be observed between the curves for 656 and 760 nm, since both the scattering and absorption coefficients are different at these two wavelengths for polystyrene foam. For further comparison, a curve obtained with 355 nm laser light from a frequency tripled Nd:YAG laser is shown. In this experiment, carried out with the mobile LIDAR system, the distance to the polystyrene foam target is 60 m. The temporal resolution of this system is lower than for the laboratory system. No scattering tail can be seen in the signal curve, compared to the direct laser pulse temporal shape. Although the cross section according to Mie scattering theory strongly increases for short wavelengths, this effect is overwhelmed by a stronger absorption in polystyrene for the UV wavelength used. Actually, this was confirmed also in test experiments at about 330 nm using frequency-doubled dye laser radiation in our laboratory set-up. Even with the considerably better temporal resolution, no multiple-scattering tail was observed. However, by a proper combination of material and wavelength, such as polystyrene foam studied at 760 nm, the multiple scattering tail should be observable, as suggested from Fig. 4(b), also with the lower temporal resolution of the present mobile LIDAR system.

## 4 Discussion and outlook

We have demonstrated the possibility to perform remote sensing measurements on free gas distributed in a solid scattering medium. The technique has connection to both multiple scattering LIDAR and in particular to GASMAS measurements and can be considered as LIDAR-GASMAS. The

challenge is to achieve a sufficient rejection of the direct target echo light in combination with having a sufficient temporal resolution of the system. The right combination of target material and LIDAR wavelength must also be attained to avoid strong absorption of the multiply scattered light, which would effectively quench a temporally delayed tail. Clearly, the gas to be studied also must have a sufficient absorption in such an optical window.

Considering possible practical applications of LIDAR-GASMAS in the open environment, measurements on snow, a material which is certainly strongly scattering, come to mind. Water has a wide transmission window from about 190 to 1400 nm. Molecular oxygen has its A band around 760 nm, which is useful in combination with snow as well as polystyrene foam. The VUV Shumann–Runge band of oxygen, extending with a weak and useful tail of sharp lines up till about 200 nm could also be considered. We have already demonstrated the observation of suppression of the natural oxygen signal due to a displacement gas. If the presence of this latter gas is to be ascertained, clearly a substantial concentration is needed to suppress the oxygen signal due to the dilution of oxygen. In principle, any dilution gas could then be observed indirectly through the suppression of the oxygen DIAL signal. More desirable is clearly to make direct DIAL monitoring on the gas of interest, requiring the compatibility of bulk transmission and realistic specific absorption lines. Direct detection yields signals rising from a basically zero background, rather than observing a small reduction in a strong oxygen signal as the signature of the presence of the gas under study.

Two very demanding possible real-world LIDAR-GASMAS applications could be considered, as already indicated in Fig. 3(b). One is the localization of snow-avalanche victims based on the high percent of carbon dioxide (5 percent) in exhaled air or the corresponding reduction from the ambient 21 percent abundance. A further application may be the inspection of gas-covered natural gas pipelines for possible methane leaks. Since the gas is trapped and the path lengths are long, in the strongly scattering snow even small leaks might be detectable. Helicopter-borne installation might be the most realistic one in both cases.

We note that methane has weak absorptive features around 1.35  $\mu\text{m}$ , which should be compatible with the optical properties of snow. Materials not containing high concentrations of liquid water may have more relaxed conditions regarding wavelength extension into the IR region, where most gases have strong absorption bands.

It should be noted that once the remote GASMAS technique is fully established, it could be scaled down to small range but still being basically LIDAR, allowing non-contact monitoring at a short distance. For example, food inspection and moisture measurements using hand-held instruments could be envisaged. Normal GASMAS applications so far used contact injection of light into the sample and the detector in contact with the sample as well. In this way, problems with the strong direct “echo” are avoided. With the spatial imaging techniques developed here for LIDAR-GASMAS, ways to suppress this signal are demonstrated, opening up the possibility for close-range non-contact measurements in many contexts.

**Acknowledgements** This work was supported by the Swedish Research Council (VR) and the Knut and Alice Wallenberg Foundation.

## References

1. T. Fujii, T. Fukuchi (eds.), *Laser Remote Sensing* (CRC Press, Boca Raton, 2005)
2. C. Weitkamp, *Lidar: Range-Resolved Optical Remote Sensing of the Atmosphere* (Springer, Heidelberg, 2005)
3. D. Killinger, Lidar and laser remote sensing, in *Handbook on Vibrational Spectroscopy* (Wiley, New York, 2002)
4. S. Svanberg, LIDAR, in *Springer Handbook of Lasers and Optics*, ed. by F. Träger (Springer, Heidelberg, 2007), pp. 1031–1052
5. S. Svanberg, Fluorescence spectroscopy and imaging of LIDAR targets, in *Laser Remote Sensing* (CRC Press, Boca Raton, 2005), Chap. 7
6. Conference Proceedings, *24th International Laser Radar Conference*, NOAA, NCAR Boulder, Colorado, 23–27 June 2008
7. S. Svanberg, Differential absorption LIDAR (DIAL), in *Air Monitoring by Spectroscopic Techniques*, ed. by M. Sigrist (Wiley, New York, 1994), Chap. 3
8. A.G. Borovoi (ed.), in *Proc. 13th International Workshop on LIDAR Multiple Scattering Experiments*, SPIE, vol. 5829 (2005)
9. G. Müller, B. Chance, R. Alfano, S. Arridge, J. Beuthan, E. Gratton, M. Kaschke, B. Masters, S. Svanberg, P. van der Zee (eds.), *Medical Optical Tomography, Functional Imaging and Monitoring*, SPIE Institute Series, vol. 11 (SPIE, Bellingham, 1993)
10. T. Vo-Dinh, *Biomedical Photonics Handbook* (CRC Press, Boca Raton, 2003)
11. C. af Klinteberg, A. Pifferi, S. Andersson-Engels, R. Cubeddu, S. Svanberg, In vivo absorption spectroscopy of tumor sensitizers using femtosecond white light. *Appl. Opt.* **44**, 2213 (2005)
12. C. Abrahamsson, T. Svensson, S. Svanberg, S. Andersson-Engels, J. Johansson, S. Folestad, Time and wavelength resolved spectroscopy of turbid media using light continuum generated in a crystal fibre. *Opt. Express* **12**, 4103 (2004)
13. M. Sjöholm, G. Somesfalean, J. Alnis, S. Andersson-Engels, S. Svanberg, Analysis of gas dispersed in scattering solids and liquids. *Opt. Lett.* **26**, 16 (2001)
14. G. Somesfalean, M. Sjöholm, J. Alnis, C. af Klinteberg, S. Andersson-Engels, S. Svanberg, Concentration measurement of gas imbedded in scattering media employing time and spatially resolved techniques. *Appl. Opt.* **41**, 3538 (2002)
15. L. Persson, H. Gao, M. Sjöholm, S. Svanberg, Diode laser absorption spectroscopy for studies of gas exchange in fruits. *Lasers Opt. Eng.* **44**, 687 (2006)
16. T. Svensson, L. Persson, M. Andersson, S. Svanberg, S. Andersson-Engels, J. Johansson, S. Folestad, Noninvasive characterization of pharmaceutical solids by diode laser oxygen spectroscopy. *Appl. Spectrosc.* **61**, 784 (2007)
17. M. Andersson, L. Persson, M. Sjöholm, S. Svanberg, Spectroscopic studies of wood-drying processes. *Opt. Express* **14**, 3641 (2006)
18. L. Persson, K. Svanberg, S. Svanberg, On the potential for human sinus cavity diagnostics using diode laser gas spectroscopy. *Appl. Phys. B* **82**, 313 (2006)
19. L. Persson, M. Andersson, M. Cassel-Engquist, K. Svanberg, S. Svanberg, Gas monitoring in human sinuses using tunable diode laser spectroscopy. *J. Biomed. Opt.* **12**(5), 54001 (2007)
20. M. Cassel-Engquist, R. Grönlund, M. Andersson, L. Persson, S. Svanberg, Remote gas detection in solid scattering media using differential absorption LIDAR. CLEO Europe, Munich (2007)
21. P. Weibring, H. Edner, S. Svanberg, Versatile mobile LIDAR system for environmental monitoring. *Appl. Opt.* **42**, 3583 (2003)
22. Z.S. Li, J. Norin, A. Persson, C.G. Wahlström, S. Svanberg, P.S. Doidge, E. Biémont, Radiative properties of neutral germanium obtained from excited state lifetime and branching ratio measurements and comparison with theoretical calculations. *Phys. Rev. A* **60**, 198 (1999)



## PAPER III

### **Aerosol sounding at a rural Swedish area and in a major Chinese city - A comparative study with the Lund lidar system**

P. Lundin, Z.G. Guan, L. Mei, G. Somesfalean, E. Swietlicki, S. Svanberg.

*Proceedings of the 25th International Laser Radar Conference*  
**Volume I (S4P - 50)**, 663 - 666 (2010).





## AEROSOL SOUNDING AT A RURAL SWEDISH AREA AND IN A MAJOR CHINESE CITY – A COMPARATIVE STUDY WITH THE LUND LIDAR SYSTEM

Patrik Lundin<sup>1,2</sup>, Zuguang Guan<sup>1,2</sup>, Liang Mei<sup>2,3</sup>, Gabriel Somesfalean<sup>1,2,3</sup>, Erik Swietlicki<sup>4</sup>, Sune Svanberg<sup>1,2</sup>

<sup>1</sup> Atomic Physics Division, Lund University, P.O. Box 118, SE-221 00 Lund, Sweden, [patrik.lundin@fysik.lth.se](mailto:patrik.lundin@fysik.lth.se)

<sup>2</sup> Joint Research Centre of Photonics, Zhejiang University, Hangzhou 310058, P.R. China

<sup>3</sup> Centre for Optical and Electromagnetic Research, Zhejiang University, Hangzhou 310058, P.R. China

<sup>4</sup> The Aerosol Group of the Nuclear Physics Division, Lund University, P.O. Box 118, SE-221 00 Lund, Sweden

### ABSTRACT

The vertical distribution of atmospheric aerosol particles was measured with the Lund mobile lidar system both at a mainly rural location in southern Sweden and in a major city in the south-east of China. Thereby, two sites with completely different prerequisites regarding, e.g. population density, could be compared straightforwardly. Since exactly the same system and sampling methods were used, the lidar signals obtained at the two sites could be compared already in their raw form and still provide information about the differing scattering properties. Results showing the extinction coefficient profiles at the two sites are also presented.

### 1. INTRODUCTION

Man's impact on Earth has for many years grown to alarming levels. A very important factor is the steadily increasing global population, currently being 6.8 billion people. Increasing needs for transportation and living standard have made human energy consumption and pollution impact a significant issue.

Recently, the awareness about the importance of reducing these impacts and creating a sustainable environment has increased. The situation is generally considered to be critical and tremendous global efforts have to be put into research, education and designing proper policies. Many countries around the world have set up regulations to decrease pollution from traffic and factories. To evaluate and assure the effectiveness of these interventions, it is crucial to continuously measure their effects.

Hazardous anthropogenic aerosol particles constitute a major pollution component and cause a direct risk factor. However, many aerosols have natural origin and do usually not pose any direct hazards. Still, all particles in the atmosphere affect its physics and chemistry and thereby also the climate forcing effects, which are very much in focus of the discussions today.

The lidar technique has over many years developed to become an important method to measure the aerosol particle concentration with the help of the backscattered light.

The general lidar equation in Eq. 1 describes how the signal,  $P$ , at the detector depends on the backscattering coefficients for aerosols and molecules,  $\beta_A$  and  $\beta_M$ , respectively, and the corresponding extinction coefficients,  $\alpha_A$  and  $\alpha_M$ .

$$P(R) = K(R) \left( \beta_A(R) + \beta_M(R) \right) e^{-2 \int_0^R (\alpha_A(r) + \alpha_M(r)) dr} / R^2 \quad (1)$$

Here,  $K$  is a system response coefficient which is generally varying through the short range.

The main advantage of the lidar approach is that, e.g., vertical concentration profiles can be obtained directly from ground-based measurement stations without any need for time consuming point sampling. The information about the particle concentration is, however, not directly obtained from lidar measurements, but extensive signal processing is necessary to evaluate the results. These 'lidar inversion methods' have developed and increased in complexity along with improved processor power and knowledge. This process has been of great importance to get more reliable data and to be able to better compare measurements from lidar systems located at different global positions, but continued improvements are still necessary.

Here we present measurement results acquired at completely different locations but obtained with the same mobile lidar system and sampling methods. In this way the results could be compared, even without advanced data processing and differences between the sites are obvious already from the raw lidar recordings.

### 2. LIDAR SYSTEM

The mobile Lund lidar system is, apart from the possibility of removing the transmitting dome which is normally used for weather protection and beam steering, thoroughly described in [1]. However, a short overview of the most essential elements used in the campaigns is given below.

The lidar system is shown at the sites in Sweden and China in Figure 1.



Figure 1. The lidar system at (A) the Swedish and (B) Chinese site. The transmitting dome is on both pictures currently mounted.

The light source consist of two 20-Hz Nd:YAG lasers. The possibility to generate arbitrary wavelengths is provided by an OPO system, however; in the present work the 3<sup>rd</sup> harmonic emission at 355 nm from one of the lasers was used with pulse energies of around 100 mJ. The light is expanded and transmitted vertically without any further optics or horizontally via a folding mirror situated on the roof. Generally, the vertical mode is utilized during aerosol measurements, but by transmitting horizontally, system calibration (mainly related to geometrical compression) to homogenous air is possible. The backscattered light is focused on to a photomultiplier by a coaxial Newtonian telescope.

3. MEASUREMENTS AND RESULTS

3.1 Raw lidar signals

In April 2009 measurements were performed at the rural Vavihill background air monitoring station location in the south of Sweden. The site is far from any industry or heavy traffic, thus the amount of locally produced anthropogenic particles is expected to be low. However, during this time of the year – Spring – pollen and other natural aerosols may be present in non-negligible amounts. During the four days of the measurement campaign, there was no extended time period of perfectly clear weather; only shorter clear periods occurred.

The measurements in southern China were performed in November the same year. The measurement site was located in a major city with a population of several millions, with abundant traffic and some industrial emissions. In Figure 2 lidar recordings obtained on

April 8 and November 22 in China and Sweden, respectively, are presented.

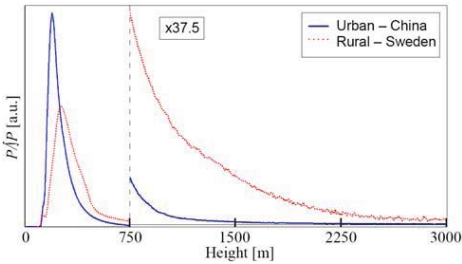


Figure 2. Raw vertical lidar signals obtained in urban China and rural Sweden, shown in solid (blue) and dotted (red), respectively. The curves have been normalized to each other with respect to their integrals.

Both these curves represent clear weather conditions at the two locations to minimize impact of temporal moisture etc. As the emitted energy might fluctuate slightly from pulse to pulse, but also over extended time periods, the recordings are normalized to each other with respect to their integrals.

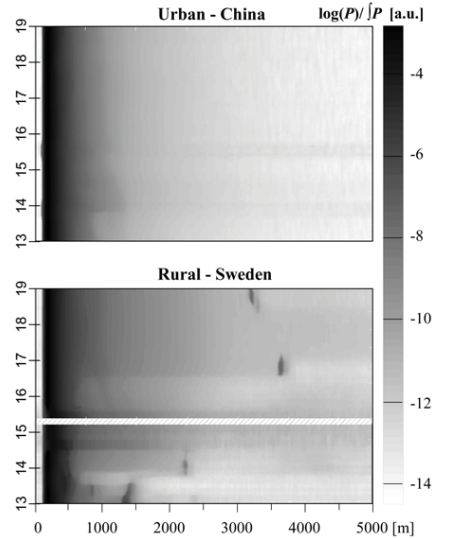


Figure 3. Raw lidar signals obtained at the two sites shown in a logarithmic colour scale. The time (y) axes in the figures correspond to hour of the day on November 22 in China and April 8 in Sweden. During the measurements in Sweden, the recording was stopped for a few minutes at around 15:20. This time period is shown with diagonal lines.

## 25th International Laser Radar Conference

In Figure 3 a similar comparison between raw signals is shown for recordings obtained during several hours at the two sites. Again, the signals have been normalized to each other; however, here they are shown in logarithmic form to clearer reveal differences in the colour scale.

### 3.2 Processed lidar signals

Even though the raw lidar recordings directly can reveal differences between the atmospheres at the two sites, processed data will normally provide more information.

The connection between extinction and backscattering is for both aerosols and molecules given by the extinction-to-backscattering ratio,  $S$ . For the molecular part this ratio is governed by Rayleigh theory,  $S_M = \alpha_M / \beta_M = 8\pi/3$ . For the particles the corresponding ratio is set to 8.0 with guidance from ground reference measurements at the Swedish site.

The inversion used in these examples, given by Eq. 2, was presented by Frederick G. Fernald already in 1983 [2].

The aerosol extinction coefficient,  $\alpha_A$ , at the height position number,  $i$ , is in the numeric iterative form given by:

$$\alpha_A(i-1) = -\frac{S_A}{S_M} \alpha_M(i-1) + \frac{X(i-1)e^{A(i-1,i)}}{\frac{X(i)}{\alpha_A(i) + S_A \beta_M(i)/S_M} + \{X(i) + X(i-1)e^{A(i-1,i)}\} \Delta R}, \quad (2)$$

where  $A(i-1,i) = (S_A/S_M - 1)[\alpha_M(i-1) + \alpha_M(i)]\Delta R$  and  $X(R) = P(R)R^2/K(R)$ .

#### 3.2.1 Calibration procedures

At the rural Swedish measurement site, a nephelometer was used in parallel to the lidar measurements to provide a ground reference. With the help of this, the data from Sweden were analyzed with a variant of Eq. 2 with incessant calibration to the nephelometer at low altitudes.

In the comparative study presented here, the possibility of a ground truth reference was not realized in the measurements in China. The inversion was therefore performed with the assumption of a constant extinction coefficient at a height of 5 km, set to the same value,  $\alpha_A = 2 \cdot 10^{-6} \text{ m}^{-1}$  for both sites. This value generated extinction coefficients at low altitudes at the Swedish site which corresponded well to the values given by the nephelometer.

Horizontally recorded data provided a calibration to minimize the impact of the range varying system constant,  $K(R)$ . Still, the non-linear system response at very low altitudes is considered too large to provide reliable analyzed results below 340 m.

The calibration and sampling procedure is described in detail in [3], which elucidates on the measurements in Sweden.

#### 3.2.2 Results for the extinction coefficient

In Figure 4 the total extinction coefficient,  $\alpha_A + \alpha_M$ , calculated from the recordings presented in Figure 2 is shown for the range 340 m – 3.0 km.

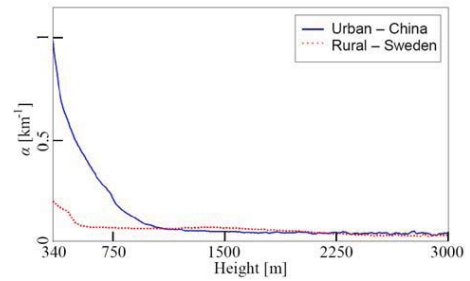


Figure 4. The total extinction coefficient,  $\alpha_A + \alpha_M$ , corresponding to the lidar recordings shown in Figure 2. The solid (blue) and dotted (red) curves represent the extinction coefficients at the urban Chinese and rural Swedish sites, respectively.

The curves in Figure 4, especially the one at the urban site, showing a strongly increased extinction coefficient at low altitudes suggest that the particle loaded air is mainly situated below 1 km.

From Figure 2 it is clear that little light returns from the scattering events at altitudes above 1.5 km at the site in China. This obviously complicates the analysis at high altitudes and the data is therefore more reliable closer to the ground. Nevertheless, during certain times strong signals, mainly from clouds, could be seen up to at least 7.5 km also at this site.

In Figure 5 a ‘time-scan’ calculation of the aerosol extinction coefficient for the time periods shown in Figure 3 is presented.

During the hours of the presented recordings from China the extinction coefficient profile was quite stable in time compared to the one from Sweden. The instability of the latter originates from the, at the time, rapidly changing weather conditions in this rural area where both low moisture and haze, clouds, and clear weather were represented.

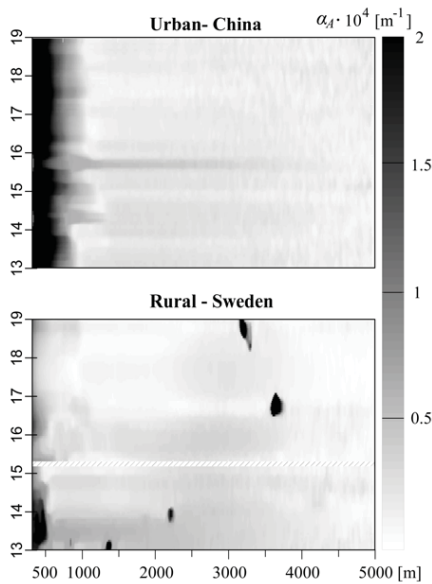


Figure 5. The aerosol extinction coefficient calculated for the time period between 13:00 and 19:00 in urban China and in rural Sweden.

4. DISCUSSION

The results from the measurements show that large scale differences between the atmospheric conditions can be distinguished already in unanalyzed lidar data, however, inversion of the lidar signals more clearly indicates stronger scattering at low altitudes in the urban area.

In this abstract we present a comparison between data obtained during a time period of six hours. As weather conditions are constantly changing, both as diurnal variations, and over the year, general conclusions should not be drawn. Similar measurements during a time period of several months would provide evident information of the general air quality situation.

The weather conditions in the Chinese city during the measurements were very dry and sunny, while as mentioned, the conditions were changing in Sweden. If the clearest periods, e.g. at around 14:30 – 16:00 and 17:00 – 18:00, of the rural Swedish measurements are compared to the clearest in urban China, the low-height extinction is obviously stronger in the latter.

ACKNOWLEDGEMENTS

This project was supported by the Swedish Research Council through a SIDA-VR Research Link grant, and also by a regular Linnaeus grant to the Lund Laser Centre. The authors are very grateful to Sailing He, Jun Hu, Chunsheng Yan, Haojiang Zhou, and Binhao Wang of ZJU for valuable help and assistance. Thanks also to the Lund University Aerosol Physics Group for providing calibration data and help.

REFERENCES

[1]. Weibring P., Edner H., Svanberg, S., 2003: Versatile Mobile Lidar System for Environmental Monitoring, *Appl. Opt.*, **42**, pp. 3583.  
[2]. Fernald F. G., 1983: Analysis of Atmospheric Lidar Observations: some comments, *Appl. Opt.*, **23**, pp. 652.  
[3]. Lundin P., 2009: Light Scattering by Atmospheric Particles – from Molecules to Birds, Master’s thesis, Lund Reports on Atomic Physics, *LRAP*, **413**.

# PAPER IV

## **Insect monitoring with fluorescence lidar techniques: feasibility study**

M. Brydegaard, Z.G. Guan, M. Wellenreuther, S. Svanberg.  
*Applied Optics* **48**, 5668 - 5677 (2009).



# Insect monitoring with fluorescence lidar techniques: feasibility study

Mikkel Brydegaard,<sup>1,\*</sup> Zuguang Guan,<sup>1</sup> Maren Wellenreuther,<sup>2</sup> and Sune Svanberg<sup>1</sup>

<sup>1</sup>Atomic Physics Division, Lund University, P.O. Box 118, SE-221 00 Lund, Sweden

<sup>2</sup>Department of Ecology, Lund University, SE-223 62 Lund, Sweden

\*Corresponding author: mikkel.brydegaard@fysik.lth.se

Received 22 July 2009; revised 27 September 2009; accepted 27 September 2009;  
posted 28 September 2009 (Doc. ID 114651); published 12 October 2009

We investigate the possibilities of light detection and ranging (lidar) techniques to study migration of the damselfly species *Calopteryx splendens* and *C. virgo*. Laboratory and testing-range measurements at a distance of 60 m were performed using dried, mounted damselfly specimens. Laboratory measurements, including color photography in polarized light and spectroscopy of reflectance and induced fluorescence, reveal that damselflies exhibit reflectance and fluorescence properties that are closely tied to the generation of structural color. Lidar studies on *C. splendens* of both genders show that gender can be remotely determined, especially for specimens that were marked with Coumarin 102 and Rhodamine 6G dyes. The results obtained in this study will be useful for future field experiments, and provide guidelines for studying damselflies in their natural habitat using lidar to survey the air above the river surface. The findings will be applicable for many other insect species and should, therefore, bring new insights into migration and movement patterns of insects in general. © 2009 Optical Society of America

OCIS codes: 280.3640, 010.1100, 300.2530, 350.4238, 240.5698, 030.1670.

## 1. Introduction

### A. Background

Light detection and ranging (lidar) techniques have been developed for almost half a century and have since been widely used in, e.g., aerosol monitoring [1–6]. Stationary lidars and mobile systems have been employed with a wide variety of platforms, ranging from submarines, ships, trucks, cranes, airplanes, to satellites [7–10]. Aerosol studies typically involve vertical soundings or the generation of three-dimensional distribution maps. The data are usually obtained by time-resolved measurements of elastic backscattering using a limited number of laser frequencies. Even polarization of backscattered light can be analyzed to provide information regarding the number of scattering events and particle size distribution [10,11]. Apart from the strongly dominat-

ing elastic backscattering methods, three further lidar methods have been developed for detailed spectral analysis and classification of aerosols. These methods are based on (laser-induced fluorescence (LIF) spectroscopy [12–16], Raman spectroscopy [17], and laser-induced breakdown spectroscopy (LIBS) [18–22]). LIF methods have been employed in the past to distinguish between different types of pollen and aerosols that can potentially be used in biological warfare [16]. Raman lidar gives weak signals and has mostly been employed on water and nitrogen [17]. The LIBS method is more difficult to employ, but recent work has demonstrated assessment of aerosol salinity [22], following very early Russian work on cement particles [18]. Traditionally, aerosol particles are considered to be solid or liquid particles that can range from smoke, which has a particle size of a few nanometers, to friction particles and raindrops of several hundred micrometers in size. In addition to these advances, insects and even vertebrates, such as birds and bats, could potentially be detected using lidar techniques. In the past, bird

0003-6935/09/305668-10\$15.00/0  
© 2009 Optical Society of America



and insect monitoring and tracking have been extensively investigated using radar methodologies [23–26], including the classification of animals by multiband (matched) illumination [27,28]. Such applications of remote sensing techniques have important implications for local agriculture, as they allow pest forecasting. Reflectance signatures measured with multiband radar methods are typically given by interference arising from the structures of the reflecting object. However, similar advances in the use of lidar techniques have been slow, and until now, only a few studies have directly investigated the feasibility of lidar in insect and vertebrate monitoring. One example comes from a lidar study on honey bees in land mine detection [11]. That study measured backscattered light at a single wavelength and in two polarizations to detect bee echoes and to build up stochastic histograms to summarize the bee concentration in relation to the actual land mine locations. In addition, lidar sounding of fish demonstrated the possibility to detect moving live scatterers [29,30]. The bee study was followed up by investigations involving background rejection by wing beat modulation of reflected light [31,32]. Such an approach has also been used in the bird radar community [33], with the difference that the modulation frequencies are several magnitudes smaller.

#### B. Motivation and Strategy

The present paper describes spectroscopic studies of two odonate species (Odonata: damselflies and dragonflies), the banded demoiselle *Calopteryx splendens* and the beautiful demoiselle *C. virgo* [34]. In particular, the main focus of this study was to test the feasibility of lidar for damselfly monitoring and study of movement patterns. Damselfly larvae are highly sensitive to water pollution and oxygen concentrations and have thus been used as biomarkers in the past [35]. Another important characteristic of damselflies is that, like all other insects, they are ectotherms and are particularly sensitive to changes in temperatures. Therefore, increasing ambient temperatures are expected to force insect species to shift their distributions by expanding into new geographic areas and by trying to escape from areas that become climatically unsuitable [36]. In Europe, many documented cases of range shifts among insects have been attributed directly to increasing temperatures [37]. For example, out of the 35 European butterfly species that were studied [38], 22 have shifted their ranges northward by 35–240 km over the last century, whereas only two have shifted south. There is also direct evidence that the species studied in the present work, *Calopteryx splendens* and *C. virgo*, are currently affected by climate change. In a recent study [39] Hickling *et al.* showed that 23 of the 24 temperate Odonata species in the United Kingdom, including the two *Calopteryx* species, significantly expanded their range size and northern range limit between 1960 and 1995. Together, these data strongly indicate that European

populations of these insects are currently moving northward.

Migration studies of insects are crucial for understanding the roles of gene flow in connecting population over a wide spatial scale [40,41], but progress in this area has been hampered by the difficulty of marking individuals. As a consequence, studies typically involve neighboring and low numbers of populations. Migration in insects is relatively difficult to study with traditional methods, such as radio transmitters or light loggers, because the size and weight of damselflies makes the attachment of the disproportionately large devices difficult. An alternative approach would be to mark neighboring populations with combinations of two or three different fluorescent dyes, such as Rhodamine variants, and then detect migrated marked individuals at a given population [42], by correlating the spectral fingerprint of each detected individual with the population of origin. Such dyes could either be sprayed or powdered on individual specimens or absorbed by the individual through the metabolic uptake of food or water (e.g., during the aquatic larval stage) [42–46]. A number of fluorescent dyes have already been used for freshwater tracking and environmental studies, and other dyes already exist due to detergents in wastewater [47]. Even with only a few appropriate and noninterfering dyes, a much larger number of site locations could be monitored simultaneously by using various nonparallel spectral combinations of the few dye types. This is especially true if the probability of detecting two individuals in a single voxel is small.

This paper presents optical spectroscopic features and the feasibility of damselfly monitoring using lidar and lidar LIF methods, and is organized in the following way. In Section 2 the general photophysical aspects of Odonata are discussed. Then, in Section 3, we develop strategies for the remote classification of the two damselfly species and the respective genders in order to produce species and gender selective three-dimensional distributions and behavioral studies over a temporal scale [48]. In particular, we demonstrate how to generate broadband “white” light by autofluorescence on the surface layers of *C. splendens* and *C. virgo* in order to detect how structural colors affect fluorescence. Such surface probed fluorescence studies have resemblance to those presented in [49]. In addition, laboratory and outdoor test range measurements are also described, including descriptions of methods for damselfly marking [42] to study migration of individuals between populations. For this we further investigate lidar LIF methods enhanced by fluorescent dye marking. In the latter case, individuals are marked with dye either by spraying or powdering dyes directly on the individual [46] or by adding dyes to the water, which is then incorporated into the body by the individual during the larval phase [50]. We further show how the structural imprint of the dye-enhanced fluorescence can be used for remote classification

of species and genders. Finally, in Section 4, we discuss the results and give suggestions for future work.

## 2. Damselfly Species Description and Relevant Photophysics

Photographs of *Calopteryx splendens* and *C. virgo* of both genders are shown in Fig. 1. The optical properties of the majority of insects are determined both by the chemical absorption imprint yielding “classical” colors, and structural colors, due to interference [51–58]. This becomes particularly clear when damselflies are observed in polarized light [58]. While common lidar methods like LIF lidar, differential absorption lidar (DIAL), and LIBS lidar commonly measure chemical colors, structural colors have never been measured in the lidar community, due to the fact that organized cells or organelles and layered structures on the nanoscale are required for the effect to be noteworthy. Even though ordinary cells might leave weak structural imprints in traditional reflectance, absorption, or fluorescent measurements [59,60], such effects are typically neglected. The main features of the reflectance of the damselfly abdomen can be explained by the arrangement of approximately 100 nm sized scattering nanospheres. (This is illustrated in Fig. 7(c) adopted from [61], to be discussed later.) This arrangement provides damselflies with their typical retroreflective properties, and an approximately 100 nm broad reflection band shifting from the blue to the green region, depending on the sizes of the nanospheres and on the angle of observation with respect to surface orientation and illumination. The nanosphere arrangement is situated just below the chitin cuticulum; the cuticulum can be more or less melanized [62]. Both chitin and melanin absorption peaks around 330 nm and both chitin and melanin produce broad fluorescence spectra covering the structural features in the blue and green region [63–65]. Further, certain Odonates are known to have wax covered wings [66]. Botanical waxes are well studied in LIF lidar [67]. Typically, wax absorption increases dramatically below 355 nm and the maximum fluor-

escence yield is usually obtained around 330 nm excitation. Even waxes provide broad fluorescence spectra peaking in the blue region [68]. Reflectance can be further modified by absorbing ommochrome granules, which are situated beneath the scattering arrangement and prevent nonscattered light from being reemitted and, thus, strengthen the structural color. Furthermore ommochromes in certain Odonata species react to the temperature, regulating the temperature of the ectotherms by either migrating into the nanosphere region or contracting to a deeper lying layer, which increases reflectance. Such effects can be expected to alter even the fluorescence. The lowest of the six visual spectral bands typically found in Odonata [69] goes as far as 350 nm in the UV; thus, it is not unreasonable to expect the studied species to sexually signal via altered reflectance in this band. Vibrant structural colors are exhibited by the blue males of *C. splendens* and the green males of *C. virgo* [70]. Females of both species appear less colorful, with brown, green, and golden shadings. Males and females of the two *Calopteryx* species differ significantly in the absorption properties of their wings, due to differences in the amount of melanin. Males of *C. virgo* typically have over 90% of their wings melanized, whereas males of *C. splendens* have melanized patches covering about 50% of the wing surface [71–74]. Females of both species lack the melanized wing patches, but *C. virgo* females are brown, while *C. splendens* females are typically green [50].

## 3. Methods, Measurements, and Results

Optical measurements were performed under controlled conditions, both on a macro scale in the laboratory and on a 60 m lidar testing range. Measurements were taken in order to gain insights into the optical properties of the studied species and to develop realistic and practical methods for future field work.

### A. Laboratory Measurements

The reflective properties caused by the structural colors were investigated in detail in the laboratory. To confirm that the blue and green shades are indeed structural, two samples were photographed from a distance of 60 cm with a Sony F828 digital still red-green-blue (RGB) camera with a fixed visible linear polarizing laminated film (Edmund Optics) attached to the objective. The sample was illuminated by collimated light from a filament source (100 W Oriel, halogen–tungsten blackbody source) at an angle of 15°; see Fig. 2. For the experiment, two dried specimens (*C. splendens*, male and female) were fixed on a wire, and were photographed with parallel and perpendicular polarized illumination with respect to the polarizer on the camera objective. The photographs with maintained polarization reveal green, golden, and blue shades (Fig. 3), whereas the depolarized pictures are considerably darker and show mostly brown and reddish colors. For the convenience of the viewer, the intensities of the depolarized

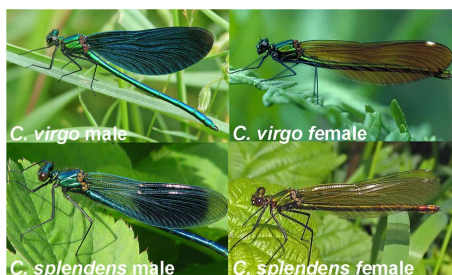


Fig. 1. (Color online) Males of *C. virgo* have almost completely melanized wings, whereas males of *C. splendens* have melanized wing patches. The wings of *C. virgo* females are brown, while the wings of *C. splendens* females are typically green.

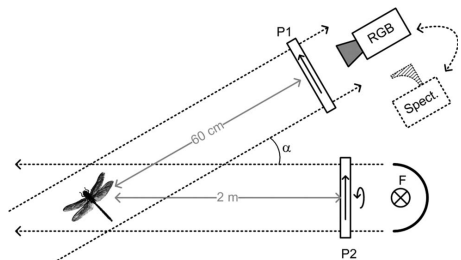


Fig. 2. Setup for color imaging and whole-body polarized reflectance studies. Samples are observed either with a color camera (RGB) or a spectrometer (Spect.) at low angle ( $\alpha = 15^\circ$ ) through a linear polarizer (P1). Collimated white illumination is provided by a tungsten filament lamp (F) which can be polarized in parallel or perpendicularly to P1 using P2.

photographs in Fig. 3 are multiplied by a factor of 5. Depolarized reflections originate mainly from the hairy parts of the specimens, more specifically, from multiple reflections of the four-folded wing and the abdomen tip. By subtracting the depolarized intensity from the polarized, we retain the pure structural color and, again, green, golden, and blue shades are observed. This finding is in contrast to the appearance of multiple-scattering biological samples, such as leaves or skin, where the structural color appears flat white, simply describing the refractive index of the sample (specular reflex). Following that, the samples were studied in a stereo microscope with a ring light configuration, and the results showed that the

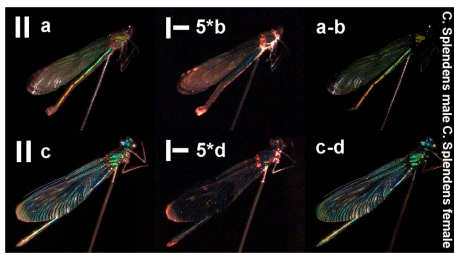


Fig. 3. (Color online) Photograph of damselflies in polarized light. Photographs a and c, indicated with ||, are photographed with parallel polarizers. Photographs b and d, indicated with  $\perp$ , show the depolarized light amplified by a factor of 5 to make it visible to the reader. Subtraction gives us the two figures to the outermost right, where structural colors remain.

structural blue and green shades were distributed over the entire body and wings, despite the fact that the effect to the naked eye was most obvious on the abdomen and thorax.

Studies of the whole-body reflectance were also performed by exchanging the RGB camera with a spectrometer (Ocean Optics USB4000) with an off-axis parabolic mirror telescope; see Fig. 2. Again, the spectral reflectance of the polarized and depolarized lights were measured for both specimens (*C. splendens* males and females); see Fig. 4. The depolarized reflectance is more than 1 magnitude smaller than the polarized, and the blue and green structural imprint disappears. The units are referenced to a  $\varnothing$  50 mm barium sulfate plug (approximately the size of

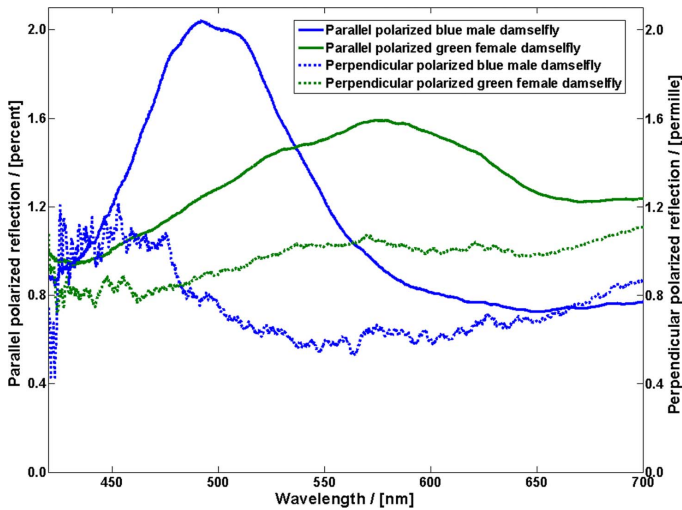


Fig. 4. (Color online) Polarized and depolarized whole-body reflectance measurements of *C. splendens* males and females. The blue and green reflectance features, respectively, disappear when polarizers are crossed. (Note the different scales.)

the specimen). The whole-body reflectances in Fig. 4 were also measured at a  $15^\circ$  angle with respect to the illumination. Further angular studies (data not presented here) reveal that the specimens have strong retroreflective properties, and that most light is reflected back directly toward the illumination. Also, the structural features are displaced to lower wavelengths when the angle between illumination and observation increases (shifts of the order of 50 nm were observed over  $60^\circ$ ). This might have biological relevance, since the appearance to aquatic predators would be more bluish and match the sky, while the appearance to terrestrial predators would be slightly more greenish and match the vegetation.

Since broadband reflectance time-resolved lidar is labor intensive to perform, considering requirements for pulsed collimated sources, it would be considerably more realistic to perform LIF lidar. For this reason, the resemblance of reflectance and fluorescence was studied. It is well known that fluorescence spectroscopy cannot be performed without the influence of reflectance and transmission or considering photon migration spectroscopy. Thus, we can expect certain correlations between the two methods. Dried *C. splendens* specimens were measured at several spots using a bifurcated fiber probe; see Fig. 5. The illuminating fiber was connected to a diode laser at 375 nm (Power Technology Incorporated) or a white-light xenon flash (Ocean Optics, PX-2) for fluorescence and reflectance measurements, respectively. The collected light was detected in a spectrometer (Ocean Optics, USB4000) through a GG400 long-pass filter [75]. The sample and probe remained fixed at a 5 mm distance from the target in the fluorescence and reflectance measurements.

It is a general phenomenon that shorter excitation wavelengths are typically absorbed in the outer layers of biological samples [49,67] and autofluorescence from a number of biological compounds is usually produced with a small Stokes shift and with broad bluish-green fluorescence spectra. The measurements were performed at various spots on

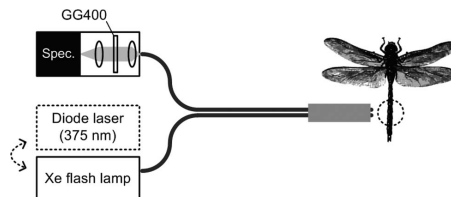


Fig. 5. Setup for fiber point measurements. Either a UV laser line or white light is passed into the bifurcated probe. The sample geometry is maintained constant between the measurements. A long-pass GG400 filter prevents blooming in the spectrometer (Spec.).

the specimens; however, not all data are presented here. Both laboratory and lidar test-range measurements suggest that bluish reflecting samples appear even more bluish under fluorescence, and greenish reflecting samples appear even more greenish under fluorescence; see Fig. 6. Our current understanding is that excitation light is absorbed in the outer layers of the cuticulum, either by wax, melanin, chitin, or in the scattering nanospheres themselves, producing broadband fluorescence light, which, in turn, is reflected by the underlying structural color-generating layers. In this way, the structural color enhances the blue or the green part of the fluorescence that is produced.

#### B. Lidar Test-Range Measurements

The Lund mobile lidar system, which is thoroughly described in [7] and displayed in Fig. 7, was used for remote measurements on damselflies. It is basically a coaxial system with a  $\varnothing$  40 cm vertically looking telescope with the optical path folded by a roof-top scanning mirror. The repetition rate is 20 Hz. One laser transmitter is a Q-switched Nd:YAG laser, where the fundamental (1064 nm), the second-harmonic (532 nm), the third (355 nm), and the forth-harmonic (266 nm) frequencies can be produced simultaneously. A second transmitter is a Nd:YAG-pumped optical parametric oscillator (OPO) system with wide

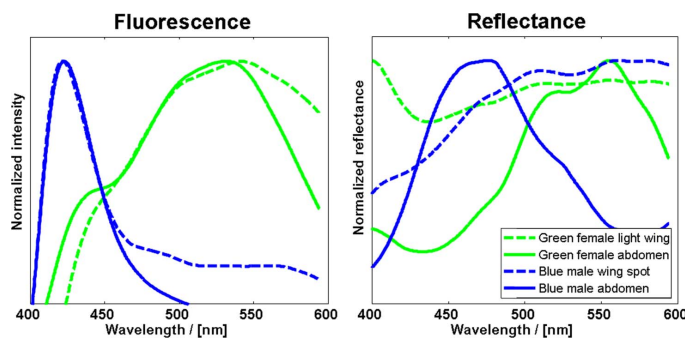


Fig. 6. (Color online) Comparison between reflectance and fluorescence spectra. In general, all measurements performed in this study suggest a positive correlation between fluorescence emission and reflectance.

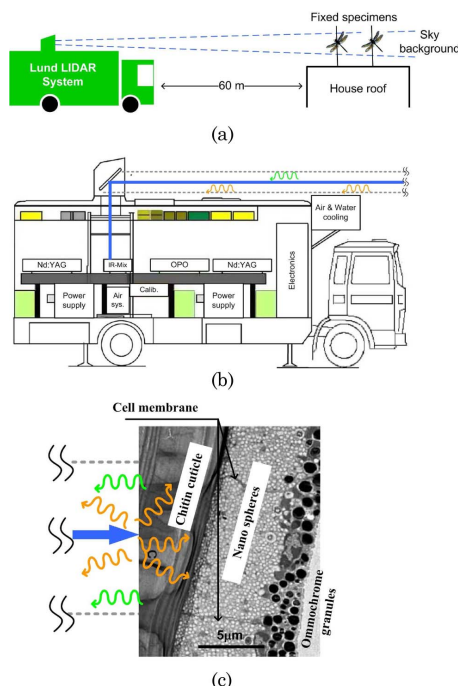


Fig. 7. (Color online) (a) Setup for test-range experiments. Insects were mounted on thin clean aluminum threads and were detected toward a bright sky background. (b) The versatile mobile lidar provides pulsed light continuously from 200 nm to 4  $\mu\text{m}$ . (c) The UV laser light induces broad fluorescent light in the wax or chitin, which is, in turn, partly reflected in the nanosphere array.

tunability, augmented by nonlinear wavelength-shifting techniques. In our initial experiments, we employed only the 355 and 266 nm radiation for demonstration. In the measurements, the pulse energies are limited to 25 and 10 mJ, respectively, for these two wavelengths. The FWHM of the laser pulse is approximately 15 ns, corresponding to about 2.25 m axial resolution. The spot size for the test-range measurements of targets at 60 m was approximately  $\varnothing$  10 cm. For the time-domain recording, a photomultiplier tube (PMT) (EMI 9816 QA) was used as the detector and an oscilloscope (Tektronix TDS544B) was used as the digitizer, sampling every 4 ns. The elastic signal was recorded through a 45° 355 nm dichroic mirror followed by a Schott UG11 filter to further suppress the background. Two fluorescence bands were recorded simultaneously by additional PMTs but will not be presented in this paper. For initial remote spectral analysis of LIF, an intensified fiber-coupled optical multiple channel analyzer (OMA) system is employed. With a 1 mm diameter fiber to transport light from the telescope focal plane to the spec-

trometer, and using the fiber end as the “slit,” a spectral resolution of 14 nm was obtained. Detailed information of the OMA system can be found in [76]. Fluorescence with excitation at 355 nm was detected from the 60 m distant target through a 5 mm GG400 Schott filter, and fluorescence with excitation at 266 nm was detected through a 3 mm WG305 Schott filter; in each case the filters were used to suppress the overwhelming elastic signal while transmitting fluorescence at the lowest wavelengths as possible.

Elastic lidar returns from damselflies, which are mounted at 60 and 80 m distances, are shown in Fig. 8. Pulses at the third-harmonic Nd:YAG wavelength, 355 nm, were sent out after initial expansion into a 5 cm diameter beam, and echoes were collected with the lidar telescope. Elastic photons were selected with a dichroic 45° laser line mirror followed by a Schott UG11 high-pass glass filter. The signal was recorded by the PMT. Measurements were performed on two dried specimens of *C. splendens*, exposed to the expanded laser beam and with the gray sky as the background. The damselflies were held by thin aluminum wires (echoes from the wires were relatively small). The orientation and the position of the two specimens in the beam were heavily randomized by high wind speeds. Apart from the strong reflection from the window of the lidar system, both specimens are clearly resolved. The second echo is slightly weaker than the first. This might be explained by different orientation and positions in respect to the beam; also, the first specimen is partly shadowing both excitation and backscattered photons. Also, the trivial LIDAR signal falloff with range is at play.

Results from fluorescence measurements with the OMA system are shown in Fig. 9, for 355 and 266 nm excitation. Slight differences between the genders of *C. splendens* can be seen. The autofluorescence spectra were recorded at a 60 m distance at 355 nm excitation and in the lidar laboratory at 266 nm excitation (due to weather conditions). The insect specimens were the same, but the orientation was random as before. Beam sizes were  $\varnothing$  10 cm and 1 cm, respectively. A GG400 and a WG305 Schott long-pass filter

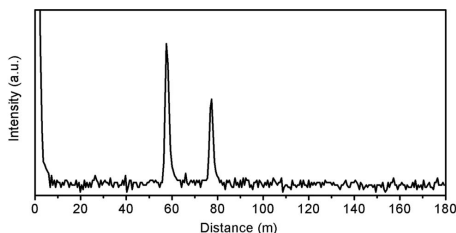


Fig. 8. Elastic lidar recording of mounted damselflies; the transmitted wavelength is 355 nm. Data are from a single laser pulse and the echoes arise from two fixed specimens (*C. splendens* female and male respectively) separated by 20 m. Fluorescence time series recording were also performed but are not presented in this paper.



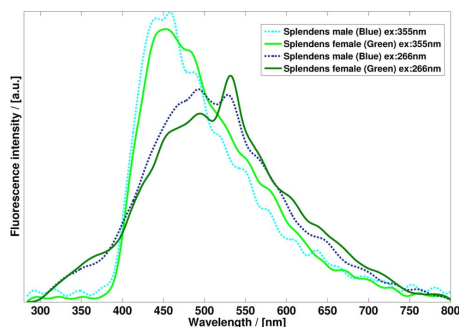


Fig. 9. (Color online) Normalized fluorescence spectra for 266 and 355 nm excitation; in both cases, imprints of the structural color are observed. Data from 20 laser shots were averaged.

were used, respectively. Emission spectra are broad and cover the region of 400–600 nm, where structural imprints are expected to occur. Emission spectra could be explained by previous measured spectra of both melanin and chitin. Even if the signal is weak, a slight difference between a blue and a green reflecting sample can be observed at both excitation wavelengths (Fig. 9). Both chitin and melanin absorption peak around 330 nm and the signal-to-noise ratio could probably be improved by moving to such an excitation wavelength.

Results of fluorescence lidar measurements on damselflies prepared with Coumarin 102 and Rhodamine 6G dye are shown in Fig. 10. In preparation for migration studies and population encoding experiments, dried specimens of both genders of *C. splendens* were sprayed with water solutions containing these dyes. Fluorescence spectra were measured at a 60 m distance with the same procedure as before. Apart from the obviously much stronger fluorescence signal from the two dyes, males and females with, respectively,

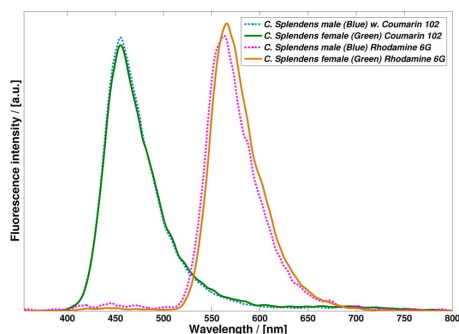


Fig. 10. (Color online) Fluorescence spectra for 355 nm excitation for dye-marked females and males of *C. splendens*. Strong dye fluorescence bands are seen with slight modifications due to structural colors. Data from 20 laser shots were averaged.

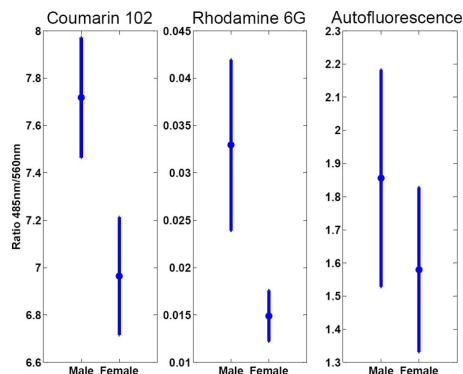


Fig. 11. *Calopteryx splendens* male/female contrast in autofluorescence and when using dye-enhanced fluorescence. Bars show standard deviation for a total of 20 shots. The overlap in autofluorescence is interpreted as lack of signal rather than lack of physical difference of the samples.

blue and green structural colors show distinct fluorescence spectra. This is in accordance with the view that the generated fluorescent light is reflected in the insect structures and, thus, the structural color imposes an imprint on the observed fluorescence.

Separation of male and female damselflies based on the measured ratio between two fluorescence intensities (at 485 and 560 nm, 25 nm FWHM, respectively) is illustrated in Fig. 11. In this case, we define the bands mathematically with the spectra provided from the OMA, but such bands could easily be implemented using optical filters in front of PMTs with much higher sensitivity. When we take the ratio between the two bands, intensity units cancel, and the influence of all geometric effects due to sample orientation, position with respect to the laser beam, collection efficiencies, etc., cancel. We see a clear distinction between the *C. splendens* male and female specimens for the dyed samples. For the autofluorescence, the tendency is the same, but the contrast is poorer. This is mainly due to noisy signals rather than lack of physical differences.

#### 4. Discussion

We have performed a feasibility study to investigate the possibilities of lidar to study interpopulation migration and movement of the damselfly species *Calopteryx splendens* and *C. virgo*. Laboratory, as well as testing-range measurements, of dried, mounted specimens at distances of 60 to 80 m were performed. The damselflies exhibit reflectance and fluorescence properties that are closely tied to the generation of structural colors. Laboratory measurements, including color photography in polarized light and spectroscopy of reflectance and induced fluorescence, revealed these phenomena and an interesting connection between reflectance and fluorescence features. To our knowledge, we are the first group to acquire

structural colors using lidar. The number of *C. virgo* samples was limited as the dried samples are considerably fragile; hence, they quickly disintegrate in the measurement wind conditions. Laboratory measurements on *C. virgo* involving polarized color photographing and point reflectance/fluorescence were carried out. The results of these measurements also confirmed that the reflectance is indeed largely influenced by nanostructures and, as for *C. splendens*, the emitted fluorescence is positively correlated with the reflectance at the same wavelength region. Studies on lidar data of *C. splendens* of both genders showed that males and females can be remotely distinguished, especially for specimens that were marked with the dyes Coumarin 102 and Rhodamine 6G. The strength of the fluorescence signals (when studied with an optical multichannel analyzer connected to the lidar telescope) indicated that an arrangement of a small number of PMTs, each detecting a chosen spectral band, is advantageous for realistic single-shot recordings of flying insects. With such a setup, range-resolved recordings are obtained, which is advantageous compared to the gated spectrometer approach, where the time gate has to be preset. Such an approach is now being implemented in preparation for upcoming field experiments, where damselflies in their natural habitat will be studied with the lidar beam positioned at different heights over the river surface. Field studies have the potential to bring new insights into the migration, movement, and flying patterns of *Calopteryx* damselflies, and will provide guidelines for studies of other insect species. One concern when using LIF lidar at 266 nm is the transmission of the excitation light in the atmosphere; depending on varying conditions, ozone absorption and air scattering will attenuate the excitation pulse. Early work experience from previous field campaigns tells us that lidar returns can be detected in horizontal soundings at kilometer ranges even at 254 nm, where ozone absorbs the most [77,78]. The conditions might, however, not always be feasible. Alternative solutions for acquisition of structural colors by lidar might be found in multiband illumination with several laser lines, or with pulsed supercontinuum light sources [79,80]. However, the issues concerning eye safety in field settings would be much more severe than for the eye-safe UV used in, e.g., LIF lidar.

This work was supported by a Swedish Research Council project grant and by a Linnaeus grant to the Lund Laser Centre, Sweden. Fruitful discussions with and kind help from Patrik Lundin, Richard Prum, Joseph A. Shaw, Eric Warrant, Erik Svensson, Lisa Orr, and Can Xu are gratefully acknowledged.

## References

1. R. M. Measures, *Laser Remote Sensing: Fundamentals and Applications* (Wiley, 1984).
2. R. M. Measures, ed., *Laser Remote Chemical Analysis* (Wiley-Interscience, 1988).
3. M. Sigrist, ed., *Air Pollution Monitoring with Optical Techniques* (Wiley, 1993).
4. C. Weitkamp, ed., *LIDAR: Range-Resolved Optical Remote Sensing of the Atmosphere*, Springer Series in Optical Sciences (Springer, 2005).
5. T. Fujii and T. Fukuchi, eds., *Laser Remote Sensing* (CRC, 2005).
6. S. Svanberg, "LIDAR," in *Springer Handbook of Lasers and Optics* F. Träger, ed. (Springer, 2007), pp. 1031–1052.
7. P. Weibring, H. Edner, and S. Svanberg, "Versatile mobile lidar system for environmental monitoring," *Appl. Opt.* **42**, 3583–3594 (2003).
8. S. Harsdorf, M. Janssen, R. Reuter, B. Wachowicz, and R. Willkomm, "Lidar as part of an ROV-based sensor network for the detection of chemical pollutants on the seafloor," in *Oceans '98 Conference Proceedings* (IEEE, 1998), Vol. 3, pp. 1250–1253.
9. M. Sowinska, B. Cunin, F. Heisel, and J. A. Miehe, "New UV-A laser-induced fluorescence imaging system for near-field remote sensing of vegetation: characteristics and performances," *Proc. SPIE* **3707**, 91–102 (1999).
10. D. M. Winker, C. A. Hostetler, M. A. Vaughan, and A. H. Omar, "Mission, Instrument, and Algorithms Overview," PC-SCI-202.01 (NASA, 2006), [www-calipso.larc.nasa.gov](http://www-calipso.larc.nasa.gov).
11. J. A. Shaw, N. L. Seldomridge, D. L. Dunkle, P. W. Nugent, L. H. Spangler, J. J. Bromenshank, C. B. Henderson, J. H. Churnside, and J. J. Wilson, "Polarization lidar measurements of honey bees in flight for locating land mines," *Opt. Express* **13**, 5853–5863 (2005).
12. S. Svanberg, "Laser fluorescence spectroscopy in environmental monitoring," in *Optoelectronics for Environmental Science*, S. Martellucci and A. N. Chester, eds. (Plenum 1990), pp. 15–27.
13. H. Edner, J. Johansson, S. Svanberg, and E. Wallinder, "Fluorescence lidar multicolor imaging of vegetation," *Appl. Opt.* **33**, 2471–2479 (1994).
14. P. Weibring, Th. Johansson, H. Edner, S. Svanberg, B. Sundner, V. Raimondi, G. Cecchi, and L. Pantani, "Fluorescence lidar imaging of historical monuments," *Appl. Opt.* **40**, 6111–6120 (2001).
15. S. Svanberg, "Fluorescence spectroscopy and imaging of LIDAR targets," in *Laser Remote Sensing*, T. Fujii and T. Fukuchi eds. (CRC, 2005), Chap. 6.
16. Ø. Farsund, G. Rustad, I. Käsen, and T. V. Haavardsholm, "Required spectral resolution for bioaerosol detection algorithms using standoff laser induced fluorescence measurements," *IEEE Sens. J.* **6** (2009).
17. D. N. Whiteman, S. H. Melfi, and R. A. Ferrare, "Raman LIDAR system for the measurement of water-vapor and aerosols in the earth's atmosphere," *Appl. Opt.* **31**, 3068–3082 (1992).
18. V. E. Zuev, Y. D. Kopytin, V. A. Korolkov, M. E. Levitskii, M. F. Nebolsin, B. G. Sidorov, and N. P. Soldatkin, in *Proceedings of the 13th International Laser Radar Conference* (NASA Langley Research Center, 1986).
19. S. Palanco, J. M. Baena, and J. J. Laserna, "Open-path laser-induced plasma spectrometry for remote analytical measurements on solid surfaces," *Spectrochim. Acta B* **57**, 591–599 (2002).
20. K. Stelmaszczyk, P. Rohwetter, G. Méjean, J. Yu, E. Salmon, J. Kasparian, R. Ackermann, J.-P. Wolf, and L. Wöste, "Long-distance remote laser-induced breakdown using filamentation in air," *Appl. Phys. Lett.* **85**, 3977–3979 (2004).
21. R. Grönlund, M. Lundqvist, and S. Svanberg, "Remote imaging laser-induced breakdown spectroscopy and laser-induced fluorescence spectroscopy using nanosecond pulses from a mobile lidar system," *Appl. Spectrosc.* **60**, 853–859 (2006).
22. T. Fujii, N. Goto, M. Miki, T. Nayuki, and K. Nemoto, "Lidar measurement of constituents of microparticles in air by

- laser-induced breakdown spectroscopy using femtosecond terawatt laser pulses," *Opt. Lett.* **31**, 3456–3458 (2006).
23. M. Skolnik, *Introduction to Radar Systems*, 3rd ed. (McGraw-Hill, 2002).
  24. J. C. Toomay and P. J. Hannen, *Radar Principles for the Non-Specialist*, 3rd ed. (SciTech, 2004).
  25. S. A. Gauthreaux Jr. and C. G. Belser, "Radar ornithology and biological conservation," *The Auk* **120**, 266–277 (2003).
  26. J. W. Chapman, D. R. Reynolds, and A. D. Smith, "Vertical-looking radar: a new tool for monitoring high-altitude insect migration," *BioScience* **53**, 503–511 (2003).
  27. D. T. Gjessing, *Target Adaptive Matched Illumination Radar: Principles and Applications* (Institution of Engineering and Technology, 1986).
  28. S. P. Lohmeier, S. M. Sekelsky, J. M. Firda, G. A. Sadowy, and R. E. McIntosh, "Classification of particles in stratiform clouds using the 33 and 95 GHz polarimetric cloud profiling radar system (CPRS)," *IEEE Trans. Geosci. Remote Sens.* **35**, 256–270 (1997).
  29. K. Fredriksson, B. Galle, K. Nyström, S. Svanberg, and B. Öström, "Underwater laser-radar experiments for bathymetry and fish-school detection," Göteborg Institute of Physics Reports GIPR-162 (Chalmers University of Technology, Göteborg, 1978).
  30. K. Fredriksson, B. Galle, K. Nyström, S. Svanberg, and B. Öström, "Marine laser probing: results of a field test," *Meddelanden från Havsfiskelaboratoriet* No. 245 (Swedish Department of Fishery, Stockholm, 1979).
  31. K. S. Repasky, J. A. Shaw, R. Scheppele, C. Melton, J. L. Carsten, and L. H. Spangler, "Optical detection of honeybees by use of wing-beat modulation of scattered laser light for locating explosives and land mines," *Appl. Opt.* **45**, 1839–1843 (2006).
  32. D. S. Hoffman, A. R. Nehrir, K. S. Repasky, J. A. Shaw, and J. L. Carsten, "Range-resolved optical detection of honeybees by use of wing-beat modulation of scattered light for locating land mines," *Appl. Opt.* **46**, 3007–3012 (2007).
  33. Von R. Bloch, B. Bruderer, and P. Steiner, "Flugverhalten nächtlich ziehender Vögel—Radardaten über den Zug verschiedener auf einem Alpenpass," *Die Vögelwarte* **31**, 119–146 (1981).
  34. P. S. Corbet, *Behavior and Ecology of Odonata* (Harley, 1999).
  35. M. Campero, F. Ollevier, and R. Stoks, "Ecological relevance and sensitivity depending on the exposure time for two biomarkers," *Environ. Toxicol.* **22**, 572–581 (2007).
  36. C. A. Deutsch, J. J. Tewksbury, R. B. Huey, K. S. Sheldon, C. K. Ghalambor, D. C. Haak, and P. R. Martin, "Impacts of climate warming on terrestrial ectotherms across latitude," *Proc. Natl. Acad. Sci. USA* **105**, 6668–6672 (2008).
  37. C. Parmesan, "Ecological and evolutionary responses to recent climate change," *Annu. Rev. Ecol. Evol. Syst.* **37**, 637–669 (2006).
  38. C. N. Parmesan, C. Ryrholm, C. Steganesco, J. K. Hill, C. D. Thomas, B. Descimon, B. Huntley, L. Kaila, J. Kullberg, T. Tammara, W. J. Tennent, J. A. Thomas, and M. Warren, "Poleward shifts in geographical ranges of butterfly species associated with regional warming," *Nature* **399**, 579–583 (1999).
  39. R. Hickling, D. B. Roy, J. K. Hill, and C. D. Thomas, "A northward shift of range margins in British Odonata," *Glob. Change Biol.* **11**, 502–506 (2005).
  40. T. J. Case and M. L. Taper, "Interspecific competition, environmental gradients, gene flow, and the coevolution of species' borders," *Am. Nat.* **155**, 583–605 (2000).
  41. D. Garant, S. E. Forde, and A. P. Hendry, "The multifarious effects of dispersal and gene flow on contemporary adaptation," *Funct. Ecol.* **21**, 434–443 (2007).
  42. J. R. Hagler and C. G. Jackson, "Methods for marking insects: current techniques and future prospects," *Annu. Rev. Entomol.* **46**, 511–543 (2001).
  43. M. D. Ginzel and L. M. Hanks, "Evaluation of synthetic hydrocarbons for mark-recapture studies on the red milkweed beetle," *Journal of chemical ecology* **28**, 1037–1043 (2002).
  44. R. W. Piper, "A novel technique for the individual marking of smaller insects," *Entomol. Exper. Appl.* **106**, 155–157 (2003).
  45. A. E. A. Stephens, A. M. Barrington, V. A. Bush, N. M. Fletcher, V. Mitchell, and J. D. M. Suckling, "Evaluation of dyes for marking painted apple moths (*Teia anartoides* Walker, *Lep. Lymantriidae*) used in a sterile insect release program," *Aust. J. Entomol.* **47**, 131–136 (2008).
  46. T. P. Gosden and E. I. Svensson, "Density-dependent male mating harassment, female resistance and male mimicry," *Am. Nat.* **173**, 709–721 (2009).
  47. L. Celander, K. Fredriksson, B. Galle, and S. Svanberg, "Investigation of laser-induced fluorescence with applications to remote sensing of environmental parameters," Göteborg Institute of Physics Reports GIPR-149 (Chalmers University of Technology, Göteborg 1978).
  48. T. D. Schultz, C. N. Anderson, and L. B. Symes, "The conspicuousness of colour cues in male pond damselflies depends on ambient light and visual system," *Anim. Behav.* **76**, 1357–1364 (2008).
  49. H. Edner, J. Johansson, S. Svanberg, E. Wallinder, M. Bazzani, B. Breschi, G. Cecchi, L. Pantani, B. Radicati, V. Raimondi, D. Tirelli, G. Valmori, and P. Mazzinghi, "Laser-induced fluorescence monitoring of vegetation in Tuscany," *EARSeL Adv. Remote Sens.* **1**, 119–130 (1992).
  50. G. Ruppel, D. Hilfert-Ruppel, G. Rehfeldt, and C. Schütte, *Die Prachtlibellen Europas*, Die neue Brehm-Bücherei Bd. 654 (Westarp Wissenschaften, 2005).
  51. Lord Rayleigh, "The iridescent colours of birds and insects," *Proc. R. Soc. A Biol. Sci.* **128**, 624–641 (1930).
  52. M. Srinivasarao, "Nano-optics in the biological world: beetles, butterflies, birds, and moths," *Chem. Rev.* **99**, 1935–1961 (1999).
  53. A. R. Parker and N. Martini, "Structural colour in animals—simple to complex optics," *Opt. Laser Technol.* **38**, 315–322 (2006).
  54. S. Kinoshita, S. Yoshioka, Y. Fujii, and N. Okamoto, "Photophysics of structural color in the morpho butterflies," *Forma* **17**, 103–121 (2002).
  55. P. Vukusic, J. R. Sambles, and C. R. Lawrence, "Structurally assisted blackness in butterfly scales," *Proc. R. Soc. Biol. Sci.* **271**, 237–239 (2004).
  56. P. Vukusic, J. R. Sambles, C. R. Lawrence, and R. J. Wootton, "Now you see it—now you don't," *Nature* **410**, 36 (2001).
  57. I. R. Hooper, P. Vukusic, and R. J. Wootton, "Detailed optical study of the transparent wing membranes of the dragonfly *Aeshna cyanea*," *Opt. Express* **14**, 4891–4897 (2006).
  58. J. A. Noyes, P. Vukusic, and I. R. Hooper, "Experimental method for reliably establishing the refractive index of buprestid beetle exocuticle," *Opt. Express* **15**, 4351–4358 (2007).
  59. V. Backman, R. Gurjar, K. Badizadegan, I. Itzkan, R. R. Dasari, L. T. Perelman, and M. S. Feld, "Polarized light scattering spectroscopy for quantitative measurement of epithelial cellular structures *in situ*," *IEEE J. Sel. Top. Quantum Electron.* **5**, 1019–1026 (1999).
  60. T. Wagner, S. Beirle, T. Deutschmann, M. Grzegorski, and U. Platt, "Satellite monitoring of different vegetation types by differential optical absorption spectroscopy (DOAS) in the red spectral range," *Atmos. Chem. Phys.* **7**, 69–79 (2007).
  61. R. O. Prum, J. A. Cole, and R. H. Torres, "Blue integumentary structural colours in dragonflies (*Odonata*) are not produced by incoherent Tyndall scattering," *J. Exp. Biol.* **207**, 3999–4009 (2004).



62. S. Fizeau-Braesch, "Pigments and color changes," *Annu. Rev. Entomol.* **17**, 403–424 (1972).
63. J. M. Gallas and M. Eisner, "Fluorescence of melanin—dependence upon excitation wavelength and concentration," *Photochem. Photobiol.* **45**, 595–600 (1987).
64. G. Luna-Bárcenas, B. Gonzalez-Campos, E. A. Elizalde-Peña, E. Vivaldo-Lima, J. F. Louvier-Hernández, Y. V. Vorobiev, and J. González-Hernández, "FEMO modelling of optical properties of natural biopolymers chitin and chitosan," *Phys. Stat. Sol.* **5**, 3736–3739 (2008).
65. L. Q. Wu, R. Ghodssi, Y. A. Elabd, and G. F. Payne, "Biomimetic pattern transfer," *Adv. Funct. Mater.* **15**, 189–195 (2005).
66. S. N. Gorba, A. Keselb, and J. Bergera, "Microsculpture of the wing surface in *Odonata*: evidence for cuticular wax covering," *Arthropod Struct. Dev.* **29**, 129–135 (2000).
67. A. Ounis, Z. G. Cerovic, J. M. Briantais, and I. Moya, "DEFLIDAR: a new remote sensing instrument for estimation of epidermal UV absorption in leaves and canopies," in *Proceedings of European Association of Remote Sensing Laboratories (EARSeL)-SIG-Workshop LIDAR, Dresden/FRG (EARSeL, 2001)*, Vol. 1, pp. 196–204.
68. J. F. Jacobs, G. J. M. Koper, and W. N. J. Ursem, "UV protective coatings: a botanical approach," *Prog. Org. Coatings* **58**, 166–171 (2007).
69. E. Warrant, ed., *Invertebrate Vision* (Cambridge U. Press, 2006).
70. M. Wellereuther, M. Brydegaard, and E. Svensson are preparing a manuscript called "Role of female wing colour and male mate choice in premating isolation in allopatric and sympatric populations of damselflies".
71. G. De Marchi, "Precopulatory reproductive isolation and wing colour dimorphism in *Calopteryx splendens* females in southern Italy (*Zygoptera: Calopterygidae*)," *Odonatologica* **19**, 243–250 (1990).
72. M. J. Rantala, J. Koskimäki, J. Suhonen, J. Taskinen, and K. Tynkkynen, "Immunocompetence, developmental stability and wing spot size in *Calopteryx splendens*," *Proc. R. Soc. B* **267**, 2453–2457 (2000).
73. E. I. Svensson, L. Kristoffersen, K. Oskarsson, and S. Bensch, "Molecular population divergence and sexual selection on morphology in the banded demoiselle (*Calopteryx splendens*)," *Heredity* **93**, 423–433 (2004).
74. K. Tynkkynen, J. S. Kotiaho, M. Luojumäki, and J. Suhonen, "Interspecific territoriality in *Calopteryx* damselflies: the role of secondary sexual characters," *Anim. Behav.* **71**, 299–306 (2006).
75. U. Gustafsson, S. Pålsson, and S. Svanberg, "Compact fiber-optic fluorosensor using a continuous-wave violet diode laser and an integrated spectrometer," *Rev. Sci. Instrum.* **71**, 3004–3006 (2000).
76. C. af Klinteberg, M. Andreasson, O. Sandström, S. Andersson-Engels, and S. Svanberg, "Compact medical fluorosensor for minimally invasive tissue characterization," *Rev. Sci. Instrum.* **76**, 034303 (2005).
77. H. Edner, P. Ragnarson, S. Svanberg, E. Wallinder, R. Ferrara, B. E. Maserti, and R. Bargagli, "Atmospheric mercury mapping in a cinnabar mining area," *Sci. Total Environ.* **133** 1–15 (1993).
78. E. Wallinder, H. Edner, P. Ragnarson, and S. Svanberg, "Vertically sounding ozone LIDAR system based on a KrF excimer laser," *Phys. Scr.* **55**, 714–718 (1997).
79. C. af Klinteberg, A. Pifferi, S. Andersson-Engels, R. Cubeddu, and S. Svanberg, "In vivo absorption spectroscopy of tumor sensitizers using femtosecond white light," *Appl. Opt.* **44**, 2213–2220 (2005).
80. Ch. Abrahamsson, T. Svensson, S. Svanberg, S. Andersson-Engels, J. Johansson, and S. Folestad, "Time and wavelength resolved spectroscopy of turbid media using light continuum generated in a crystal fibre," *Opt. Express* **12**, 4103–4112 (2004).

# PAPER V

## **Insect monitoring with fluorescence lidar techniques: field experiments**

Z.G. Guan, M. Brydegaard, P. Lundin, M. Wellenreuther,  
A. Runemark, E.I. Svensson, S. Svanberg.

*Applied Optics* **49**, (2010).



# Insect monitoring with fluorescence lidar techniques: field experiments

Zuguang Guan,<sup>1,\*</sup> Mikkel Brydegaard,<sup>1</sup> Patrik Lundin,<sup>1</sup> Maren Wellenreuther,<sup>2</sup>  
Anna Runemark,<sup>2</sup> Erik Svensson,<sup>2</sup> and Sune Svanberg<sup>1</sup>

<sup>1</sup>Atomic Physics Division, Lund University, P.O. Box 118, SE-221 00 Lund, Sweden

<sup>2</sup>Department of Biology, Lund University, SE-223 62 Lund, Sweden

\*Corresponding author: zuguang.guan@fysik.lth.se

Received 9 June 2010; accepted 20 July 2010;  
posted 26 July 2010 (Doc. ID 129890); published 0 MONTH 0000

Results from field experiments using a fluorescence lidar system to monitor movements of insects are reported. Measurements over a river surface were made at distances between 100 and 300 m, detecting, in particular, damselflies entering the 355 nm pulsed laser beam. The lidar system recorded the depolarized elastic backscattering and two broad bands of laser-induced fluorescence, with the separation wavelength at 500 nm. Captured species, dusted with characteristic fluorescent dye powders, could be followed spatially and temporally after release. Implications for ecological research are discussed. © 2010 Optical Society of America

OCIS codes: 280.3640, 300.2530.

## 1. Introduction

Lidar techniques have been developed for almost 50 years for atmospheric monitoring by analyzing the return echo from the aerosols distributed in the atmosphere [1–3]. The fluorescence lidar variety is useful in assessing phenomena in addition to those relying on elastic backscattering from aerosols. Because of the existence of alkali atoms and iron ions in an extremely low-pressure environment, fluorescence lidar is a unique technique for monitoring conditions in the upper atmosphere [3]. At a shorter range, the Swedish research group at Lund University, and others, have shown that remote targets within a few hundred meters can be analyzed successfully using laser-induced-fluorescence (LIF) spectroscopy [4]. Based on a well-developed mobile lidar system [5], the applications range from the optical diagnosis of historical monuments to the analysis of hydrological and vegetation targets. With the knowledge of measurements ranging from aerosols with sizes of less than 1  $\mu\text{m}$  to macro solid targets,

such as the Roman Colosseum [6], we are currently at the intermediate spatial scale by studying flying insects.

Monitoring insects and studying their movements is of great importance in biological research and environmental monitoring. For instance, damselfly larvae are highly sensitive to water pollution and dissolved oxygen concentrations and, thus, are used as biomarkers [7]. Like other ectotherms, damselflies are sensitive to ambient temperature, and many species have undergone a northward shift in their distribution due to global warming [8]. Dispersal studies of insects are also critical for understanding the role of dispersal between populations over wide spatial scales [9], which is important when developing conservation policies. The traditional method is limited to marking individuals with different dyes and then collecting individuals from neighboring populations [10]. Advanced remote detection techniques in this field have developed slowly. Pioneering work using elastic lidar to study honeybees for land mine detection has been reported [11–13].

Noticing the potential advances of LIF techniques in insect monitoring and the natural connection with the dye markers used for traditional tracing, we

demonstrated for the first time fluorescence lidar techniques for damselfly (*Calopteryx splendens* and *C. virgo*) monitoring at a distance of 60 m [14]. For initial remote spectral analysis of LIF, an intensified fiber-coupled optical multiple channel analyzer system [15] is employed. By averaging signals, even the autofluorescence from mounted dead damselflies was useful for distinguishing between species and sexes [14]. Importantly, damselflies dusted with different types of dye can be spatially resolved and distinguished from the fluorescence signature in a single lidar pulse. To further test the feasibility of such a technique, two weeks of field experiments were carried out in southern Sweden, where three geometrical arrangements were set up over a river surface [see Fig. 1(a)], and damselflies that were flying into the laser beam were detected and counted statistically. During the campaign, three groups of damselflies were dusted with dye powder and released into the natural environment. The fluorescence signatures in lidar signals reveal their presence, dispersal patterns, and activity in later measurements.

This paper is organized as follows. First, the fluorescence lidar equipment is introduced in Subsection 2.A, followed by a description, in Subsection 2.B, of the geographic setting of the field experiment where three lidar paths are set up. The selection and use of fluorescence dyes in the short-range test and in the field experiments are described in Subsection 2.C. Subsection 3.A shows a method used to distinguish three species of damselflies (dusted with different dyes) using their fluorescence signatures. In Subsection 3.B, the statistical results are presented and discussed in the spatial domain, as well as in the time domain, also taking weather conditions into account. In addition, the application of a method used to extract insect echoes out from the electronic perturbation is introduced in Subsection 3.C. Finally, we discuss the general applicability of the technique in biological systems and the biological implications of the findings.

## 2. Experimental Methods

### A. Lidar Equipment

The experimental facility is based on the Lund mobile lidar system [5], which is modified for the current study in important ways. The main equipment is presented in Fig. 1(b). The third harmonic (355 nm) of the Nd:YAG laser radiation is used with an energy of 40 mJ/pulse, and with a pulse width of 10 ns. After expanding to a beam diameter of 5 cm, the laser beam is transmitted by a mirror (40 cm × 56 cm) placed in a transmission dome, which can scan vertically and horizontally. A quartz window in the dome is used to protect the mirror from atmospheric dirt and dust. The elastic scattering and the fluorescence from the targets are reflected by the same mirror and collected by a telescope system with a diameter of 40 cm. The collected light is distributed by several

mirrors and is filtered, and then detected by three photomultipliers (PMTs). As shown in Fig. 1(b), the elastic scattering from the target is selected by a laser line mirror (LM) and recorded by PMT-1 in the time domain. A polarizer (P) is set at a crossed angle against the polarization state of the transmitted laser beam. Therefore, PMT-1 is sensitive only to depolarized backscattering, but blind to the copolarized echo from the target surface, and, hence, insensitive to the flying orientation of the insect in the laser beam. An extra-short-pass filter (SF) is used to suppress the fluorescence light from the target and background light from the sky thereafter. The fluorescence light passing through the LM is

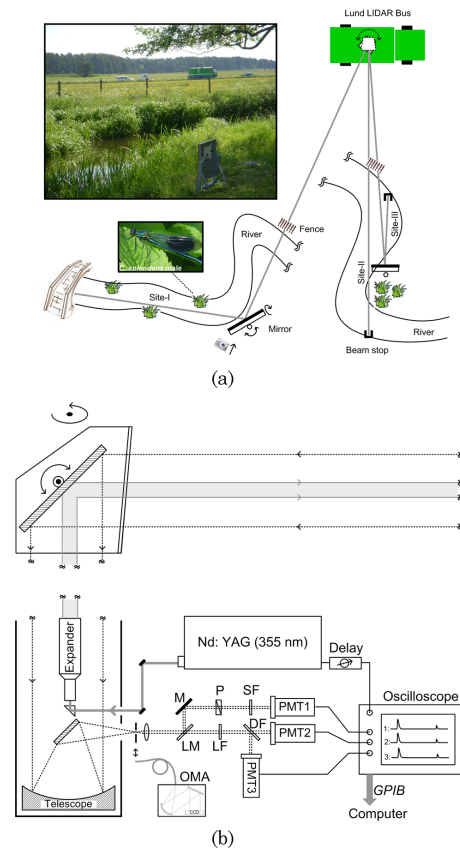


Fig. 1. (Color online) (a) Geographic diagram of the measurement locations. The inserted scenery picture is taken from the indicated position and direction; also shown is a male *C. splendens* damselfly. (b) Key equipment/components of the fluorescence lidar (PMT-1 is for detection of elastic scattering, while PMT-2 and PMT-3 are for yellow and blue bands of fluorescence, respectively).

4/CO

divided by a dichroic filter (DF) into two wavelength bands, blue (400–500 nm) and yellow (500–750 nm), and measured by PMT-3 and PMT-2, respectively. Before the DF, a long-pass filter (LF) is used to suppress the leakage of the elastic scattering through the LM. Three channels of signals from the PMTs are simultaneously recorded by a high-speed oscilloscope (Tektronix TDS544B), which samples every 8 ns. The start time of the sampling period is controllable by adding a tunable delay onto the synchronization trigger from the Nd:YAG laser. The recorded data are then read out through a GPIB connection by a computer in real time. The repetition rate of the whole system is limited to 10 Hz by communication speed, although the repetition rate of the laser system is 20 Hz. By using such a three-PMT system, both the elastic scattering and two bands of fluorescence can be analyzed in the time/spatial domain.

### B. Field Site

Insect measurements were performed with the Lund mobile lidar system at the Klingavälsån river, Veberöd (5538'N, 1329'E), in southern Sweden, during two weeks (1–7 and 24–30 June 2009); see Fig. 1(a). The vehicle was parked near the river, and the laser beam passed over a pasture enclosure, and was measuring in three different geometrical arrangements over the surface of the river. In the first week, the measurements were carried out at Site I, where the laser beam was folded by a plane mirror (~50 × 60 cm<sup>2</sup>) in order to be close to the water surface, and then terminated below a bridge. The insects flying through the laser beam could be measured and analyzed in real time. In the second measurement week, the laser beam was moved to Sites II and III. At Site II, the laser beam followed a section of the river that included a peninsula and the beam was terminated by a black beam stop that was set up at the riverbank. Close to Site II, Site III was set up by folding the laser beam closer to the river surface, using the same plane mirror, but now mounted on the peninsula.

Single-pulse lidar echoes corresponding to three paths of the laser beam are shown in Fig. 2, correlated to a satellite image (obtained via the Google Earth tool) of the field. The backscattered signals from the static targets, including the quartz window (protecting the rooftop lidar mirror), a fence, the folding mirror, and the termination, are shown to be stable in all three bands during the long-term measurements. Ranges of interest are marked out in Fig. 2(a) and corresponding lidar echo signals are shown in Fig. 2(b). For instance, in Path I, the range between the mirror and the bridge, corresponding to Site I [compare with Fig. 1(a)], is from 186 to 260 m. Any small “blips” in between the fixed target echoes that show up in the elastic band are recorded by the system, and later counted as one detection in the histogram. The two fluorescence bands are basically used for analyzing dusted-and-released damselflies in the second measurement week, since the auto-

fluorescence from natural damselflies was too weak to be measured in a single pulse in daylight conditions, while the dye-induced fluorescence can easily be distinguished. From the static targets, we can see fluorescence signatures from the quartz window (due to the dust and dirt attached on the surface), but not (or very weakly) from the metal fence, while they saturate the PMTs at the black-painted terminations. We realized that the intensity of the fluorescence signal from the quartz window can be used for normalization, so that the instabilities of the fluorescence signals, depending on the laser power, PMT sensitivity, etc., can be compensated for.

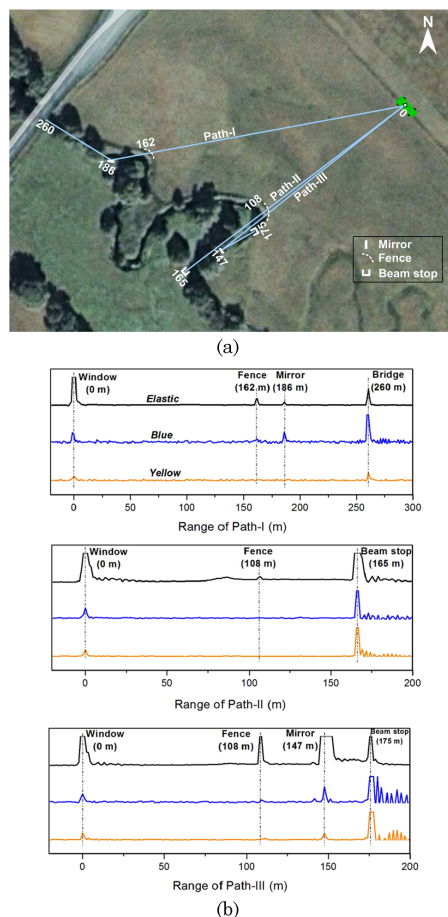


Fig. 2. (Color online) (a) Three lidar paths are shown on a satellite map; numbers indicate the lidar-target distances in meters; (b) lidar echoes from the static targets in Path I (top), Path II (middle), and Path III (bottom).

4/CC

C. Application of Dyes

Before the field experiments, the performance of the lidar system was tested in Lund. Two dead *Calopterygidae* damselflies marked with different dyes (Coumarin 102 and Rhodamine 6G) were placed at different distances (60 and 80 m, respectively) within the laser path; see Fig. 3(a). The single-pulse reflection signal burst from the damselflies was then recorded by the three-PMT systems, as shown in Fig. 3(b). Obviously, the intensity (ratio) of the two fluorescence bands are different for the damselfly positioned at a closer distance, which is marked by Coumarin 102, a bluish dye, and the other one at a larger distance, marked by Rhodamine 6G, which is reddish. The fluorescence spectra of these two dyes for 355 nm excitation are shown in Fig. 10 of Ref. [14]. The above tests indicate that the fluorescence signature from a single lidar pulse is sufficient to distinguish damselflies marked with different dyes, which was encouraging for studying flying damselflies in their natural habitats.

In the later field experiments, three types of dye powder from Swada Inc. were used to dust three groups of captured damselflies belonging to the species *C. splendens* and *C. virgo*. Specifically, 43 *C. splendens* males were marked with Stellar green, 19 *C. splendens* females were marked with Comet blue, and 20 *C. virgo* males were marked with Nova red. It is worth mentioning that these dye powders are used regularly by biologists for dispersal and mating studies (see, e.g., [10]), and have been tested to not harm the insects. The fluorescence spectra for 355 nm excitation are shown in Fig. 4. With the cutoff wavelength of the dichroic filter, which distributes the light energy into two PMTs, at 500 nm, one can expect that the blue dye will mainly be seen by the blue-band PMT, while the red dye will be seen by the yellow-band PMT, and the green dye by both. Dusted damselflies were released at Site III during

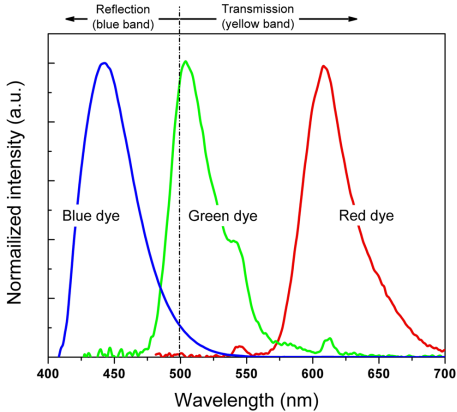


Fig. 4. (Color online) Fluorescence spectra of three dye powders used in the field experiments, with excitation wavelength at 355 nm. The dashed-dotted line indicates the cutoff wavelength of the dichroic filter.

4/CC

the measurement in the second week, 29 and 30 June 2009. They appear occasionally in the laser path together with unmarked damselflies, and are distinguished by the lidar system from them by the fluorescence signatures. Since the different species and sexes are dusted with different powders, information on species- and sex-specific habitat preferences and dispersal patterns can be obtained if a large enough number of insects is dusted and released. For calibrating the signals at the two fluorescence bands, glass tubes with the individual dyes are moved in and out of the laser beam (close to the fence) to get the standard fluorescence signatures. A detailed analysis of this procedure is given in Section 3.

3. Data Analysis

A. Fluorescence Signature

The method of the fluorescence analysis of damselflies is described here. Figure 5(a) shows several examples of single-pulse lidar curves corresponding to different situations/events happening at Site III. The background consists of static signals (in the situation of no damselfly), and obvious “blips” (with the underlying area filled in) can be occasionally seen between the fence and the mirror (marked by light yellow shaded band), when damselflies fly into the laser beam. For the unmarked damselflies, the signals in the two fluorescence bands are not obvious due to the weak autofluorescence; however, the elastic backscattering is enough for statistical counting (see Subsection 3.B). For the dusted-and-released ones, the fluorescence signatures are clearly different for the three dye species. As expected, the blue dye shows a stronger bluish fluorescence, while the red dye shows stronger fluorescence in the yellow

1

2

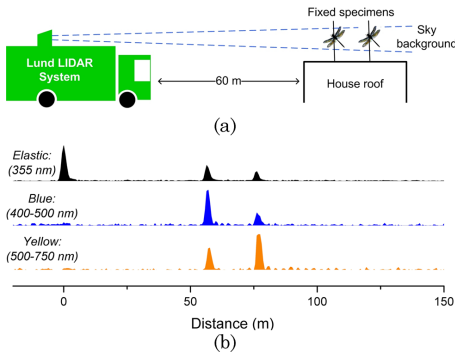


Fig. 3. (Color online) (a) Setup for the test-range measurements, and (b) range-resolved signals of the three channels, from two serially placed damselflies marked with different dyes (Coumarin 102 and Rhodamine 6G).

4/CC

band, and the green one shows a relatively equal intensity in both bands.

The echo signals corresponding to the damselflies observed in the two fluorescence bands are normalized to those arising from the quartz window at distance 0, before they are plotted in the scatter plot in Fig. 5(b). Here the echo energy is calculated by integrating the echo return intensity in the time domain. By doing so we obtain higher accuracy than by simply selecting the peak intensity, considering that the laser pulse width (10 ns) is comparable with the sampling temporal interval (8 ns). As mentioned above, the dye tubes were used for calibration. The normalized signals corresponding to these “standard” samples are first plotted in Fig. 5(b) as crossed marks, which separate clearly. The blue and red dyes occupy the upper-left and bottom-right areas, respectively, due to relatively strong bluish and yellowish fluorescence, while the green dye signals, with equal intensities in both bands, are situated in between. With such a calibration method, the signals corresponding to the dusted damselflies can be plotted into the same scatter plot and their respective dyes can be determined based on which area they are located in. The data from the field measurement of flying dusted-and-released damselflies are shown as round marks in the figure, and the three groups are well distinguished.

#### B. Statistical Analysis

Using the strategy described in Subsection 3.A, damselflies that appear in the laser beam were detected and statistically counted. The range-resolved results are shown in Fig. 6. For Site I, the data close to the mirror are disturbed by the riverbank vegetation moving in the wind. Many of the measured insects that were found close to the bridge were mosquitoes (according to visual observations), which cause weaker echoes than the damselflies. Mosquitoes and damselflies can thus be separated by adjusting the threshold for selecting echoes. The decay of the lidar curve with range ( $R$ ), following  $R^{-2}$ , has been considered when setting the threshold. Damselflies were mainly detected between 210 and 250 m. Three signal locations, indicating positions in which damselflies frequently appeared, were correlated with reed stands (preferred territories of damselflies [16]). For Site II, damselflies were mostly found around the peninsula, which was consistent with our visual observations. It is interesting to compare the results with Site III, where the peninsula was occupied by the mirror. During the measurements at Site III, we released three groups of damselflies near the fence on 29 and 30 June 2009. In later measurements, they are recorded, distinguished, and plotted in Fig. 6(c). The spatial distribution of the marked damselflies is comparable with that of the unmarked individuals.

Statistical analyses were also performed in the time domain. Figure 7 shows the result obtained at Site I, on 2 June 2009, together with the weather

parameters. The damselflies were identified (shown in black) using the threshold method described above. The number of actively flying insects (including both mosquitoes and damselflies) decreased considerably as the temperature dropped and wind speed increased. The observed increase of damselflies in activity between 15:00 and 16:00 is probably due to other environmental factors, such as increased Sun radiation due to local cloud movements. Results from the three consecutive measurement days at Site

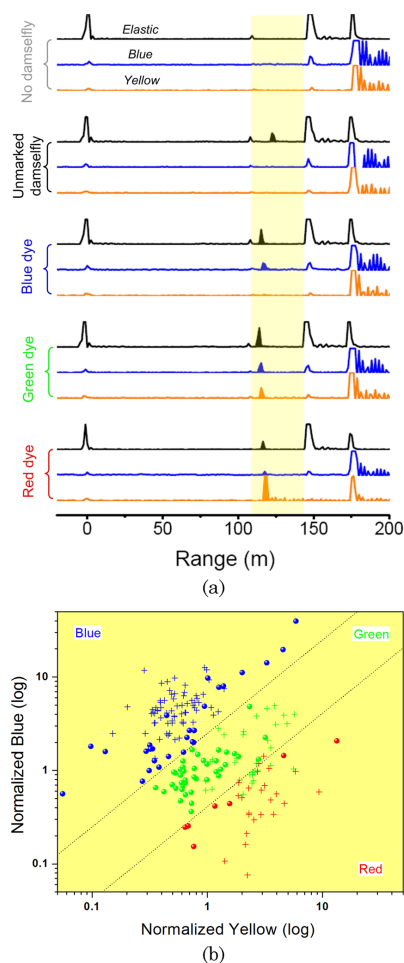


Fig. 5. (Color online) (a) Lidar signals showing different events at Site III, and (b) the scatter plot showing the fluorescence properties of three types of dyes; the crosses and the round marks indicate the calibrating dye tubes and the dusted damselflies, respectively.

4/CC



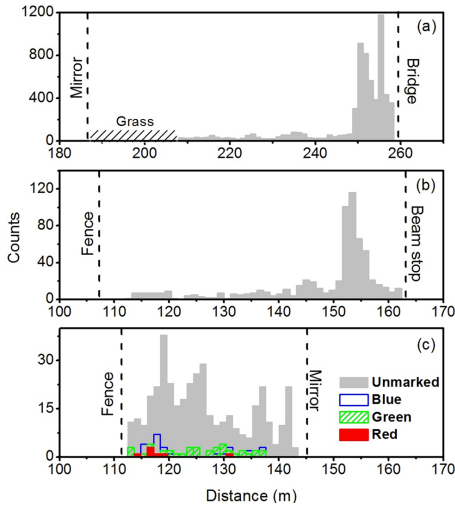


Fig. 6. (Color online) Spatial distributions of the flying damselflies at (a) Site I, (b) Site II, and (c) Site III. The colored histograms in (c) indicate dusted-and-released damselflies. The females marked with blue dye and males marked with green dye belong to the species *C. splendens*, whereas the males marked with red dye are *C. virgo*.

III, where dusted damselflies were released on 29 and 30 June 2009, are shown in Fig. 8. From the figure, it can be seen that several of the marked damselflies were alive on 30 June 2009, which corresponds to 1–2 days after they were originally marked.

#### C. Perturbation Removal for Enhanced Damselfly Detection

One particular feature of insects in lidar data is their sudden temporal occurrence and disappearance, which is in great contrast to influences of perturbing static objects along the line of propagation of the light pulse. Such completely static features could, in principle, have been removed simply by subtracting an “empty” curve that contains only static information [such as the curves shown in Fig. 2(b)] from all measurements. In the real world, the strong reflections from the fence and the mirror in this case, can induce nonoptical features, e.g., oscillations caused by electronic reflections in the PMT cables or depletion of the charges in the dynodes. Such an unstable perturbation, together with a triggering uncertainty from the quasi-static features in the backscattering signal, makes the simple subtraction approach inapplicable, especially in the range closely after the mirror [see Fig. 5(a) from Site III], where the insect signals can be easily masked. Therefore, we investigated the possibility of removing these quasi-static effects from the data by using the singular value decomposition (SVD) method [17]. SVD is generally not con-

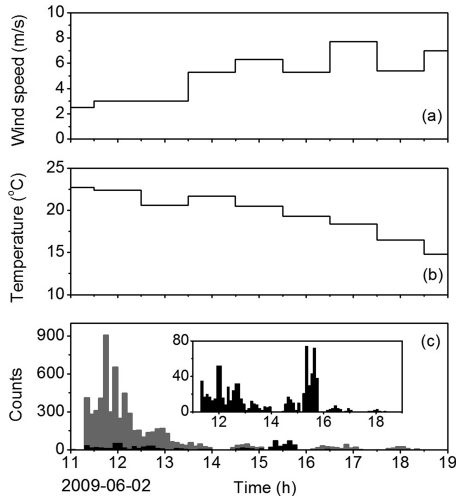


Fig. 7. (c) Measured counts of all insects (gray) and damselflies only (black) activity correlated to (a) the wind speed and (b) the temperature, at Site I. The inset of (c) shows the details of the histogram corresponding to damselflies.

sidered suitable for describing temporal phenomena; however, it can be applicable in some cases as a quick tool that requires no detailed information, as traditional input–output system identification methods would [18,19]. We successfully managed to describe the quasi-static background as a linear combination of three time series generated with SVD. As the insects only occur in about one out of a thousand shots, these events will be heavily suppressed by the data not involving a hit. The result of the removal can be seen in the example in Figs. 9(a) and 9(b). In this case, the insect echo is completely hidden in the ringing of the elastic PMT after the strong diffuse reflectance from the mirror [Fig. 9(a)]. While single pulses in any of the PMTs might be caused by “ghost photons” with intensity levels above the background, it is much less likely that such pulses occur simultaneously in two of the PMTs. One way to increase the contrast of true hits in respect to the ghost photons is

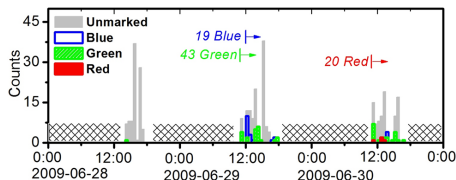


Fig. 8. (Color online) Three days of measurements at Site III. Gray and colored histograms indicate unmarked and dusted damselflies, respectively. Times for release of the dusted damselflies are marked. No measurements are performed during the periods marked by cross-hatching.

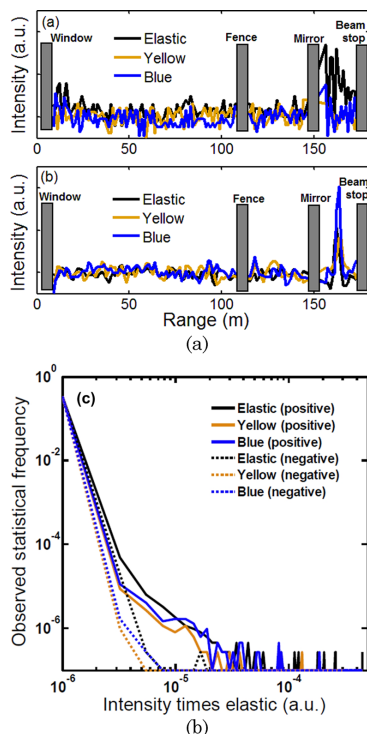


Fig. 9. (Color online) (a) Typical raw echo return after subtraction of "empty" curves (see the text). (b) Signal from the same shot after removing the quasi-static contribution from electronic oscillations, etc. The hit was detected on 29 June 2009, 11:35:27. (c) The insects give rise to a skewness in the intensity histogram. The dotted curves are the negative values. The separation indicates that the insects do, in fact, give an increased intensity return.

to make use of the fuzzy logical AND operator, namely, to multiply the fluorescence signal by the elastic signal. This method is especially valid for marked damselflies that show obvious signals in fluorescence bands. After the removal of the quasi-static contribution, unbiased histograms can be produced on the returned fluorescent intensities times the elastic. In Fig. 9(c), we have produced such a histogram for the range between the fence and the mirror at Site III. The statistics are carried out on three time sections of totally 3 h on 29 and 30 June 2009. To study the insects in particular, the data containing information of road dust plumes from passing cars (discussed below) were excluded. The negative values generally represent the noise level; their amplitudes are plotted with dotted curves to compare with the positive values plotted as solid curves. Clearly, the reflection signals from the insects produce much higher positive values compared with noise and,

hence, induce a skewness in the histogram; see the mismatch between histograms in Fig. 9(c) corresponding to positive and negative values. Similar graphs were observed from the window to fence and the mirror to the termination stretch, although with less and more skewness, respectively. This is in accordance with the ecological *a priori* knowledge, with lower damselfly numbers at the closer range where the laser beam passes the pasture field, but a higher possibility of capturing the flying damselflies over the river surface at the farther range. The SVD method discussed above for quasi-static signature removal works consistently, and was applied successfully over several days of measurements. Figure 10 shows an example in which the removal method works on 25 s of data recorded in the afternoon of 29 July 2009. The three (elastic, blue, and yellow) bands of signals, with quasi-static features removed, are plotted as blue, green, and red, respectively, into a red–green–blue (RGB) false color map. All three channels are multiplied by the elastic channel to further enhance the contrast. Before the fence, a road dust plume induced by a passing car can be clearly seen on a zero background, thanks to the successful removal of the static/quasi-static features. Particularly, in the range between the insect and the termination, where originally the insect echo was impossible to see before the removal operation, now clear information appears in different false colors due to different fluorescence performance. The green-dyed damselfly, with reflection signals in all three channels, shows as white in the map, while the natural (nondyed) one shows up as blue and the blue-dyed one shows up as cyan.

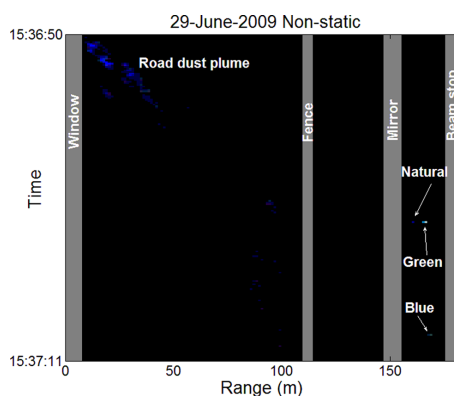


Fig. 10. (Color online) False color RGB representation of 25 s of lidar data with the quasi-static signal removed. Blue, elastic; green, blue fluorescence; red, yellow fluorescence. The inorganic road dust from a passing car gives rise to distributed elastic scattering signals, moving in the wind. The insect signatures appear only for a fraction of a second.

#### 4. Discussion

In this paper, we demonstrate the potential of lidar as a remote-sensing technique to model the spatial and temporal activity of *Calopteryx splendens* and *C. virgo* damselflies in the wild. Although several review articles on the potential of lidar in habitat modeling have appeared in the last few years, the number of applications on natural populations is low, and most of the studies until now have concentrated on bird habitats [20,21] rather than on birds themselves. In particular, we show that lidar can be applied to monitor unmarked damselflies in their natural habitats, and how the use of fluorescent dust helps to differentiate between damselfly sexes and species using a single lidar pulse. Applying such a computerized imaging setup on scales ranging from 100 m to a couple of kilometers will enable biologists to design new experiments and to address new and interesting questions regarding insect ecology, evolution, or optimal wing morphology. In addition, lidar monitoring is an efficient way to assess, for example, population sizes, lifetimes, and dispersal distances and rates, and such data are commonly needed for conservation planning.

Studying the ecological requirements and habitat use of invertebrates in a quantitative way is usually both time consuming and difficult. By using lidar, we show that quantitative data on the temperature and wind speed requirements of *C. splendens* and *C. virgo* can easily be collected during only a few days in the field. For ectotherms, like these damselflies, data on thermal tolerance ranges will be increasingly important in the face of global warming [22,23], since it might tell us about the prospects for local extinction or predict potential northward shifts in the distribution of species. In addition, we have estimated the type of vegetation and at which distances from the water the two species of damselflies occurred, and this adds additional important information about the environmental requirements of these species. Furthermore, the stationary nature of lidar allows the rapid assessment of temporal and spatial activities of individuals in a population. Data collection in such a setting would also be more objective, compared to commonly employed visual censuses by humans, which would increase comparability between sites and observers. Through the marking of different species and sexes with different types of fluorescent dyes, we could also estimate the dispersal patterns and rates of the marked damselflies, and study if habitat use is sex or species specific. This approach would also be useful for mark-recapture studies, a common technique for estimating population sizes where the recapture rate is usually the limiting factor.

From Fig. 6, a tendency for male *C. splendens* (marked by green powder) to be more dispersed along the river than *C. splendens* females and *C. virgo* males can be seen. The difference in dispersion between males of the two species can be attributed to two factors. First, *C. virgo* males have been shown

to be more aggressive than *C. splendens* males and are, thus, more dominant [24–26]. This difference in competitive ability is likely to result in the displacement of some *C. splendens* males from their preferred territories, and interspecific contests between males will also often lead to males of *C. splendens* being chased away by *C. virgo* males. Hence, *C. splendens* males might more often be actively displaced from their river territories than males of *C. virgo* and, hence, be in search for new territories. Second, male *C. splendens* commonly force copulations with females, while *C. virgo* males are more likely to perform a courtship display to initiate mating [27]. Forced copulations are being achieved by following flying females and then by forcing the females to bring up their abdomen to engage genitalia [28]. The chasing of females probably contributes to the wide dispersion of *C. splendens* males, thus further increasing the overall spread of males along a river. It should be noted from our result that *C. splendens* males were more dispersed along the river than females, contradicting previous findings, but this might be an artifact of the scale of different studies. A tendency for females to disperse greater distances than males has been observed in both *C. splendens* [29] and in the blue-tailed damselfly *Ischnura elegans* [30]. However, our study measured fine-scale dispersion patterns (scale of a few meters), while the two aforementioned studies investigated large-scale dispersion patterns (hundreds of meters), which were not measured in the current study. Thus, it is possible that the different results are caused by different scales at which the studies were conducted, and that small and large dispersion patterns differ between the sexes of *C. splendens*. In order to address this explicitly, more studies are needed to rigorously test this prediction. The finding that males prefer vegetated habitat near the water is consistent with previous studies on habitat use in these species [26,31]. Aquatic plants provide *C. splendens* males with good oviposition territory and perching spots [32].

Biodiversity is diminishing at an accelerating pace [33], and, therefore, data on biodiversity and spatial distribution are urgently needed for conservation planning. However, the lack of taxonomists and funds precludes particularly the mapping of taxonomically diverse groups, such as invertebrates [21]. Therefore, management strategies mostly concentrate on charismatic vertebrates and only a few conspicuous invertebrates and ignore most other species [34]. However, the diversity of invertebrates is declining even more rapidly than that of plants and vertebrates [35], even though invertebrates are involved in important ecosystem functions, such as pollination and food webs. We thus clearly need better methods to rapidly, effectively, and cheaply assess the abundance and distribution of invertebrate species. The results of our study are, therefore, encouraging and timely for future assessments of invertebrates.

## 5. Conclusions

Following proof-of-principle measurements [14], we have now performed successful real-world field experiments on insects *in vivo* and demonstrated the potential of the technique. Lidar provides simple but ecologically meaningful variables for a rapid extrapolation of activity, richness, and composition of insect assemblages across large areas. This enables conservationists to evaluate habitat over large areas and to define diversity hot spots, as well as to monitor changes in the distribution and abundance in response to environmental change. Low fluorescence yield of chitin at 355 nm excitation is a limitation when using nondyed species. However, improvement could be expected by employing, e.g., 266 nm (quadrupled Nd:YAG laser), or 308 nm (XeCl excimer laser) for a better match to the chitin absorption band. Further, the extended fluorescence band available then would also enhance the chance for classification without marking. We did not note any perturbation of the measured species when hit by 355 nm light; however, a shorter excitation wavelength would also be desirable to decrease such a possibility. Full sunlight measurement conditions were shown to be possible; clearly performance is improved for lower light levels. The fact that we estimate a probability rather than a concentration as in, e.g., aerosol lidar applications, implies that a large number of laser shots, in our case thousands of shots, are required to produce a good statistical distribution. Thus, the insect concentration should be considerable to produce a measurement in a limited time. This is particularly true if two-dimensional or three-dimensional mappings are desired.

With the experience gathered in the present work, it should be possible to perform lidar monitoring of insects of considerable impact on the ecology community.

The authors gratefully acknowledge the support from the Swedish Research Council through a project grant, and through a Linnaeus grant to the Lund Laser Centre. Further, we are grateful to the Knut and Alice Wallenberg Foundation for equipment grants.

## References

1. R. M. Measures, *Laser Remote Sensing: Fundamentals and Applications* (Wiley, 1984).
2. S. Svanberg, "LIDAR," in *Springer Handbook of Lasers and Optics* F. Träger, ed. (Springer, 2007), pp. 1031–1052.
3. X. Chu and G. C. Papen, "Resonance fluorescence lidar," in *Laser Remote Sensing* T. Fujii and T. Fukuchi, ed. (CRC, 2005), Chap. 5, pp. 179–432.
4. S. Svanberg, "Fluorescence spectroscopy and imaging of lidar targets," in *Laser Remote Sensing* T. Fujii and T. Fukuchi, ed. (CRC, 2005), Chap. 6, pp. 433–468.
5. P. Weibring, H. Edner, and S. Svanberg, "Versatile mobile lidar system for environmental monitoring," *Appl. Opt.* **42**, 3583–3594 (2003).
6. L. Palombi, D. Lognoli, V. Raimondi, G. Cecchi, J. Hällström, K. Barup, C. Conti, R. Grönlund, A. Johansson, and S. Svanberg, "Hyperspectral fluorescence lidar imaging at the Colosseum, Rome: elucidating past conservation interventions," *Opt. Express* **16**, 6794–680 (2008).
7. M. Campero, F. Ollevier, and R. Stoks, "Ecological relevance and sensitivity depending on the exposure time for two biomarkers," *Environ. Toxicol.* **22**, 572–581 (2007).
8. R. Hickling, D. B. Roy, J. K. Hill, and C. D. Thomas, "A northward shift of range margins in British odonata," *Glob. Change Biol.* **11**, 502–506 (2005).
9. T. J. Case and M. L. Taper, "Interspecific competition, environmental gradients, gene flow, and the coevolution of species borders," *Am. Nat.* **155**, 583–605 (2000).
10. M. Joron and P. M. Brakefield, "Captivity masks inbreeding effects on male mating success in butterflies," *Nature* **424**, 191–194 (2003).
11. J. A. Shaw, N. L. Seldomridge, D. L. Dunkle, P. W. Nugent, L. H. Spangler, J. J. Bromenshank, C. B. Henderson, J. H. Churnside, and J. J. Wilson, "Polarization lidar measurements of honey bees in flight for locating land mines," *Opt. Express* **13**, 5853–5863 (2005).
12. K. S. Repasky, J. A. Shaw, R. Scheppele, C. Melton, J. L. Carsten, and L. H. Spangler, "Optical detection of honeybees by use of wing-beat modulation of scattered laser light for locating explosives and land mines," *Appl. Opt.* **45**, 1839–1843 (2006).
13. D. S. Hoffman, A. R. Nehrir, K. S. Repasky, J. A. Shaw, and J. L. Carlsen, "Range-resolved optical detection of honeybees by use of wing-beat modulation of scattered light for locating land mines," *Appl. Opt.* **46**, 3007–3012 (2007).
14. M. Brydegaard, Z. G. Guan, M. Wellenreuther, and S. Svanberg, "Insect monitoring with fluorescence lidar techniques: feasibility study," *Appl. Opt.* **48**, 5668–5677 (2009).
15. C. af Klinteberg, M. Andreasson, O. Sandström, S. Andersson-Engels, and S. Svanberg, "Compact medical fluorosensor for minimally invasive tissue characterization," *Rev. Sci. Instrum.* **71**, 2004–2006 (2005).
16. P. S. Corbet, *Dragonflies: Behavior and Ecology of Odonata* Essex (Harley, 1999).
17. E. Anderson, Z. Bai, C. Bischof, S. Blackford, J. Demmel, J. Dongarra, J. Du Croz, A. Greenbaum, S. Hammarling, A. McKenney, and D. Sorensen, *LAPACK User's Guide*, 3rd ed. (Society for Industrial and Applied Mathematics, 1999).
18. R. Johansson, *System Modeling and Identification* (Prentice Hall, 1993).
19. E. M. C. Hillman and A. Moore, "All-optical anatomical co-registration for molecular imaging of small animals using dynamic contrast," *Nat. Photon.* **1**, 526–530 (2007).
20. R. B. Bradbury, R. A. Hill, D. C. Mason, S. A. Hinsley, J. D. Wilson, H. Balzter, G. Q. A. Anderson, M. J. Wittingham, I. J. Davenport, and P. E. Bellamy, "Modeling relationships between birds and vegetation structure using airborne lidar data: a review with case studies from agricultural and woodland environments," *Ibis* **147**, 443–452 (2005).
21. K. T. Vierling, L. A. Vierling, W. A. Gould, S. Martinuzzi, and R. M. Clawges, "Lidar: Shedding new light on habitat characterization and modeling," *Front. Ecol. Environ.* **6**, 90–98 (2008).
22. C. N. Parmesan, "Climate and species' range," *Nature* **382**, 765–766 (1996).
23. C. N. Parmesan, C. Ryrholm, C. Steganescu, J. K. Hill, C. D. Thomas, B. Descimon, B. Huntley, L. Kaila, J. Kullberg, T. Tamaru, W. J. Tennent, J. A. Thomas, and M. Warren, "Poleward shifts in geographical ranges of butterfly species associated with regional warming," *Nature* **399**, 579–583 (1999).
24. K. Tynkkynen, M. J. Rantala, and J. Suhonen, "Interspecific aggression and character displacement in the damselfly *Calopteryx splendens*," *J. Evol. Biol.* **17**, 759–767 (2004).
25. K. Tynkkynen, J. S. Kotiaho, M. Luojumäki, and J. Suhonen, "Interspecific aggression causes negative selection on sexual characters," *Evolution* **59**, 1838–1843 (2005).

26. K. Tynkkynen, J. S. Kotiaho, M. Luojumäki, and J. Suhonen, "Interspecific territoriality in *Calopteryx* damselflies: the role of secondary sexual characters," *Anim. Behav.* **71**, 299–306 (2006).
27. G. Rüppel, D. Hilfert-Rüppel, G. Rehfeldt, and C. Schütte, *Die Prachtlibellen Europas* (Westarp Wissenschaften, 2005).
28. A. Cordero, "Forced copulations and female contact guarding at a high male density in a *Calopterygid* damselfly," *J. Insect Behav.* **12**, 27–37 (1999).
29. A. Chaput-Bardy, A. Gregoire, M. Baguette, A. Pagano, and J. Secondi, "Condition and phenotype-dependent dispersal in a damselfly, *Calopteryx splendens*," *PLoS ONE* **5**, e10694 (2010).
30. K. F. Conrad, K. H. Willson, K. Whitfield, I. F. Harvey, C. J. Thomas, and T. N. Sherratt, "Characteristics of dispersing *Ischnura elegans* and *Coenagrion puella* (odonata): age, sex, size morph and ectoparasitism," *Ecography* **25**, 439–445 (2002).
31. L. Ward and P. J. Mill, "Habitat factors influencing the presence of adult *Calopteryx splendens* (odonata: Zygoptera)," *Euro. J. Entomol.* **102**, 47–51 (2005).
32. D. W. Gibbons and D. Pain, "The influence of river flow rate on the breeding behaviour of calopteryx damselflies," *J. Anim. Ecol.* **61**, 283–289 (1992).
33. F. S. Chapin, E. S. Zavaleta, V. T. Eviner, R. L. Naylor, P. M. Vitousek, H. L. Reynolds, D. U. Hooper, S. Lavore, O. E. Sala, S. E. Hobbie, M. C. Mack, and S. Diaz, "Consequences of changing biodiversity," *Nature* **405**, 234–242 (2000).
34. P. M. Hammond, "Species inventory," in *Global Diversity Status of the Earth Living Resources*, B. Groombridge ed. (Chapman and Hall, 1992), pp. 17–39.
35. J. A. Thomas, M. G. Telfer, D. B. Roy, C. D. Preston, J. J. D. Greenwood, J. Asher, R. Fox, R. T. Clarke, and J. H. Lawton, "Comparative losses of British butterflies, birds, and plants and the global extinction crisis," *Science* **303**, 1879–1881 (2004).

# PAPER VI

## **Feasibility study: fluorescence lidar for remote bird classification**

M. Brydegaard, P. Lundin, Z.G. Guan, A. Runemark, S. Åkesson, S. Svanberg.

*Applied Optics* **46**, 4531 - 4544 (2010).



# Feasibility study: fluorescence lidar for remote bird classification

Mikkel Brydegaard,<sup>1,\*</sup> Patrik Lundin,<sup>1</sup> Zuguang Guan,<sup>1</sup> Anna Runemark,<sup>2</sup>  
Susanne Åkesson,<sup>2</sup> and Sune Svanberg<sup>1</sup>

<sup>1</sup>Atomic Physics Division, Lund University, P.O. Box 118, SE-221 00 Lund, Sweden

<sup>2</sup>Animal Ecology Division, Lund University, Sölvegatan 37, SE-223 62 Lund, Sweden

\*Corresponding author: mikkel.brydegaard@fysik.lth.se

Received 15 March 2010; revised 1 June 2010; accepted 25 June 2010;  
posted 16 July 2010 (Doc. ID 125454); published 13 August 2010

We present a method for remote classification of birds based on eye-safe fluorescence lidar techniques. Mechanisms of quenching are discussed. Plumage reflectance is related to plumage fluorescence. Laboratory measurements on reflectance and fluorescence are presented, as well as test-range measurements. Also we present examples of birds' in-flight lidar returns. The methods are suitable for studies of night migrating species and high-altitude classification with implications for the detailed understanding of bird migration and global virus spread. © 2010 Optical Society of America

OCIS codes: 010.3640, 300.2530, 280.1100.

## 1. Introduction

Birds, with their highly mobile lifestyle, have been able to successfully colonize new geographic areas and thereby have extended their breeding ranges to include most habitats of all continents [1]. At certain times of the year, millions of birds depart on migration flights across continents and seas. Many of these migration flights are performed at night, hidden from our eyes. Some birds have adapted to perform long migration flights across vast inhospitable areas, such as the Saharan desert and the Mediterranean Sea during their migrations between their summer breeding grounds in Northern Europe, and areas where they spend the winter in tropical Africa [2,3]. A large proportion of migratory songbirds fly at night and at high altitudes (>500 m) between these remote destinations [4,5]. By flying at night, the flight will potentially be less disturbed by turbulent wind conditions compared to daytime [6], and the birds will reduce the risk of being taken by predators [7]. Furthermore, by migrating at night, the birds can maximize the time spent on feeding during daytime [2,8].

## 2. Existing Methods

The intensity of migration, flight altitude, and directions of nocturnal bird migration flights have been studied by using a number of remote sensing methods, such as surveillance and tracking radars [9–14], ceilometers [15,16], infrared (IR) cameras [13,17], as well as lunar obscuration [18,19]. The surveillance and tracking radars and IR cameras enable the observer to get a relatively good estimate of the height distributions and numbers of birds passing overhead, while the ceilometer providing the same type of data is very limited in range (applicable altitude range is from a few meters to about 200 m) [15,16] and is not able to cover dominating flight altitudes under natural conditions. Moon watching (i.e., lunar obscuration) gives more crude estimates of directions and altitude ranges, but can be useful when there are limited possibilities to use major equipment (i.e., surveillance and tracking radar) because a pair of binoculars is all that is needed for observations, and large areas can be covered with many observation sites [20,21]. So far, it has not been possible to identify the species observed with the moon watching or the other methods. In some areas, migrating birds might even be confused with nocturnal insects and



mammalian migrants, such as bats, since some of the species explore the same time interval for migration.

All remote methods used so far to record nocturnal migration in free-flying birds have been limited by not being able to reveal what species have been observed. With a few exceptions, like the common swift (*Apus apus*), which has a very characteristic wing-beat pattern during flight and which can be identified by a tracking radar [22,23], most birds migrating at night and at high altitude will have to pass unidentified, as the flight speed and wing-beat frequency for birds of the same size range is similar, making only classifications of a few size groups possible by using tracking radar [24]. Another confounding factor is the altitude at which the birds migrate, which often exceeds 500 m during normal migration flights across the landscape [4,5,25]. For example, soaring birds normally occur up to a few thousand meters [26], making it difficult to visually identify the species, not only at night, but also during the day. To study the special adaptations for nocturnal as well as diurnal flight, the timing of migration for different age and sex classes of birds and the passage relative to topography, winds, and weather parameters, it would be of great interest to identify the individual birds down to the species, but also—when possible—to sex and age level. In this paper, we examine the possibility of using a fluorescence (light detection and ranging (lidar) system to identify the species of birds, on the basis of their size, plumage characteristics, and spectral features from their plumage.

### 3. Lidar Technique

Lidar techniques have been successively developed following the invention of the laser 50 years ago, but even a search-light-based variety was tested before that (for overviews of the field see, e.g., [27,28]). In a lidar system, an intense and short-duration laser pulse is transmitted into the atmosphere, and light, as scattered from objects or aerosol particles, returns to a receiving telescope placed adjacent to the transmitter. The optical return is converted to an electronic signal in a photomultiplier tube (PMT) and is recorded in a transient recorder/digital oscilloscope. Range resolution is obtained from the time-of-flight information (a fixed target 150 m in front of the system yields an echo after 1  $\mu$ s), and the best resolving ability is limited by the pulse duration (a 7 ns pulse yields an echo half-width of 1 m; nonoptimal electronics prolong the echo). Apart from ranging applications yielding target distance, elastic back-scattering from aerosols can yield information on their distribution and properties. Distributions of pollutant gases with sharp absorptive imprints can be obtained with the differential absorption lidar (DIAL) variety of the technique, where the laser source is intermittently tuned between an absorbed and a nonabsorbed wavelength. The laser light can also induce fluorescence, which is utilized in fluorescence lidars. In particular, this is being exploited in long-range systems, where meteorite-produced alkali atoms and

iron ions in the upper atmosphere are monitored. At closer range, broadband fluorescence in solid targets can be induced, as discussed in, e.g., [27]. Applications include characterization of oil spills at sea, algal blooms, vegetation, and building facades (cultural heritage). In the zoological realm, lidar techniques have also been employed for studies of fish (see [29] and references therein), honeybees [30,31], and damselflies [32,33]. The present project on bird fluorescence lidar emerged out of the damselfly studies performed in our group.

### 4. Motivation

There are a number of bird flight and migration phenomena that would be of great interest to study if it were possible to identify the species (and age and sex) of the birds migrating at night and at high altitude during the day. For instance, more general questions related to selection of time of migration and flight directions relative to winds and topography, as well as the altitude of migration, could be studied for migrants with different morphology and flight adaptations. Comparative studies of bird migration could be performed at different geographic areas and during different times of the year. It would also be possible to study the composition of bird migrants for a given area, how their migration flight behavior might differ between species, and how the bird movements might lead to the spread of bird-borne diseases, such as avian flu and avian malaria, tick-borne diseases, and seeds [1,34].

### 5. Bird-Light Interaction

In the ultraviolet, visible, and near-IR (UV-VIS-NIR), plumage reflectance arises from microstructures of the barbs and leaflike barbule sheets, which range in thickness down to a couple of micrometers, with the even smaller barbicel hooks attached [see common wood pigeon *Columba palumbus* feather in Fig. 1(a)]. The barbules are neatly arranged, overlapping, and generally there is no line of sight through a single feather. The many air-solid interfaces between feather structures in the hollow feathers and in vacuoles cause the incident light to be reflected and transmitted according to Snell's law and the Fresnel equations. On the macroscopic scale, the many dispersion events cause incident light to behave diffusively, as is known from the theories of multiple scattering, photomigration, and tissue optics [35,36], and it eventually leaves the plumage to reach the observer. After such migration, light loses information regarding polarization and coherence; for this reason, this contribution to the total reflectance is referred to as incoherent scattering.

Along the migrated path, the light can be absorbed by chromophores that are embedded in the  $\beta$ -keratin matrix [37,38], which is the main constituent in feather structures [39]. The refractive index in the visible range is typically 1.55 [40]. The absorption of both  $\beta$ -keratin and the mammalian-occurring  $\alpha$ -keratin increases slowly from 400 to 300 nm,

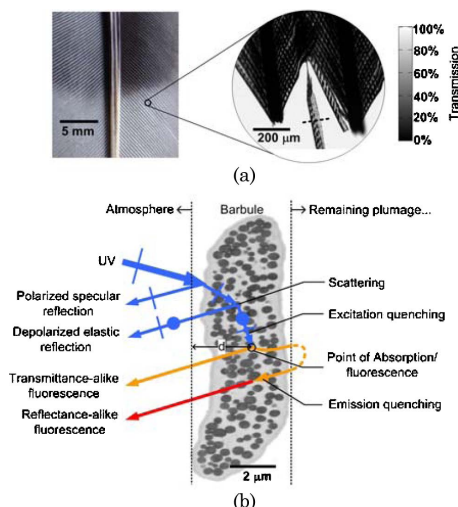


Fig. 1. (Color online) (a) Left, typical feather from pigeon; the melanin concentration is higher in the top part. Barbs are connected to the central trunk. Right, transmittance image at 590 nm; the barbules are attached to the two barbs and are neatly arranged, covering each other. A single barbule dangling from its barbicels transmits roughly half of the light. (b) When a UV laser pulse impinges on the plumage, a polarized specular angle-dependent elastic echo returns. After internal scattering events, polarization is lost and the echo is emitted omnidirectionally. Part of the excitation light will be quenched by the melanin granules with low fluorescent yield; remaining UV light is absorbed in the keratin matrix and produces broad emission. Emitted light will, in turn, be quenched by present chromophores on its way to the surface. The shorter the wavelength, the shorter the mean absorption depth,  $d$ , the less excitation quenching, and the more fluorescence resembles reflectance. See Eq. (1). Transmission electron image (TEM) (with permission from M. D. Shawkey [76]). The darker embedded spots arise from melanin granules.

increases dramatically below 300 nm, and peaks at 280 nm [41]. The most common chromophores are the black eumelanins and the reddish pheomelanin, which have dull spectral features with a monotonically increasing absorption toward lower wavelengths, and produce black, grayish, and brownish colors, whereas the second most common class of chromophores is carotenoids, which exhibit relatively sharp and characteristic spectral features and give rise to yellow, orange, and red colors ([37], Chaps. 5, 6). In certain taxa, chromophores such as pterins, porphyrins, and psittacofulvins can also be found ([37], Chap. 8). The number of chromophores used for bird–bird communication is not expected to be much higher than the number of spectral bands in the focal species [42]. The spectral features used in communication are also expected to appear in the full region covered by the available spectral bands of the focal species [42]. Birds have four spectral bands, ranging from approximately 350 to 700 nm [43]. This

range includes a UV band, which is not visible to the human eye, as well as light visible to humans; however, the remaining spectral bands are not positioned identically to those of humans. It is worthwhile to recall that the color space of birds is typically of higher dimensionality than ours, which complicates bird studies considerably [38].

In addition to the absorption taking place in the keratin matrix and the embedded chromophore granules, the reflectance of the feathers also depends on the presence of oils and waxes with a slightly lower refractive index. The large majority of birds secrete a preen oil, consisting mainly of diesters, from the uropygial gland [44]. Such grease films are typically less than 100 nm in thickness (thus thinner than the evanescence field), and transparent in the region of 350–700 nm. However, they do typically exhibit strong absorption below 320 nm [45].

Blue, UV reflecting, and iridescent plumages are typically based on constructive interference. Reflectance of such plumages will depend strongly on the angles of illumination and observation with respect to the surface orientation [46]. Structural color is typically produced by repetitive structures; that is, dominant spatial frequencies of changing refractive index along the optical axis in nanostructures in the feathers [37], Chap. 7, [47]. Such nanostructures can consist of ordered arrays of air-filled vacuoles or melanin granules. Structural effects alter the ratio between reflected and transmitted light from a single nanoarray. For effective structural colors, chromophores are required to prevent transmitted light from escaping the plumage after multiple scattering in the underlying plumage [Fig. 1(b), bobolink, *Dolichonyx oryzivorus*]. Because a structural color occurs because of interference, the effect cannot be described either by diffusion theory or by the Monte Carlo simulation commonly applied in tissue optics. For this reason, the structural contribution to the total reflectance is referred to as coherent scattering.

When considering laser-induced fluorescence (LIF) in birds for remote classification, the natural choice of excitation wavelength would be 266 nm, considering the bird eye-safety issue of using 355 nm excitation, as is common in remote LIF setups. Bird reflectance at 266 nm is not well studied because it is well below the UV sensitivity bands of any animal [48]. Preen oils and waxes and keratins increase heavily in absorption below 320 nm and produce a considerable broad bluish fluorescence, peaking around 400 (for botanical waxes) [49] and 380 nm ( $\alpha$ -keratin) [50]. In certain more rare taxa, including parrots, by using porphyrins as chromophores we can expect high fluorescence yield and relatively sharp and characteristic spectral features. Even if not directly pumped at 266 nm, the fluorescence emission from keratin might serve as an indirect pump for porphyrins. Fluorescence yields of melanins and carotenoids are low in comparison to those of greases and keratin. Embedded melanin granules are, however, expected to quench both excitation and

emission from keratin fluorescence. For this reason, we can expect to be able to classify birds by quantifying both eumelanin and pheomelanin content by spectrally analyzing the fluorescent emission from plumage, even if the fluorophores are identical for most feathers.

A typical effect in fluorescence spectroscopy is that the interrogation volume becomes more superficial the lower the excitation wavelength is [51]. The scattering coefficient is roughly  $600\text{ cm}^{-1}$  in solid keratin without granules or vacuoles, and the absorption cross section of solid keratin at 266 nm is roughly  $2400\text{ cm}^{-1}$  [41]. This implies that half of the light is deposited in the outermost  $2\text{ }\mu\text{m}$  in solid keratin, corresponding to the thickness of a single barbule. The preen wax coatings have absorption coefficients of the same order of magnitude but are typically not thicker than 100 nm. Melanins have a cross section that is roughly a factor of 10 higher than that of keratin at 266 nm [52] and reach volumetric fill factors of up to 50% [53]. Because of the high scattering coefficient and absorption cross section at 266 nm, we can expect most of the excitation energy in the outermost  $1\text{ }\mu\text{m}$  of the plumage. The resulting fluorescence light is created omnidirectionally in the interrogation volume. One part is quenched (reabsorbed) by the chromophores upon leaving the volume before reaching the surface, and the other part, propagating inward, is reflected in the plumage before reaching the observer [Fig. 1(b)]. For this reason, we can expect the fluorescence to be highly correlated with reflectance as long as the dominant fluorophores involved are the same from sample to sample and their emission covers the region where the chromophores absorb. We refer to this method as *on-target white-light generation*, which allows us to measure reflectance, including structural features [32], in the UV-VIS region with LIF lidar without risk of blinding the sample species.

Temporal delays in fluorescence from plumage might arise from the excited state lifetimes. The lifetime of keratin is 1.4 ns and of melanin is 2.2 ns [54]. Scattering lifetimes are expected to be at least 1 order of magnitude faster, where most visible photons have left the plumage after 100 ps, corresponding to a 3 cm path.

There is a great spatial variance in plumage colors in birds. The color can vary even within a single feather and barbule [37,38], and birds often differ in coloration between different body parts. Sexual dichromatism, where the sexes have different color patterns, is also common in birds [55]. Seasonal variation [56–58] and molt [59] are also known to affect plumage color, and some bird species also have a different nuptial plumage. In addition, color can be condition dependent, especially for carotenoid-based colors [60].

Museum specimens have been shown to accurately represent the coloration of wild birds [45], but some of the substances used for preservation can change

the reflectance spectra of the plumage, although the frequency of damaged skins is very low [61].

In the thermal-IR region between  $2.5$  and  $25\text{ }\mu\text{m}$ , plumage emissivity is approximately 80%, regardless of the chromophores. The plumage provides isolation and has been demonstrated to maintain large temperature gradients. Down is known to have exceptionally low transmittance in the mid- and thermal-IR region [62]. Down and feathers exhibit several strong features in the whole region and have a remarkable point close to  $5.8\text{ }\mu\text{m}$  where scattering disappears and the plumage becomes completely transparent due to Christiansen's effect [63,64]. While IR features do not reflect the chromophores, there seem to be several structural imprints in the mid-IR within the atmospheric windows on both sides of the  $\text{CO}_2$  band from  $3.5$  to  $5.5\text{ }\mu\text{m}$ . Such structural features might be species specific and feasible for passive remote classification (measurements not presented here). Further out in the radio frequency (RF) region, the reflectance or radar cross section (RCS) is governed by the entire naked body structure of the bird. As for optical structural colors, the RF reflectance is highly dependent on the illumination and observation angles and is often measured as a spherical function in relation to the bird pitch and roll orientation, which can be estimated from the flight trajectory. The spherical RCS function depends on the polarization with respect to the body orientation of the bird. The elastic return can be expected to be partly depolarized according to the linear depolarization ratio for the given wavelength in any of the regions: RF, IR, VIS, and UV. Spectral reflectance features in the RF appear when the wavelength matches the dominant features of the body from the angle of observation, with a maximum around 10 cm [65]. Finally, the phase in the wing-beat cycle will change the properties of fluorescence, emissivity, and reflectance in the UV, VIS, IR and RF.

## 6. Proposed Strategy

We propose the use of LIF lidar to acquire additional parameters for classification of nighttime migrating birds. We plan to use 266 nm, the fourth harmonic of a commercial pulsed Nd:YAG laser, as excitation because this wavelength is eye safe for birds [66]. The UV light will induce broadband whitish light in the plumage, which, in turn, will be partially reabsorbed (quenched) by the chromophores present and eventually be detected through a telescope. For the purpose of consistency of the geometry, vertical sounding should be performed to induce the fluorescence on the chest. For a field test, a main focus will be on migration points where the hit probability is high. Also, for upcoming field studies, the methods are planned to be integrated with IR and RF instrumentation, which provides additional information regarding trajectories and wing beats.

## 7. Methods and Setup






























We will now describe the materials, techniques, and equipment used in our measurements. Twenty-four bird samples were borrowed from the Lund Zoological Museum. The samples were selected in terms of being representative species, genders, and ages that could potentially be sighted during summertime in Sweden. Several of the same or similar species with several genders without sexual dimorphism yielded similar results and are not included in this paper. The more interesting samples presented throughout this paper are presented in Table 1. Most samples are less than 100 years old, are well conserved in plastic envelopes in catalog loggers, and have not been exhibited.

### A. Point Measurements

Samples were air dusted and measured with a point fiber probe operating in reflectance and fluorescence modes [Fig. 2(a)]. The museum skins can be assumed to accurately reproduce the reflectance of living samples. Considering that no new fluorophores have been observed [46,61] and considering the principle

of conservation of energy, we can derive that, if reflectance remains the same in the range of keratin excitation and emission, then the fluorescence signature cannot change significantly. The plumage is illuminated angled at  $30^\circ$  to the surface normal in order to reject the specular reflection. Although this geometry slightly diminishes structural imprints, the effect could still be observed. In the spectroscopic measurements, we used light-emitting diode (LED) illumination switched among a 255 nm AlGaIn/GaN LED (255UVTOP); 355, 375, and 395 nm AlGaIn LEDs (NS355L-5RLO, NS375L-ERLM, RLU395-8-30); and a 450–700 nm InGaIn + Ce:YAG LED (5W4HCA-H30, Roithner-Lasertechnik). The current was kept constant by a LM317 regulator and the internal temperature was estimated from the current–voltage characteristics to compensate for the temperature-conversion-efficiency dependence. The sample geometry is identical between the reflectance and the 355 nm excited fluorescence measurements. Light is collected in a  $600\text{ }\mu\text{m}$  UV fiber and fed to a compact spectrometer (Ocean Optics, USB4000). The reflectance and the fluorescence at 355 nm excitation

Table 1. Latin Names, Popular Names, Apparent Color and Sex of All Samples Presented in Figures Throughout This Paper<sup>a</sup>

| Latin Species Name                | Trivial Name       | Color/Body Part   | Sex               | Comments             | Figure    | Symbol  |
|-----------------------------------|--------------------|-------------------|-------------------|----------------------|-----------|---|
| <i>Acrocephalus arundinaceus</i>  | Great reed warbler | Brown/back        | Adult             |                      | 3 and 4   |    |
|                                   |                    | Beige/side        | Adult             |                      | 12        |    |
| <i>Acrocephalus s. scirpaceus</i> | Reed warbler       | Light brown/chest | Female            | Adult                | 3–6       |    |
|                                   |                    | Brown/back        | Female            | Adult                | 5 and 6   |    |
|                                   |                    | Brown/side        | Female            | Adult                | 11        |    |
| <i>Columba palumbus</i>           | Common wood pigeon | Gray/feather      | Adult             |                      | 1         |    |
| <i>Corvus monedula</i>            | Jackdaw            | Dark gray/front   | Female            | Adult                | 11        |    |
| <i>Corvus f. frugilegus</i>       | Rook               | Black/chest       | Female            | Adult                | 3 and 4   |    |
|                                   |                    | Black/side        | Female            | Adult                | 12        |   |
| <i>Dolichonyx oryzivorus</i>      | Bobolink           | Black/feather     | Adapted           |                      | 1         |  |
|                                   |                    | barbule           | from [76]         |                      |           |   |
| <i>Erithacus r. rubicula</i>      | European robin     | Red/chest         | Male              | Adult                | 3–6       |  |
|                                   |                    | Front             | Male              | Adult                | 11        |  |
| <i>Larus michahellis</i>          | Yellow-legged gull | Entire bird       | Adult             |                      | 2         |  |
| <i>Motacilla a. alba</i>          | White wagtail      | Light gray/chest  | Male              | Adult                | 3 and 4   |  |
|                                   |                    | Gray/back         | Male              | Adult                | 5 and 6   |  |
|                                   |                    | White/forehead    | Male              | Adult                | 5 and 6   |  |
|                                   |                    | Gray/groin        | Male              | Adult                | 5 and 6   |  |
|                                   |                    | Black/chest part  | Male              | Adult                | 5 and 6   |  |
| <i>Parus caeruleus</i>            | Blue tit           | Yellow/chest      | Male              | Adult                | 3–7       |  |
|                                   |                    | Blue/head         | Male              | Adult                | 3 and 4   |  |
|                                   |                    | Blue/tail         | Male              | Adult                | 5 and 6   |  |
|                                   |                    | Blue/side         | Male              | Adult                | 11        |  |
| <i>Sturnus v. vulgaris</i>        | European starling  | Black-irid./chest | Male              | Adult                | 5 and 6   |  |
|                                   |                    | Many birds/side   | M/F               | Juveniles, in flight | 8         |  |
|                                   |                    | Black-irid./side  | Male              | Adult                | 10        |  |
|                                   |                    | Black-irid./side  | After autumn molt |                      | 11 and 12 |  |
| <i>Saxicola rubetra</i>           | Whinchat           | Orange/chest      | Male              | Adult                | 3 and 4   |  |
| <i>Sylvia atricapilla</i>         | European blackcap  | White/chest       | Male              | Adult                | 3 and 4   |  |
|                                   |                    | Gray/side         | Male              | Adult                | 12        |  |

<sup>a</sup>Samples giving rise to similar reading have been omitted for the convenience of the reader. Museum samples were selected to be representative of their kind. The choice of species was based on the expectation for sightings in the season and habitat where the lidar was stationed.

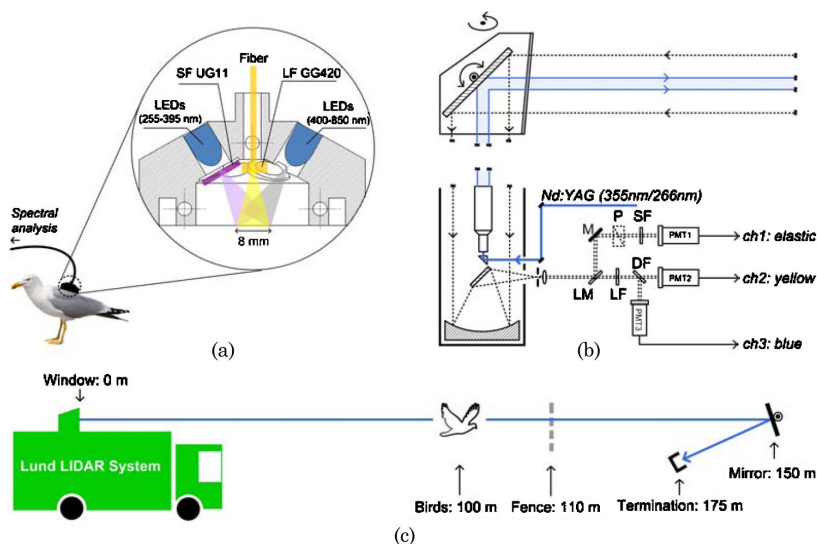


Fig. 2. (Color online) (a) Ground truth measurements were performed with a compact combined reflectance and fluorescence sensor. Various excitation wavelengths for fluorescence, as well as broadband light for elastic measurement, is provided by a selection of LEDs. (b) The Lund mobile lidar system was emitting at 266 and 355 nm in this study. A two degrees of freedom scanning mirror allows the beam direction to be controlled. The returning light is collected by a 40 cm telescope. The return can be discretized according to polarization and wavelength with a number of PMTs. (c) In-flight European starlings were recorded at an 85 m distance during another experiment on damselfly dispersal [33].

are filtered with a 5 mm thick long-pass filter (GG420, Schott), which suppresses the excitation. The excitation spectrum at 355 nm is cleaned up with a 1 mm excitation filter (UG11, Schott). The reflectance is calculated using a flat 50% gray reference (Oriol) and the fluorescence at 355 nm excitation is white-light calibrated against a blackbody reference (Oriol). The fluorescence induced by 255 nm radiation is observed directly without any spectral filters; it is not white-light calibrated, but spectra can be compared relatively.

Fluorescence lifetimes were measured on a number of samples, including eumelanized, pheomelanized, carotenoid, and structural colored plumage. The instrument is a multi-excitation, multi-emission, single-photon counting system developed by the Photonics Group, Department of Physics, at Imperial College London [67]. The plumage was excited by mode-locked lasers at 355 and 435 nm with a repetition rate of 37 MHz. The resulting fluorescence is detected in 16 bands in the range of approximately 385–600 nm. Time-resolved fluorescence instruments are typically developed to measure characteristics that are independent of reabsorption, which otherwise influences the fluorescence spectra.

Initial total transmittance measurements in the range of 2–25  $\mu\text{m}$  have been conducted with a Fourier transform spectrometer (ATI Mattson, Infinity series

FTIR). The results will not be discussed further in this paper.

#### B. Lidar Measurement

The lidar facility for the experiments is based on the Lund mobile lidar system [68]. The main equipment is presented in Fig. 2(b). The third (355 nm) and fourth (266 nm) harmonics of a Nd:YAG laser radiation with energy of around 40 and 6 mJ/pulse, respectively, and with pulse width around 15 and 4 ns, respectively, were used for excitation. After expanding into a beam diameter of about 5 cm, the laser beam is transmitted by a horizontally and vertically scanning mirror with a size of  $\sim 40 \text{ cm} \times 56 \text{ cm}$  and mounted in a rooftop dome. A quartz window is used to protect the dome from dirt and dust in the atmosphere. The elastic scattering and the fluorescence from the targets are reflected by the same mirror and collected by a telescope system with a diameter of 40 cm. The collected light is distributed by a number of mirrors and filters to three PMTs for analysis. As shown in Fig. 2(b), the elastic scattering from the target is filtered out by a laser line mirror (LM) and recorded by PMT 1 in the time domain. A polarizer (P) is set at a crossed angle against the polarization state of the transmitted laser and, therefore, PMT 1 is only sensitive to depolarized backscattering. An additional short-pass filter (SF) is used to further suppress the fluorescence light



Table 2. Optical Component List for the Three-PMT System

| Components             | Excitation         |                    |
|------------------------|--------------------|--------------------|
|                        | 355 nm             | 266 nm             |
| Laser line mirror (LM) | 45° 355 nm         | 45° 266 nm         |
| Polarizer (P)          | Film polarizer     | none               |
| Short-pass filter (SF) | UG11—1 mm          | UG11—1 mm          |
| Long-pass filter (LF)  | GG400—5 mm         | WG305—3 mm         |
| Dichroic filter (DF)   | Edmund Blue/Yellow | Edmund Blue/Yellow |

from the target and background light from the sky. On the other hand, the fluorescence light transparent through the LM is divided by a dichroic filter (DF) into two wavelength bands (blue and yellow) and measured by PMT 2 and PMT 3, respectively. Before the DF, a long-pass filter (LF) is used to suppress the leakage of the elastic scattering through the LM. The list of the optical components mentioned above is shown in Table 2 for different excitation wavelengths. The three channels of signals from the PMTs are simultaneously recorded by a high-speed oscilloscope (Tektronix TDS544B), which samples every 8 ns. The recorded data are read out through a GPIB connection by a computer in real time. However, the repetition rate of the whole system is limited to 10 Hz by the communication speed, although the laser system is running at 20 Hz. By using such a three-PMT system, both the elastic scattering and the two bands of fluorescence signals can be analyzed in the time/spatial domain.

The field experiments were originally arranged for studying the migration of damselflies. Details will be found in a forthcoming publication [33]. As shown in Fig. 2(c), geometrically there is a metal fence at ~110 m away from the lidar bus, and a mirror at ~150 m is used to fold the laser beam for possible measurements at a longer distance over the surface of a river. Finally, a termination is set at ~175 m distance. During the damselfly measurements, by accident a group of starlings flew into the laser beam at a distance of ~100 m and were recorded by our system. This observation stimulated us to obtain the 24 bird samples from the Lund University Zoological Museum to measure them at the same place in the field (where the natural birds were encountered). It is worthwhile to mention that the weather conditions were sunny during the measurements. The illumination from sunlight can be easily quantified by analyzing the background intensities at the two fluorescence channels.

## 8. Analysis

### A. Point Measurements

Reflectance spectra of nine particularly characteristic samples of special interest are presented on a logarithmic scale in Fig. 3. White, gray, and black varieties resulting from different eumelanin contents are observed with flat reflectance curves at different levels. Brownish, orange, and reddish pheomelanin-containing feathers bend and attenu-

ate reflectance toward the blue, as, for example, the orange chest of a whinchat (*Saxicola rubetra*). A yellow feather from a blue tit (*Parus caeruleus*) shows the characteristic double absorption dip of a carotenoid, while tail feathers with structurally generated blue shades from the same bird show a monotonic increase in reflectance toward the blue. In the 355 nm excited fluorescence in Fig. 4, white, gray, and black feathers maintain the same shape, but are scaled differently. For the brown, orange, and reddish pheomelanin feathers, the slope toward the red is different, indicating that the plumage is indeed redder even in fluorescence. In the case of the yellow carotenoid (lutein) feather, again, the double absorption dip can be observed, but this time in fluorescence quenching. The blue feather is harder to interpret in this measurement. The low values might indicate that even excitation light at 355 nm is reflected rather than absorbed and consequently reemitted as fluorescence.

The fluorescence measurements with 255 nm excitation were performed in a similar geometry as the previous measurements. These measurements are

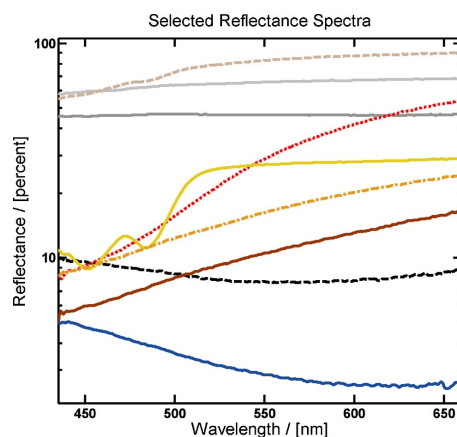


Fig. 3. (Color online) Reflectance spectra, curves colored according to appearance to humans. From top: light brown, reed warbler; white, white wagtail head; light gray, white wagtail chest; red, European robin; yellow, blue tit (note the sharp feature of the carotenoid lutein); orange, whinchat; brown, reed warbler; black, rook; and structural blue, blue tit.

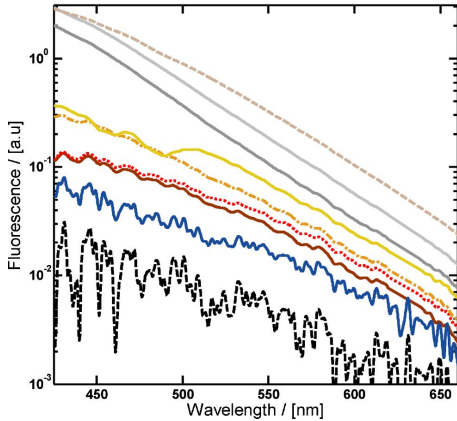


Fig. 4. (Color online) Fluorescence spectra excited at 355 nm, curves colored according to appearance to humans. From top: light brown, reed warbler; white, white wagtail head; light gray, white wagtail chest; yellow, blue tit; orange, whinchat; red, European robin; brown, great reed warbler; structural blue, blue tit; and black, rook.

presented on a logarithmic scale in Fig. 5. The curves are not white-light calibrated but can be compared in between. All the spectra have been normalized on the elastic light around 255 nm, even if we can expect the absolute reflectance to vary at 255 nm due to melanin variations. As in the previous measurement, white, gray, and black eumelanized plumages maintain the same shapes but they are scaled differently. Brown and reddish pheomelanized plumages are shifted to-

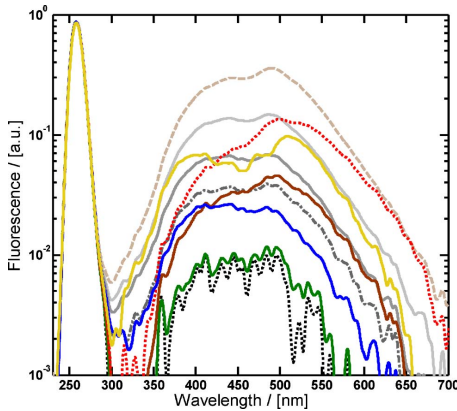


Fig. 5. (Color online) Fluorescence spectra excited at 255 nm, selected examples; curves colored according to appearance to humans. From top: light brown, reed warbler; white, white wagtail head; red, European robin; yellow, blue tit; light gray, white wagtail chest; brown, reed warbler; gray, white wagtail; structural blue, blue tit; black iridescent, European starling; and black, rook.

ward the red. The blue plumage is shifted toward the blue; thus, we conclude that even structural colors are positively correlated with the fluorescence, from which we understand that the interrogation volume of the fluorescence measurement is more superficial than the nanostructures causing the blue reflectance. The double absorption peak of the carotenoid is observed in the yellow feathers from the blue tit.

Even if we can expect somewhat lower sensitivity on the spectrometer at 255 nm, we notice that the fluorescence is considerable in comparison to the elastic light for the bright feathers. This is a major problem and might to some extent invalidate all elastic reflectance work performed with deuterium lamps in the avian and reptilian community, because using a broadband light source sums along the columns of the emission excitation matrix (EEM) (Fig. 6); thus, such reflectance measurements require the sample to have negligible fluorescence, which obviously might not always be the case.

The 14 spectra, out of which the more interesting ones were presented in Fig. 5, including varieties of eumelanized and pheomelanized plumages, a carotenoid, and a structural blue plumage, were analyzed using singular value decomposition (SVD) [69,70]. From the eigenvalues, we could read that 81% of the variance could be explained by the first principal component, 91% including the second, and 96% including the third one. The first component represents

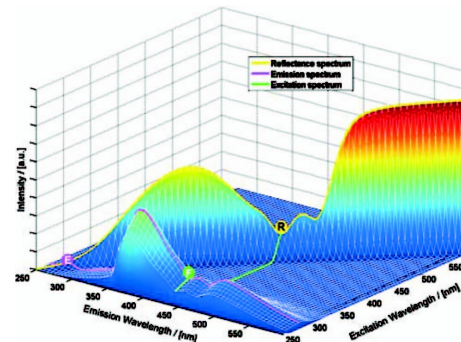


Fig. 6. Correlations in the EEM for a yellow-chested blue tit, with fluorescence exaggerated for demonstration purposes. The elastic diagonal (yellow curve, R) shows the reflectance of solid keratin with a carotenoid absorption dip. The fluorescence emission spectrum at 266 nm excitation (purple curve, E) shows the imprint of the absorbing carotenoid. Traditional methods for reflectance in ornithology sum all excitation elements (green curve, F) and assume fluorescence to be negligible. In ornithological LIF lidar, we can expect a fluorescence element  $F(\lambda_{ex}, \lambda_{em})$  to be negatively correlated with the reflectance  $E(\lambda_{ex})$ ; this explains why the structural blue plumage with high UV reflectance appears dark in fluorescence in Figs. 4 and 5. This is known as excitation quenching. In contrast,  $F(\lambda_{ex}, \lambda_{em})$  can be expected to be positively correlated with the reflectance  $R(\lambda_{em})$  due to emission quenching; this explains why red reflecting plumage appear even redder in fluorescence. Data extracted and remodeled from [37], Chap. 5, pp. 40, 49.

total keratin fluorescence and describes eumelanized plumages; the second component represents a redshift of the fluorescence and manages to describe pheomelanized plumages and also the blue structural color with negative loadings. This can be understood when comparing the dark brown and blue reflectance spectra in Fig. 3. The relatively sharp features caused by the carotenoid can only be accounted for when including a third principal component. Estimating the number of independent spectral components and localizing them in the spectral domain is crucial for designing spectral bands of a system for remote discrimination. According to this analysis, the optimal band choice for discriminating eumelanized, pheomelanized, and blue structural plumages is B1, 370–485, and B2, 485–600 nm. Including the carotenoid, the band choices should rather be B1, 370–420; B2, 420–500; and B3, 500–600 nm. In addition, a polarized or depolarized elastic band at 266 nm, B0, for estimating the beam–bird overlap on lidar hits is valuable; in this case, the different atmospheric attenuation of the returning elastic light should be considered, and the elastic returned energy would correlate with the amount of total energy deposited in the plumage. By dividing the returned energies in the remaining bands with this estimate, the scenario-dependent variance could be reduced. Because the specular reflectance might be highly dependent on the surface orientation, using depolarized elastic scattering could further contribute to confinement in the color space.

When normalizing with the elastic band and projecting the spectra on total fluorescence (first principal component from the SVD analysis) and redshift base spectra (second principal component from the above SVD analysis), the two-dimensional (2D) scatterplot presented in Fig. 7 is obtained. Plumage with different reflective characteristics can easily be separated, even in fluorescence. Clusters from plumage with similar reflective characteristics are more likely

to overlap in the scatterplot. The overlap in these scatterplots will eventually determine the success of remote classification. Obviously, overlaps are less likely in color spaces of higher dimensionality, but such scatterplots tend to be difficult to present on flat paper. Also, no improvement in discrimination can be expected by adding more spectral bands than the number of significant chromophores with independent spectral components involved. In Fig. 7, we notice the great spatial variance of measurements from different regions on the same sample, in a complete hit lidar situation, the acquired fluorescent signature is spatially averaged over the entire body; thus a gray bird might give identical echo as a black- and white-spotted bird; see for, example the different body parts of the white wagtail (*Motacilla alba*).

From the time-resolved data not presented in this paper, we could indeed conclude that the lifetime decays hold no information regarding the embedded chromophores, confirming our understanding of the quenching processes. Two spectral components were found in the decay; the lifetime at 390 nm was approximately 1.0 ns, whereas the lifetime was 1.6 ns at 580 nm.

To conclude this section, we propose the relation between plumage reflectance and fluorescence:

$$\frac{R_{\text{sample}}(\lambda)}{R_{\text{white}}(\lambda)} = (1 - \text{exq}(\lambda_{\text{ex}})) \frac{F_{\text{sample}}(\lambda_{\text{em}})}{F_{\text{white}}(\lambda_{\text{em}})}, \quad (1)$$

where  $R_{\text{sample}}(\lambda)$  is the diffuse reflectance,  $R_{\text{white}}(\lambda)$  is the diffuse reflectance of white plumage,  $F_{\text{sample}}(\lambda_{\text{em}})$  is the fluorescence spectrum,  $F_{\text{white}}(\lambda_{\text{em}})$  is the fluorescence of white plumage, and  $\text{exq}(\lambda_{\text{ex}})$  is the probability of embedded chromophores quenching the excitation.

Empiric results not presented in this paper show that  $\text{exq}$  is of the order of 20% at 355 nm excitation and that  $\text{exq}$  diminishes as the excitation wavelength decreases; thus, the lower the excitation wavelength, the more superficial the absorption field [shorter  $d$  in Fig. 1(b)] and the more resemblance to reflectance. A number of refinements can be done to the model—these include a bias taking into account the missing first specular reflection in the fluorescence ratio since the light is internally generated; however, this effect is compromised by the fact that the fluorescence is created omnidirectionally, whereas the superficial light in the elastic measurement would still remember its initial propagation in the very superficial layers. It is reasonable to presume dull dependency of the refractive index and dull exponential spectral effect due to differences in migrated path lengths; however, most such refinements of the models and estimation of additional parameters are numerically ill-conditioned with the dull features of the melanins.

#### B. Remote Lidar Measurements

To explore the feasibility of using lidar to locate and distinguish between bird species, measurements

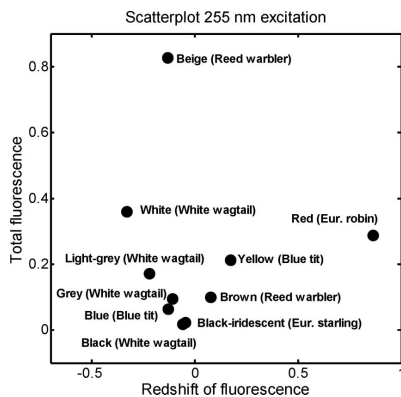


Fig. 7. Scatterplot of first and second principal components from Fig. 5.



were done in the field, both on birds in flight and on museum specimens. The investigations were done with 266 and 355 nm excitation.

Figure 8 shows an example of a lidar return signal from a starling in flight obtained at a distance of  $\sim 100$  m. The signal is time/distance resolved in one elastic, E, reflectance channel at 355 nm, one fluorescence channel ranging from 400 to 500 nm, denoted blue fluorescence, B in figures, and one channel ranging from 500 to 750 nm and denoted yellow fluorescence, Y in figures. Further, a linear polarizer on the elastic channel allows either polarized or depolarized light to be detected. The reflection from the weather protecting quartz window in the dome [see Fig. 2(b)] is clearly seen in the elastic channel, while almost no fluorescence is observed. This observation shows that the leakage/filter fluorescence between the elastic and the fluorescence channels is small and any signal in the latter channels will indeed be fluorescence. At a distance of  $\sim 100$  m, all three channels show strong signals from a bird, demonstrating a broad fluorescence emission in both the blue and the yellow wavelength range. Direct intermediate comparison between the signals in the different channels is, however, not meaningful because of arbitrary gain settings. Shortly after 110 m, the reflection from a nonfluorescent metal fence wire is seen. Again, only the elastic channel is giving an output.

The possibility of distinguishing between different species with lidar was further investigated by recording the return signal in a similar way as for the starlings *in vivo*, but for the same museum birds that were investigated with laboratory point measurements. The birds were each put in and out of the lidar beam pathway in a fluctuating manner to simulate birds passing through the field of view of our system.

Since the lidar return is discretized in three spectral bands, we are able to overview the entire data set with a red-green-blue (RGB) representation. Figure 9 shows a RGB color image of all data acquired in a small time period, during which a museum bird was moved in and out of the beam several times. Elastic

signals at 355 nm are shown in blue, fluorescence between 400 and 500 nm in green, and fluorescence between 500 and 750 nm in red. The first blue line is the stationary elastic signal from the quartz window. As the bird is moved into the beam, all channels show increased return signals at the corresponding distance marked in the figure. Consequently, both the elastic signal from the folding mirror and the return signals from all channels at the position of the termination go down, since the incident energy was reduced from the earlier impact. These observations are presented more quantitatively in Fig. 10, where the echo energy (fast-time integral of intensity return), being a measure on the total recorded signal from the bird, the termination point, and the background light level (refer to regions in Fig. 9) for each laser pulse, is exposed as a function of time.

It is essential to have a measure of how much light was illuminating the bird, i.e., the bird-beam overlap, to be able to quantize the fluorescence strength, not least when considering species classification. The bird-beam overlap has to be found for each laser pulse producing the fluorescent return. One approach is to normalize the fluorescence with the elastic signal, as in Fig. 5; however, the elastic reflectance, including the specular reflectance, might be highly dependent on the surface orientation of the plumage. Another approach to estimate the bird-beam overlap is to estimate the energy drop from later returns. In Figs. 9 and 10 middle, we observe how the obstruction of the bird is decreasing the signal from any light that is reflected or generated behind the bird. The amount to which these signals are affected is a measure of the overlap between the beam and the bird. The termination point in the case of vertical measurements could, for example, be a cloud base. Another similar possibility is to observe the decrease of the total backscattered atmospheric signal from air and aerosols behind the bird. Both these are examples of active techniques to quantify the

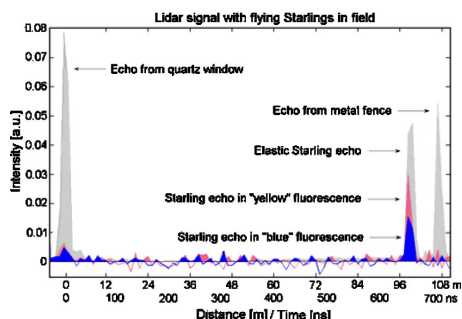


Fig. 8. (Color online) Single-shot echo from starling in flight. Elastic echoes arise from quartz window and metal fence. The relative areas under the European starling echo can be used for classification purpose.

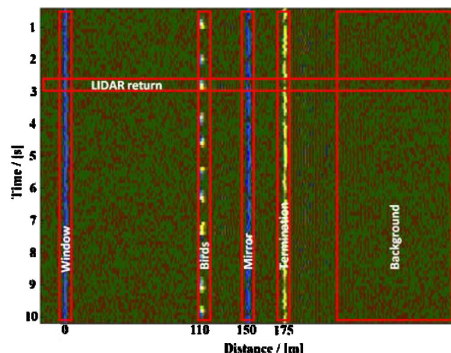


Fig. 9. (Color online) False color RGB representation or T-scan of complete lidar data acquired during 10 s. Blue, elastic; green, blue fluorescence; red, yellow fluorescence. Regions of interest are marked.

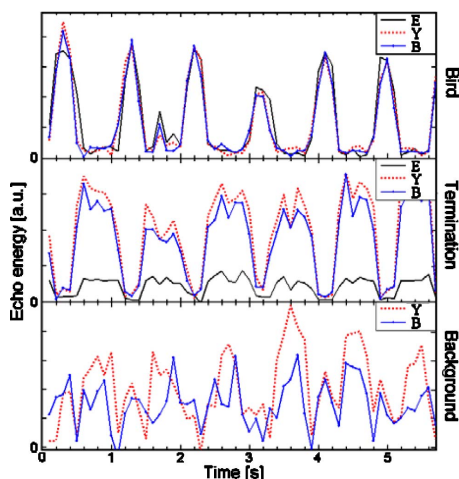


Fig. 10. (Color online) Intensity of the three cross sections marked in Fig. 9 plotted versus time. Notice the interplay, which allows estimating bird-beam overlap and also simultaneous determination of active fluorescence and passive reflectance.

bird-beam overlap. We also observe that the background light level after pulse termination is affected by the presence of a bird in the field of view; this can be explained by the amount of sunlight reflected in the plumage and into the telescope during the 1 ms the recording is done. This suggests that, not only do we acquire blue and yellow laser-induced fluorescence, but even blue and yellow passive reflectance simultaneously. In the case of the black European starling in Fig. 10, we observe an anticorrelation, meaning that the starling plumage is darker than our termination point. This could even be accomplished in vertical soundings with a cloud layer termination or the blue sky.

In earlier studies [33], as well as in this study, we have noticed one particular characteristic of zoological lidar; while clouds and dust plumes appear as distributed backscatters with a relatively slow time dependency matching the wind speeds, insects and birds in nature appear as sudden blips, giving rise to a much larger echo confined in spatial range as well as in temporal occurrence. The range confinement matches the lifetime of the matrix, typically around 1 ns if resolved by the system. The temporal confinement matches the overlap of the flight trajectory and the point spread function of the system. With our system we typically observed temporal occurrence in the order of a fifth of a second. This very unique feature simplifies separating the species echo from a quasi static background such as moving clouds.

The normalized fluorescence from the *in vivo* starlings and the museum samples were analyzed to explore the feasibility of remote species classification. The echo energy for the time/range resolved

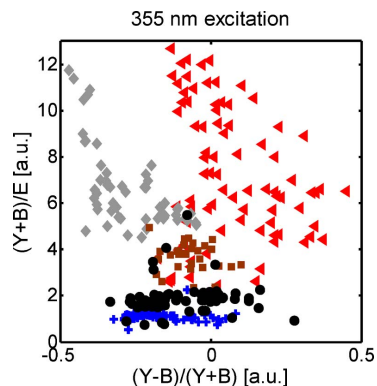


Fig. 11. (Color online) Scatterplot showing selected species with 355 nm excitation; total normalized fluorescence on the Y axis and redshift on the X axis. Dots are colored according to the human visual perception. From upper left: brown, reed warbler; red, European robin; black, European starling; black, rook; and blue, blue tit.

return signals were analyzed and intercompared. Figures 11 and 12 show the results of two such comparisons. Figure 11 is a 2D scatterplot obtained from measurements done in the field with 355 nm illumination. Each point in the plot corresponds to the reflection and fluorescence from a single laser pulse. As in Fig. 7, the vertical axis shows total fluorescence, while the horizontal axis represents the redshift. The five birds represented in the figure are a European robin (*Erithacus rubecula*), a blue tit, a reed warbler (*Acrocephalus scirpaceus*), a European starling (*Sturnus vulgaris*), and a jackdaw (*Corvus monedula*).

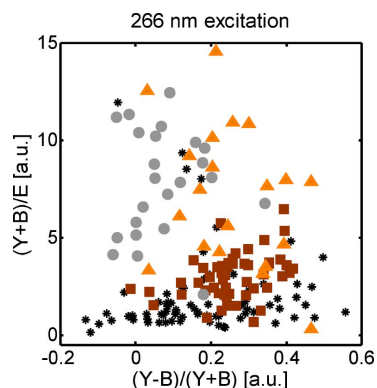


Fig. 12. (Color online) Scatterplot showing selected species with 266 nm excitation; total fluorescence on the Y axis and redshift on the X axis. Dots are colored according to the human visual perception. From upper left: gray, European blackcap; beige, reed warbler; black, European starling; and black, rook.

The scatterplot in Fig. 11 shows promising results, indicating that it, in fact, is possible to separate different species of birds with the help of a multichannel fluorescence lidar. The five different species of birds tend to gather at different positions in the plot, illustrating the variation in fluorescence between them. The European robin, which has a clear red belly, tends to go to the right side of the plot and also shows a relatively strong fluorescence compared to the other birds. Another species that fluoresces much is the reed warbler, which, on the other hand, has a hue more shifted toward the blue. In the center of the plot, the points from the somewhat darker starling gather with less strong fluorescence. The fluorescence color is as expected between the red robin and the more grayish great reed warbler. The jackdaw also shows a low fluorescence, which goes well with the fact that it is dark gray and black, it can also be observed that the blue tit shows a very low ratio between fluorescence and elastic reflection. The reason for this, as is revealed by the point fluorescence measurements in Fig. 4, is that the fluorescence is indeed very low for the bird at this wavelength. Because the reflectance for the blue feathers is high, the denominator in the y axis becomes large, while, at the same time, there is little light left to generate fluorescence.

Figure 12 is a similar scatterplot obtained from rooftop measurements at the test range in Lund [33] with 266 nm excitation. The four birds presented are a great reed warbler (*Acrocephalus arundinaceus*), a European black cap (*Sylvia atricapilla*), a European starling, and a rook (*Corvus frugilegus*).

The measurements done with 266 nm excitation were performed with a much lower output power from the laser than the ones with 355 nm excitation. This fact and other ones made the signals weaker, and the resulting scatterplot is not as clear as the one for 355 nm excitation. Still, some separation can be distinguished in the backscattering and fluorescence. As an example, the black rook shows low fluorescence, the relatively dark starling somewhat more, while the generally brighter European black cap and great reed warbler fluoresce more. One might discern that the European black cap is more shifted to the blue than the great reed warbler.

## 9. Discussion, Conclusions, and Perspectives

We have demonstrated eye-safe remote measurements of chromophore concentration and structural colors in plumages on distances of 100 m. From earlier experiences with elastic DIAL lidar on atomic mercury, at 254 nm, and the equally well-suited wavelengths of 308 and 313 nm for ozone monitoring [71,72], we know that returns from a solid target could be acquired from a single shot in a couple of kilometers. For several shots averaged, even the upper biosphere at 10 km is accessible [73]. In fluorescence lidar, which is an inelastic spectroscopic method, the UV light is only attenuated by the atmosphere one way, in contrast to elastic methods. We have explained the mechanisms relating the reflectance to the fluorescence of plumages.

We cannot expect to classify species with the same or similar plumage reflectance, nor would we be able to classify birds with the same or similar spatial average reflectance, e.g., a gray pigeon and a black-and-white wag-tail, in a single shot. At the 266 nm experiments, our laser system was not running optimally and our output power was further limited by the damage threshold of the general purpose scanning mirror, which does not reflect optimally at 266 nm. In vertical sounding, we would avoid this issue and the cross section of an in-flight bird in vertical sounding would obviously be larger. The other main limitation of our method is that plenty of continuous background light is binned by the broad fluorescence channels. For this reason, we can expect the method to perform much better at night. We have demonstrated that a refined analysis of the background signal carries information on the passive Sun-induced reflectance or transmittance (depending on the geometry). For this reason, it might be of interest to track the Moon with the lidar during the night, compromising background levels for simultaneous passive transmission spectroscopy.

In terms of improved bird classification, not much information would be gained by more than four spectral bands. However, we suspect that large improvements could be achieved by fusing fluorescence lidar with radar or thermal-imaging methods. While excellent in acquiring chemical information, the big disadvantage of this type of stochastic lidar, in comparison to, e.g., DIAL lidar, is the fact that we do not get a measurement for certain in each shot. Thermal-IR imaging seems incapable of acquiring properties of the chromophores; on the other hand, it can easily acquire an entire night sky in real time. If a dedicated system was to be developed, the thermal image could be used for lidar tracking, providing complete sky coverage and several shots for each migrating bird. Of special interest is the fact that indexing the fluorescence return in the phase of the wing-beat cycle should provide clues on the spatial variation on the bird. Such a system would probably take a couple of years to develop, even if an existing commercial lidar solution could be suitable [74,75]. Eventually, ornithological preknowledge of the limited number of expected migrant species would help in the classification process.

From an ornithological point of view, several experiments of interest could be performed. These would include nighttime classification, and high-altitude classification at migration points for purposes of counting and migration statistics. Typical migration points in Scandinavia would be geographic northward-pointing tips in the spring, such as Skagen, Kullaberg, and Andøya, and southward pointing confinements in the autumn, e.g., Falsterbo and Ottenby at the southern point of the island of Öland in the Baltic Sea. At locations of capture sites at bird observatories, such as Anacapri, Italy, comparisons can be made to the species of migrants

captured during different parts of the migration seasons. Observations could be related to morphological traits and weather conditions for more profound physiological studies. Other experiments could consist of marking without recapturing studies. This would be achieved by attaching fluorescing material, e.g., nylon strings or rings to the captured species. The string could be fluorescence encoded with effective fluorophore mixtures that clearly separate in clusters in the color spaces. The markings could consist of gender, age, or breeding habitat, which would be registered at the position of the lidar. We see several new applications of lidar to nocturnal bird migration studies and observations of free-flying birds, and we intend to perform further tests in real field situations in the near future.

We acknowledge the Knut and Alice Wallenberg Foundation for their support throughout the development of lidar techniques in Lund. *Ex vivo* specimens were borrowed with the kind collaboration by the Zoological Museum, Lund. We thank the Chris Dunsby group, Photonics, at the Department of Physics, Imperial College London, for time-resolved fluorescence measurements. Thanks to Matthew D. Shawkey for kind permission to reproduce a TEM micrograph in Fig. 1(b). We acknowledge Kullabergsfonden for future support of field campaigns. This is a report from Lund Laser Centre (LLC) and the Centre for Animal Movement Research (CANMove) supported by Linnaeus grants from the Swedish Research Council and Lund University.

## References

1. I. Newton, *The Migration Ecology of Birds* (Academic, 2008).
2. T. Alerstam and Å. Lindström, "Optimal bird migration: the relative importance of time, energy and safety," in *Bird Migration: Physiology and Ecophysiology*, E. Gwinner, ed. (Springer-Verlag, 1990), pp. 331–351.
3. T. Alerstam, A. Hedenström, and S. Åkesson, "Long-distance migration: evolution and determinants," *Oikos* **103**, 247–260 (2003).
4. B. Bruderer and F. Liechti, "Höhe und Richtung von Tag- und Nachtzug im Herbst über Südwestdeutschland," *Ornitol. Beob.* **95**, 113–128 (1998).
5. S. Zehnder, S. Åkesson, F. Liechti, and B. Bruderer, "Nocturnal autumn bird migration at Falsterbo, South Sweden," *J. Avian Biol.* **32**, 239–248 (2001).
6. P. Kerlinger and F. R. Moore, "Atmospheric structure and avian migration," in *Current Ornithology*, D. M. Power, ed. (Plenum, 1989), Vol. 6, pp. 109–141.
7. Å. Lindström, "The role of predation risk in stopover habitat selection in migrating bramblings, *Fringilla montifringilla*," *Behav. Ecol.* **1**, 102–106 (1990).
8. S. Åkesson and A. Hedenström, "How migrants get there: migratory performance and orientation," *BioScience* **57**, 123–133 (2007).
9. M. B. Casement, "Migration across the Mediterranean observed by radar," *Ibis* **108**, 461–491 (1966).
10. J. L. F. Parslow, "The migration of passerine night migrants across the English channel studied by radar," *Ibis* **111**, 48–79 (1969).
11. D. H. W. Adams, "Radar observations of bird migration in Cyprus," *Ibis* **104**, 133–146 (1962).
12. T. Alerstam, "Nocturnal migration of Thrushes *Turdus*-Spp in Southern Sweden," *Oikos* **27**, 457–475 (1976).
13. B. Bruderer and F. Liechti, "Quantification of bird migration—different means compared," in *Proceedings of the Bird Strike Committee, Europe* (1994), Vol. 22, pp. 243–254.
14. T. Alerstam, J. Bäckman, G. A. Gudmundsson, A. Hedenström, S. S. Henningsson, H. Karlsson, M. Rosén, and R. Strandberg, "A polar system of intercontinental bird migration," *Proc. R. Soc. London Ser. B* **274**, 2523–2530 (2007).
15. S. A. Gauthreaux, Jr., "A portable ceilometer technique for studying low level nocturnal migration," *Bird Banding* **40**, 309–320 (1969).
16. S. Åkesson, "Coastal migration and wind drift compensation in nocturnal passerine migrants," *Ornis Scand.* **24**, 87–94 (1993).
17. S. Zehnder, S. Åkesson, F. Liechti, and B. Bruderer, "Seasonal and diurnal patterns of nocturnal bird migration at Falsterbo, South Sweden," *J. Avian Biol.* **32**, 239–248 (2001).
18. F. Liechti, D. Peter, R. Lardelli, and B. Bruderer, "Herbstlicher Vogelzug im Alpenraum nach Mond-Beobachtungen—Topographie und Wind beeinflussen den Zugverlauf," *Ornitol. Beob.* **93**, 131–152 (1996).
19. F. Liechti, "Calibrating the moon-watching method—changes and limits," *Avian Ecol. Beh.* **7**, 27–41 (2001).
20. F. Liechti, D. Peter, R. Lardelli, and B. Bruderer, "The Alps, an obstacle for nocturnal broad front migration—a survey based on moon-watching," *J. Ornithol.* **137**, 337–356 (1996).
21. P. H. Zehndtindjev and F. Liechti, "A quantitative estimate of the spatial and temporal distribution of nocturnal bird migration in south-eastern Europe—a coordinated moon-watching study," *Avian Sci.* **3**, 37–45 (2003).
22. B. Bruderer and E. Weitnauer, "Radar observations of the migration and night flights of the swift *Apus-Apus*," *Rev. Suisse Zool.* **79**, 1190–1200 (1972).
23. J. Bäckman and T. Alerstam, "Confronting the winds: Orientation and flight behaviour of roosting swifts, *Apus apus*," *Proc. R. Soc. London Ser. B* **268**, 1081–1087 (2001).
24. T. Alerstam, M. Rosén, J. Bäckman, P. G. P. Ericson, and O. Hellgren, "Flight speeds among bird species: allometric and phylogenetic effects," *PLoS Biol.* **5**, e197 (2007).
25. F. Liechti, B. Bruderer, and H. Paproth, "Quantification of nocturnal bird migration by moonwatching: comparison with radar and infrared observations," *J. Field Ornithol.* **66**, 457–468 (1995).
26. C. J. Pennycuik, "Soaring behavior and performance of some East African birds observed from a motor glider," *Ibis* **114**, 178–218 (1972).
27. S. Svanberg, "Fluorescence spectroscopy and imaging of LIDAR targets," in *Laser Remote Sensing*, T. Fujii and T. Fukuchi, eds. (CRC Press, 2005).
28. S. Svanberg, "LIDAR," in *Springer Handbook of Lasers and Optics* F. Träger, ed. (Springer, 2007), pp. 1031–1052.
29. S. Svanberg, "Laser fluorescence spectroscopy in environmental monitoring," in *Optoelectronics for Environmental Science*, S. Martellucci and A. N. Chester, eds. (Plenum, 1990).
30. K. S. Repasky, J. A. Shaw, R. Scheppele, C. Melton, J. L. Carsten, and L. H. Spangler, "Optical detection of honeybees by use of wing-beat modulation of scattered laser light for locating explosives and land mines," *Appl. Opt.* **45**, 1839–1843 (2006).
31. D. S. Hoffman, A. R. Nehrir, K. S. Repasky, J. A. Shaw, and J. L. Carsten, "Range-resolved optical detection of honeybees by use of wing-beat modulation of scattered light for locating land mines," *Appl. Opt.* **46**, 3007–3012 (2007).
32. M. Brydegaard, Z. G. Guan, M. Wellenreuther, and S. Svanberg, "Insect monitoring with fluorescence lidar techniques: feasibility study," *Appl. Opt.* **48**, 5668–5677 (2009).
33. Z. G. Guan, M. Brydegaard, P. Lundin, M. Wellenreuther, A. Runemark, E. Svensson, S. Åkesson, and S. Svanberg,

- "Fluorescence lidar for studies of movements of insects and birds," in *Proceedings of the 25th International Laser Radar Conference ILRC25* (2010).
34. H. Dingle, *Migration: The Biology of Life on the Move* (Oxford U. Press, 1996).
  35. S. Jaques and B. Pogue, "Tutorial on diffuse light transport," *J. Biomed. Opt.* **13**, 041302 (2008).
  36. V. Tuchin, "Tissue optics," in *Light Scattering and Instruments for Medical Diagnosis*, 2nd ed. (SPIE Press, 2007).
  37. G. E. Hill and K. J. McGraw, eds., *Bird Coloration Volume 1: Mechanisms and Measurements* (Harvard U. Press, 2006).
  38. G. E. Hill and K. J. McGraw, eds., *Bird Coloration Volume 2: Function and Evolution* (Harvard U. Press, 2006).
  39. L. Pauling and R. B. Corey, "The structure of feather rachis keratin," *Proc. Natl. Acad. Sci. USA* **37**, 256–261 (1951).
  40. D. J. Brink and N. G. van der Berg, "Structural colours from the feathers of the bird *Bostrychia hagedash*," *J. Phys. D* **37**, 813–818 (2004).
  41. E. G. Bendit and D. Ross, "A technique for obtaining the ultraviolet absorption spectrum of solid keratin," *Appl. Spectrosc.* **15**, 103–105 (1961).
  42. D. Osorio and M. Vorobyev, "A review of the evolution of animal colour vision and visual communication signals," *Vision Res.* **48**, 2042–2051 (2008).
  43. A. T. Bennett and M. Thery, "Avian color vision and coloration: multidisciplinary evolutionary biology," *Am. Nat.* **169**, S1–S6 (2007).
  44. J. Reneerkens and P. Korsten, "Plumage reflectance is not affected by preen wax composition in red knots *Calidris canutus*," *J. Avian Biol.* **35**, 405–409 (2004).
  45. S. M. Doucet and G. E. Hill, "Do museum specimens accurately represent wild birds? A case study of carotenoid, melanin, and structural colours in long-tailed manakins *Chiroxiphia linearis*," *J. Avian Biol.* **40**, 146–156 (2009).
  46. D. Osorio and A. Ham, "Spectral reflectance and directional properties of structural coloration in bird plumage," *J. Exp. Biol.* **205**, 2017–2027 (2002).
  47. R. O. Prum, E. R. Dufresne, T. Quinn, and K. Waters, "Development of colour-producing beta-keratin nanostructures in avian feather barbs," *J. R. Soc. Interface* **6**, S253–S265 (2009).
  48. E. Warrant and D. E. Nilsson, eds. *Invertebrate Vision* (Cambridge U. Press, 2006).
  49. J. F. Jacobs, G. J. M. Koper, and W. N. J. Ursem, "UV protective coatings: a botanical approach," *Prog. Org. Coatings* **58**, 166–171 (2007).
  50. A. M. Pena, M. Strupler, T. Boulesteix, and M. C. Schanne-Klein, "Spectroscopic analysis of keratin endogenous signal for skin multiphoton microscopy," *Opt. Express* **13**, 6268–6274 (2005).
  51. A. Ounis, Z. G. Cerovic, J. M. Briantais, and I. Moya, "DE-FLIDAR: a new remote sensing instrument for estimation of epidermal UV absorption in leaves and canopies," in *Proceedings of European Association of Remote Sensing Laboratories (EARSeL)-SIG-Workshop LIDAR* (EARSeL, 2000), Vol. 1, pp. 196–204.
  52. G. B. Altschuler, K. Ilyasovand, C. V. Prikhodko, "Optical properties of human hair," *Tech. Phys. Lett.* **21**, 216–218 (1995).
  53. S. Jaques, "Origins of tissue optical properties in the UVA, visible and NIR regions," in *TOPS on Advances in Optical Imaging and Photon Migration II* (Optical Society of America, 1996), pp. 364–367.
  54. A. Ehlers, I. Riemann, M. Stark, and K. König, "Multiphoton fluorescence lifetime imaging of human hair," *Microsc. Res. Tech.* **70**, 154–161 (2007).
  55. J. K. Armenta, P. O. Dunn, and L. A. Whittingham, "Quantifying avian sexual dichromatism: a comparison of methods," *J. Exp. Biol.* **211**, 2423–2430 (2008).
  56. J. Ornborg, S. Andersson, S. C. Griffith, and B. C. Sheldon, "Seasonal changes in a ultraviolet structural colour signal in blue tits, *Parus caeruleus*," *Biol. J. Linn. Soc.* **76**, 237–245 (2002).
  57. K. J. McGraw and G. E. Hill, "Plumage color as a dynamic trait: carotenoid pigmentation of male house finches (*Carpodacus mexicanus*) fades during the breeding season," *Can. J. Zool.* **82**, 734–738 (2004).
  58. K. Delhey, A. Peters, A. Johnsen, and B. Kempenaers, "Seasonal changes in blue tit crown color: do they signal individual quality?," *Behav. Ecol.* **17**, 790–798 (2006).
  59. E. J. Willoughby, M. Murphy, and H. L. Gorton, "Molt, plumage abrasion, and color change in Lawrence's Goldfinch," *Wilson Bull.* **114**, 380–392 (2002).
  60. A. Peters, K. Delhey, S. Andersson, H. van Noordwijk, and M. I. Foerschler, "Condition-dependence of multiple carotenoid-based plumage traits: an experimental study," *Funct. Ecol.* **22**, 831–839 (2008).
  61. G. Pohland and P. Mullen, "Preservation agents influence UV-coloration of plumage in museum bird skins," *J. Ornithol.* **147**, 464–467 (2006).
  62. X. Wan, J. Fan, and H. Wu, "Measurement of thermal radiative properties of penguin down and other fibrous materials using FTIR," *Polym. Test.* **28**, 673–679 (2009).
  63. C. J. Dove, A. M. Rijke, X. Wang, and L. S. Andrews, "Infrared analysis of contour feathers—the conservation of body heat radiation in birds," *J. Therm. Biol.* **32**, 42–46 (2007).
  64. S. C. V. Raman, "The theory of the Christiansen experiment," *Proc. Indian Acad. Sci.* **A29**, 381–390 (1949).
  65. G. P. Kulemin, *Millimeter Wave Radar Targets and Clutter* (Artech House, 2003).
  66. I. C. Cuthill, J. C. Partridge, A. T. D. Bennett, S. C. Church, N. S. Hart, and S. Hunt, "Ultraviolet vision in birds," *Adv. Study Behav.* **29**, 159–214 (2000).
  67. P. A. A. de Beule, C. Dunsby, N. P. Galletly, G. W. Stamp, A. C. Chu, U. Anand, P. Anand, C. D. Benham, A. Naylor, and P. M. W. French, "A hyperspectral fluorescence lifetime probe for skin cancer diagnosis," *Rev. Sci. Instrum.* **78**, 123101 (2007).
  68. P. Weibring, H. Edner, and S. Svanberg, "Versatile mobile lidar system for environmental monitoring," *Appl. Opt.* **42**, 3583–3594 (2003).
  69. P. Weibring, T. Johansson, H. Edner, S. Svanberg, B. Sundnér, V. Raimondi, G. Cecchi, and L. Pantani, "Fluorescence lidar imaging of historical monuments," *Appl. Opt.* **40**, 6111–6120 (2001).
  70. P. Weibring, T. Johansson, H. Edner, S. Svanberg, B. Sundnér, V. Raimondi, G. Cecchi, and L. Pantani, "Fluorescence lidar imaging of historical monuments: erratum," *Appl. Opt.* **41**, 434–436 (2002).
  71. E. Wallinder, H. Edner, P. Ragnarson, and S. Svanberg, "Vertically sounding ozone LIDAR system based on a KrF excimer laser," *Phys. Scr.* **55**, 714–718 (1997).
  72. H. Edner, P. Ragnarson, S. Svanberg, E. Wallinder, R. Ferrara, B. E. Maserti, and R. Bargagli, "Atmospheric mercury mapping in a cinnabar mining area," *Sci. Total Environ.* **133**, 1–15 (1993).
  73. U. P. Hoppe, G. H. Hansen, and W. Eriksen, "ALOMAR—Ground-based monitoring of stratospheric ozone and related atmospheric parameters," in *27th International Symposium on Remote Sensing of Environment* (1998), pp. 244–247.
  74. Kipp & Zonen, Delft, the Netherlands (2010), [www.kippzonen.com](http://www.kippzonen.com).
  75. Alternatively Optech Inc., Kiln, Miss., USA (2010), [www.optech.com](http://www.optech.com).
  76. M. D. Shawkey, M. E. Hauber, L. K. Estep, and G. E. Hill, "Evolutionary transitions and mechanisms," *J. R. Soc. Interface* **3**, 777–786 (2006).



## PAPER VII

**Quasi zero-background tunable diode laser  
absorption spectroscopy employing a balanced  
Michelson interferometer**

Z.G. Guan, M. Lewander, S. Svanberg.

*Optics Express* **16**, 21714 - 21720 (2008).



# Quasi zero-background tunable diode laser absorption spectroscopy employing a balanced Michelson interferometer

Zuguang Guan<sup>1,2</sup>, Märta Lewander<sup>1</sup>, and Sune Svanberg<sup>1\*</sup>

<sup>1</sup> Atomic Physics Division, Lund University, P.O. Box 118, S-221 00, Lund, Sweden

<sup>2</sup> Centre for Optical and Electromagnetic Research, State Key Laboratory for Modern Optical Instrumentation, Zhejiang University, Hangzhou 310058, PR China

\*Corresponding author: [Sune.Svanberg@fysik.lth.se](mailto:Sune.Svanberg@fysik.lth.se)

**Abstract:** Tunable diode laser spectroscopy (TDLS) normally observes small fractional absorptive reductions in the light flux. We show, that instead a signal increase on a zero background can be obtained. A Michelson interferometer, which is initially balanced out in destructive interference, is perturbed by gas absorption in one of its arms. Both theoretical analysis and experimental demonstration show that the proposed zero-background TDLS can improve the achievable signal-to-noise ratio.

©2008 Optical Society of America

**OCIS codes:** (300.6260) Spectroscopy, diode laser; (060.2370) Fiber optics sensors.

## References and links

1. M. Gehrtz, G. C. Bjorklund and E. A. Whittaker, "Quantum-limited laser frequency-modulated spectroscopy," *J. Opt. Soc. Am. B* **2**, 1510-1526 (1985).
2. J. Ye, L.-S. Ma and J. L. Hall, "Ultrasensitive detections in atomic and molecular physics: Demonstration in molecular overtone spectroscopy," *J. Opt. Soc. Am. B* **15**, 6-15 (1998).
3. H. I. Schiff, G. I. Macay and J. Bechara, "The use of tunable diode laser absorption spectroscopy for atmospheric measurements," *Air Monitoring by Spectroscopic Techniques*, M. W. Sigrist, ed., (Wiley, New York 1994), p. 239-333.
4. P. Werle and F. D'Amato, eds., *Special Issue: Field Laser Applications in Industry and Research*, *Appl. Phys. B*, **92**, 303-474 (2008).
5. W. M. Fairbank, Jr., T. W. Hänsch and A. L. Schawlow, "Absolute measurement of very low sodium-vapor densities using laser resonance fluorescence," *J. Opt. Soc. Am.* **65**, 199-204 (1975).
6. W. Neunhauser, M. Hohenstatt, P. Toschek and H. Dehmelt, "Localized visible Ba<sup>+</sup> mono-ion oscillator," *Phys. Rev. A* **22**, 1137-1140 (1980).
7. M. W. Sigrist, "Air monitoring by laser photoacoustic spectroscopy," *Air Monitoring by Spectroscopic Techniques*, M. W. Sigrist, ed., (Wiley, New York 1994), p. 163-238.
8. C. Wieman and T. W. Hänsch, "Doppler-free polarization spectroscopy," *Phys. Rev. Lett.* **36**, 1170-1173 (1976).
9. T. W. Hänsch, I. S. Shahin and A. L. Schawlow, "High resolution saturation spectroscopy of the sodium D line with a pulsed tunable dye laser," *Phys. Rev. Lett.* **27**, 707-710 (1971).
10. J. P. Dakin, H. O. Edwards and B. H. Weigl, "Progress with optical gas sensors using correlation spectroscopy," *Sens. Actuators B* **29**, 87-93 (1995).
11. L. S. Rothman, et al., "The HITRAN 2004 molecular spectroscopic database," *J. Quant. Spectrosc. Radiat. Transfer*, **96**, 139-204 (2004).
12. B. Couillaud, L. A. Bloomfield and T. W. Hänsch, "Generation of continuous-wave radiation near 243 nm by sum frequency mixing in an external ring cavity," *Opt. Lett.* **8**, 259-261 (1983).
13. D. B. Mortimore, "Fiber loop reflectors," *J. Lightwave Technol.* **6**, 1217-1224 (1988).

## 1. Introduction

Tunable diode laser spectroscopy (TDLS) has been proven to be a successful technique for trace-gas environmental monitoring [1-4]. By using frequency modulation (FM) or wavelength modulation (WM) methods, TDLS can measure optical absorption in atomic or molecular samples, with a high resolution and sensitivity in real time. In FM-TDLS, for instance, the minimum detectable absorption could be as low as  $10^{-7}$  [1]. The high sensitivity



originates from the dramatically increased signal-to-noise ratio (SNR), which can be expressed as

$$SNR = \frac{\kappa I}{\sqrt{(N_s I)^2 + (\beta \sqrt{I})^2 + N_t^2}}. \quad (1)$$

$I$  is the intensity of light arriving at the detector and  $\kappa$  describes the absorption signal.  $N_s I$ ,  $\beta \sqrt{I}$ , and  $N_t$  are the laser source noise, the detector quantum noise and the detector thermal noise, respectively.  $N_s I$ , which is induced by the fluctuations of the laser source, dominates at low frequencies but can be suppressed efficiently by going to high frequencies ( $N_s \propto 1/f$ ).

In FM-TDLS where the laser source is modulated at radio frequencies,  $\beta \sqrt{I}$  and  $N_t$  (light-intensity independent) instead dominate, and therefore, the SNR can be improved by increasing the laser intensity. This ultimately corresponds to quantum limited measurements.

Apart from the absorptive technique just described, a group of zero-background methods exists. Here a spectroscopic signal ( $I_s$ ) rises from a zero or low background. For instance, laser-induced fluorescence spectroscopy produces a signal only when the laser frequency is tuned to the molecular absorption line. This technique is sensitive enough to track a single ion or atom [5, 6]. Likewise, in photo-acoustic spectroscopy, the acoustic signal appears solely when the laser wavelength matches an absorption line to excite the molecules [7]. A further example is polarization spectroscopy, developed for low absorption signal applications by Wieman and Hänsch [8]. Here a crossed polarizer placed in front of the detector will normally block out the linearly polarized laser light background. Only at the line center the polarization plane is rotated by the polarized sample and a signal occurs from zero background providing a higher sensitivity compared with standard saturation spectroscopy [9]. The SNR of such zero-background techniques is described by

$$SNR = \frac{I_s}{\sqrt{(N_s I_s)^2 + (\beta \sqrt{I_s})^2 + N_t^2}}. \quad (2)$$

Here, a high SNR can still be obtained even if  $N_s I_s$  ( $N_s \ll 1$ ) dominates in the absence of high-frequency modulation. Most importantly, the small quantity  $I_s$  now replaces the large quantity  $I$  when measuring small signals.

In the present paper, we propose and demonstrate, as we believe, for the first time, a TDLS scheme working on a zero background. By using laser beams with equal strength but with a phase shift of  $\pi$  causing destructive interference in a Michelson interferometer, the recorded light intensity can be balanced out to zero. When one light beam used for gas probing suffers an absorption induced by a gas sample, the balance is disrupted and a non-zero signal appears. In the paper, we demonstrate, through theoretical analysis and experimental work, that the zero-background TDLS presented can improve the SNR compared with a direct absorption TDLS. It should be mentioned that a similar principle was used by Dakin et al. to create a spectroscopically structured broadband light source for correlation spectroscopy [10].

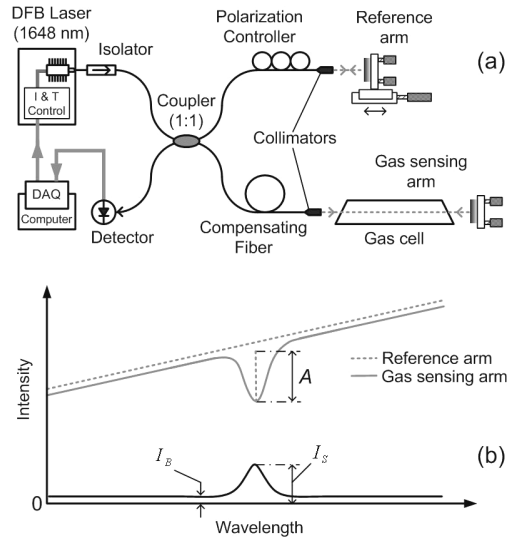


Fig. 1. (a). Schematic diagram of zero-background TDLs; (b) the principle for forming the zero background.

## 2. Measurement principle and analysis

As shown in Fig. 1(a), a fiber-optic Michelson interferometer is employed in a destructive interference mode to form a zero output intensity, which constitutes the background for the spectroscopic signal to be recorded. It is worthwhile noting that fiber-optics is not necessary for the proposed technique, thus making it also very suitable in the IR region, where fibers are not readily available. We demonstrated the technique by using a fiber-optic Michelson interferometer only because of its proper compatibility with the light source. When the optical path difference (OPD) of the two arms is adjusted to zero, the intensity of the light at the detector in the absence of gas absorption can be expressed as  $I_B = \frac{1}{4}P(1-k)^2$ , where  $P$  is the laser power and  $k$  ( $0 < k \leq 1$ ) is a balance factor for intensities of the two interfering light beams. If  $k$  is close to 1, a very low light intensity, i.e. a zero background, can be achieved (see Fig. 1(b)). When the laser wavelength is tuned to the absorption line of the sample, which is inserted in one arm of the Michelson interferometer, an absorption ( $A$ ) is induced in this arm and the balance is perturbed. The light intensity  $I_S$  at the detector in the presence of an absorption increases to  $I_S = \frac{1}{4}P(1-k\sqrt{1-A})^2$ . By defining  $\delta = 1 - k$ ,  $I_S$  can be approximately written as

$$I_S \approx \frac{1}{4}P\left(\frac{1}{4}k^2A^2 + kA\delta + \delta^2\right). \quad (3)$$

Figure 2(a) shows the calculated values of  $I_S$  as  $A$  increases from 0 to 0.1, for different unbalance factors  $\delta$ . One can see that when  $\delta = 0$ , both the signal and the responsivity ( $\frac{\partial I_S}{\partial A}$ ) rapidly drop to zero for small  $A$ . However, the responsivity for measuring a small signal can be improved by a non-zero  $\delta$  (see the second term in Eq. (3)). As an amplification coefficient,  $\delta$  is comparable with the bias angle  $\theta$  in a polarization spectroscopy [8].

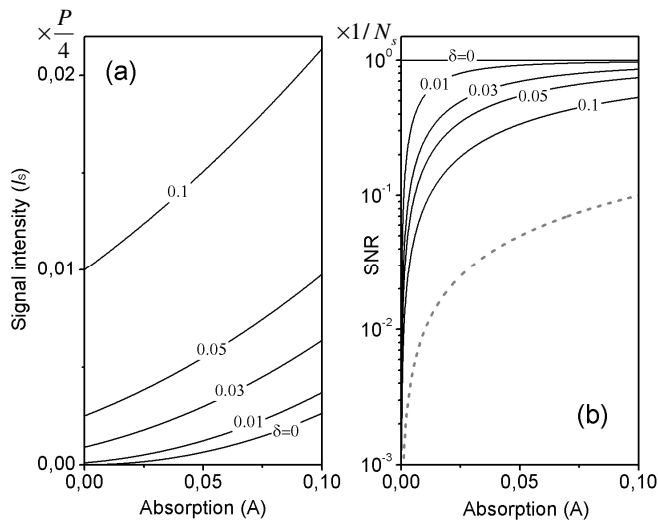


Fig. 2. Calculated results of (a) responsivity and (b) SNR for an increasing absorption ratio, for different values of  $\delta$ . The gray dashed curve in (b) shows the SNR of a direct absorption TDLS.

Further, the SNR of the system, which determines the minimal detectable signal and sensitivity, is calculated assuming that the noise  $N_s I_s$  in Eq. (2) still dominates (otherwise it is in the quantum limited range and the SNR can be improved by increasing the laser power):

$$\text{SNR} \approx \frac{1}{N_s} \frac{I_s - I_B}{I_s}. \quad (4)$$

The corresponding calculated results are shown in Fig. 2(b). It is obvious that when  $\delta = 0$  ( $I_B = 0$ , i.e. zero background), Eq. (4) turns to a constant  $1/N_s$ , which means that a good SNR can be achieved independent of the signal  $I_s$  or the absorption A. For real-world applications, SNR curves of  $\delta \neq 0$  are calculated. From Fig. 2(b), obviously better SNR can be seen compared with that of the direct absorption spectroscopy (gray dashed curve), which is known to have a  $\text{SNR} \approx A/N_s$ . For instance, when  $\delta = 0.05$  (corresponding to that the intensity ratio of the interfering light beams is 0.9), the SNR of the method presented is 17 times better than that of the direct absorption spectroscopy, when an absorption ratio of 0.01 is considered.

A trade-off can be seen by comparing Figs. 2(a) and 2(b). The unbalance factor  $\delta$  can improve the responsivity on the one hand; while the increased background will certainly decrease the SNR on the other hand. Thus, a suitable value for  $\delta$  should be carefully chosen depending on different applications.

### 3. Experiment and results

An experimental set-up was constructed as shown in Fig. 1(a). A distributed feed-back (DFB) diode laser module (Denselight, DL-BF12-CLS051B-S1648) is employed. The wavelength of this single longitudinal mode laser is around 1648.21 nm, for measuring absorption lines of methane,  $\text{CH}_4$  [11]. The laser module has an inner current and temperature ( $I$  &  $T$ ) controller.

The laser wavelength can be tuned by controlling the driving current with an external voltage signal. After passing through an optical isolator (for avoiding reflected light to damage the laser source), the light enters a fiber-optic Michelson interferometer, which is formed by a 1:1 fiber coupler and two reflecting mirrors. A 10 cm long gas cell, filled with a 12 mbar gas mixture (15% CH<sub>4</sub> and 85% air), is inserted in one arm (i.e., the gas sensing arm) of the Michelson interferometer. The glass windows of the gas cell are tilted to avoid reflected light entering the system. A fiber-optic polarization controller in the other arm (i.e., the reference arm) is used to balance the polarization states of the interfering light beams. A section of fiber can compensate the OPD between the two arms for avoiding etalon effect when the laser wavelength is scanned. The coupling efficiency of the fiber collimators can be adjusted by tuning the angles of the mirrors and therefore equal light strength can be obtained in the two beams of interfering light. The output port of the Michelson interferometer is connected to an InGaAs detector (New Focus 2033), the signal of which is recorded by a DAQ card (NI-6154) installed in a personal computer. The same card also provides controlling signal for the DFB laser module.

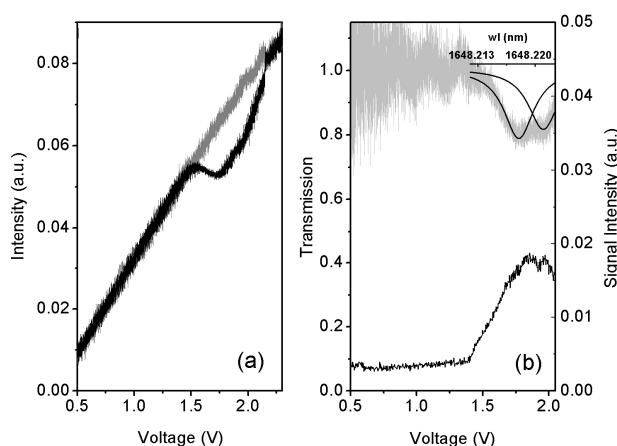


Fig. 3. (a). Measured light intensity corresponding to the reference arm (gray) and the gas sensing arm (dark); (b). SNR comparison between direct absorption TDLS (gray curve at top) and the system presented (dark curve at bottom). The inset of (b) shows that the calculated spectrum agrees with the measured one.

In order to prove that the system presented can reduce system noise extremely well and hence improve the SNR, we add extra noise on the scanning voltage (0.5 - 2.3V) of the DAQ card. The noise in the laser intensity is artificially enlarged to 6.5% of the maximum intensity value, together with noise in laser frequency and phase. Principally, all these three types of noise can be suppressed by the presented balanced Michelson interferometer. However, considering the intensity measurement in a direct absorption TDLS, the phase noise can be ignored and since the frequency noise transfers into effective intensity noise, we only study the intensity noise in the measurements. The intensities of the light passing through the reference and gas sensing arms are measured independently. From the results shown in Fig. 3(a), they overlap very well until absorption lines of CH<sub>4</sub> appear around 1648.22 nm, which corresponds to 1.7 V scanning voltage. The data after 2.1 V, where the laser unfortunately exhibits mode jumps, are not used in later experimental results. The transmission spectrum of CH<sub>4</sub>, i.e. the ratio of the curves in Fig. 3(a), is shown as the noisy gray curve in Fig. 3(b). It fits well with the calculated results of two R6 absorption lines of CH<sub>4</sub>, using the HITRAN

database [11]. Here, a direct absorption TDLS suffers from a bad SNR (3.1) even in the presence of an obvious absorption signal of about 20%. If instead the horizontal position of the mirror in the reference arm is tuned to adjust the Michelson interferometer working in a destructive interference mode, a low-intensity background is achieved, and an increasing signal instead of a signal reduction due to absorption appears at 1.7 V. From the dark curve at the bottom of Fig. 3(b), we can see that the SNR (13.8) is improved by 4.5 times, which is close to the calculated result, 5 times higher SNR for a perfect ( $\delta = 0$ ) zero-background TDLS, compared to a direct absorption measurement for the case when the absorption is 20 % (beyond the upper range in Fig. 2(b)). As an imperfection, we noted that the laser wavelength tunes considerably faster after 1.4 V when the controlling voltage is linearly scanned, which explains the kink in the curve. The non-zero background shown in the curve is induced by a non-zero  $\delta$  obtained in practice, even with efforts to minimize it as much as possible in the experiment. This shows the limitation on the minimal detectable signal when the absorption becomes small and the SNR decreases dramatically, as illustrated in Fig. 2(b).

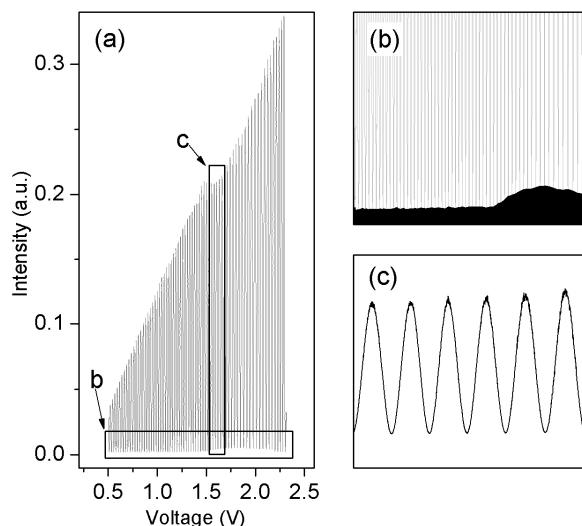


Fig. 4. (a). Oscillating pattern with an envelope including spectroscopic information; (b) and (c) show the details of windows b and c in (a).

#### 4. Discussion

Without any extra stabilizing scheme, the destructive interference setting of a Michelson interferometer cannot be kept for a long term. For better system performance, an interferometer with a stable OPD should be built. One possibility is to construct a closed-loop controlling circuit for the Michelson interferometer, in a similar way as used, e.g. in a build-up optical cavity [12]. By detecting the light intensity at the output port of the interferometer, a specific algorithm, e.g. a proportional-integral-derivative (PID) algorithm can control a piezo-driven mirror to lock the OPD of the interferometer working in destructive interference and a zero-background can be stably maintained. Another possibility is to use a self-stabilized interferometer, e.g. a Sagnac fiber loop [13]. In such an interferometer, two interfering light beams always pass through the same optical path and the destructive interference condition is naturally kept at the output port. In the fiber loop a smart scheme should be included to induce differential absorption (due to the gas) between the light beams propagating clockwise and

counter-clockwise. In such a design, many advantages are expected compared with the Michelson interferometer demonstrated in the proof-of-principle work in this paper. For instance, if a Michelson interferometer is employed in real applications, the balance factor of the two arms will degrade because of, e.g., mechanical instability, and phase noise will be induced in long optical paths of flowing sample gas. However, all these problems can be naturally solved in case the interfering light components always experience the same optical path.

Instead of developing complicated close-loop electronics to stabilize the interferometer, we find that if an active fast modulation is applied on the OPD, the slow drift is replaced by an oscillating pattern where the constructive and destructive interference is achieved alternately. It could be realized by shaking one of the mirrors piezo-electrically. The modulation range should be larger than one wavelength but sufficiently small that the etalon effects are not appearing, considering that the laser wavelength scans at the same time. For demonstration, we move the reference mirror swiftly on the linear stage. From the measured result shown in Fig. 4(a), we can see in one scan of the controlling voltage, that the interference pattern oscillates rapidly between destructive and constructive conditions. If the minimal values (corresponding to destructive conditions) are utilized, an increasing signal positioned on a low background (see Fig. 4(b)) can also be obtained, similarly as in Fig. 3(b). Although the integrated signal intensity is reduced, (which is already described in Eq. (3)), we believe that the SNR can be improved. Evidence is shown in Fig. 4(c). The noise corresponding to the destructive condition is obviously decreased compared with that corresponding to the constructive one. The noise in this modulation mode is even lower than for the case without modulation (compare with bottom curve of Fig. 3(b); note that the same extra noise is still applied), since  $N_s \propto 1/f$ . On the other hand, the spectral sampling is decreased as a penalty in this case. However, the basic features of the new technique introduced are still clearly demonstrated.

## 5. Conclusion

In conclusion, we have demonstrated an efficient method to decrease the noise in TDLS by operating at a close-to-zero background, without any high-frequency modulation on the light source. This is achievable by using a Michelson interferometer set to destructive interference. The method has similarities to polarization spectroscopy, but is a linear spectroscopy method. A fiber-optic implementation was demonstrated, constituting a realistic approach for real-world gas monitoring. The proposed technique is particularly attractive in applications where high-frequency modulation is difficult to realize.

## Acknowledgments

This work is supported by the Swedish Research Council and the Knut and Alice Wallenberg Foundation. The authors appreciate Zhongshan Li, Mikkel Brydegaard, Bo Li and Ziwei Sun, for helpful discussion and assistance.



# PAPER VIII

**Active feed-back regulation of a Michelson  
interferometer to achieve zero-background  
absorption measurements**

P. Lundin, Z.G. Guan, S. Svanberg.

Submitted to *Applied Optics* (2010).





# Active feed-back regulation of a Michelson interferometer to achieve zero-background absorption measurements

Patrik Lundin,\* Zuguang Guan, and Sune Svanberg

Atomic Physics Division, Lund University, P.O. Box 118, SE-221 00 Lund, Sweden

\* Corresponding author: patrik.lundin@fysik.lth.se

Compiled September 10, 2010

An active phase controlling scheme based on a proportional-integrative-derivative(PID)-controlled piezo-electric transducer is presented with the purpose of stabilizing a quasi zero-background absorption spectrometer. A fiber-based balanced Michelson interferometer is used, and an absorption due to a gas sample in one of its arms results in an increased light signal to a detector, which otherwise, thanks to destructive interference, experiences a very low light level. © 2010 Optical Society of America

OCIS codes: 300.1030, 300.6260

## 1. Introduction

To observe the spectrally narrow absorption lines of gases is one of the most powerful approaches to gas monitoring. Because of the specificity of the energy structure, each gas molecule has a unique absorption spectrum. Thus, by studying a spectral region with a broad-band light source in combination with a high-resolution optical spectrometer, or by spectrally scanning a narrow-band laser, gases can be identified. Tunable diode laser absorption spectroscopy (TDLAS) is, thanks to properties like narrow line-width, easy tunability, comparatively low cost and easy operation, very effective in characterization of free gas absorption lines in various situations.

In its most straight-forward form, gas absorption is measured in a ‘bright-field’ way as a reduction of an incident light intensity level. The fact that absorption in this ‘direct’ way (DLAS, direct laser absorption spectroscopy) is measured as a minor reduction of a high light level limits the achievable signal-to-noise ratio which is strongly connected to the light flux at the detector. This is obvious from Eq. 1 where the signal-to-noise ratio,  $SNR$ , is related to the total noise,  $N_{tot}$ , and the light intensity,  $I$ , at the detector.

$$SNR = \frac{S}{N_{tot}} = \frac{A \cdot I}{\sqrt{(N_s I)^2 + (\beta \sqrt{I})^2 + N_T^2}} \quad (1)$$

Here  $A$  is the absorption fraction, and  $N_s I$ ,  $\beta \sqrt{I}$  and  $N_T$  indicate laser source noise, quantum noise and thermal noise at the detector, respectively. By increasing the light intensity, the laser source noise will become dominant and the other two terms ignorable, but for further improvements other approaches are necessary. This can, e.g., be to modulate the light source and detect frequency overtones from the non-linear absorption profiles and thereby transfer the signal to higher frequencies to suppress the  $1/f$  (pink) laser source noise,  $N_s I$ . This is done in wavelength- and frequency modulation spec-

troscopy (WMS and FMS), where absorption fractions down to  $10^{-7}$ – $10^{-8}$  are reachable [1]. Another group of techniques referred to as *zero-background* or ‘*dark field*’ measurements exists in which the source noise is inherently decreased since the signal to be detected is not carried by a huge background light flux; instead all light at the detector is ideally useful signal. Examples of such techniques are laser-induced fluorescence, Raman- and polarization spectroscopy [2]. Another important example, although not generating an optical signal, is photoacoustic spectroscopy [2]. Within Fourier transform (FT) spectroscopy, low background absorption measurements by optical subtraction through destructive interference has been used to increase sensitivity, as proposed in 1967 [3]. The technique has successfully been implemented in numerous FT spectrometers to be able to use more sensitive detectors designed for low light fluxes; see e.g., [4,5]. Drawing inspiration from such approaches, Guan *et al.* [6] presented a method to transfer the idea into the diode laser field and measure gas absorption with TDLAS implemented in a balanced Michelson interferometer design. The basic principle there is that without any absorption present, the light intensity in the two arms of the interferometer is the same, and if the total path lengths in the arms differ by a half wavelength (plus an integer number of wavelengths), meaning that the phase difference is  $180^\circ$ , destructive interference forces the light level at the detector to be zero. Any absorption in one of the arms will disturb this intensity balance and complete destructive interference is no longer possible. In that setup, two approaches were used to achieve the condition of fixed phase difference between the arms. The first one was to let the interferometer drift freely, waiting for moments to occur when the desired phase difference is achieved, and then scan the absorption line of the gas. The other approach was based on a translation of one of the mirrors in the interferometer. This causes the phase difference to rapidly change, resulting in a fast oscillation between constructive and destructive interference and by only considering the points of minimum detector

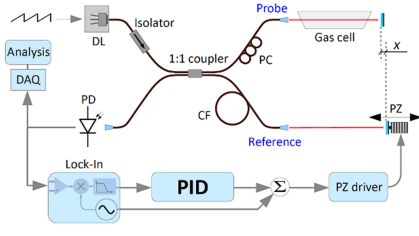


Fig. 1. Schematic diagram of the optical and electronic setup

intensity, an absorption profile can be reconstructed.

Discussed in Ref. [6] is the possibility to implement an active phase controlling system, e.g. a feed-back loop. This could improve both the performance and the usefulness of the system. Many designs have been presented to, passively or actively, phase control interferometers (see, e.g. [7-10], and references therein); some of them are even capable of maintaining any chosen phase difference between the arms. None of these schemes are, however, suitable for our application. The main reason is that we require a simple and robust design which can easily be implemented in an in situ situation. With today's highly performing feedback algorithms, e.g. Proportional-integrative-derivative (PID) controllers, the system design could be compact and reliable. We therefore present a new scheme where the phase difference is actively stabilized with the help of a lock-in assisted PID regulator and a piezo-electric transducer.

The whole setup will be described and, since the optical setup in general is common with our earlier paper, the focus will be put on the scheme for interferometer stabilization. Some requirements and performance for the stabilization are discussed. Representative results will be presented and the potential for the approach will be theoretically modeled and discussed.

## 2. System setup

The electro-optical setup is shown in Fig. 1. It is, in the optical parts, similar to the one used in our first paper. Light from a 1648 nm diode laser (DenseLight DL-BF12-CLS051B-S1648) passes through a protective isolator and is split into two equal parts in a 1:1 fiber coupler. For the probe arm, a polarization controller (PC) is installed to assure equal polarization of the light in the reference and probe arms (when returning to the coupler the second time). In the reference arm, a compensating fiber (CF) is installed to make the arms the same length within approximately 1 mm to enable interference control during wavelength scan. The beams from the two fibers are each reflected on a mirror after a short free space propagation. The probe beam passes through a 7.5-cm cell with pure methane (standard isotope com-

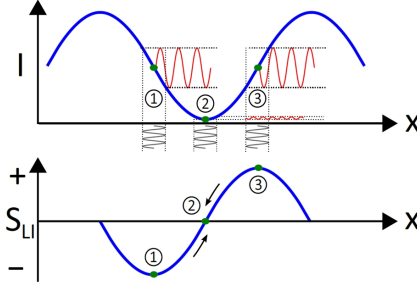


Fig. 2. The intensity at the detector (top) and the output,  $S_{LI}$ , from the lock-in amplifier (bottom) as a function of mirror displacement. At position 1 and 3 the mirror dithering results in large intensity modulations, but with a phase shifted  $180^\circ$  between them. At position 2 the dithering results in a small or non-existing intensity modulation. Demodulation at the lock-in amplifier gives the signal in the bottom drawing. This signal is suitable as input to the PID which now can push the mirror towards a null position.

position, 10 mbar). As the light from the two beams arrives at the detector (PD, NEW FOCUS 2033), it will interfere depending on the difference in path length. During the measurement, this path length difference,  $2x$ , is controlled by a piezo-electric transducer, to maintain a low light level at the photo diode detector. Generally, PID algorithms cannot directly regulate to a local minimum position. Here, however, it is necessary to control the intensity to the local minimum position of perfectly destructive interference (freely referred to as the 'null' position). The approach to circumvent this problem is to adapt designs used since long, e.g. within laser stabilization (see, e.g. [11,12]). The idea is to implement a small modulation and employ lock-in techniques.

## 3. Stabilizing the interferometer

The intensity of light at the detector varies depending on the mirror displacement,  $x$ , is described by Eq. 2.

$$I(x) = I_1 + I_2 + 2\sqrt{I_1 I_2} \cos(2\pi \cdot \frac{2x}{\lambda}), \quad (2)$$

where  $I_1$  and  $I_2$  [W/m<sup>2</sup>] are the intensities in the two arms and  $\lambda$  [m] is the wavelength of the light.

If the position of one of the mirrors is modulated with a signal from an oscillator (in this case forming part of the lock-in amplifier, EG&G Princeton 5209), this will result in a modulation of the light intensity at the detector as well. The amplitude and phase of this intensity modulation depend on the interference situation as can be seen in the upper part of Fig. 2, where a solid thick

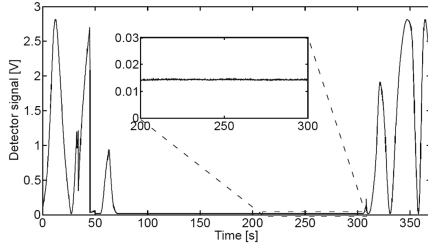


Fig. 3. The output signal from the detector with and without active stabilization. During the first 75 s the interferometer is free-running, the stabilizing scheme is then implemented and after around 300 s, the system is again running free. The offset from zero during the stabilization is due partly to a detector offset but also a non-perfect polarization matching and power balance.

(blue) curve shows the intensity of the light at the detector as a function of mirror displacement ( $x$ ), according to Eq. 2. At the position of perfect destructive interference the resulting intensity modulation will be small or non-existing (and at double the modulation frequency), while it will be larger at each side of this null position, although with opposite ( $180^\circ$  shifted) phase between the sides. If this intensity-modulated signal (having the same frequency as the mirror dithering) is demodulated at the lock-in amplifier by the signal from the same oscillator with a certain fixed phase delay, this will (under the condition of small modulation) result in an output signal,  $S_{LI}$ , proportional to the derivative of the interference signal, as shown at the bottom of Fig. 2.

The PID regulator (SRS SIM960) is now, by proper choices (depending on dithering amplitude and frequency, lock-in sensitivity, etc.) of the proportional (P), integrating (I) and (possibly) differentiating (D) parameter, suitable for keeping the interference at a destructive position, by pushing  $S_{LI}$  toward zero. The parity of the controller constants should match the slope direction of  $S_{LI}$ , which depends on the relative phase between the input signal at the lock-in amplifier and the local reference oscillation. If the parity (set by the sign of P) is shifted, or if the phase delay is changed so that the oscillator reference and  $S_{LI}$  are completely out of phase, a position of complete constructive interference will instead be found. In principle, it is possible with this scheme to control to various phase angles by adjusting the set-point and parity of the PID, however, in our application, only the complete destructive mode is of interest.

The stabilization scheme, crucial for the absorption measurements, shows stable performance in the normal laboratory environment. Fig. 3 shows the behavior of the system during a few minutes of operation.

During the time of controlling the intensity RMS (root-mean-square) variation is less than  $5 \times 10^{-5}$  of the

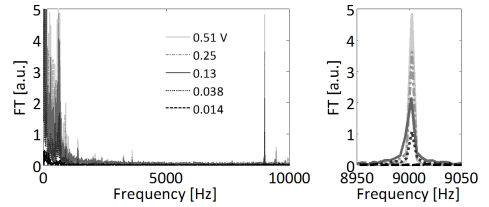


Fig. 4. The FT of the signal for different conditions of interference resulting in mean detector outputs of 0.51, 0.25, 0.13, 0.038 and 0.014 V, corresponding to mirror positions 50, 34, 23, 11 and  $0.59^\circ$  off from  $180^\circ$ . When the system is driven towards the point of complete destructive interference, the FT at the modulation frequency of 9 kHz decreases rapidly and finally diminishes into the noise.

maximum value without stabilization. This would, if all noise came from regulation instability, correspond to controlling the phase difference within 10 mrad or  $0.6^\circ$  RMS. Some of the noise, however, comes from thermal noise at the detector etc.; the controlling is thus better than the stated values.

An argument for non-modulating approaches to stabilize interferometers is that the modulation is itself inherently disturbing the stability. It is therefore crucial to keep the modulation amplitude sufficiently small to prevent such impacts, while at the same time large enough to be detected by the lock-in amplifier at small drifts from the null position. The amplitude of the dithering is here adjusted directly on the signal generator of the lock-in amplifier. To make sure that the oscillation is not too large, the frequency spectrum of the detected light signal was studied and scrutinized for any residual oscillations at the piezo dithering frequency, 9 kHz. When the phase difference approaches  $180^\circ$ , the residual intensity modulation decreases rapidly and finally vanishes into the noise at the null position. The DC component, which forms the background level, is greatly reduced as well. Fig. 4 shows the Fourier transform (FT) of the detected light signal as the interferometer approaches the desired position.

#### 4. Absorption measurements

To show the function of the presented gas absorption technique compared to DLAS, the absorption of methane at around 1648.2 nm was measured with the two methods. The direct measurement is performed in the way that the diode laser is swept over the two absorption peaks of the gas (see the blue, dotted line in Fig. 5) while the reference arm is blocked with black paper and the signal from the photo diode detector is recorded. The same wavelength interval is then swept with the probe arm instead blocked (red, dashed) as a reference of the

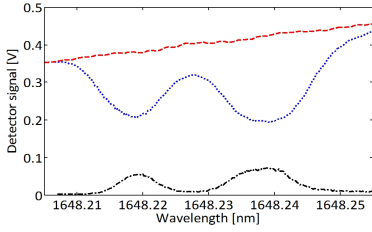


Fig. 5. Absorption measurements of methane with DLAS and the interferometric method. Included is a scan of the reference arm without gas in dashed (red), a direct scan of the cell in dotted (blue) and the interferometric scan in dash-dotted (black).

laser RAM (residual amplitude modulation).

The interferometric mode was then utilized with both arms cleared and the stabilization system implemented. The corresponding signal is seen as an increase from zero (black, dash-dotted curve).

In this case, the absorption in the gas cell is strong and the SNR is high for both the direct and the interferometric measurement, so, to show the potential of the technique, the performance is modeled in the case of smaller absorption and for systems with different performance regarding phase control.

## 5. Simulations

In the following section we will discuss how the detectable absorption fraction depends on how well the interference phase is kept by the system. If the phase difference between the two arms of the interferometer deviates from  $180^\circ$ , the signal at the detector will vary according to Eq. 2. This will induce additional noise in the measurement and quickly limit the smallest detectable absorption. The presented technique inherently strongly suppresses source noise, which often is the limiting factor in sensitive measurements, but as will be shown, to reach low absorption levels the controlling system needs to be precise and not allow the phase to deviate far from the null position.

In Fig. 6, results from simulations based on the data measured and presented in Fig. 5 are shown. Data from the measurement were collected and smoothed to be able to precisely control the noise. Gaussian noise with an RMS of 0.5% of the absolute intensity was then added on the probe and reference arm signals. Half of the noise is the same in both arms and half is unique to each arm; the reason for this is that fluctuations in the source would come through the same in both arms, but on top of this each arm would experience its own shot noise. The absorption signal for a DLAS measurement, and with the presented method, was then simulated for absorption fractions with peak values 50, 10, 5.0 and 2.5% and

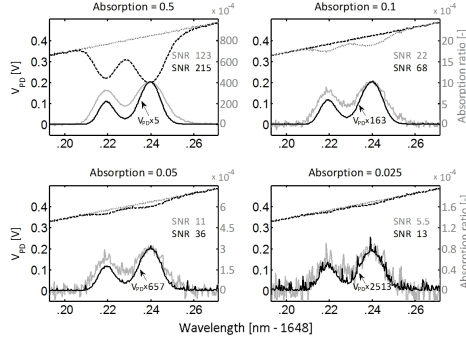


Fig. 6. Simulation of a scanned methane cell signal DLAS, shown in dashed black, the scanned reference arm (without gas), shown in dotted grey, the equivalent (magnified) scan with the interferometric method shown in solid black and the DLAS scan divided with a line fitted to the reference scan in solid grey. The last curve can be thought of as the actual absorption signal from the direct method and has the absorption ratio scale to the right of the of the plot.

the corresponding signal-to-noise ratios are presented.

Regarding the interferometric simulation, the controlling system has in this example an added random (Gaussian) phase fluctuation of RMS  $0.2^\circ$ . The cell scan signal is in this mode calculated based on Eq. 2. The SNR is calculated as the peak height (of the peak at 1648.24 nm) of the signal from an ideal absorption profile, fitted to the cell scan signal, divided by the RMS deviation of the residual between this ideal and simulated profile.

Regarding the DLAS case, the absorption signal is calculated as the difference between a line (without noise) fitted to the reference arm signal and the simulated cell scan signal. The SNR is then calculated the same way as for the interferometric case - an ideal profile is fitted to the signal and the peak height of this gives the 'S'. The noise is again the RMS deviation between the ideal and simulated signals.

Fig. 7 shows the SNR as a function of absorption fraction for a DLAS measurement and the interferometric method with different values on the phase fluctuation. Included in the figure is also the line corresponding to a frequently adapted approximate value for the SNR of a source-noise limited DLAS measurement,  $A/N_S$ . (The interferometry simulations in Fig. 6 correspond to the  $0.2^\circ$  curve.) It is obvious how, by improving the phase stability of the system, a high SNR can be kept for diminishing absorption fractions, even if the source noise is comparatively big and no signal averaging is utilized.

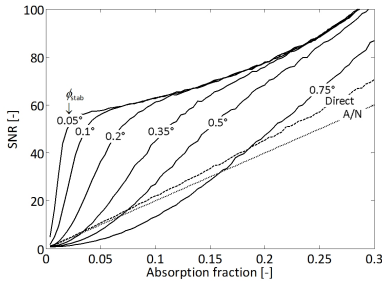


Fig. 7. Simulation of the signal-to-noise ratio as a function of absorption fraction in the gas cell for the normal TDLAS and the interferometric method with different phase stability performance. The phase stability numbers indicate the RMS phase fluctuation of the piezo position in degrees. The light intensity is the same in both arms of the interferometer.

## 6. Discussion

The absorption fraction detection limits of the newly presented technique is heavily dependent on the phase control, and with a system devoted to absorption measurements the SNR at low absorption fractions is many times better than for DLAS. The simulations presented are based on a relatively noisy system, a fact insinuating even better real-life performance with a stable laser. Another improvement possibility not mentioned here but discussed in [6] is the potential to actually amplify the absorption signal by, purposely, introducing an unbalance factor between the light intensity of the two arms of the spectrometer.

Important to remember is that the thermal noise of, e.g., the detector can become severe when the light level is small. This is, however, a limitation which can always be counter-acted with more incoming light and good (possibly cooled) detectors.

A general imperfection of the approach of stabilizing an interferometer by controlling one of the mirrors with a piezo-electric transducer the limited translation distance of this component. At certain occasions, if the interferometer drift is large, the piezo might reach one of the two position limits and the controlling thereby fails. Unavoidably, the stabilization will therefore occasionally collapse and the piezo should preferably be returned to its center position. We have, however, found that the recovery of the controlling can be very fast and the absorption measurement can rapidly be resumed.

Apart from the advantage of having quasi zero-background, the presented technique could also gain dramatically increased potential if some kind of additional modulation is employed. In the same way as in WMS and FMS, by introducing modulation, shifting the signal to higher frequencies, the absorption detection limit

could be improved. One possibility could be to modulate the unbalance factor by introducing a time varying loss in the reference arm.

## 7. Conclusions

We present a powerful new technique for sensitive gas detection based on molecular absorption. In contrast to normal absorption techniques, where a minute light reduction is observed in a high light intensity, the absorption is manifested in a signal rise from a basically zero background. Such a favorable detection condition resembles features typical in sensitive techniques such as fluorescence and photoacoustic spectroscopy, or in polarization spectroscopy. The new method is based on destructive light interference, similar to approaches previously used within broad-band light Fourier transform spectroscopy, but now brought into the field of tunable narrow-band lasers. The versatility of such a system can improve applied gas sensing systems in many situations, e.g. industry. The traditional delicacy in handling interferometers was overcome by a robust electronic stabilizing approach. The case of methane detection was illustrated, methane being an important green-house gas and a major cause of devastating coal-mine explosions.

## Acknowledgements

This work was supported by the Swedish Research Council. We would like to thank Michele Giunta and Clément Derrez for assistance in the initial parts of implementing the PID, and Prof. Stefan Andersson-Engels for valuable comments.

## References

1. P. Werle, F. Siemr, M. Gehrtz, and C. Bräuchle, "Quantum-limited FM-spectroscopy with a lead-salt diode laser," *Appl. Phys. B* 49, 99-108 (1989).
2. See, e.g., S. Svanberg, "Atomic and molecular spectroscopy, 4th ed.," Springer, Heidelberg (2004).
3. H. Bar-Lev, "A dual-beam infrared interferometer-spectrometer," *Infrared Phys.* 7, 93-98 (1967).
4. D. Kuehl, and P.R. Griffiths, "Dual-beam Fourier transform infrared spectrometer," *Anal. Chem.* 50, 418-422 (1978).
5. P.S. Jensen, and J. Bak, "Measurements of urea and glucose in aqueous solutions with dual-beam near-infrared Fourier transform spectroscopy," *Appl. Spectrosc.* 56, 1593-1599 (2002).
6. Z.G. Guan, M. Lewander, and S. Svanberg, "Quasi zero-background tunable diode laser absorption spectroscopy employing a balanced Michelson interferometer," *Opt. Expr.* 16, 21714-21720 (2008).
7. D.B. Neumann, and H.W. Rose, "Improvement of recorded holographic fringes by feedback control," *Appl. Opt.* 6, 1097-1104 (1967).
8. V.V. Krishnamachari, E.R. Andresen, S.R. Keiding, and E.O. Potma, "An active interferometer-stabilization scheme with linear phase control," *Opt. Expr.* 14, 5210-5215 (2006).

9. A.A. Freschi, and J. Frejlich, "Adjustable phase control in stabilized interferometry," *Opt. Lett.* 20, 635-637 (1995).
10. A.D. Kersey, D.A. Jackson, and M. Corke, "Passive compensation scheme suitable for use in the single-mode fibre interferometer," *Electron. Lett.* 18, 392-393 (1982).
11. T. W. Hänsch, and B. Couillaud, "Laser frequency stabilization by polarization spectroscopy of a reflecting reference cavity," *Opt. Commun.* 35, 441-444 (1980)
12. J. L. Hall, "Stabilized lasers and precision measurements," *Science* 202, 147-156 (1978)

# PAPER IX

## **Food monitoring based on diode laser gas spectroscopy**

M. Lewander, Z.G. Guan, L. Persson, A. Olsson, S. Svanberg.  
*Applied Physics B* **93**, 619 - 625 (2008).





## Food monitoring based on diode laser gas spectroscopy

M. Lewander · Z.G. Guan · L. Persson · A. Olsson ·  
S. Svanberg

Received: 16 April 2008 / Revised version: 14 July 2008 / Published online: 30 September 2008  
© Springer-Verlag 2008

**Abstract** Food is frequently packed in a controlled environment of gas, in order to extend shelf life. It is of great importance to be able to monitor the status of the packed food to ensure quality. We demonstrate a technique to monitor the gas inside packages non-intrusively by using a laser spectroscopic method in scattering solid materials. The technique named GASMAS (GAs in Scattering Media Absorption Spectroscopy) is based on tunable diode laser absorption spectroscopy and relies on the fact that free gas inside solid materials absorbs much sharper spectrally than the bulk material. Results from time dependent measurements of molecular oxygen and water vapour in packages of minced meat, bake-off bread, and the headspace of a milk carton are presented. We show that the technique allows gas measurements inside the food through the package, and assessment of the integrity of the package.

**PACS** 42.61.-Fi · 42.55.-Px · 82.80.-Dx

M. Lewander · Z.G. Guan · L. Persson · S. Svanberg (✉)  
Division of Atomic Physics, Lund University, P.O. Box 118,  
221 00 Lund, Sweden  
e-mail: [sune.svanberg@fysik.lth.se](mailto:sune.svanberg@fysik.lth.se)  
Fax: +46-46-2224250

A. Olsson  
Packaging Logistics Division, Lund University, P.O. Box 118,  
221 00 Lund, Sweden

*Present address:*  
L. Persson  
Sony Ericsson, 221 88 Lund, Sweden

### 1 Introduction

Food handling, preservation and packaging is an important aspect of great public interest and concern. The natural presence of oxygen in food products and packaging environments, hastens chemical breakdown and microbial spoilage of the food products. Traditional packaging methods are therefore largely being replaced by newer techniques, frequently falling under the Modified Atmosphere Packaging (MAP) or Controlled Atmosphere Packaging (CAP) categories. These methods replace the natural oxygen content inside the package with other gases such as carbon dioxide (CO<sub>2</sub>) or nitrogen (N<sub>2</sub>). Food decay and fouling are largely the result of oxidative processes on the one hand, and microbial action on the other hand. Such deteriorating processes are further accelerated with an increased storage temperature. Foods are frequently packed in plastic films, mostly made of polyethylene (PE), polyethylene terephthalate (PET), polyvinyl chloride (PVC), polypropylene (PP), or mixtures thereof. Films may be completely tight or being semi-permeable. An equilibrium of gas concentrations may arise due to the interaction with the product and the gas contained in the package. Here, different permeability of the film to different gases is an important aspect. Frequently, the gas composition is actively changed at the time of packaging, either by flowing gas during the packaging or by first subjecting the product to vacuum followed by inlet of the desired gas mixture [1–4].

Oxygen is a very active gas and it is therefore important to control its concentration in food packaging. Generally, it is desirable to reduce its concentration from ambient (21 percent) to a few percent, reducing the oxidative processes and thereby extending the shelf life. Reducing the oxygen concentration even further can lead to the onset of fermentation, which is unwanted in, e.g. fruit storage [5].

However, other products, such as bakery, poultry and bacon, can advantageously be stored in an oxygen-free surrounding. There is one instance when an oxygen concentration above the ambient (even up to 80%) is applicable; for the treatment of meat to keep the red pigment of myoglobin that gets reduced to deoxymyoglobin in anoxic environments, resulting in brown or greyish meat colours [6].

Carbon dioxide is an effective replacement to oxygen as an anti-microbiological gas. High concentrations of this gas prevent the growth of aerobic bacteria. In addition, low temperatures are good to prevent such growth, also because water and lipids dissolve carbon dioxide much better at low temperatures. Nitrogen behaves like an inert gas in food packaging. It does not dissolve well in water or lipids and thus ensures that a package looks filled and is not collapsing. Pasta is often packed in 100% nitrogen. Frequently, a combination of high carbon dioxide and nitrogen concentrations is used in MAP, e.g. in cheese and cured-meat packaging.

The packaging obviously also prevents a product from drying out and it protects the product from external microbial attack. *Aeromonas hydrophila*, *Clostridium botulinum*, *Yersina enterocolitica*, *Listeria spp.*, and *Escherichia coli* are examples of pathogens which grow even under refrigerated conditions [4].

It is of great importance to be able to assess the status of packed food to ensure its quality and suitability for consumption. Many sensing techniques have been developed. However, some spoilage micro-organisms do not cause overt evidence of spoilage [4, 7]. Gas chromatography and other sampling techniques require puncturing the package for gas extraction. Measurement techniques should preferably be non-intrusive in nature, in order to maintain packaging integrity and reduce waste of samples. In particular, not breaking the package is a matter of considerable importance in the MAP community. Measurement of the oxygen contents in a sealed package can be done by performing optical measurements. This can be done using small sensor disks prepared to change in colour in the presence of oxygen. Alternatively, and more commonly used, the sensor disk is prepared with a ruthenium- or platinum-containing dye, the fluorescence of which is quenched by oxygen [8]. However, the techniques are intrusive from the point of view that the small disks have to be introduced in the package at the time of sealing. There is a cost and a safety aspect ensuring that the active reactive agent does not influence the product or the consumer.

Gas absorption spectroscopy in a spectral region where the packaging material as well as the product is transparent is of particular interest to ensure non-intrusive, real-time measurements. This is the route we have taken, and below we will report our initial experience on gas monitoring in packages of meat, bakery products and milk.

Natural products, such as foods, frequently exhibit a very strong light scattering, making the application of normal gas

spectroscopic techniques [9] difficult. Normally, gas monitoring, whether pursued with classical or optical techniques, is limited to the headspace in transparent packages. Recently (in 2001), a method for gas analysis in scattering materials was introduced in our group. The GASMAS (GAs in Scattering Media Absorption Spectroscopy) technique analyses the sharp absorptive imprint in the scattered light leaving the organic material [10–12]. This means that the gas inside the product in the form of pores can be analysed optically for the first time non-invasively. The pores can be small compartments or a larger cell surrounded by scattering material. Mostly, molecular oxygen gas has been explored using semiconductor lasers operating around 760 nm, but also water vapour has been studied [12]. Examples of previously studied samples with the GASMAS technique are polystyrene foam, fruit, wood, and human sinuses [11–15]. The possibility to measure two gases simultaneously is a particular asset when using GASMAS, since the multiple scattering in porous/inhomogeneous media makes the optical path length undefined, complicating the straightforward application of the Beer–Lambert law for concentration evaluation. Water vapour (interrogated around 935 nm) can be used as a reference gas. Under the condition of a 100% saturation, which is the case in an enclosed volume with liquid water present, the concentration of water vapour is known, since it is only determined by the temperature. In this way the concentration of, e.g. oxygen can be determined by normalisation, assuming that the optical properties are close to similar for the two wavelengths employed, or that proper correction can be applied. This normalisation procedure has been used in connection with diagnostic gas monitoring for human sinuses and is discussed in [13] and [15].

In the food-related area, we have performed initial oxygen measurements on fruits, especially apples [14]. We have now extended these types of measurements to minced meat, bakery products and an intact gable top carton with milk.

In the next section we describe the experimental setup used for the measurements which are described in a subsequent section. The data analysis employed is then explained. Finally, the results are discussed and an outlook for the future is made.

## 2 Method

### 2.1 Experimental setup

An overview of the spectroscopic equipment used to monitor gases in food products in packages is given in Fig. 1. The setup is basically the same as developed for human sinus cavity monitoring, and a detailed description can be found in [15].

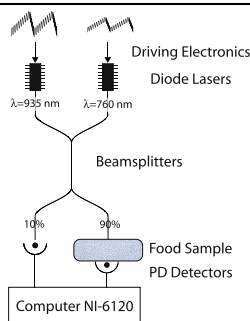


**Fig. 1** Experimental arrangement for simultaneous measurements of free molecular oxygen gas and water vapour

The wavelength of two pigtailed distributed feedback (DFB) lasers (Nanoplus) are scanned across the R11R11 absorption line of molecular oxygen at a vacuum wavelength of 760.564 nm, and the rotation-vibrational transition (vibration;  $(000) \rightarrow (121)$ , rotation;  $J'' = 3 \rightarrow J' = 4$ ,  $K''_a = 0 \rightarrow K'_a = 0$ ,  $K''_c = 3 \rightarrow K'_c = 4$ ) of water vapour at 935.686 nm, by employing sawtooth ramps at 5 Hz on the injection currents. At these wavelengths the food stuffs and the packages are transparent, enabling gas detection non-intrusively. Sinusoidal modulations of 10295 Hz for molecular oxygen and 9015 Hz for water vapour are superimposed on the sawtooth ramps to enable phase sensitive detection. The laser light is fibre-optically coupled together and divided into two arms, the reference arm and the sample arm. The reference arm carries a small fraction of the laser light and is directly guided to a photo diode (S3590-01, Hamamatsu). The sample arm contains a large portion of the laser light and is guided to the food sample. The diffusely emerging light of the food package is detected with a large area,  $18 \times 18$  mm, photo diode (S3204-08, Hamamatsu). The current signals from the detectors are amplified in two steps, first with a trans-impedance amplifier (DHPCA-100 and DHPCA-200, Femto Messtechnik GmbH) and then with Stanford Research Model SR560 units which also function as a high-pass filter (12 dB/octave at 3 kHz), removing the sawtooth part of the signals. The high-passed signals are synchronously sampled with a PCI card (National Instrument 6120 with maximum sample rate 800 000 S/s and 16 bits). The sample rate used in the experiments was 400 000 S/s. The collected data are then analysed by a Matlab program performing the digital wavelength modulation procedure enabled by the synchronised sampling.

## 2.2 Gas investigation

Packages of minced meat, bake-off bread, and milk in a gable top carton were investigated using the technique described.

To study the possibility to monitor changes in a modified atmosphere the gas composition was measured for one minced meat tray package over three days. The meat packages were purchased in a local grocery store, which had packed the minced meat in a tray of polystyrene foam, and covered it by a plastic film. The fibre-coupled light was injected through the plastic film covering the minced meat and the light passing through the meat and tray was detected. To reduce the data analysis process and due to previous experience of slow time dependencies an average time of 10 minutes was used despite that an average time of 1 minute was sufficient regarding photon statistic. Previous to the measurements the package was placed in a cold environment. However, the measurements were performed in surrounding room temperature, resulting in different temperatures of the sample over time. The temperature was monitored with a temperature logger (Picotechnology TH-03). Two temperature sensors were used. One was placed on top of the plastic film of the studied minced meat sample and one was inserted into the contents of a similar package as the one under-going the spectroscopic study. The temperature values were also averaged for 10 minutes.

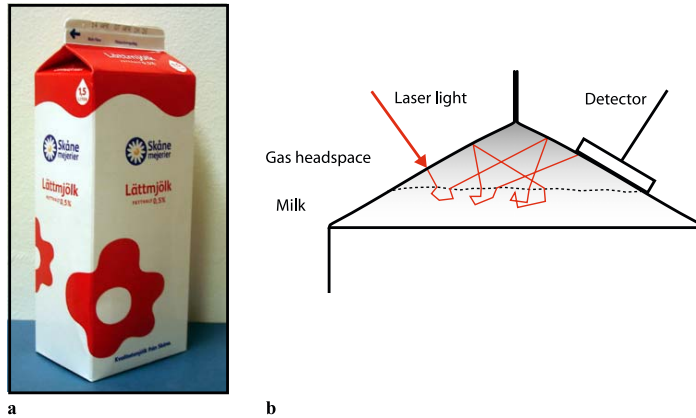
For the bake-off bread a plastic package containing eight buns packed in a modified oxygen-free atmosphere was used. The light was injected through the plastic film into one bun. The light was detected in a transmission mode. After one hour a large sized hole of about 1 cm in diameter was made in the package, resulting in air flowing into the package. The signal was measured for 24 further hours. An average time of 10 minutes was used to reduce the data evaluation process. The package was all the time at room temperature.

The headspace of a milk container was monitored by injecting the light through one surface and detecting scattered light through a different surface as shown in Fig. 2. The milk carton is made of white and red paper, about 0.5 mm thick. An averaging time of 1 minute was used. After around 30 minutes a small hole of about 2 mm diameter was introduced.

## 2.3 Data analysis

From the data collected with the PCI card, each laser, and hence the different gases, can be distinguished due to the different sinusoidal modulation frequencies. The synchronised sampled data enable post analysed phase-sensitive detection. Here this is done by using fast Fourier transformation. A detailed description of the technique is found

**Fig. 2** (a) Photograph of a milk carton. (b) Milk carton measurement geometry, one possible light path illustrated



in [16]. Briefly, the collected data are Fourier transformed. A window function selects the desired harmonic and down-converts it to zero frequency, before inverse Fourier transformation is made. The absolute value of the complex signal after phase adjustment results in the wavelength modulation spectroscopy (WMS) signal.

The 2f WMS signal is normalised by division with the offset of the 1f WMS signal, since this offset for given laser driving conditions is proportional to the light intensity. To correctly utilise such normalisation for quantitative gas analysis, it is necessary that calibration measurements on gas with known concentrations are performed for identical laser driving conditions. The normalised 2f WMS signal is then subjected to balanced detection. This process is made to subtract interference phenomena that occur in the setup, and other systematic defects. The balanced detection is made by minimising the difference between the normalised 2f WMS signal,  $y_{\text{samp}}(x)$ , and a function containing both a polynomial  $p(x)$ , a polynomial  $q(x)$  times the reference 2f WMS signal  $y_{\text{ref}}(x)$ , and an ideal signal shape  $y_{\text{ideal}}(x)$  (the 2f WMS signal obtained for a measured long air path). The variable  $x$  refers to sample point of the data:

$$y_{\text{samp}}(x) = p_0 + p_1x + p_2x^2 + (q_0 + q_1x)y_{\text{ref}}(x) + c \cdot y_{\text{ideal}}(x - x_0). \quad (1)$$

The shift of the ideal signal centered at  $x_0$  is present to account for small drifts. The amplitude of the fitted ideal signal is proportional to the absorption of the species- and the path length the photons have traveled in the sample. As a calibration the standard-addition method is used, by converting the amplitude to an equivalent mean path length  $L_{\text{eq}}$ . This property is the length the light has to travel through ambient air (at 24°C and a relative humidity of 20%) to obtain

the same signal, and is dependent of both the absorption of the gas and the traveled path length in the gas of the sample. We note that it is important to measure temperature and relative humidity accurately, since errors directly transfer into the evaluated oxygen concentration.

Due to the complex dependence of  $L_{\text{eq}}$  on the bulk properties, it is of interest to divide it with the  $L_{\text{eq}}$  of another species of known concentration for which the interrogated light has traveled the same path length. Under the assumption that scattering and absorption of the bulk material of the sample are equal for the two wavelengths used for measurement on the two gases, the path lengths are equal. If liquid water is present in a sample with closed volume, then the concentration of water vapour can be determined if the temperature is known.

### 3 Results and discussion

#### 3.1 Minced meat

Typical molecular oxygen and water vapour signals obtained in measurements of minced meat are shown in Fig. 3. The grey line is an ideal signal fitted according to (1).

Figure 4a shows the obtained  $L_{\text{eq}}$  values of water vapour in a minced meat package over time. The temperature measured inside a similar package is shown in Fig. 4b. The corresponding partial pressure is calculated through the Arden Buck equation [17] and presented in Fig. 4c. The temperature measured on top of the minced meat sample correlated with the one measured inside the meat, only with an offset as a difference. The sharp increase of signal can be seen to originate from the temperature dependence of the water vapour signal. To eliminate the temperature effect the ratio

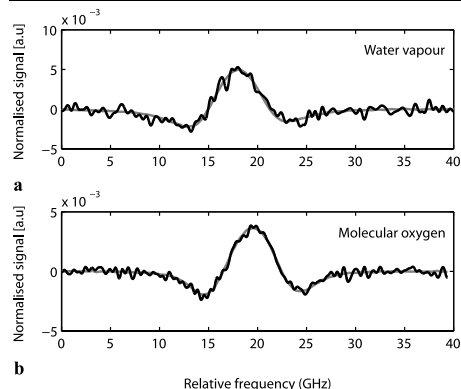


**Fig. 3** Signal obtained in measurements of a package of minced meat in transmission mode. The grey line indicates the fit of an ideal signal according to (1). (a) Water vapour signal. (b) Molecular oxygen signal

of the water vapour signal and the partial pressure of water vapour at the different times was calculated and is shown in Fig. 4d. The normalised water vapour curve increases slightly, which should not correspond to a concentration increase, since a relative humidity of 100% is expected in the closed volume. The change in the temperature normalised water vapour signal could thus be considered to be due to the change in the optical properties in the bulk material or in pore size for the packed minced meat.

The  $L_{eq}$  value of molecular oxygen in the minced meat package over time is presented in Fig. 5a. In Fig. 5b, the temperature-compensated water vapour signal, used as a reference to diminish the influence of the sample changes, is shown. The ratios of the  $L_{eq}$  values of molecular oxygen and the temperature-compensated water vapour values are presented in Fig. 5c. Division with reference gas measurement results in values not including the scattering and absorption properties of the bulk material, under the assumption that the optical properties in the bulk material are the same for the two wavelengths used. The calculated ratio corresponds to the molecular oxygen in the package, and can be seen to decrease over time, interpreted as the minced meat consuming ambient oxygen by oxidation.

### 3.2 Bake-off bread

Data for the bake-off bread are shown in Fig. 6. At the dashed line a hole of about 1 cm is made in the package, providing ambient air to freely pass into the package. The initial values of molecular oxygen signal, close to zero, show an absence of oxygen which indicated that the package is tight to oxygen prior to penetration. At puncture,

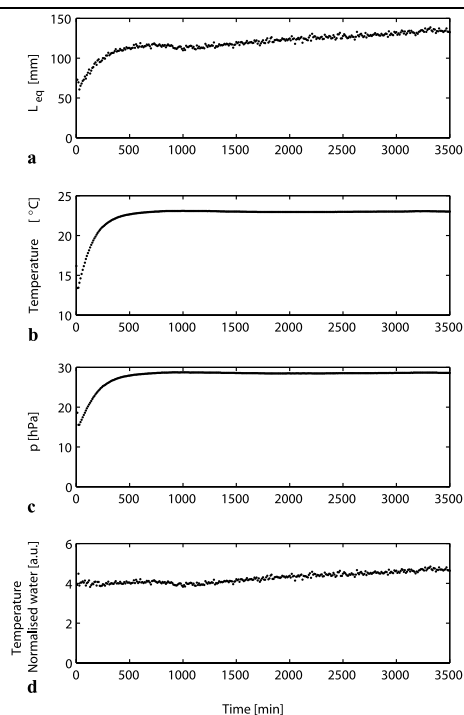


**Fig. 4** Measurement of minced meat over time: (a)  $L_{eq}$  of water vapour, (b) temperature measured inside a similar package, (c) saturated partial pressure of water vapour corresponding to measured temperature, (d) ratio between the  $L_{eq}$  of water vapour and the partial pressure of water vapour at different times

an immediate change is measured in the molecular oxygen and water vapour content. This can be interpreted as the bake-off bread trying to reach a new equilibrium in the new ambient situation. The increase of the water vapour signal shows that a 100% relative humidity was not present in the non-perforated package due to lack of water, not allowing saturation. However, water vapour was present in the non-perforated package since an initial value of 450 mm was measured. The time constant of the diffusion of molecular oxygen and water vapour into the bread bun was  $\tau = 211$  min and  $\tau = 258$  min, respectively, using an exponential fit.

### 3.3 Milk carton headspace

Headspace measurements through a scattering package were performed by studying the gable top of a milk carton. Typical signals from the milk carton measurements are shown

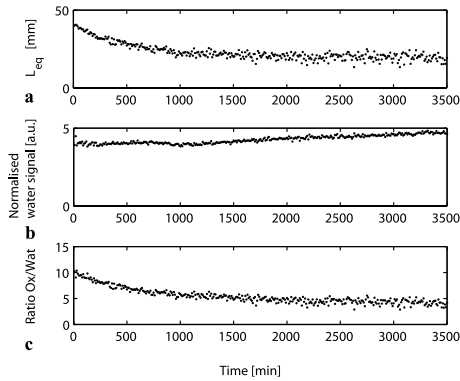


**Fig. 5** Measurement of minced meat over time: (a)  $L_{eq}$  values of molecular oxygen, (b) temperature normalised water vapour signal, (c) ratio of  $L_{eq}$  of oxygen and the temperature-compensated water vapour signal

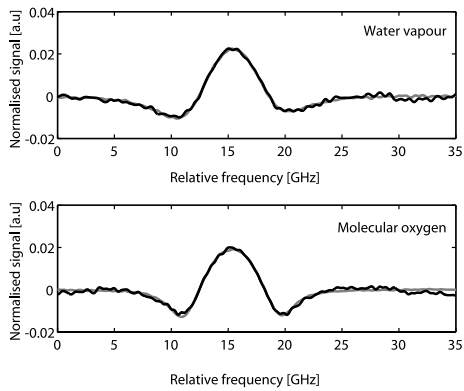


**Fig. 7** Signals from measurement on the headspace of a milk carton, with fitted ideal curves (grey). The accumulation time was 60 s

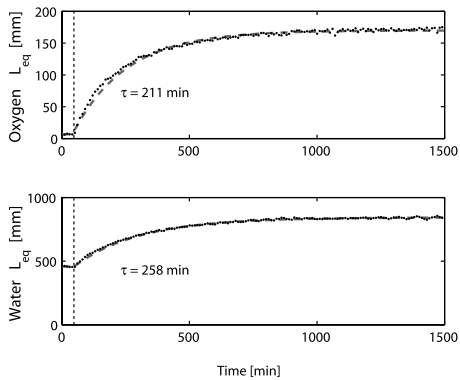


**Fig. 6** A bake-off bun inside a modified atmosphere. The vertical dashed line indicates when a hole was made in the package. The grey dashed lines are exponential fits to the data resulting in the indicated time constants  $\tau$

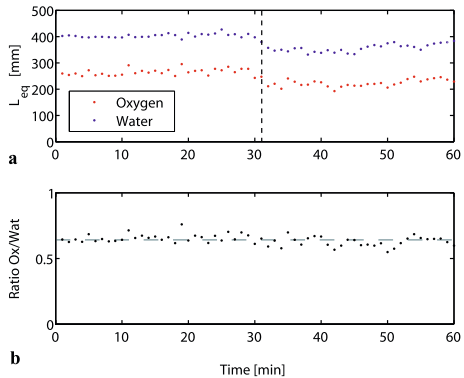


**Fig. 8** Data obtained for the headspace of a milk carton. For each data point an accumulation time of 60 s was used. At time around 30 minutes a small hole was punctured at the top of the package. The grey dashed line is drawn for the guidance of the eye

in Fig. 7 and correspond to an  $L_{eq}$  of 220 mm of molecular oxygen and an  $L_{eq}$  of 380 mm of water vapour. Multiple passages over the headspace due to the scattering package and milk indicated in Fig. 2 result in a larger signal than corresponding to the physical geometry. Data for water vapour and molecular oxygen from the measurements over time are shown in Fig. 8a. As the package is perforated an offset in the water vapour and oxygen signal is seen. Under the perforating process small displacements of the detector and injecting fibre are noted, which can provide an explanation for the offset. Small displacements of especially the injecting fi-

bre can give effects on the path length of the detected light. In Fig. 8b, the ratio of the oxygen and water vapour signal is presented and is stable over the whole investigation. A 100% relative humidity is expected since the large wet surface fully moisturises the gas in the head space in spite of the ventilation. This behaviour has also been observed for human sinus cavities [13]. The stable ratio suggests that the oxygen concentration in the headspace in the milk carton is the same as in the ambient air. It can be noted that the variations seen in the stable part of the measurement are not

diminished with the normalisation process with a reference gas. Slow varying residual interference effects are possible explanations to this phenomenon which demands further examination.

#### 4 Conclusions

We present results from measurements showing the feasibility of the GASMAS technique as a powerful tool for studying food stuffs and food packaging. Measurements on minced meat packages, bake-off bread packages and the headspace in a milk carton illustrate the possibility to monitor the packed food stuff, as well as the package integrity, non-intrusively. The stable or only small increase in the temperature-compensated water vapour signal in the minced-meat measurement suggests that in minced-meat monitoring the reference gas might not be necessary in an industrial monitoring device. The increase of water vapour signal as the bake-off bread package is penetrated reflects that a 100% relative humidity was not reached in the non-punctured package. The concentration of water vapour can thus not be calculated and not used as a reference gas. The non-response for puncture of the ratio in the milk carton measurement indicates that the oxygen concentration in the headspace is the same as in the ambient air. The change in the optical path length due to the small displacement in the perforating process was shown to be eliminated by using water vapour as a reference gas. This supports the use of a known water vapour concentration for extracting the oxygen concentration. The oxygen signal referenced to a temperature-compensated water vapour signal is then related to the oxygen concentration, and might be used for non-intrusive checking of fouling. The assumption that the sampled volume of the two wavelengths used is similar has been discussed in [13] where the validity for the case of human sinus monitoring was experimentally noted. At any rate, a correction factor could be determined by independent gas concentration measurement. These aspects will be further explored.

The measurements of the bake-off bread are promising in the way that they indicate that the GASMAS technique is

suitable for non-intrusive monitoring of the tightness of the food package. After these proof-of-principle measurements we now aim at in-depth studies of different products in close cooperation with expertise in the corresponding fields.

**Acknowledgements** We are thankful to Gunilla Jönson for support. This work was financially supported by VINNOVA through the Next Generation Innovative Logistic Centre under contract NGIL F4A 07-007, the Swedish Research Council (VR) and the Knut and Alice Wallenberg Foundation.

#### References

1. I.J. Church, A.L. Parsons, J. Sci. Food Agric. **67**, 143 (1995)
2. C.A. Phillips, Int. J. Food Sci. Technol. **31**, 463 (1996)
3. J.N. Farber, L.J. Harris, M.E. Parish, L.R. Beuchat, T.V. Suslow, J.R. Gorney, E.H. Garrett, F.F. Busta, Comp. Rev. Food Sci. Food Safety (Suppl.) **2**, 142 (2003)
4. E.H. Marth, Food Technol. **52**, 57 (1998)
5. R.M. Beaudry, Postharvest Biol. Technol. **15**, 293 (1999)
6. C.G. Bailey, D.S. Jayas, R.A. Holley, L.E. Jeremiah, C.O. Gill, Food Res. Int. **30**, 743 (1997)
7. E. Kress-Rodgers, Instrumentation for food quality assurance, in *Instrumentation and Sensors in the Food Industry*, ed. by E. Kress-Rodgers (Woodhead Publishing, London, 1998), pp. 1–34
8. D.B. Papkovsky, Sensors for food safety and security, in *Optical Chemical Sensors*, NATO Science Series, vol. 224, ed. by F. Baldina, A.N. Chester, J. Homola, S. Martellucci (Springer, Heidelberg, 2006)
9. M. Sigrist (ed.), *Air Monitoring with Spectroscopic Techniques* (Wiley, New York, 1994)
10. M. Sjöholm, G. Somesfalean, J. Alnis, S. Andersson-Engels, S. Svanberg, Opt. Lett. **26**, 16 (2001)
11. G. Somesfalean, M. Sjöholm, J. Alnis, C. af Klinteberg, S. Andersson-Engels, S. Svanberg, Appl. Opt. **41**, 3538 (2002)
12. M. Andersson, L. Persson, M. Sjöholm, S. Svanberg, Opt. Express **14**, 3641 (2006)
13. L. Persson, M. Andersson, M. Cassel-Engquist, K. Svanberg, S. Svanberg, J. Biomed. Opt. **12**, 054001 (2007)
14. L. Persson, H. Gao, M. Sjöholm, S. Svanberg, Opt. Laser Eng. **44**, 687 (2006)
15. L. Persson, M. Lewander, M. Anderson, K. Svanberg, S. Svanberg, Appl. Opt. **47**, 2028 (2008)
16. T. Svensson, M. Andersson, L. Rippe, S. Svanberg, S. Andersson-Engels, J. Johansson, S. Folestad, Appl. Phys. B **90**, 345 (2008)
17. A. Buck, J. Appl. Meteorol. **20**, 1527 (1981)





# PAPER X

## **Clinical system for non-invasive *in situ* monitoring of gases in the human paranasal sinuses**

M. Lewander, Z.G. Guan, K. Svanberg, S. Svanberg, T. Svensson.  
*Optics Express* **17**, 10849-10863 (2009).



# Clinical system for non-invasive *in situ* monitoring of gases in the human paranasal sinuses

Märta Lewander<sup>1</sup>, Zuguang Guan<sup>1</sup>, Katarina Svanberg<sup>2</sup>, Sune Svanberg<sup>1</sup>, and Tomas Svensson<sup>1</sup>

<sup>1</sup>Department of Physics, Lund University, Sweden

<sup>2</sup>Department of Oncology, Lund University Hospital, Sweden

[marta.lewander@fysik.lth.se](mailto:marta.lewander@fysik.lth.se)

**Abstract:** We present a portable system for non-invasive, simultaneous sensing of molecular oxygen (O<sub>2</sub>) and water vapor (H<sub>2</sub>O) in the human paranasal cavities. The system is based on high-resolution tunable diode laser spectroscopy (TDLAS) and digital wavelength modulation spectroscopy (dWMS). Since optical interference and non-ideal tuning of the diode lasers render signal processing complex, we focus on Fourier analysis of dWMS signals and procedures for removal of background signals. Clinical data are presented, and exhibit a significant improvement in signal-to-noise with respect to earlier work. The *in situ* detection limit, in terms of absorption fraction, is about  $5 \times 10^{-5}$  for oxygen and  $5 \times 10^{-4}$  for water vapor, but varies between patients due to differences in light attenuation. In addition, we discuss the use of water vapor as a reference in quantification of *in situ* oxygen concentration in detail. In particular, light propagation aspects are investigated by employing photon time-of-flight spectroscopy.

© 2009 Optical Society of America

**OCIS codes:** (170.4940) Otolaryngology; (170.1610) Clinical applications; (170.3890) Medical optics instrumentation; (170.6510) Spectroscopy, tissue diagnostics; (300.6260) Spectroscopy, diode lasers; (300.6320) Spectroscopy, high-resolution; (170.7050) Turbid media; (170.5280) Photon migration; (300.6500) Spectroscopy, time-resolved

## References and links

1. P. Martin, "Near-infrared diode laser spectroscopy in chemical process and environmental air monitoring," *Chem. Soc. Rev.* **31**, 201–210 (2002).
2. I. Linnerud, P. Kaspersen, and T. Jæger, "Gas monitoring in the process industry using diode laser spectroscopy," *Appl. Phys. B* **67**, 297–305 (1998).
3. G. Galbacs, "A review of applications and experimental improvements related to diode laser atomic spectroscopy," *Appl. Spectrosc. Rev.* **41**, 259–303 (2006).
4. M. Sjöholm, G. Somesfalean, J. Alnis, S. Andersson-Engels, and S. Svanberg, "Analysis of gas dispersed in scattering media," *Opt. Lett.* **26**, 16–18 (2001).
5. T. Svensson, M. Andersson, L. Rippe, J. Johansson, S. Folestad, and S. Andersson-Engels, "High sensitivity gas spectroscopy of porous, highly scattering solids," *Opt. Lett.* **33**, 80–82 (2008).
6. J. Alnis, B. Anderson, M. Sjöholm, G. Somesfalean, and S. Svanberg, "Laser spectroscopy of free molecular oxygen dispersed in wood materials," *Appl. Phys. B* **77**, 691–695 (2003).
7. T. Svensson, M. Andersson, L. Rippe, S. Svanberg, S. Andersson-Engels, J. Johansson, and S. Folestad, "VCSEL-based oxygen spectroscopy for structural analysis of pharmaceutical solids," *Appl. Phys. B* **90**, 345–354 (2008).

#109769 - \$15.00 USD

(C) 2009 OSA

Received 7 Apr 2009; revised 4 May 2009; accepted 5 May 2009; published 15 Jun 2009

22 June 2009 / Vol. 17, No. 13 / OPTICS EXPRESS 10849

8. L. Persson, M. Andersson, M. Cassel-Engquist, K. Svanberg, and S. Svanberg, "Gas monitoring in human sinuses using tunable diode laser spectroscopy," *J. Biomed. Opt.* **12**, 054,001 (2007).
9. T. Svensson, "Pharmaceutical and biomedical applications of spectroscopy in the photon migration regime," PhD Thesis, Lund University (2008). URL [www.atomic.physics.lu.se/biophotonics/publications/phd\\_theses](http://www.atomic.physics.lu.se/biophotonics/publications/phd_theses).
10. S. Svanberg, "Gas in scattering media absorption spectroscopy - GASMAS," *Proc. SPIE* **7142**, 714202 (2008).
11. J. A. Silver, "Frequency-modulation spectroscopy for trace species detection: theory and comparison among experimental methods," *Appl. Opt.* **31**, 707–717 (1992).
12. P. Kluczynski, J. Gustafsson, Å. Lindberg, and O. Axner, "Wavelength modulation absorption spectrometry - an extensive scrutiny of the generation of signals," *Spectrochim. Acta B* **56**, 1277–1354 (2001).
13. T. Fernholz, H. Teichert, and V. Ebert, "Digital, phase-sensitive detection for in situ diode-laser spectroscopy under rapidly changing transmission conditions," *Appl. Phys. B* **75**, 229–236 (2002).
14. M. Andersson, L. Persson, T. Svensson, and S. Svanberg, "Flexible lock-in detection system based on synchronized computer plug-in boards applied in sensitive gas spectroscopy," *Rev. Sci. Instrum.* **78**, 113,107 (2007).
15. W. Fokkens, V. Lund, and J. Mullol, "European position paper on rhinosinusitis and nasal polyps 2007," *Rhinol. Suppl.* **20**, 1–136 (2007).
16. C. Bachert, K. Hormann, R. Mosges, G. Rasp, H. Riechelmann, R. Muller, H. Luckhaupt, B. A. Stuck, and C. Rudack, "An update on the diagnosis and treatment of sinusitis and nasal polyposis," *Allergy* **58**, 176–191 (2003).
17. L. Persson, M. Andersson, T. Svensson, M. Cassel-Engquist, K. Svanberg, and S. Svanberg, "Non-intrusive optical study of gas and its exchange in human maxillary sinuses," *Proc. SPIE* **6628**, 662804 (2007).
18. L. Persson, M. Lewander, M. Andersson, K. Svanberg, and S. Svanberg, "Simultaneous detection of molecular oxygen and water vapor in the tissue optical window using tunable diode laser spectroscopy," *Appl. Opt.* **47**, 2028–2034 (2008).
19. "Application Note 1040: Coherent Sampling vs. Window Sampling," Tech. rep., Maxim (2002).
20. A. Buck, "New equations for computing vapor-pressure and enhancement factor," *J. Appl. Meteorol.* **20**, 1527–1532 (1981).
21. T. Svensson, E. Alerstam, M. Einarsson, K. Svanberg, and S. Andersson-Engels, "Towards accurate in vivo spectroscopy of the human prostate," *J. Biophoton.* **1**, 200–203 (2008).
22. E. Alerstam, S. Andersson-Engels, and T. Svensson, "Improved accuracy in time-resolved diffuse reflectance spectroscopy," *Opt. Express* **16**, 10,434–10,448 (2008).
23. B. Chance, J. Leigh, H. Miyake, D. Smith, S. Nioka, R. Greenfield, M. Finander, K. Kaufmann, W. Levy, M. Young, P. Cohen, H. Yoshioka, and R. Boretsky, "Comparison of time-resolved and time-unresolved measurements of deoxyhemoglobin in brain," *P. Natl. Acad. Sci. USA* **85**, 4971–4975 (1988).
24. R. Engelbrecht, "A compact NIR fiber-optic diode laser spectrometer for CO and CO<sub>2</sub>: analysis of observed 2f wavelength modulation spectroscopy line shapes," *Spectrochim. Acta A* **60**, 3291–3298 (2004).

## 1. Introduction

High-resolution tunable diode laser absorption spectroscopy (TDLAS) is a powerful tool for selective and sensitive gas sensing, and is widely used in science and technology [1, 2, 3]. The conventional experimental configuration involves either open path monitoring or gas cells (single or multi-pass), while data evaluation typically relies on lineshape theory in combination with the Beer-Lambert-Bouguer law of light transmission. In 2001, it was demonstrated that TDLAS can be used also for sensing of gases inside porous and highly scattering (turbid) solids [4]. In contrast to the conventional conditions described above, measurements of gases in pores of solids involve working with diffuse light, heavy attenuation, severe optical interference and unknown optical pathlengths [5]. To emphasize these unusual and aggravating experimental conditions, the technique is often separately termed *gas in scattering media absorption spectroscopy* (GASMAS). The technique has been used to characterize various porous materials, such as polystyrene foam [4], wood [6], pharmaceutical tablets [7], and human sinus cavities [8]. Reviews of GASMAS are available in Refs. [9, 10].

A fundamental aspect of GASMAS is the great contrast between the spectrally sharp absorption lines of free gases (lines used in this work are about 0.006 nm FWHM) and the slowly varying absorption spectra of solids. This contrast allows detection of weak gas absorption even under heavy background absorption. So far, GASMAS has been used to detect molecular oxygen (O<sub>2</sub>) at around 760 nm, or water vapour (H<sub>2</sub>O) around 935 or 980 nm. Since

the corresponding absorption lines are weak, GASMAS has relied on wavelength modulation spectroscopy (WMS) to increase sensitivity. WMS is a well established tool in TDLAS [11], and involves sinusoidal modulation of the laser wavelength and detection at harmonics of the modulation frequency (detection at the second harmonic,  $2f$ , is a common choice). The WMS technique shifts the absorption signal to a frequency range less affected by low-frequency noise of system components, and allows baseline-free recordings of derivative-like versions of the actual absorption feature [12, 9]. Traditionally, WMS relies on analog function generators for laser modulation, lock-in amplifiers for detection of signal harmonics, and oscilloscopes for data acquisition. By synchronizing data acquisition with function generators for laser modulation, it is possible to simultaneously record multiple WMS harmonics without the need of lock-in amplifiers [13]. The WMS system can be further simplified by employing a single plug-in board with synchronized outputs and inputs for laser modulation and data acquisition [14]. These approaches can be termed digital wavelength modulation spectroscopy (dWMS), and is based on recording of the raw detector signals. Equivalents to the traditional WMS signal, as generated by a lock-in amplifier, are obtained by employing a digital lock-in amplifier (e.g. the LabVIEW lock-in toolkit) [14] or by means of Fourier analysis [13, 7].

Diagnostics of the human sinuses is a particularly interesting application of the GASMAS technique [8]. The maxillary and frontal sinuses are located behind the cheek bones and the frontal bone, respectively. In a healthy state the sinuses are air filled cavities ventilated through the nasal ventricle. Sinusitis, now often termed rhinosinusitis, is an infection of the sinuses, causing nasal blockage and mucus obstruction [15]. Current diagnostic methods of the paranasal sinuses include case history and, in selected cases, computed tomography (CT) [16]. The diagnostic potential of the GASMAS technique has been demonstrated on volunteers with a laboratory system for oxygen spectroscopy [17, 8]. As discussed in Ref. [8], the diagnostic value of the approach may be significantly increased by incorporating simultaneous sensing of both water vapor and molecular oxygen. The reason is that cavities in the human body often can be assumed to be at  $37^\circ\text{C}$  and at 100% relative humidity, and that the *in situ* concentration of water vapor thus can be considered known. Assuming that the optical pathlength through the gas-filled cavity is the same at 760 nm and 935 nm, the water vapor data can then provide the information on optical pathlength needed to estimate the *in situ* oxygen concentration. Sequential sensing of  $\text{H}_2\text{O}$  and  $\text{O}_2$  in human sinuses has been demonstrated using a laboratory setup based on traditional, analog WMS [8].

In this work, we present a portable system designed for a clinical trial aimed at monitoring gas in the paranasal sinuses of 40 patients undergoing investigation for sinus-related problems. The system is based on dWMS, and allow simultaneous sensing of  $\text{H}_2\text{O}$  and  $\text{O}_2$ . The clinical performance is significantly better than previous reported clinical work [18] (tenfold improvement in signal-to-noise). We report our experiences from using pigtailed diode lasers and optical fibers in TDLAS instruments, and the signal processing required to reach the improved performance is described in detail. In addition, for the first time, we employ photon time-of-flight spectroscopy (PTOFS) to investigate the photon migration aspects of optical sinus diagnostics. By estimating photon pathlengths at 786 nm and 916 nm, we can scrutinize the idea of using the water vapor absorption at 935 nm to estimate optical pathlength at 760 nm. Finally, we discuss the possibility of constructing a simpler TDLAS system for monitoring of gas in the paranasal sinuses.

## 2. Materials and methods

### 2.1. TDLAS instrumentation

The TDLAS system for our clinical application is a fiber-based dual beam system based on coherent sampling and digital wavelength modulation spectroscopy (dWMS). A schematic of

the instrumentation is given in Fig. 1. The wavelength of two pigtailed DFB lasers (Nanoplus, Germany) are scanned across single absorption lines of molecular oxygen (at 760.445 nm, peak absorption  $2.6 \times 10^{-5} \text{ mm}^{-1}$  for 21%  $\text{O}_2$ ) and water vapor (at 935.686 nm, peak absorption  $2.4 \times 10^{-4} \text{ mm}^{-1}$  for  $\text{H}_2\text{O}$  at 100% relative humidity and 37 °C). Diode laser modulation and data acquisition is managed by a PCI board with synchronized outputs and outputs (NI-6120, National Instruments). The modulation consists of a  $f_{scan} = 5 \text{ Hz}$  triangular waveform for wavelength scanning together with a faster sinusoidal waveform for wavelength modulation. The amplitude of the wavelength modulation is chosen so that the  $2f$  harmonics are maximized, i.e. set to 2.2 times the absorption linewidth (half width at half maximum). Straightforward separation of the two absorption signals is ensured by choosing different modulation frequencies,  $f_m$ , for the wavelength modulation of the two lasers (9,015 and 10,295 Hz for the oxygen and water vapor lasers, respectively) [18]. Modulation signals are sent to two diode laser drivers (06DLD103, Melles Griot), which are used to operate injection currents as well as for temperature stabilization.

Severe optical interference originating from optical components makes single beam TDLAS operation unfeasible. Instead, single mode optical fiber couplers are used to create a dual beam configuration (sample and reference arms). The output from the two pigtailed diode lasers are about 4 mW each. Due to non-ideal performance of these couplers, the optical powers available in the sample arm are only 0.25 mW (935 nm) and 1 mW (760 nm). A fiber probe is used to inject light into the tissue, and a  $18 \times 18 \text{ mm}^2$  unbiased large-area photodiode (S3204-8, Hamamatsu) is used to detect transmitted diffuse light. Light in the reference arm is detected by a  $10 \times 10 \text{ mm}^2$  unbiased photodiode (S3590-01, Hamamatsu). Low-noise transimpedance amplifiers (DLPCA-200, FEMTO Messtechnik, Germany) convert photodiode currents, and the amplification is typically set to  $10^6$  or  $10^7 \text{ V/A}$  in clinical measurements. The resulting voltage signals are coherently sampled at  $f_s = 400,000 \text{ samples/s}$  by the PCI board. Averaged voltage data are stored on disc and post-processing of data is required to obtain absorption imprints. Each dataset corresponds to one full period of the scan frequency, i.e. 80,000 samples (and is in general a result of averaging over several scans). The signal processing is described in detail in the following section. Note that both modulation frequencies, as well as the scan frequency, satisfy the criteria for coherent sampling (i.e. an integer number of cycles are sampled) [19].

## 2.2. Signal processing

As described in the previous section, the system stores an amplified version of the raw photodiode output. In contrast to conventional WMS, where a lock-in amplifier is used to monitor a single frequency channel, this means that the data contains information on multiple harmonics, as well as on detected intensities. For the case of single beam setups, Fourier methods for extracting WMS signals from such data have been described by Fernholz *et al.* [13] and Svensson *et al.* [7]. However, due to complex background signals, the dual beam data generated by the system used in this work requires special treatment. A detailed description of the signal processing is therefore given below.

An example of acquired raw data from the sample arm,  $u_s(t)$ , and its corresponding Fourier spectrum is shown in Fig. 2. Data from the two arms, i.e.  $u_s(t)$  and  $u_r(t)$ , are processed in similar ways, and we therefore drop the subscripts in steps that apply for both signals. The initial processing steps are performed in the Fourier domain (Eq. 1).

$$U(\omega) = \mathcal{F}\{u(t)\} \quad (1)$$

As can be seen in Fig. 2, individual harmonics of the modulation frequencies appear as separated peaks in the Fourier spectrum. In order to study a specific harmonic  $n$  of a specific modulation frequency  $\omega_m$ , the signal simply needs to be bandpass filtered. The bandpass filter-

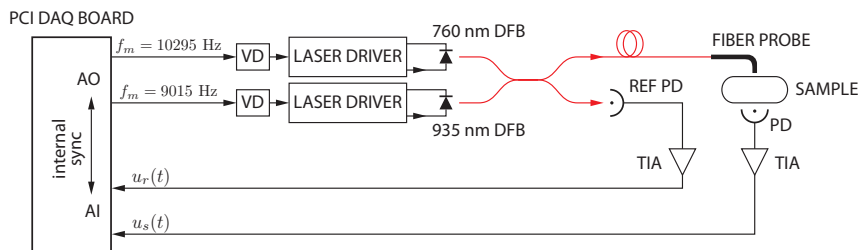


Fig. 1. A schematic of the instrumentation. A PCI board with synchronized analog outputs (AO) and analog inputs (AI) manages both laser modulation and data acquisition. In order to utilize the full dynamic range of the AO, voltage dividers (VD) are used to reduce the signal level before modulation signals reach the diode laser drivers. Simultaneous sensing of  $O_2$  and  $H_2O$  is achieved by using two pigtailed DFB diode lasers operating around 760 nm and 935 nm, respectively. In order to allow separation of the two corresponding absorption signals, the two lasers are operated at different modulation frequencies,  $f_m$ . The laser outputs are arranged in a dual beam configuration: one photodiode (PD) provides the reference signal, and a second records a signal carrying gas absorption information. Transimpedance amplifiers (TIA) convert and amplify the photodiode currents, and the resulting voltages are coherently sampled and averaged.

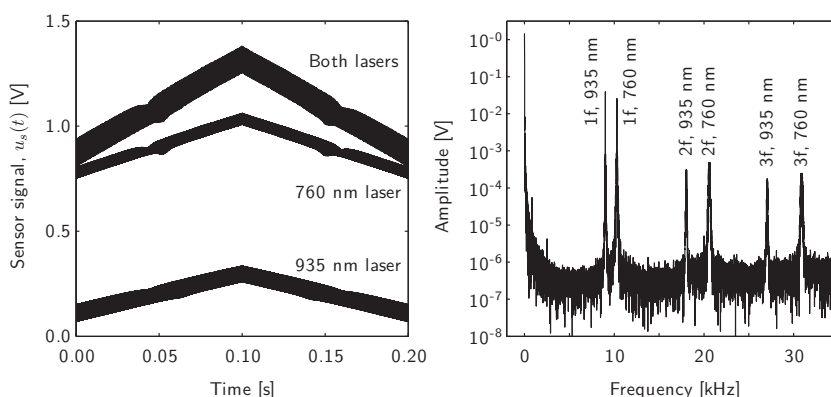


Fig. 2. Raw data exemplified by a measurement on a 1000 mm path through ambient air. Two lasers contribute to the detected signal, and the individual contributions and their sum are shown in (left). A single-sided amplitude spectrum of the full signal (both lasers) is given in (right), showing 1-3 $f$  WMS components due to interactions with absorption features. Note that the 1 $f$  components are dominated by residual amplitude modulation (RAM) of the diode lasers (see text for a discussion on RAM).



ing is achieved in the frequency domain by using a super-Gauss window centered at  $+\omega_m$  with the width  $\delta\omega$ . The operation is stated in Eq. 2 (where the factor 2 is included to compensate for the signal amplitude lost by neglecting the negative frequencies), and the resulting signal is denoted  $U_{nf}(\omega)$ .

$$U_{nf}(\omega) = 2 \times U(\omega) \times \exp\left(-\left(\frac{\omega - n \times \omega_m}{\delta\omega}\right)^8\right) \quad (2)$$

In order to study the evolution of  $\omega_m$  frequency content as the laser is scanned, we down-convert  $\omega_m$  to zero frequency,

$$V_{nf}(\omega) = U_{nf}(\omega + n \cdot \omega_m), \quad (3)$$

and perform a subsequent inverse Fourier transformation:

$$v_{nf}^*(t) = \mathcal{F}^{-1}\{V_{nf}(\omega)\}. \quad (4)$$

The resulting time-dependent signal,  $v_{nf}^*(t)$ , is complex valued and can be studied in phase-amplitude plots (a plot of the real versus the imaginary part) [13, 7]. In a phase-amplitude plot, a pure sinusoidal signal will thus appear as a single dot. The signal amplitude is given by the distance to the origin, and its phase is given by the angle with respect to e.g. the real axis. In WMS experiments, the strength of harmonics vary as the laser is scanned across an absorption feature (or other transmission profiles). In the ideal case (linear tuning characteristics), the phase-amplitude plot will therefore show values along a line (pure amplitude changes and  $180^\circ$  phase jumps). For the  $1f$  harmonic, the line will have a significant offset due to the residual amplitude modulation (RAM) of the laser diode (modulation of the laser frequency is accompanied by power modulation). For higher harmonics, WMS is ideally free from baseline, and the line will therefore cross the origin. It is important to realize that a phase-amplitude plot with values along a line does not guarantee a good signal-to-noise ratio. The reason is that all transmission profiles, not only gas absorption, will give rise to line-type phase-amplitude plots (including etalon fringes and other interference effects that typically limit TDLAS).

Before taking a look at experimental signals, it is, however, useful to make some additional processing. In order to reach a quantitatively relevant signal, it is necessary to perform intensity correction (signals are proportional to the detected intensity). The detected signal is, however, a sum of the contributions from the two lasers (wavelengths). In order to determine the individual contribution of a specific light source, we use the  $1f$  RAM of the lasers. Since the two laser are modulated using different frequencies, the  $1f$  RAM signals are easily distinguished (and given by the average of  $v_{1f}^*(t)$ ). The exact procedure for intensity correction is stated in Eq. 5, and the resulting normalised quantity is denoted  $\bar{v}_{nf}^*(t)$ . Note that a time-dependent calibration factor,  $k(t)$ , is introduced and used to convert the  $1f$  RAM into a measure of average signal level and its evolution as the laser is scanned. This manoeuvre makes it possible to compare obtained signal levels with WMS theory (e.g. that the  $2f$  WMS peak signals should corresponds to about 0.3 times the actual absorption fraction). Note also, that the procedure includes removal of offsets (these are not of any diagnostic value in subsequent analysis).

$$\bar{v}_{nf}^*(t) = \frac{v_{nf}^*(t) - \text{mean}(v_{nf}^*(t))}{k(t) \times \text{mean}(v_{1f}^*(t))}. \quad (5)$$

Figure 3 shows  $1-3f$  phase-amplitude plots originating from interactions with an absorption line of molecular oxygen. As can be seen in the left column, strong absorption results in the expected line-type phase-amplitude plots. The middle column shows sample arm data from experiments on  $L=2$  cm ambient air, giving an absorption fraction typical to that encountered in the clinical experiments. There, the phase-amplitude plot no longer exhibit the line-type structure expected in ideal WMS experiments. In order to emphasize this, the figure compares data

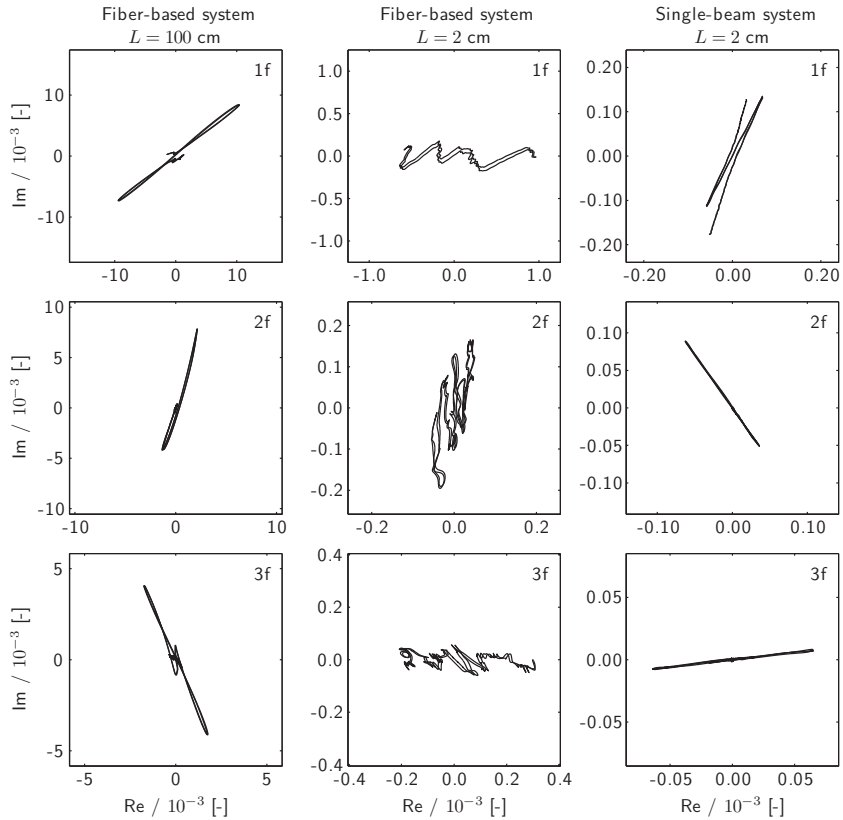


Fig. 3. Phase-amplitude plots of sample arm  $\nabla_{nf}^*(t)$ -signals originating from ambient air (free-space) measurements. In order to show the signal structure, offsets have been removed. For the fiber-based system used in the present work, large absorption is required to produce a line-type phase-amplitude plot (left column,  $L=100$  cm pathlength through ambient air,  $3 \times 10^{-2}$  absorption fraction). In the case of low absorption, the phase plot is completely dominated by background effects (middle column,  $L=2$  cm,  $5 \times 10^{-4}$  absorption fraction). In contrast, single beam operation without optical fibers results in line-type phase-amplitude plots even at low absorption (right column,  $L=2$  cm, optical system as in Ref. [5] while data acquisition and laser control is managed by the system presented in this paper).

obtained using the fiber-based system (left and middle columns) with data obtained using an optical system that involves nothing but a VCSEL diode laser and a photodiode (right column). When utilizing our fiber-based setup, the observed signal structure is a complex result of non-ideal laser tuning, interference fringes and gas absorption. In order to extract the often minor contribution from gas absorption, we have developed a scheme for subtraction of background effects. We assume that the signal registered in the sample arm,  $\bar{v}_s^*$ , can be described by a combination of the simultaneously recorded reference arm signal,  $\bar{v}_r^*$ , and a so called absolute reference recording of a strong, well-known gas absorption,  $\bar{v}_{a.r.}^*$  (recorded using the same system, but not simultaneously). In this work, the absolute reference originates from measurements in ambient air ( $L_{a.r.} = 1$  m for evaluation of clinical data). The model is explicitly stated in Eq. 6 (note that the  $nf$ -subscript has been dropped).

$$\bar{v}_s^*(t) \simeq p^*(t) + q^*(t) \times \bar{v}_r^*(t) + c \times \bar{v}_{a.r.}^*(t - t_0). \quad (6)$$

Here,  $p^*(t)$  and  $q^*(t)$  are complex polynomials introduced to handle baseline differences between the reference and sample arms.  $c$  is a real coefficient and gives the fraction of the absolute reference needed to explain the gas absorption registered in the sample arm. Phase difference between new experimental data and absolute reference recording can be handled by replacing  $c$  with a complex valued coefficient ( $c^*$ ). Such differences can occur due to changes in ambient temperature and diode laser operation settings. Differences in the location of the absorption within the scan is accounted for by introducing the shift parameter  $t_0$ . The best model fit is determined by means of non-linear Levenberg-Marquardt optimization on  $t_0$  (note that for a given  $t_0$ , the optimization problem reduces to linear regression). The absorption signal,  $\bar{w}^*$ , is reached after subtraction of fitted background signals:

$$\bar{w}^*(t) = \bar{v}_s^*(t) - p_{\text{fit}}^*(t) + q_{\text{fit}}^*(t) \times \bar{v}_r^*(t) \quad (7)$$

A conventional WMS signal is reached by determining the signal phase,  $\beta_n$ , and extracting the amplitude variation, as stated in Eq. 8.

$$\text{WMS}_{nf}(t) = \text{Real} \left\{ \left( \bar{w}_{nf}^*(t) - \text{mean}(\bar{w}_{nf}^*(t)) \right) \times \exp(-i\beta_n) \right\} \quad (8)$$

Figure 4 illustrates the importance of background subtraction, showing model fits and resulting WMS signals. As customary in GASMAS, experimental signals are measured in terms of equivalent pathlength in ambient air,  $L_{eq}$ . If needed, a superscript is used to differentiate between water vapor,  $L_{eq}^{H_2O}$ , and oxygen signals,  $L_{eq}^{O_2}$ . When evaluation is performed using the scheme described above, the  $L_{eq}$  is related to the pathlength used in the recording of the absolute reference,  $L_{a.r.}$ , as stated in Eq. 9.

$$L_{eq} = c_{\text{fit}} \times L_{a.r.} \quad (9)$$

While the concentration of molecular oxygen in air can be assumed fixed at 21%, the abundance of water vapor varies strongly with temperature and relative humidity. In this work, water vapor signals are measured with respect to equivalent pathlength in air at 37 °C and 100% relative humidity, e.g. the condition expected in cavities of the human skull. The absolute reference recording used in evaluation of water vapor absorption is measured in ambient air, simultaneous to the recording of an absolute reference for oxygen. The water vapor concentration in these experiments is inferred from measurements of temperature and relative humidity. The Arden-Buck equation provides the saturation pressure of water vapor [20], and is used to convert the 1000 mm pathlength in ambient air into its equivalent pathlength with respect to 37 °C and 100% relative humidity. The Arden-Buck equation is given in Eq. 10, where  $p$  is the pressure in atmospheres, and  $T$  the temperature in °C.

$$p = 6.032 \times 10^{-3} \exp \left( \frac{17.502 T}{240.97 + T} \right) \quad (10)$$

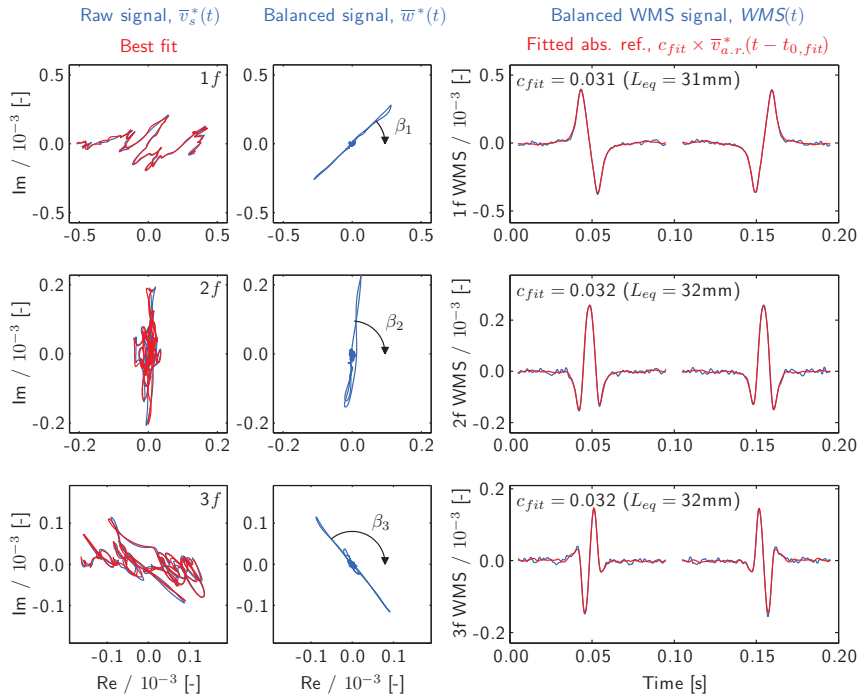


Fig. 4. Background subtraction exemplified using clinical data (molecular oxygen in the frontal sinus). Due to the triangular modulation used for laser modulation, each scan (dataset) include two interactions with the absorption feature. Differences in laser response in up- and downwards scanning requires that the imprints are evaluated separately. Despite fairly strong absorption, the absorption imprint is heavily distorted by background signals (left column). The observed structure can, however, be explained by the model in Eq. 6. Line-type phase-amplitude plot is obtained after background subtraction (middle column), and the resulting WMS signals (right column) exhibit good signal-to-noise ratio. The absolute reference was recorded on 1000 mm path of ambient air, and  $c_{fit} = 0.032$  thus suggest an absorption that corresponds to 32 mm in air, i.e.  $9 \times 10^{-4}$  in absorption fraction ( $L_{eq} = 32$  mm).

Note, for example, that a 150 mm pathlength at 37 °C and 100% relative humidity generates the same absorption of water vapor as a 1000 mm pathlength at 25 °C and 30% relative humidity (i.e. typical laboratory conditions).

### 2.3. Water vapor as a reference gas

The equivalent mean path length,  $L_{eq}$ , is of course dependent on both gas concentration and pathlength through gas. Since the pathlength is unknown in GASMAS, it is generally not possible to determine gas concentration. This complication may be circumvented if one performs simultaneous measurements on a gas with known concentration. For sinus diagnostics, water vapor has been used for this purpose [8]. If (i) the concentration of oxygen in the sinuses equals the atmospheric concentration, (ii) the optical properties (scattering and absorption) is the same at the two wavelengths used, and (iii) the gas in the sinus is at 37 °C and 100% relative humidity,  $L_{eq}^{O_2}$  should equal  $L_{eq}^{H_2O}$ . Unfortunately, since water vapor is measured at 935 nm and oxygen at 760 nm, differences in equivalent pathlengths may be assigned to differences in optical properties rather than a change in oxygen concentration. Nonetheless, the ratio of the two has proven to be fairly stable [8]. In this work we employ photon time-of-flight spectroscopy (PTOFS) to investigate differences in optical properties (see below in Sect. 2.4 and Sect. 3.3).

### 2.4. Photon time-of-flight instrumentation

Differences in light propagation between 760 nm to 935 nm is studied by employing photon time-of-flight spectroscopy (PTOFS). The utilized system has been described in detail elsewhere, and has for example been used for *in vivo* spectroscopy of human prostate tissue [21, 22]. Briefly, the system is based on pulsed diode lasers and time-correlated single photon counting. Picosecond laser pulses are injected into the tissue, and transmitted diffuse light is collected and resolved in time. The obtained photon time-of-flight histograms can be used to determine optical pathlengths, average absorption and scattering coefficients. The two diode laser used operate at 786 nm and 916 nm, respectively, thus only slightly deviating from the two wavelengths used for the gas spectroscopy.

## 3. Results

### 3.1. System performance

The general system performance was analyzed by investigating how well the system can resolve differences in pathlength through ambient air. The results for the 2 $f$  harmonic are presented in Fig. 5, and show that the precision is on the order of 1 mm. The performance varies slightly between the different harmonics, as reported also in Ref. [7]. Such effects may be assigned to problems of interference fringes occurring in experiments involving source-detector separations in the mm range. For example, the free spectral range of a 50 mm air etalon matches the width of the absorption linewidth (at atmospheric conditions), and may therefore be detrimental to the measurement.

### 3.2. Clinical data

Clinical data are acquired at the Radiology Clinic of the Lund University Hospital, within the framework of a clinical study aimed at comparing laser-based gas sensing with conventional CT diagnostics. The study is approved by the local committee of ethics, and patients are enrolled after informed consent. The maxillary sinuses, behind the cheekbone, are studied by placing the fiber probe in contact with one side of the mouth cavity roof, close to the sinus under study. The diffuse light is detected on the cheekbone. To monitor the frontal sinuses, behind the frontal bone, the fiber probe is placed under one side of the eyebrow, close to the nasal bone, injecting

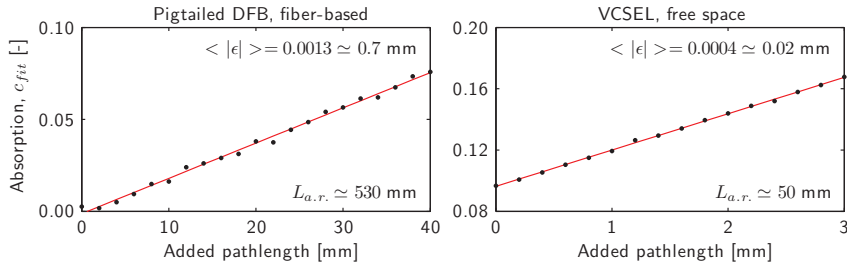


Fig. 5. Investigation of system performance by measurements on series of distances of ambient air ( $2f$  signals, molecular oxygen). When using the fiber-based clinical system, the resolution is about 1 mm  $L_{eq}$ , i.e. about  $3 \times 10^{-5}$  (average absolute deviations from the fitted line,  $\langle |\epsilon| \rangle$ ). The resolution is significantly better, about 0.02 mm  $L_{eq}$ , when the optical system is replaced with a non-collimated VCSEL and a single large-area photodiode (this system is described and used in Refs. [5, 7]). For this series, note the initial pathlength offset of about 5 mm.

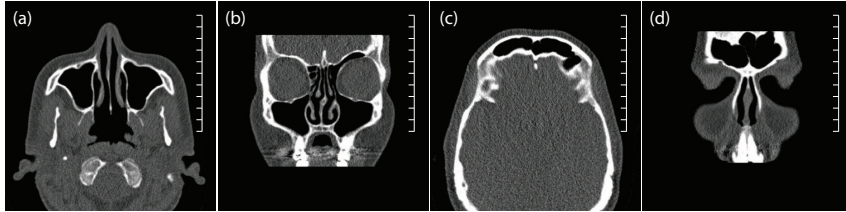


Fig. 6. CT images of the maxillary (a-b) and frontal sinuses (c-d). Black areas surrounded by white borders (bone) correspond to air filled cavities. Each division on the scale corresponds to 1 cm.

the light up in the frontal bone. The scattered light is detected on the forehead, with the bottom part of the detector located about 1 cm above the eyebrow. Light is acquired during 20 s (100 scan averages). Ambient light sources are turned off or blocked during the measurement.

Figure 6 shows CT images of the frontal and maxillary sinuses of one of the patients enrolled in the clinical study. The results of gas measurements on this particular patient is given in Fig. 7 (frontal sinuses) and Fig. 8 (maxillary sinuses). The signal-to-noise ratio, SNR, is calculated by taking the ratio of the WMS peak and the maximum absolute value of fit residuals. The SNR obtained suggest a detection limit of about 2 mm for both oxygen and water vapour (when using the  $1f$  or  $2f$  harmonics). This corresponds to absorption fractions of about  $5 \times 10^{-5}$  for oxygen and  $5 \times 10^{-4}$  for water vapour. The measurement resolution is better than the maximum residual value, and is thus expected to be significantly better than 2 mm. It should, however, be noted that the performance varies between patients due to large variations in light attenuation. The improvement in signal quality, with respect to earlier clinical data, is significant [18].

### 3.3. Photon time-of-flight data

The results of photon time-of-flight (TOF) experiments are reported in Fig. 9 and Tab. 1. The total optical pathlength is on the order of 100 mm, but varies strongly. Clearly, there are significant differences with respect to light propagation between the two wavelengths used for gas

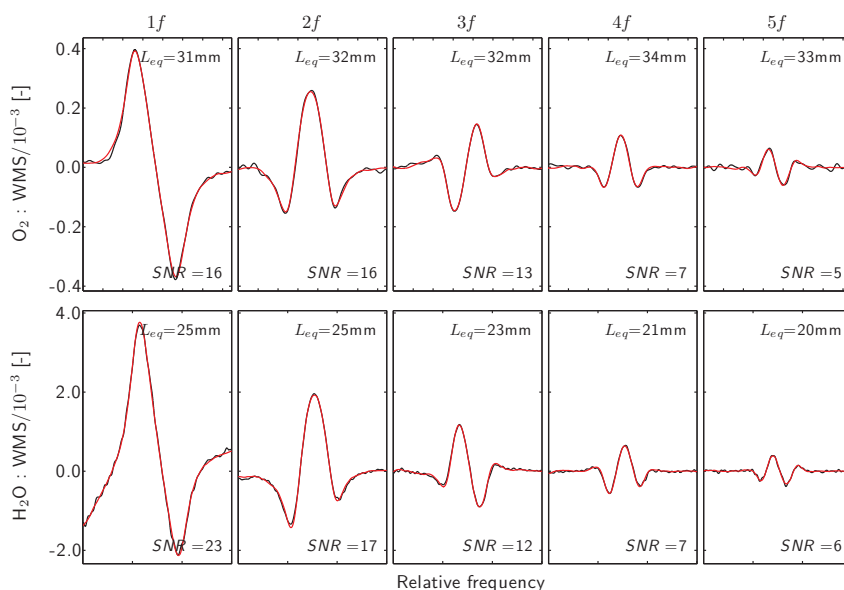


Fig. 7. 1-5f WMS signals from measurements on the left frontal sinus of a patient (black) together with fitted absolute reference data (red). CT images of this frontal sinus is found in Fig. 6. The detected power was  $9 \mu\text{W}$  for 760 nm and  $1 \mu\text{W}$  for 935 nm (transimpedance amplification was set to  $10^6$ ). The slightly lower  $L_{eq}$  for water vapor is typical, and is investigated in Sect. 3.3. Note the weak signal strength at higher harmonics, reducing the signal-to-noise ratio and causing increased uncertainty in  $L_{eq}$  estimation. Note also that the water absorption is about ten times stronger than the oxygen absorption.

spectroscopy. The data suggests that light used for oxygen sensing (760 nm) travels between 30 and 50% longer than light used for sensing of water vapour (935 nm). This fact explains why  $L_{eq}^{H_2O}$  typically is systematically lower than the  $L_{eq}^{O_2}$  (see e.g. Fig. 7). The differences between the two  $L_{eq}$ -values are, however, typically lower than the 30-50% implied by PTOFS. This discrepancy can be assigned to the non-trivial division of the total pathlength between tissue and sinus cavity. Considering the complexity of light propagation in strongly heterogeneous materials such a discrepancy is not unexpected. The issue may deserve further attention, and could be studied by Monte Carlo simulation.

Since the geometry of sinus measurements is complex and unknown, no appropriate model for light propagation is available. However, at late photon time-of-flights, the shape of the TOF distribution is mainly governed by the Beer-Lambert-Bouguer exponential decay  $\exp(-\mu_a ct)$ , where  $\mu_a$  is the absorption coefficient, and  $c$  the speed of light in the medium. Absorption coefficients can thus be estimated from the decay of the TOF distribution (the final slope of the intensity plotted in log-scale) [23]. This estimation should, however, be considered rough, since geometry and scattering properties greatly influence its accuracy [9].

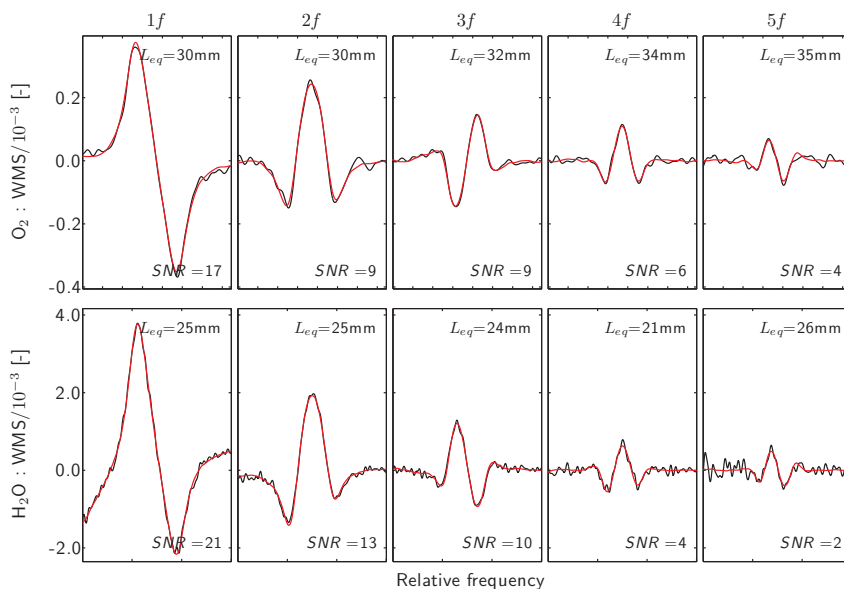


Fig. 8. 1-5f WMS signals from measurements on the left maxillary sinus of a patient (black) together with fitted absolute reference data (red). CT images of this maxillary sinus is found in Fig. 6. The detected power was  $2.7 \mu\text{W}$  for 760 nm and  $0.15 \mu\text{W}$  for 935 nm (transimpedance amplification was set to  $10^6$ ).

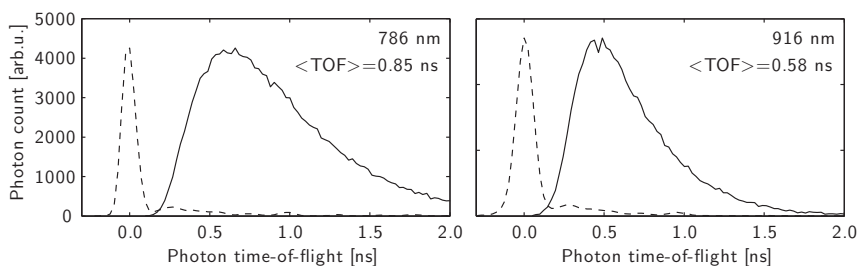


Fig. 9. Photon time-of-flight distributions obtained from measurements on the maxillary sinuses. A measurement of the instrumental response function (dashed) provides the origin for the absolute time scale.



|                         | Mean TOF [ns] |        | Mean path [mm] |        | Abs. coeff. [ $\text{cm}^{-1}$ ] |        |
|-------------------------|---------------|--------|----------------|--------|----------------------------------|--------|
|                         | 786 nm        | 916 nm | 786 nm         | 916 nm | 786 nm                           | 916 nm |
| Volunteer 1, Frontalis  | 0.54          | 0.40   | 116            | 86     | 0.13                             | 0.16   |
| Volunteer 1, Maxillaris | 1.38          | 0.90   | 296            | 193    | 0.10                             | -      |
| Volunteer 2, Frontalis  | 0.61          | 0.45   | 131            | 97     | 0.11                             | 0.14   |
| Volunteer 2, Maxillaris | 0.85          | 0.58   | 182            | 125    | 0.10                             | 0.16   |

Table 1. Photon pathlengths and estimations of average absorption coefficients, as obtained from PTOFS. Mean pathlengths are calculated from mean TOF, assuming a refractive index of 1.4. For the measurements on the maxillary sinuses of volunteer 2, low light transmission prevented proper analysis of absorption coefficient.

4. Discussion

The system described in this work is clearly capable of providing useful clinical data on the gas contents of human paranasal sinuses. There are, however, alternative system designs that could achieve similar or even better performance. The advantages of using optical fibers to deliver light is the straight forward construction of an appropriate medical probe. In addition, fibers allow convenient coupling of different light sources, rendering the use of multiple light sources fairly simple. The major drawback, however, is that the use of pigtailed diode lasers and optical fibers appears to degrade the system performance. Despite the elaborate schemes for background suppression described in this paper, the performance is still significantly poorer than comparable single-beam systems that avoid optical fibers [5, 9]. However, considering for example the high sensitivity fiber-based gas sensor developed by Engelbrecht [24], we expect that we can improve our current fiber-based system. Nonetheless, the possibilities of constructing a single-beam system, avoiding pigtailing and optical fibers, should be investigated. Potential advantages include reduced system complexity, significant cost reduction, as well as simpler and more robust data evaluation. The small size of diode lasers renders it possible to construct a medical probe that injects light directly from the output of the diode lasers. The ideal solution would be a single diode laser capsule that contains different diode lasers, operating at different wavelengths. Furthermore, replacing pigtailed DFB-lasers with e.g. VCSEL lasers (shown feasible in Ref. [14]) would make the system much more cost-efficient.

Another issue that deserves some attention is that the access to multiple WMS harmonics reveals some technical imperfections. We have observed discrepancies between the  $L_{eq}$ -values obtained from the different harmonics. Water vapor appears to be particularly affected. Possible technical explanations include differences in detector response with harmonic frequency and light distribution over the large-area photodiode. We are also investigating whether differences in conditions between the measurements of absolute references and the actual clinical measurements can effect system behavior. In order to determine and improve measurement accuracy, these effects require further attention.

Finally, since high light attenuation may degrade the sensitivity, the values given for detection limit show be considered as guidelines. Nonetheless, a look through the full clinical dataset shows that 2 mm  $L_{eq}$  most often is a fair indication of the limit of detection. We will discuss this important aspect in detail in a forthcoming article that will focus on the clinical data.

Acknowledgment

This work was supported by The Swedish Research Council through a project grant and a Linnaeus Grant for the Lund Laser Centre. the Knut and Alice Wallenberg Foundation, as well as by the Medical Faculty, Lund University. The authors also gratefully acknowledge Prof.

Stefan Andersson-Engels for the collaboration on time-of-flight spectroscopy, as well as Prof. Sven Lindberg, Prof. Kjell Jonson and Dr. Roger Siemund at the Lund University Hospital for supporting and assisting in the clinical work.



## PAPER XI

**Assessment of photon migration in scattering media using heterodyning techniques with a frequency modulated diode laser**

Z.G. Guan, P. Lundin, S. Svanberg.

*Optics Express* **17**, 16291 - 16299 (2009).



# Assessment of photon migration in scattering media using heterodyning techniques with a frequency modulated diode laser

Zuguang Guan\*, Patrik Lundin, and Sune Svanberg

Atomic Physics Division, Lund University, P.O. Box 118, S-221 00, Lund, Sweden

\*Corresponding author: [Zuguang.Guan@fysik.lth.se](mailto:Zuguang.Guan@fysik.lth.se)

**Abstract:** A novel technique for studying photon propagation in scattering media is proposed and demonstrated, as is believed, for the first time. Photons propagating through the medium, from a frequency-ramped single-mode diode laser, meet a reference beam from the same source, at a common detector, and beat frequencies corresponding to various temporal delays are observed by heterodyne techniques. Fourier transformation directly yields the temporal dispersion curve. Proof-of-principle experiments on polystyrene foam and a tissue phantom suggest, that the new method, when fully developed, may favorably compete with the more complex time-correlated single-photon counting (TCSPC) and the phase-shift methods, now much employed.

©2009 Optical Society of America

**OCIS codes:** (120.5820) Scattering measurements; (170.3660) Light propagation in tissues; (170.6920) Time-resolved imaging; (120.0280) Remote sensing and sensors.

## References and links

1. B. Chance, J.S. Leigh, H. Miyake, D.S. Smith, S. Nioka, R. Greenfield, M. Finander, K. Kaufmann, W. Levy, M. Young, P. Cohen, H. Yoshioka and R. Boretsky, "Comparison of time-resolved and -unresolved measurements of deoxyhemoglobin in the brain", *Proc. Natl. Acad. Sci. USA* **85**, 4971 (1988).
2. S. Andersson-Engels, R. Berg, S. Svanberg and O. Jarlman, "Time-resolved transillumination for medical diagnostics", *Opt. Lett.* **15**, 1179 (1990).
3. R. Berg, S. Andersson-Engels and S. Svanberg, "Time-resolved transillumination imaging", *Optical Tomography, SPIE IS11*, 397 (1993).
4. A. Taroni, A. Torricelli, L. Spinelli, A. Pifferi, F. Arpaia, G. Danesini and R. Cubeddu, "Time-resolved optical mammography between 637 and 985 nm: Clinical study on the detection and identification of breast lesions", *Phys. Med. Biol.* **50**, 2469 (2005).
5. T. Svensson, S. Andersson-Engels, M. Einarsson and K. Svanberg, "In vivo optical characterization of human prostate tissue using near-infrared time-resolved spectroscopy", *J. Biomed. Opt.* **12**, 014022 (2007).
6. S. Andersson-Engels, R. Berg, A. Persson and S. Svanberg, "Multispectral tissue characterization using time-resolved detection of diffusely scattered white light", *Opt. Lett.* **18**, 1697 (1993).
7. Ch. Abrahamsson, T. Svensson, S. Svanberg, S. Andersson-Engels, J. Johansson and S. Folestad, "Time and wavelength resolved spectroscopy of turbid media using light continuum generated in a crystal fibre", *Opt. Exp.* **12**, 4103 (2004).
8. T. Fujii and T. Fukuchi (eds), *Laser Remote Sensing* (CRC Press, Boca Raton 2005).
9. K. I. Aoyama, K. Nakagawa, and T. Itoh, "Optical-time domain reflectometry in a single-mode fiber", *IEEE J. Quant. Electr.* **17**, 862 (1981).
10. Z.G. Guan, M. Lewander, R. Grönlund, H. Lundberg and S. Svanberg, "Gas analysis in remote scattering targets using LIDAR techniques", *Appl. Phys. B* **93**, 657 (2008).
11. M. Toida, T. Ichimura and H. Inaba, "The first demonstration of laser computed tomography achieved by coherent detection imaging method for biomedical applications", *IEICE Trans. E74*, 1692 (1991).
12. D. Uttam and B. Culshaw, "Precision time domain reflectometry in optical fiber systems using a frequency modulated continuous wave ranging technique", *J. Lightwave Technol. LT-3*, 971 (1985).
13. W. V. Sorin, D. K. Donald, S. A. Newton and M. Nazarathy, "Coherent FMCW reflectometry using a temperature tuned Nd:YAG ring laser", *IEEE Photonics Technol. Lett.* **2**, 902 (1990).

14. C. J. Karlsson and F. Å. A. Olsson, "Linearization of the frequency sweep of a frequency-modulated continuous-wave semiconductor laser radar and the resulting ranging performance", *Appl. Opt.* **38**, 3376 (1999).
  15. S. R. Chinn and E. A. Swanson, "Optical coherence tomography using a frequency-tunable optical source", *Opt. Lett.* **22**, 340 (1997).
  16. K. Wårdell, A. Jakobsson and G. E. Nilsson, "Laser Doppler perfusion imaging by dynamic light scattering", *IEEE Trans. Biomed. Eng.*, **40**, 309 (1993).
- 

## 1. Introduction

Photon propagation in scattering media is a broad field with applications ranging from radiative transfer in astrophysics, atmospheric radiative balance in climatology, to light propagation in biological tissue. The latter field is much studied with regard to optical mammography, measurements of tissue oxygenation and bleeding due to vessel rupture, as well as for dosimetry in photodynamic therapy. An early application concerned brain monitoring [1]; in a subsequent study imaging of structures in living human tissue was demonstrated [2]. Studies of photon propagation in tissue can be pursued in the spatial domain (CW lasers), but more frequently in the temporal domain using pulsed lasers (time-of-flight measurements) or modulated CW lasers (the phase-shift method, where also amplitude demodulation is monitored). An early overview of different techniques for studying light propagation in biological tissue is provided in [3]. More recently, the general field of tissue optics has been much studied, where the aspects of wavelength dependence of the absorption and reduced scattering coefficients of tissue,  $\mu_a$  and  $\mu_s'$ , respectively, are important, yielding information on the concentration of tissue constituents. A number of discrete wavelengths generated in swiftly pulsed diode lasers can be used in connection with time-correlated single-photon counting (TCSPC) electronics [4]. An example is given in [5], where the optical properties of human prostate tissue were determined. Alternatively, a short-pulse white-light source can be used in conjunction with a combination of a spectrometer and a time-resolving streak camera [6]. Then, in principle the optical properties of the medium can be evaluated from data generated in a single laser pulse. Such time-resolved white-light spectroscopy has also been extended to the study of pharmaceutical preparations [7].

Time-resolved measurements are also common in the laser radar field [8] and in reflectometry in optical fiber networks [9], although the time scales then are much extended. As illustrated in recent measurements on scattering media at a few meters distance [10], there is a seam-less transition from the large to the small time scales.

In laser ranging and in reflectometry there is special emphasis on capturing the distinct echoes from interfaces. Likewise, in early medical studies much emphasis was on "gated viewing", i.e. capturing the part of the pulse propagating through a medium without suffering scattering. Numerous techniques were developed for that purpose [3]. In particular, a method was developed by Toida et al. [11], where a CW laser was used in a Mach-Zehnder interferometer configuration with one beam passing the scattering medium, and a frequency-shifted reference beam being joined on a common detector. The heterodyne signal between the two beams, detected at the difference frequency, is due to the ballistic (unscattered) signal only, since other components all have varying phase due to delays. In the present paper the same basic geometry is used; however, we now realize that also the scattered components can be analysed, and also sorted in time using the same approach, but now employing a CW laser with an added frequency ramp; a technique which is readily achieved with a diode laser with a linear current ramp superimposed on the driving current. We in this way demonstrate the recording of time-resolved photon propagation curves, such as those obtained in time-correlated single-photon counting (TCSPC), but using simpler equipment. The simplification is similar as the one obtained by using the phase-shift technique instead of the TCSPC method. The technique, to our knowledge here demonstrated for the first time, draws inspiration from heterodyne gated viewing [11], fiber optic reflectometry [9] and in particular from the frequency modulated continuous wave (FMCW) ranging technique [12], where single-scattering is assumed. We show that the extension to multiple scattering is straight

forward and that only moderate modulation and detecting speeds are needed, but still a high spatial resolution and a good signal-to-noise ratio (SNR) are achieved within a short time of averaging.

The paper is organized in the following way. The measurement principle and the analysis method used in the new method are presented in the next section. Then proof-of-principle experiments on polystyrene foam and a tissue phantom are presented and the data retrieval procedure is explained. Finally, the new method is put in relation to previous approaches in view of complexity, temporal/spatial resolution and acquisition speed, and general conclusions are drawn.

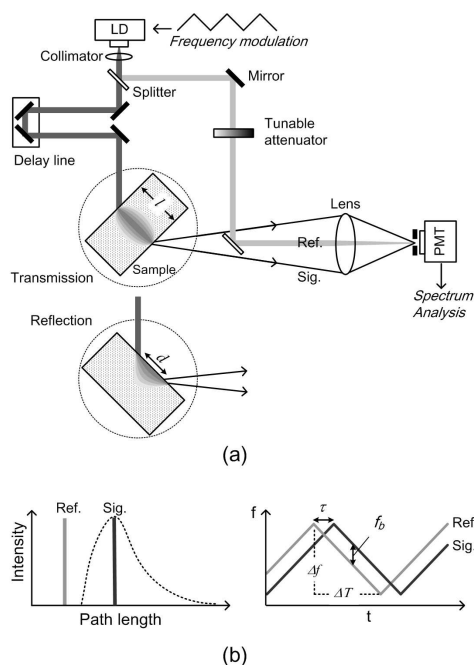


Fig. 1. (a) Schematic diagram of the technique presented; (b) Principle of analyzing photon propagation in the frequency domain.

## 2. Principle and analysis

Fig. 1 (a) and (b) show the experimental set-up used in the present experiments, and the basic idea of data retrieval, respectively. In the FMCW technique, the frequency of the laser source is linearly modulated with, e.g., a triangular waveform. The modulated light is then separated into two beams, a reference beam and a probe beam. The reference beam passes through a well-known distance while the probe beam passes through an unknown optical path length. Both beams arrive at the same detector and interfere with each other. A beat frequency ( $f_b$ ) proportional to the time delay ( $\tau$ ) between these two beams will be induced in the detected signal (see the right part of Fig. 1(b)). This specific frequency can be used to deduce the path length of the probe beam and hence realize the space ranging. In most reported applications of the FMCW technique, e.g. [12], the reflected photons are single-scattered, and the beat frequency is detected with high contrast and at a narrow bandwidth. However, in the case when the probe beam passes through a multiple scattering medium, the path lengths of the photons will show a distribution with a position of the maximum and a width, which are



dependent on  $\mu_s'$ ,  $\mu_a$  and the thickness of the sample. This part of the beam is labeled as *sig* and is shown as a dashed curve in the left part of Fig. 1(b). If we denote the field of the reference beam at the detector as

$$E_{ref} = A_{ref} \exp(-j\omega_{ref}t) \quad (1)$$

the field of the signal light that arrives to the detector at the same time can be expressed as a superposition of different components of the beam with photons which have passed through different effective path lengths,

$$E_{sig} = \sum_i A_{sig}^i \exp\{-j[\omega_{ref} - S \cdot \tau_i] \cdot t + \phi(\tau_i)\} \quad (2)$$

Here,  $S = 2\pi \cdot \Delta f / \Delta T$  is the slope of the frequency modulation (see Fig. 1(b)),  $\tau_i$  is the time delay of each component compared with the reference beam, and the square of the amplitude,  $|A_{sig}^i|^2$ , is proportional to the number of photons of the corresponding component. The interference signal of  $E_{ref}$  and  $E_{sig}$  can be detected as

$$I = DC + \sum_i A_{ref} A_{sig}^i \cos[S \cdot \tau_i \cdot t - \phi(\tau_i)] + \sum_i \sum_j A_{sig}^i A_{sig}^j \cos[S \cdot (\tau_i - \tau_j) \cdot t + \phi(\tau_j) - \phi(\tau_i)] \quad (3)$$

The first term is a DC component of the interference signal. The second term indicates the interference between  $E_{ref}$  and each component of  $E_{sig}$ . The third term corresponds to the interferences among different components of  $E_{sig}$ . The intensity of the third term is much weaker than that of the second term containing the reference signal itself, and can thus be ignored. Obviously the second term consists of components with different frequencies (proportional to the delays  $\tau_i$ ), and different amplitudes (proportional to  $A_{sig}^i$ , and  $|A_{sig}^i|^2$  is proportional to the number of photons). Therefore, the distribution of the time delays (effective path lengths) of photons passing through a scattering sample can be obtained by simply analyzing the spectral power ( $|A_{ref} A_{sig}^i|^2$ ) of the interference signal of Eq. (3) in the frequency domain.

Since the working principle is based on optical interference, the measuring range of  $\tau_i$  is limited by the coherent length of the light source. A laser with a good coherence property is needed for the technique presented. Suitable laser sources include distributed feed-back (DFB) diode lasers (with coherence length of hundreds of meters), external cavity diode lasers (ECDLs; kilometers), and Nd:YAG ring lasers (tens of kilometers) [13]. Good coherence properties ensure the heterodyne efficiency between the reference and probe beams. Similar as for the FMCW technique [12], the minimal resolvable optical path length ( $R$ ) is determined by the frequency range of the modulation ( $\Delta f$ ), i.e.,  $R \approx c/\Delta f$  ( $c$  is the speed of light in vacuum). Considering the  $\mu_a$  and  $\mu_s'$  of a scattering medium, e.g., a tissue sample, being constants even if the frequency of the laser source is tuned across 500 GHz (corresponding to ~1 nm wavelength difference when the central wavelength is located at 750 nm), the resolution,  $R$ , of the technique presented is expected to be of the order of 0.5 mm, which, however, degrades due to nonlinearity of the wavelength ramping (which has been thoroughly discussed in publications, e.g. Ref. [14]), and Doppler broadening in the frequency domain. Motion in the medium under study, e.g. blood flow in human tissue, or even Brownian motion of scatters, as well as mechanical instabilities in the interferometric apparatus are sources of broadening. A more detailed discussion will follow in Section 4. One advantage

originating from the heterodyne technique used is that the amplification is proportional to the amplitude of the reference beam (see the second term of Eq. (3)), allowing a high sensitivity of the system.

### 3. Experiments and results

For demonstration, an experimental system was built as shown in Fig. 1(a). A DFB diode laser (Toptica Photonics, LD-0760-0040-DFB-1) operating in a single longitudinal mode, was employed as the light source. The central wavelength is around 760 nm and the line-width is less than 3 MHz (corresponding to a coherence length of 100 m). By ramping the driving current with a triangular waveform, the tunable range of frequency of the diode is around 40 GHz (corresponding to an estimated resolution,  $R$ , of 0.75 cm, according to the expression  $R \approx c/\Delta f$ ). The collimated light is divided by the first beam splitter into two parts, with 4% working as reference beam and the remainder working as the probe beam. The probe beam experiences multiple scattering in the sample under test, and penetrates through as signal light, which is collected by an imaging lens. The second beam splitter is used to overlap the reference beam and the signal light at the detector, a PMT tube (Hamamatsu, R5070A). A delay line is inserted in the probe beam to set an offset delay between the signal light and the reference beam. The tunable attenuator is used to adjust the intensity of the reference beam, for optimizing the amplifying function while not saturating the PMT. The detecting direction of the PMT is specially set as  $90^\circ$  against the probing beam, for convenience to test both transmission and reflection versions of the technique, as shown in Fig. 1(a).

While the driving current is modulated by a 10 Hz triangular waveform, the signal from the PMT is amplified by a current-to-voltage amplifier (Femto, DLPCA-200), and recorded by a data-acquisition card (National Instruments, NI-6154) installed on a computer. In real time, the spectral power of the signal in the frequency domain is analyzed with a fast Fourier transform (FFT) program on the computer. The spectral curves are averaged 100 times within 10 s to achieve a better SNR. Here, averaging is required to extract the weak signal (due to multiple scattering of the samples) from the background noise of the PMT. Averaging time can be reduced by employing a more powerful light source.

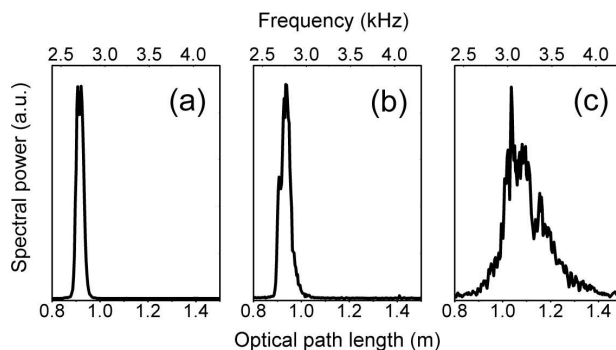


Fig. 2. Spectral responses for different samples (a) white paper, (b) tissue phantom, and (c) polystyrene foam (transmission mode). Curves are normalized by the maximum values.

Scattering samples of different materials were tested in the transmission mode. Fig. 2 shows the results corresponding to a piece of normal printing paper (white, 100  $\mu\text{m}$  thick), a tissue phantom (a 10 mm thick sample of gelatin containing ink as absorber,  $\mu_s' = 6.9 \text{ cm}^{-1}$  and  $\mu_a = 0.3 \text{ cm}^{-1}$ ), and polystyrene foam (11 mm thick,  $\mu_s'$  is  $\sim 30 \text{ cm}^{-1}$  and  $\mu_a$  is  $\sim 0.001 \text{ cm}^{-1}$ , respectively). As expected from Eq. (3), the curves of (b) and (c) show extended tails in the

frequency domain (or optical path length domain), due to massive multiple scattering in the tissue and the foam. The curve of (c) is broader than that of (b), since  $\mu_s'$  of the polystyrene foam is much higher than that of the tissue phantom in this experiment. The thin white paper exhibits a relatively narrow curve. However, the width of the curve ( $\sim 3$  cm) is broadened compared with the theoretical spatial resolution limit (0.75 cm for the 40 GHz sweep utilized). Due to lateral multiple scattering a broadening is expected and further, a Doppler broadening will occur due to the vibrations and instability of the paper sample and the interferometer structures during averaging in the measurements.

Pieces of polystyrene foam with different thickness ( $l$ ) were also tested in the transmission mode, and the resulting curves are shown in Fig. 3. With increasing  $l$ , the curve moves towards longer path length and the tail extends longer, which matches the fact that photons experience longer effective path length in a thicker scattering sample. For a piece of polystyrene foam with 1 cm of thickness, the distribution of photon arrival times shows that even path lengths of half a meter occurs.

Similar results can be obtained when the scattering sample is tested in a reflection mode. A piece of polystyrene foam (with infinite thickness) is set as shown in the inset of Fig. 1(a). Instead of changing  $l$ , the gap ( $d$ ) between the illuminating point and the observing point is varied. The result shown in Fig. 4 illustrates that with larger  $d$ , deeper penetrating photons can be detected, and longer effective path lengths can be seen. However, the SNR degrades as a penalty, since less photons survive to be observed at a position further away from the illuminating point.

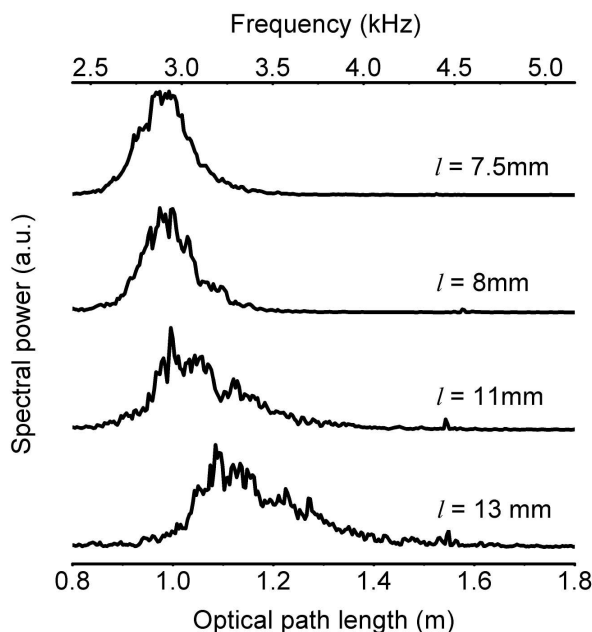


Fig. 3. Spectral responses corresponding to different thickness ( $l$ ) of polystyrene foam (transmission mode). Curves are normalized by the maximum values.

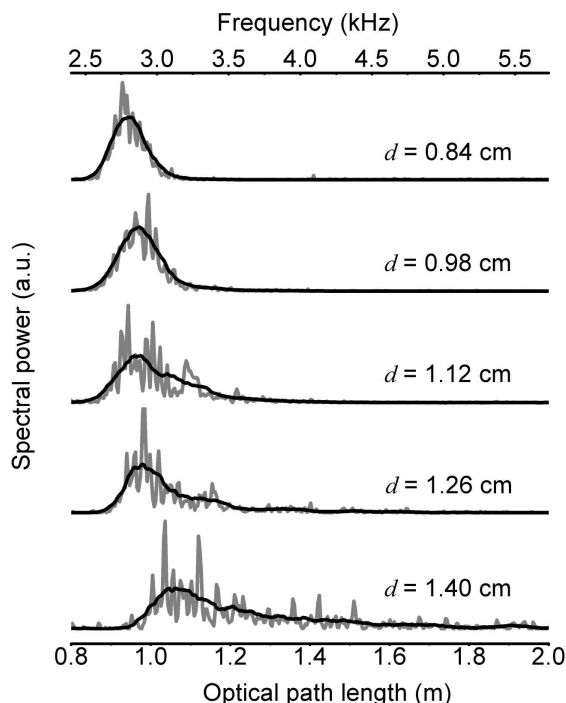


Fig. 4. Spectral responses when the gap ( $d$ ) between the illuminating and observation points is set to different values (reflection mode). Gray curves are normalized by the maximum values. Dark smoothed curves are obtained by applying a sliding average over 100 Hz.

#### 4. Discussion

Although only proof-of-principle experiments are carried out, we believe that the new technique presented can potentially compete with conventional time-resolved and phase-shift methods in view of degree of complexity, spatial resolution, and sensitivity (acquisition speed), and might even show advantages in some aspects.

In time-resolved systems, the spatial resolution in the measurements is limited by the pulse width of the light source. Initially, Q-switched solid-state lasers were frequently utilized in such systems. Later, more compact Q-switched fiber lasers were developed to replace complex and large-sized solid-state lasers. However, the output wavelengths of fiber lasers are very limited for spectroscopic applications, such as those considered, e.g., in [4] and [5]. Theoretically, if a femto-second laser is employed, a highest resolution on the sub-micrometer level can be achieved. Again, this resolution is not practical in spectroscopic applications, due to the limitation that the Fourier relationship puts between the pulse width and the bandwidth of the laser source. Diode lasers are extremely compact, cost effective, tunable and available at many wavelengths. They can be pulsed at high repetition rates, but pulse energies are minute compared to those obtained from Q-switched lasers. Thus, transient digitizer techniques cannot be used for capturing time-resolved signals. Instead, the TCSPC technique is frequently employed to generate a histogram of individual photon arrival times at the detector, a PMT which is cooled down to reduce dark current counts. Fast electronics matching the pulse width of the laser source are required. The sampling time needed depends on the repetition rate and average output power of the laser source, and the sensitivity of the

detector. An alternative technique is the phase-shift method, where the delay-induced phase shift and demodulation with regard to the source modulation depth are measured. Since both the laser and the detection system work in CW mode, the electronics required are much less complex compared with TCSPC methods. Modulation of the source and demodulation at the detector are achieved with readily available radio electronics. The spatial resolution of this technique is determined by the upper modulation (demodulation) frequency.

Both the TCSPC and the phase-shift methods operate at high frequencies since the techniques basically compete with the speed of light. In contrast, the new technique presented here transforms the fast phenomena down to audio frequencies by employing the heterodyne principle, where the slow beat frequency between two optical frequencies being different just because of the propagation delay is detected. The semiconductor laser source is repetitively ramped in frequency at a slow rate (of the order of 10 Hz) and the different beat frequencies corresponding to different delays are retrieved by Fourier transformation of the detected signal. The longer the ramp sweeps the laser optical frequency, the better the temporal resolution will be.

Using an external cavity diode laser with tuning range of several tens of nanometer, a resolution of tens of micrometer can be realized, which has been proven for the FMCW technique, e.g. in [15]. However, in many spectroscopic applications, the tuning bandwidth of the laser source is more limited and the expected resolution degrades. One extremely attractive feature of the FMCW technique, being of heterodyne nature, is that signal amplification is achieved by making the reference beam suitably strong, and noisy signal amplification electronics are thus largely eliminated. These attractive features in combination make the technique here presented viable and competitive. We realize, however, that for heavy multiple scattering the light at the detector is distributed over a substantial area. The reference beam must thus likewise be expanded for spatial matching. We believe that by optimizing beam overlap the signal-to-noise ratio obtained in our preliminary work presented here could be substantially improved.

We note, that the new heterodyning technique by its nature is sensitive to Doppler shifts and Brownian motion. We recall, that tissue perfusion can be measured using the Doppler flowmetry technique (see, e.g. [16]), where also heterodyning between moving blood cells and fixed cellular structures is utilized to retrieve a distribution of Doppler-shifted frequencies. Actually, the situation has many similarities with the one presented in our paper. Not unexpectedly we noticed a signal broadening when measuring on an instable paper sample. Such phenomena can be expected to be seen in clinical applications, where tissue blood flow, heart beating, etc., can obviously superimpose a Doppler broadening on top of the beat frequencies induced by true photon propagation delays. While the perfusion induced broadening information can be useful in some contexts, its detrimental influence could be reduced by deconvoluting the Doppler broadening from the measured curve to yield a true propagation delay curve. This might be done by measuring the frequency-shift distribution when not ramping the laser frequency.

We note, that blood flow and instability-induced effects can be minimized by simply increasing the ramping rate of the diode laser, inducing larger propagation delay frequency shifts, while the Doppler broadening, due to physical motion, remains the same. For a typical superficial blood cell speed of  $3 \text{ mm s}^{-1}$  the Doppler broadening will be of the order of kHz, which is similar to the propagation delay shifts measured in our experiments. If the ramping rate is increased from 10 Hz to 1 kHz in the experiments, the propagation time delay frequency shifts will be 100 times larger, and a 1 kHz Doppler broadening will become insignificant. The only fundamental temporal resolution factor will now be the frequency excursion of the ramp. Clearly, the detection bandwidth needs to be extended from  $\sim 10 \text{ kHz}$  to  $\sim 1 \text{ MHz}$ , which is, however, still reasonably modest.

## 5. Conclusion

In conclusion, we have demonstrated a new frequency-resolved technique to study photon migration in multiple-scattering media. Both transmission and reflection measurement modes were realized. Short averaging times, low ramping rates and low signal recovery frequencies are attractive features in first proof-of-principle applications of the technique presented. The new method is inherently technically less complex than customary time- or phase-resolving techniques, and it could be expected, that when fully refined it might favorably compete with such techniques, which have benefitted from decades of development. A detailed comparison with customary techniques will be the subject of forthcoming work. In particular, the influence of instabilities and Doppler effects due to blood flow (in clinical applications) on the technique presented needs to be further investigated.

## Acknowledgements

This work was supported by a project grant from the Swedish Research Council and a Linnaeus grant to the Lund Laser Centre. Fruitful discussions with Tomas Svensson and helpful assistance from Erik Alerstam are gratefully acknowledged.



## PAPER XII

### **An optical sensing system for the concentration of methane based on fiber Bragg gratings**

B. Zhou, G. Liu, Z.G. Guan, S. He.

*Journal of Optoelectronics and Laser (China)* **19**, 378 - 380 (2008).





基于 FBG 的 CH<sub>4</sub> 浓度传感系统<sup>\* \*</sup>周 斌<sup>1,2</sup>, 刘国荣<sup>1</sup>, 管祖光<sup>1\* \*</sup>, 何赛灵<sup>1</sup>

(1. 浙江大学现代光学仪器国家重点实验室, 光及电磁波研究中心, 浙江 杭州 310058; 2. 浙江大学光学研究所, 浙江 杭州 310058)

**摘要:**提出了一种基于光纤布拉格光栅(FBG)的新型 CH<sub>4</sub> 浓度传感方案。利用 CH<sub>4</sub> 催化元件将 CH<sub>4</sub> 浓度信息转化为温度信息,并映射为 FBG 反射波长的漂移量。将自制的 FBG 封装成 CH<sub>4</sub> 传感器,并实验获得了 FBG 反射波长漂移量与环境 CH<sub>4</sub> 浓度的曲线。验证了采用传感 FBG 和参考 FBG 的斜边检测方案可提高系统检测分辨率和温度稳定性。

**关键词:**CH<sub>4</sub> 浓度传感; 光纤布拉格光栅(FBG); 斜边检测

**中图分类号:**TP212.14 **文献标识码:**A **文章编号:**1005-0086(2008)03-0378-03

An optical sensing system for the concentration of CH<sub>4</sub> based on FBGZHOU Bin<sup>1,2</sup>, LIU Guo-rong<sup>1</sup>, GUAN Zu-guang<sup>1\* \*</sup>, HE Sai-ling<sup>1</sup>

(1. Centre for Optical and Electromagnetic Research, State Key Laboratory for Modern Optical Instrumentation, Zhejiang University, Hangzhou 310058, China; 2. Institute of Optics, Zhejiang University, Hangzhou 310058, China)

**Abstract:**Based on a special catalyst and fiber Bragg gratings (FBGs), an optical sensing system is proposed to measure the concentration of CH<sub>4</sub>. The temperature around the catalyst rises rapidly as the CH<sub>4</sub> concentration increases, which can be detected by an FBG-type sensor through monitoring the wavelength shift of the reflection spectrum. By employing a well-matched FBG as a reference, the wavelength shift of the sensing FBG can be transformed effectively into the variation in the measured optical intensity. An experiment is demonstrated to show the good performances of our system, such as the high resolution and good stability to the environmental temperature.

**Key words:**sensor the concentration of methane; fiber Bragg grating(FBG); edge-detection

## 1 引 言

由于主要成分为 CH<sub>4</sub> 的瓦斯超标是引发煤矿爆炸的最主要原因,井下 CH<sub>4</sub> 浓度的准确、实时和安全测量对于预防矿难意义重大。现在矿井普遍使用的 CH<sub>4</sub> 浓度计多数基于催化氧化原理,一般利用温敏电阻及惠更斯电桥获得 CH<sub>4</sub> 的浓度信息<sup>[1,2]</sup>。由于电信号易受煤矿井下大型采矿设备的电磁干扰,这类 CH<sub>4</sub> 浓度计测量可靠性受环境影响大,目前对 CH<sub>4</sub> 浓度的分辨率一般为 0.01%,并且很难实现远距离传感。相比电学类传感器,光纤型传感器具有测量精度高、不受电磁干扰和适于远距离传感等优点,尤其是最近兴起的光纤布拉格光栅(FBG)传感器,由于其对应力、温度<sup>[3,4]</sup>的高灵敏度以及利用波分复用原理易于实现分布式测量方案的特点,被广泛应用于建筑的智能结构健康监测<sup>[5~9]</sup>。

本文利用 FBG 反射峰波长位置对温度敏感的特性,通过读出催化氧化元件附近的温度信号来获得环境中的 CH<sub>4</sub> 浓度信息。为了消除环境温度变化对测量的影响以及降低系统成

本,引入参考 FBG 并采用斜边检测的方法,获得了  $64 \times 10^{-6}$  的测量分辨率和环境温度从 30℃ 上升到 60℃ 测量值波动小于 0.013% 的温度稳定性。

## 2 系统原理分析

2.1 根据 FBG 反射峰波长位置测量 CH<sub>4</sub> 浓度

FBG 是一种在光纤芯层形成的折射率一维周期性结构,能将某一波长的前向芯层导模耦合到背向导模,引起反射。该反射波长可以表示为<sup>[6]</sup>

$$\lambda = 2n_{\text{eff}}\Lambda \quad (1)$$

其中: $n_{\text{eff}}$ 为光纤芯层有效折射率; $\Lambda$ 为光栅周期。FBG 的反射波长位置随外界温度的变化而呈线性变化<sup>[7]</sup>,可表示为

$$\Delta\lambda = 2(n_{\text{eff}} \frac{\partial\Lambda}{\partial T} + \Lambda \frac{\partial n_{\text{eff}}}{\partial T})\Delta T \quad (2)$$

根据这一原理,FBG 被广泛地应用于温度传感。

CH<sub>4</sub> 催化氧化剂是一种重金属催化剂,主要由 Pt 等组成,当被加热到催化初始温度以上时,这类催化剂能催化大气中的

\* 收稿日期:2007-03-09 修订日期:2007-05-08

\* 基金项目:浙江省科技厅资助项目(2004C31G2010019);杭州市科技局科技创新资助项目(20051321B14)

\* \* E-mail:guan zuguang@coer.zju.edu.cn

CH<sub>4</sub> 发生氧化反应,从而改变催化剂附近的温度场分布。靠近催化剂附近某一点温度与 CH<sub>4</sub> 的浓度成线性关系。将 FBG 固定在催化剂附近位置,通过观察 FBG 反射波长的变化,可获得该点 CH<sub>4</sub> 浓度的信息。

2.2 利用参考 FBG 实现斜边检测

利用光谱分析仪、多波长计等测量设备可获得 FBG 反射波长信息,但这些设备相对价格较高,无法满足大规模工业使用的需求。本文采用 2 根 FBG 和斜边检测的方法,以降低系统成本,同时还提高了系统测量分辨率和系统的温度稳定性。

如图 1 所示,传感用 FBG 固定在 CH<sub>4</sub> 催化元件附近,而参考 FBG 与催化元件隔离,传感 FBG 和参考 FBG 的反射峰波长位置基本重叠。参考 FBG 可以认为是某一波长范围的带通滤波器。当 CH<sub>4</sub> 浓度为零时,传感 FBG 的反射峰在带通滤波器最大透过波长位置,因此光电二极管得到的光强最大;当 CH<sub>4</sub> 浓度上升时,传感 FBG 的反射波长位置向长波方向漂移,刚好落在参考 FBG 的滤波斜边上,见图 1 插图,光电二极管获得的光强逐渐变小。此方法将 FBG 的波长信息转化为光强信息,从而大大降低了设备成本。同时,由于参考 FBG 的滤波斜边很陡(—20%/0.1 nm),系统的测量灵敏度大大提高。并且,传感 FBG 的反射波长位置 also 对环境温度的变化敏感,如果测量传感 FBG 反射峰的绝对波长位置,则获得的 CH<sub>4</sub> 浓度信息中也同时包含了外界温度信号的干扰。系统中,传感 FBG 和参考 FBG 的反射波长位置同时对环境温度敏感,从而通过差分的方法去除了环境温度对测量结果的影响,提高了系统的温度稳定性。

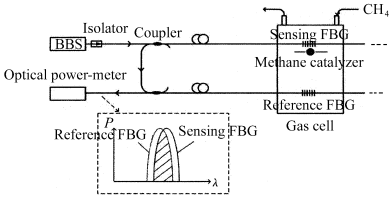


图 1 斜边检测系统的原理示意图

Fig. 1 Schematic diagram of the proposed system

3 系统搭建和实验结果

3.1 FBG 反射波长位置与 CH<sub>4</sub> 浓度的关系

首先运用相位掩模板侧面紫外曝光技术在光敏光纤上制作反射波长为 1550.85 nm 的 FBG,其反射光谱见图 2 插图所示。将该 FBG 与 CH<sub>4</sub> 催化元件封装在特殊设计的机构中,并将封装好的传感头放入 CH<sub>4</sub> 气室。CH<sub>4</sub> 气体与空气分别经过高精度流量计并混合充分后,通入气室,此时气室内 CH<sub>4</sub> 浓度可通过 CH<sub>4</sub> 和空气流量计算获得。

利用光谱分析仪(ANDO AQ6317)获得了 FBG 反射波长位置与 CH<sub>4</sub> 浓度之间的关系,如图 2 所示。FBG 反射波长随着 CH<sub>4</sub> 浓度升高向长波方向漂移,斜率为 0.051 nm/1%。由于光谱分析仪的分辨率为 0.02 nm,故 CH<sub>4</sub> 浓度最小测量值为 0.39%。

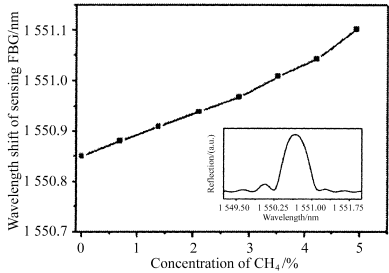


图 2 FBG 反射波长位置随 CH<sub>4</sub> 浓度升高

向长波方向漂移,插图为 FBG 反射光谱

Fig. 2 The reflection spectrum of the sensing FBG shifts towards the longer wavelength as the concentration of the CH<sub>4</sub> in the gas cell increases. Inset shows the reflection spectrum of the sensing FBG

3.2 斜边检测系统的搭建

根据图 1 搭建斜边检测的系统。宽带光源产生的宽谱光经过光隔离器(防止反射光破坏光源)和 1:1 光纤耦合器到达远处检测点的传感 FBG,由传感 FBG 反射的窄带光经另一光纤耦合器进入参考臂,参考臂中的参考 FBG(与传感 FBG 具有相同的反射峰波长)同样放置在检测点的气室中。传感 FBG 的反射光经参考 FBG 再次滤波反射,到达用光电二极管自制的的光功率计处。

实验结果表明,随着气室中 CH<sub>4</sub> 浓度的升高,光功率计接收到的光强逐渐变弱,如图 3 所示。同时,用光谱分析仪对到达光功率计的信号光进行光谱测量,见图 3 插图所示,发现 CH<sub>4</sub> 浓度的上升导致传感 FBG 的中心波长逐渐偏离参考 FBG 的中心波长,因此总的透过光强逐渐变弱。由图 3 数据可得,本系统的最大灵敏度达 0.783 V/1%,最小分辨率经测试达 64 × 10<sup>-6</sup>。同时,对本 CH<sub>4</sub> 浓度传感方案进行了温度稳定性分析。由于传感 FBG 与参考 FBG 放置在同一测量地点,环境温

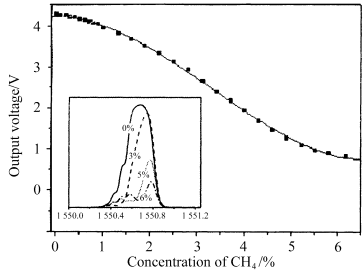


图 3 光功率计输出电压随气室中 CH<sub>4</sub> 浓度增大而减小

Fig. 3 The output of the optical power meter decreases as the concentration of CH<sub>4</sub> in the gas cell increases

度改变时传感 FBG 和参考 FBG 的反射光谱的波长漂移量相同,因此具有很高的温度稳定性。实验中,保持测量点  $\text{CH}_4$  浓度不变,将环境温度由  $30^\circ\text{C}$  上升到  $60^\circ\text{C}$ ,光功率计输出电压不超过  $0.013\%$ 。

#### 4 结 论

综上所述,我们提出的新型  $\text{CH}_4$  浓度传感方案。利用  $\text{CH}_4$  催化元件,环境中的  $\text{CH}_4$  浓度信息被转化为温度信息,从而引起 FBG 反射峰的波长漂移。除了使用 FBG 作为传感头,还引入另一参考 FBG,采用斜边检测的方案,增大了系统的测量分辨率( $0.0064\%$ )。同时利用参考 FBG 对传感 FBG 的温度补偿原理,提高了系统的温度稳定性。并且,本系统还非常适用于远距离测量,利用波分复用方案易于构成分布式传感网络。

#### 参考文献:

- [1] ZHU Zheng-he, LIAO De-lin, LI Wei-cheng, et al. Study of sensitivity and stability of methane carrier catalytic element[J]. Mining Safety & Environmental Protection(矿业安全与环保), 2003, 30(1): 147-148. (in Chinese)
- [2] LU Yu-xiang, LIU Hong-lin. The design and application of methane-concentration detector with multiple function and low consumption [J]. Journal of North University of China(中北大学学报), 2006, 27(3): 268-271. (in Chinese)
- [3] SHAO Jun, LIU Jun-hua, QIAO Xue-guang, et al. A FBG pressure sensor based on bourdon and cantilever beam of uniform strength[J]. Journal of Optoelectronics • Laser(光电子 • 激光), 2006, 17(7): 807-809. (in Chinese)
- [4] WEI Ting, QIAO Xue-guang, JIA Zhen-an, et al. Study of temperature compensated FBG pressure sensor based on widened bandwidth[J]. Journal of Optoelectronics • Laser(光电子 • 激光), 2007, 18(4): 418-421. (in Chinese)
- [5] Lin T K, Lin Y B. Application of FBG sensors to strain and temperature monitoring of full scale prestressed concrete bridges[A]. Optical Fiber Sensors Conference Technical Digest[C], 2002, 1: 211-214.
- [6] Morey W W. Bragg-grating temperature and strain sensors[A]. OFS' 89[C]. 1989, 526.
- [7] Erdogan T. Fiber grating spectra[J]. Journal of Lightwave Technology, 1997, 15(8): 1277-1294.
- [8] Kersey A D, Davis M A, Patrick H J, et al. Fiber grating sensors[J]. Journal of Lightwave Technology, 1997, 15(8): 1442-1463.
- [9] Kersey A D, Berkoff T A. Fiber optic Bragg grating differential temperature sensor[J]. IEEE Photonics Technology Letters, 1992, 4(10): 1183-1185.

#### 作者简介:

周 斌 (1982—), 男, 博士研究生, 主要从事光纤传感等的研究。

# An optical sensing system for the concentration of methane based on fiber Bragg gratings\*

ZHOU Bin<sup>1,2</sup>, LIU Guo-rong<sup>1</sup>, GUAN Zu-guang<sup>1\*\*</sup>, and HE Sai-ling<sup>1</sup>

1. Centre for Optical and Electromagnetic Research, State Key Laboratory for Modern Optical Instrumentation, Zhejiang University, Hangzhou 310058, China

2. Institute of Optics, Zhejiang University, Hangzhou 310058, China

(Received 4 June 2007)

Based on a special catalyst and fiber Bragg gratings (FBGs), an optical sensing system is proposed to measure the concentration of methane. The temperature of the catalyst rises rapidly as the concentration of methane increases, and hence it can be detected by an FBG-type sensor through monitoring the wavelength shift of the reflection spectrum. The experimental results show the good performances of our system, such as the high resolution and temperature stability.

**CLC numbers:** TN253 **Document code:** A **Article ID:** 1673-1905(2007)06-0410-03

**DOI** 10.1007/s11801-007-7065-4

Recently, the accidents happened frequently under Chinese coal mines and people have paid more attention to the safety of coal mines. Since methane is an essential component of the explosion gases in a coal mine, it is very important to develop a sensing system for the coal mine to monitor the concentration of methane accurately, safely and in real-time. The sensor of the conventional technique of measuring the methane concentration is based on a special catalyst. The temperature of the catalyst will increase as the concentration of methane in the air rises and the increased temperature can be detected by a temperature sensitive platinum resistance with a Wheatstone-bridge structure<sup>[1,2]</sup>. The resolution of such a sensor is about 0.01%. However, the performance of this electronic sensor may be degraded by the electromagnetic interference (EMI) from some high-power equipments in the coal mine. On the other hand, it is dangerous to utilize the electric sensors under coal mine since the electronic circuit may produce spark to cause explosion. Except those drawbacks, it is not easy to connect multiple electronic sensors to form a sensing network, which is often required in the coal mine.

Compared with the electronic sensors, optical fiber sensors are immune to the EMI, easier to form a network and more sensitive to the measurands. The fiber Bragg grating (FBG) is very sensitive to stress and temperature<sup>[3,4]</sup>. Based on the wavelength division multiplexing (WDM) technology,

multiple FBGs are easy to form a sensing network, which is widely used in monitoring structure health<sup>[5,6]</sup>.

In this letter, we proposed for the first time to employ FBGs to measure the concentration of methane in the air. Since the reflection spectrum of a FBG shifts towards a longer wavelength as the ambient temperature increases, the concentration of the methane in the air can be detected by monitoring the spectrum of the FBG which is close to the catalyst. In order to reduce the system cost and the crosstalk induced by the variation of the environmental temperature, we employ a reference FBG to interrogate the sensing signal from the sensing FBG with an edge-detection technology. The experimental results show that the resolution of our system is pretty high (a minimal value of 64 ppm can be detected) and the crosstalk induced by the environmental temperature is quite low (the variation of the output voltage is less than 0.52 mV when the temperature in gas cell changes from 30 °C to 60 °C).

The FBG is a periodic perturbation of the refractive index in the fiber core. The mode propagating forward in the fiber core can be coupled into a count-propagating mode by the FBG at a special wavelength position, which can be expressed as<sup>[6]</sup>:

$$\lambda = 2n_{\text{eff}}\Lambda \quad (1)$$

where  $n_{\text{eff}}$  is the effective refractive index of the fiber core, and  $\Lambda$  is the period of the FBG. This wavelength position is proportional to the temperature around the FBG<sup>[7]</sup> and the relationship can be expressed as follows:

$$\Delta\lambda = 2(n_{\text{eff}} \frac{\partial\Lambda}{\partial T} + \Lambda \frac{\partial n_{\text{eff}}}{\partial T})\Delta T \quad (2)$$

\* This work is partially supported by Zhejiang provincial government (under grant No. 2004C31G2010019) and Hangzhou municipal government (under grant No. 20051321B14)

\*\* E-mail: guan.zuguang@coer.zju.edu.cn

Based on this principle, FBG can be used as a temperature sensor.

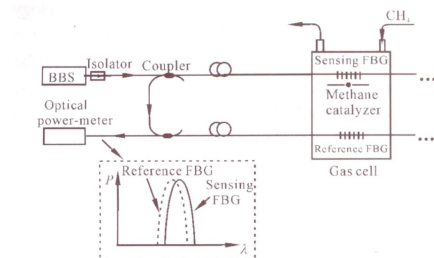


**Fig.1** Schematic diagram of the proposed system. The inset illustrates the sensing principle: the light intensity received by the optical power-meter decreases as the mismatch of the reflection spectra between sensing and reference FBGs increases.

As we described in the introduction, the surface temperature of the catalyst for the methane will increase as the concentration of the methane in the air rises. Through monitoring the shift of the spectrum of the FBG that is fixed close to the catalyst, the concentration of methane can be detected. Although optical spectrum analyzer (OSA), multi-wavelength meter and some other commercial instruments can be used to monitor the reflection spectrum of the sensing FBG, they are not recommended in industrial applications due to their high prices. Instead, we employ a reference FBG to interrogate the sensing signal with an edge-detection technology. As shown in Fig.1, a sensing FBG is fixed close to the methane catalyst in a gas cell while a reference FBG is also located in the cell (but shielded from the catalyst). The reflection spectra of the sensing and reference FBGs are designed to be identical (when there is no methane in the cell) and the measurand-induced spectral mismatch between these two FBGs can reduce the intensity received by the optical power-meter (please see the inset of Fig.1). Since the spectrum of the reference FBG has a narrow bandwidth (less than 0.2 nm), the sensitivity of our scheme is pretty high. The spectrum of the sensing FBG is also influenced by the variation of the environmental temperature. However, in our edge-detection technique, this kind of crosstalk can be eliminated by the same-level shift of the spectrum of the reference FBG located in the same environment.

We fabricated a FBG with a reflection wavelength ( $\lambda$ ) of 1550.85 nm (please see the inset of Fig.2). The sensing FBG and methane catalyst are packaged in a well designed mechanical device which is placed in a gas cell (please see Fig. 3). The concentration of the methane in the gas cell can be

adjusted by controlling the volume of the input methane with a high-precision flow-meter.

The relationship between the reflection wavelength of the sensing FBG and the methane concentration is measured by an OSA (ANDO AQ6317), which is shown in Fig.2. The spectrum of the sensing-FBG shifts towards a longer wavelength as the methane concentration in the gas cell increases and the sensitivity is about 0.051 nm/1%. The resolution of measuring the methane concentration of this scheme is about 0.39%, which is limited by the wavelength-resolution (0.02 nm) of the employed OSA.

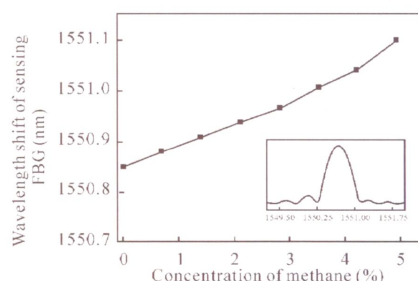


**Fig.2** The reflection spectrum of the sensing FBG shifts towards the longer wavelength as the concentration of the methane in the gas cell increases. The inset shows the reflection spectrum of the sensing FBG

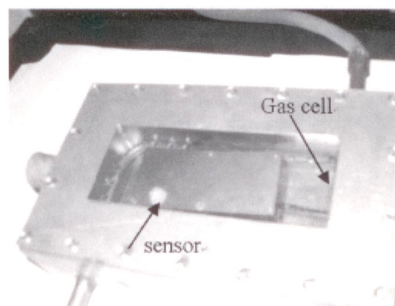


**Fig.3** The picture of the well-packaged methane-sensor (inside the gas cell)

We developed an edge-detection system as shown in Fig. 1. A broadband light passes through an isolator to avoid the reflective light damaging the light source and a fiber coupler, and then is reflected by a sensing FBG close to a methane catalyst. The reflected light with a narrow-band spectrum will pass through another fiber coupler and meet a reference FBG

with a spectrum well-matched to that of the sensing FBG. Finally, a photodiode is used to detect the intensity of the double-reflected light. As the concentration of the methane in the gas cell increases, the temperature around the catalyst rises and leads to a mismatch between the spectra of the sensing and reference FBG. Consequently, the light intensity received by the photodiode decreases. Since the reference FBG is located close to the sensing FBG (but shielded from the catalyst), our system is sensitive to the methane concentration but insensitive to the variation of the environmental temperature. The sensitivity of this system is 0.783 V/1% and the resolution can be as high as 64 ppm (which is 60 times higher than the resolution achieved by using an OSA).

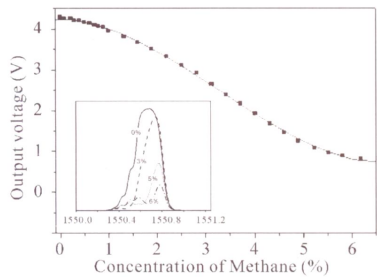


**Fig.4 The output of the optical power meter decreases as the concentration of methane in the gas cell increases. The inset shows the evolution of the spectra (of the light received by the power meter) when concentration of methane is 0%, 3%, 5%, and 6%.**

The variation of the output voltage is less than 0.52 mV when the temperature in the gas cell changes from 30°C to 60°C.

A novel methane concentration measurement technology based on a pair of FBGs is proposed. A methane catalyst is employed to transduce the concentration of methane into the temperature information, which can induce the shift of the spectrum of a sensing FBG. By employing another FBG as a reference, an edge-detection system is set up to improve the resolution of our sensing system. In the meanwhile, the crosstalk induced by the variation of the environmental temperature is also reduced by this technique.

References

[1] ZHU Zheng-he, LIAO De-lin, and LI Wei-cheng, Mining Safety & Environmental Protection, **30** (2003), 147. (in Chinese)  
[2] LV Yu-xiang, and LIU Hong-lin, Journal of North University of China, **27** (2006), 268. (in Chinese)  
[3] WANG Hong-liang, QIAO Xue-guang, and FU Hai-wei, Journal of Optoelectronics-Laser, **16** (2005), 259. (in Chinese)  
[4] ZHANG Xiao-jing, WU Zhan-jun, and ZHANG Bo-ming, Journal of Optoelectronics-Laser, **16** (2005), 566. (in Chinese)  
[5] T.-K. Lin, Y.-B. Lin, Optical Fiber Sensors Conference Technical Digest. Portland: [s.n.], **1** (2002), 211.  
[6] W. W. Morey, Proc. OFS'89. Paris, France: [s.n.], (1989) 526.  
[7] T. Erdogan, Journal of Lightwave Technology, **15** (1997), 1277  
[8] A. D. Kersey, M. A. Davis, and H. J. Patrick, Journal of Lightwave Technology, **15** (1997), 1442.  
[9] A. D. Kersey, and T. A. Berkoﬀ. IEEE Photonics Technology Letters, **4** (1992), 1183.

## PAPER XIII

**Coherence multiplexing of distributed sensors  
based on pairs of fiber Bragg gratings of low  
reflectivity**

Z.G. Guan, D. Chen, S. He.

*Journal of Lightwave Technology* **25**, 2143 - 2148 (2007).





# Coherence Multiplexing of Distributed Sensors Based on Pairs of Fiber Bragg Gratings of Low Reflectivity

Zu-Guang Guan, *Student Member, OSA*, Daru Chen, and Sailing He, *Senior Member, IEEE*

**Abstract**—A coherence multiplexing scheme for distributed sensors based on fiber Bragg grating (FBG) pairs is introduced. Each pair of identical FBGs forms a Fabry–Pérot (FP) interferometer (FPI) and induces an additional optical path difference (OPD) that is proportional to the center-to-center interval between the two FBGs (one for sensing and the other for reference). The interference intensity reaches its maximum when the FPI-induced OPD is compensated by scanning one arm of a Michelson interferometer to a certain position. The variation of the measurand induces a mismatch between the central reflection wavelengths of two FBGs and consequently reduces interference intensity. To separate the interferometric signals for demultiplexing, the intervals between the two FBGs are preset to different values for different sensors. In order to improve the multiplexing ability of the system and reduce the crosstalk among the sensors, we use gratings of low reflectivity. Temperature sensing is demonstrated to show the high sensitivity ( $-1.92\%/^{\circ}\text{C}$ ) and low crosstalk of our distributed sensing system.

**Index Terms**—Coherence multiplexing, distributed sensors, fiber Bragg grating pair (FBGP), interference intensity, interferogram, scanning Michelson interferometer (MI).

## I. INTRODUCTION

FIBER BRAGG gratings (FBGs) play an important role in fiber-optic sensing because of their intrinsic nature and advantages such as wavelength-encoded operation [1]–[5]. With the development of some multiplexing techniques, including wavelength division multiplexing (WDM) and time division multiplexing (TDM), the FBG array has also been widely utilized recently in fiber-optic distributed sensing such as structural health monitoring. The WDM technique requires each FBG sensor to operate at a different peak reflection wavelength, and hence, a broadband light source is necessary. In addition, some special wavelength-sensitive devices (such as a tunable Fabry–Pérot (FP) filter [2], a Fourier transform spectrometer [3], or a wavelength division coupler [4]) are needed in analyzing the sensing signals. In the TDM technique [5], the optical input is typically pulsed, and each FBG sensor at a different sensing location will reflect a pulsed signal with different time delays, which will be demultiplexed by a high-speed switching gate at the central processing office.

Coherence multiplexing is a different technique that can multiplex many sensors to a single optical signal, without requiring relatively complex time or wavelength multiplexing. By arranging the geometry of each sensor (usually an interferometer), the optical path differences (OPDs) induced by different remote sensing interferometers are in different ranges so that the multiplexed signals can be demultiplexed by a local scanning interferometer. Recently, such technique has widely been applied in fiber-optical distributed sensing [6]–[10].

In this paper, we propose, for the first time (to the best of our knowledge), a coherence multiplexing system using many pairs of FBGs (i.e., replacing each sensing interferometer mentioned above with a pair of FBGs), as shown in Fig. 1. A pair of identical FBGs with low reflectivity forms an in-fiber FP interferometer (FPI), and the OPD induced by the sensing FPI is a product of the effective index and two times of the center-to-center grating interval (here, only the first round trip of light propagation is considered due to the low reflectivity of the FBGs). When the OPD induced by the FPI is compensated by a scanning Michelson interferometer (MI), interference between the light fields reflected by the first and second FBGs will produce an interferogram. By arranging the grating intervals of different FBG pairs (FBGPs) at different ranges (each range should be wide enough to avoid overlapping between the adjacent interferograms), the interferograms corresponding to different sensing FBGPs can be distinguished in one scan of the MI. In each FBGP, one FBG is shielded from the measurand, as the reference and the other FBG are exposed to the measurand for sensing. The interference intensity (i.e., the maximal value of the envelope of the interferogram) will decrease as the mismatch between the central reflection wavelengths of the two FBGs increases [see Fig. 4 and Fig. 1(b)]. One advantage of the present sensing system is that neither broadband nor narrow-pulsed light source is needed. All the FBGs used in this system can be identical, and this can significantly reduce the manufacture complexity. Besides those, the cost of our system can be much cheaper than a WDM or a TDM system since the interrogation device is simply based on a mechanical scan.

## II. THEORY

Based on the general principle describing the optical low-coherence reflectometry (OLCR) [11], we develop a theoretical model to explain the sensing mechanism of the present system shown in Fig. 1. The spectral filtering effect should also be considered in our model since an FBG is a wavelength-dependent device. In a conventional OLCR, the sample to be measured is placed at one arm of the MI. However, the

Manuscript received July 26, 2006; revised May 15, 2007. This work was supported in part by the Zhejiang Provincial Government under Grant 2007C21159 and in part by the Hangzhou Municipal Government under Grant 20051321B14.

The authors are with the Centre for Optical and Electromagnetic Research and the Joint Research Center of Photonics (JORCEP), Zhejiang University, Hangzhou 310058, China (e-mail: guanzuguang@coer.zju.edu.cn; daru@coer.zju.edu.cn; sailing@kth.se).

Digital Object Identifier 10.1109/JLT.2007.901330

0733-8724/\$25.00 © 2007 IEEE

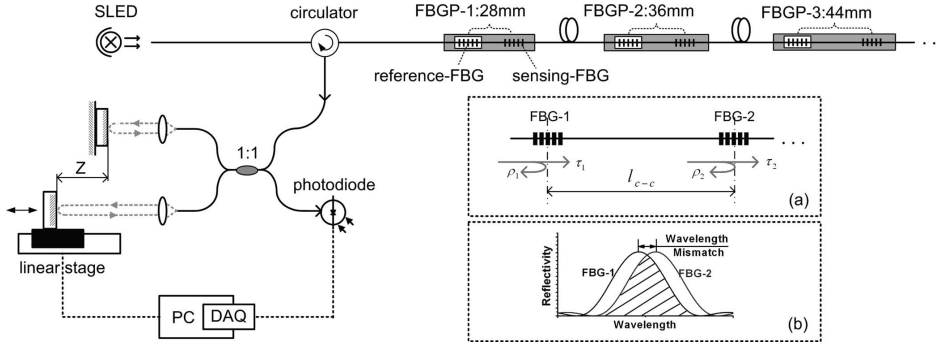


Fig. 1. Schematic diagram of the present coherence multiplexing system for FBGP sensors. The insets show the sensing mechanism of the presented system. (a) FP interferometer formed by a pair of FBGs. (b) Mismatch between reflectance spectra of the two FBGs induced by some measurands.

sample/measurand in the present sensing system is actually related to an FBGP-formed FPI (not in any arm of the MI), which induces an additional OPD to the input light entering the MI. When the FPI-induced OPD is compensated by the MI and the remaining OPD is within the coherence length of the light, the interference occurs between the light fields reflected by FBG-1 and FBG-2. We are not interested on the variation of the OPD induced by each sensing element, as in most systems of coherence multiplexed sensors [7], [8], but on the variation of the interference intensity induced by the mismatch between the reflectance spectra of two FBGs.

Let  $E_0(\omega)$  denote the field of the input light source. We can approximate the field reflected from the FPI as (here, only one reflection from each FBG is considered due to a low reflectivity of the FBGs)

$$E_1(\omega) \cong (\rho_1(\omega) + \tau_1^2(\omega)\rho_2(\omega) \exp(-i\Delta\phi)) E_0(\omega) \quad (1)$$

where  $\rho_1(\omega)$  and  $\rho_2(\omega)$  are the reflection coefficients of FBG-1 and FBG-2, respectively, and  $\tau_1(\omega)$  is the transmission coefficient of FBG-1. The detailed expressions for these reflection/transmission coefficients can be found in [12]. The additional phase difference  $\Delta\phi$  induced by one round trip of OPD inside the FBGP can be expressed as

$$\Delta\phi = \frac{2n_{\text{eff}}l_{c-c}}{c}\omega \quad (2)$$

where  $l_{c-c}$  is the center-to-center interval between two FBGs,  $n_{\text{eff}}$  is the effective index of the fiber for the guided fundamental mode, and  $c$  is the speed of light in a vacuum.

The field then enters a scanning MI, as shown in Fig. 1. By neglecting the wavelength-dependence of the fiber coupler (with a coupling ratio of 1:1), the field at the detector can be given by

$$E_2(\omega) = \frac{1}{2} (1 + \exp(-i\Delta\phi)) E_1(\omega) \quad (3)$$

where  $\Delta\phi$  (the phase difference induced by the unbalanced MI) can be expressed as

$$\Delta\phi = 2z\omega/c \quad (4)$$

where coordinate  $z$  is the relative position (with respect to the reference mirror) of the translating mirror.

Therefore, the light intensity received by the detector can be written as

$$I(z) \propto \frac{1}{2\pi} \Re \left\{ \int_{-\infty}^{+\infty} E_2^*(\omega) E_2(\omega) d\omega \right\} \quad (5)$$

where  $\Re$  denotes the real part. By considering only the terms dependent on  $(\Delta\phi - \Delta\phi)$ , i.e., oscillating parts, the above equation can be simplified as

$$I(z) \propto \frac{1}{4\pi} \Re \left\{ \int_{-\infty}^{+\infty} [\tau_1^*(\omega)]^2 \rho_1(\omega) \rho_2^*(\omega) |E_0(\omega)|^2 \times \exp \left[ -i \left( \frac{2\omega}{c} \cdot z - \Delta\phi \right) \right] d\omega \right\}. \quad (6)$$

From (6), one can find that the interference intensity (i.e., the maximal value of the interference envelope) is roughly proportional to the overlap integral of  $\rho_1(\omega)$  and  $\rho_2^*(\omega)$ . This indicates that the mismatch of the central reflection wavelengths of the two FBGs, which is caused by the variation of the sample/measurand, will reduce quickly the interference intensity since the slopes of  $|\rho_1(\omega)|$  and  $|\rho_2(\omega)|$  are quite sharp [see the overlap of the two reflection spectra in Fig. 1(b)].

From (2), (4), and (6), one can deduce that the interference pattern is a cosine oscillation with a Gauss-like envelope. The shape of the envelope is related to the reflectance spectra of the FBGs and their overlapping degree. The maximal interference intensity occurs at  $z \cong n_{\text{eff}}l_{c-c}$ . The FBGP-induced OPD is totally compensated by the MI at this position. The whole envelope occupies a range around  $|z - n_{\text{eff}}l_{c-c}| \leq l_{\text{co}}/4$ , where

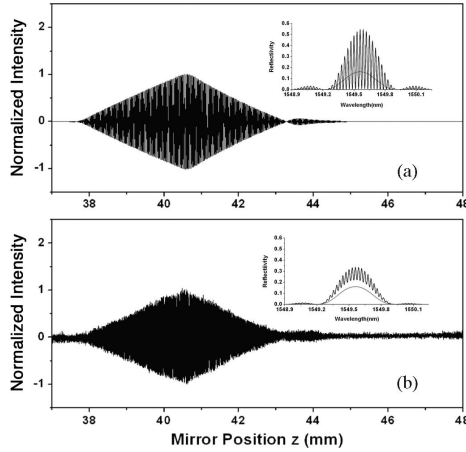


Fig. 2. Comparison of the (a) simulated and (b) measured ac part of the interferograms of an FBGP. The insets show the simulated and measured reflectance spectra of a (smooth gray curve) single FBG and (rapidly oscillating black line) FBGP.

$l_{co}$  is the coherence length of the reflective light (inversely proportional to the bandwidth of the reflectance spectrum). This indicates that the interference signal, including the sensing information of the corresponding FBGP, can be obtained when the mismatch between the OPDs of the FBGP and the MI is within  $l_{co}/2$ . Otherwise, when the OPD mismatch is larger than  $l_{co}/2$ , the interference intensity approaches to zero. If the center-to-center intervals of different FBGPs are preset to different values and the minimal difference of these intervals is larger than  $l_{co}/2n_{eff}$ , the interferograms of the FBGPs can be distinguished (i.e., the crosstalk of the signals from different FBGP sensors can be avoided) by scanning position  $z$  (for one of the mirrors).

### III. SIMULATED AND EXPERIMENTAL RESULTS

In order to verify the theoretical model developed in the previous section, we present in this section both numerical simulation and experimental results on some interferograms.

Fig. 2(a) shows a simulated interferogram [i.e., the oscillating part described in (6)] based on the theory in Section II. The parameters of the FBGP used in the simulation are 535 nm for the grating period, 2 mm for the grating length,  $1.15 \times 10^{-4}$  for the dc index change,  $0.90 \times 10^{-4}$  for the ac index change, and 28 mm for the center-to-center interval of the two gratings. The effective index of the fundamental guided mode of the fiber is 1.448. For simplicity, the light-source spectrum is assumed to be constant. From Fig. 2(a), one can see that an interferogram occurs when the mirror position  $z$  is around 40.5 mm. This indicates that the OPD of the FBGP ( $2n_{eff}l_{c-c}$ ) is about 81 mm ( $2z$ ). The inset of Fig. 2(a) shows the simulated reflectance spectra of a single FBG (the smooth curve) and the FBGP (the rapidly oscillating curve).

The FBGP is fabricated on a commercial photosensitive fiber (Fibercore Ltd., U.K.;  $n_{eff} = 1.448$ ) with a side-exposure technique. The phase mask, with a pitch of 1070.6 nm, is used to achieve a grating period of 535.3 nm. The grating length (2 mm) is controlled by an optical slot, and a high-accuracy linear stage is used to fix the exposure positions of two FBGs with an interval of 28 mm. Index modulation can be tailored by adjusting the total number of laser pulses. The measured reflectance spectra of a single FBG and the FBGP are shown in the inset of Fig. 2(b). By comparing the insets of Fig. 2(a) and (b), one can see that the measured spectrum of the FBG and the fringe spacing in the measured spectrum of the FBGP agree well with the corresponding simulated results. The fringes in the measured spectrum are not as sharp as those in the simulated spectrum since the resolution of the measurement is limited by our optical spectrum analyzer.

We have set up a coherence interrogation system with a computer-controlled scanning MI (see Fig. 1). The light source used here is a superluminescent light emitting diode (SLED) with a central wavelength around 1550 nm and a bandwidth of about 80 nm. The bandwidth of the source in our system is only required to cover the spectral bandwidth ( $\sim 1$  nm) of the FBG; the broadband light source is used here simply because of its availability in our laboratory. The reflective light from the FBGP then enters a scanning MI through a circulator. The MI is composed of a fiber coupler, two collimators, a fixed mirror, and a translating mirror mounted on a computer-controlled linear stage. Light intensity is converted into an electrical signal using a photodiode, which is then sent to a Data Acquisition (DAQ) system installed in a computer. We scanned the mirror with a stable speed of 1 mm/s and acquired the signal with a sampling rate of 1 kHz. The interferogram is obtained at a mirror position ( $z$ ) of around 40.5 mm, and the oscillating part of the interferogram is subtracted using a high-pass filter (or removing the dc part of the data with a simple computer code), which is shown in Fig. 2(b). By comparing Fig. 2(a) and (b), one can see that the measured interferogram agrees well with the simulated interferogram (even the small side lobe at the right side of the main interferogram).

Figs. 3 and 4 show both the simulation and experimental results for the interference evolution induced by the mismatch between the central reflection wavelengths of two FBGs. The measured and simulated interferograms, corresponding to wavelength mismatches of 0, 0.2, 0.35, and 0.55 nm, are shown in Fig. 3, from which one can see that the interference intensity decreases rapidly as the mismatch between the central reflection wavelengths increases. The appearance of the double or triple peaks for the wavelength mismatches of 0.35 and 0.55 nm may be due to the involvement of some side lobes of the spectrum in the interference. Each point of the interference intensity (before normalization) is obtained from the measured interferogram (see Fig. 3) by taking the corresponding peak value of the envelope (see Fig. 5) of the oscillating part (see inset of Fig. 5). The interference intensity is then normalized (with the value corresponding to the case when the central reflection wavelengths of the two FBGs are matched), which is shown in Fig. 4, from which one sees that the sensitivity of the present sensing system is pretty high ( $-12.5\%/0.1$  nm).

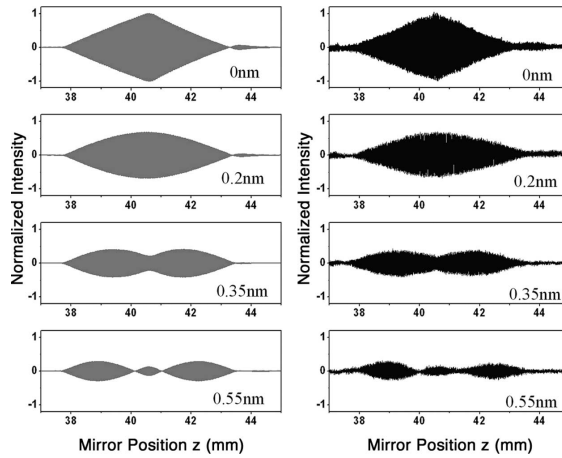


Fig. 3. (Gray line) Simulated and (dark line) measured evolutions of the interferograms when the mismatch of the central reflection wavelength of the two FBGs is 0 (matched case), 0.2, 0.35, or 0.55 nm.

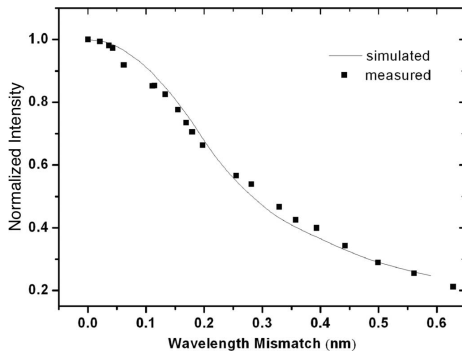


Fig. 4. Dependence of the simulated and measured interference intensity on the mismatch of the central reflection wavelength of the two FBGs.

#### IV. MULTIPLEXING OF DISTRIBUTED FBGP SENSORS

To demonstrate the multiplexing of the present distributed sensing system, we fabricated two other FBGPs (LPGP-2 and LPGP-3) with different grating intervals (36 and 44 mm, respectively) using the same technique described in Section III. The center-to-center interval of the two gratings in LPGP-1 is 28 mm. All the gratings in these three FBGPs are identical and with a reflectivity of about 15%. The reflectivity should be lower if more sensors are to be multiplexed. The three FBGPs are connected in series with delay lines (to avoid the interference between different FBGPs), as shown in Fig. 1. Within one scan of the mirror in the MI, the interferograms of the three FBGPs are obtained, and they are well separated from each other (as shown in the inset of Fig. 5). The envelope of the oscillating part of the interferograms is obtained and shown in

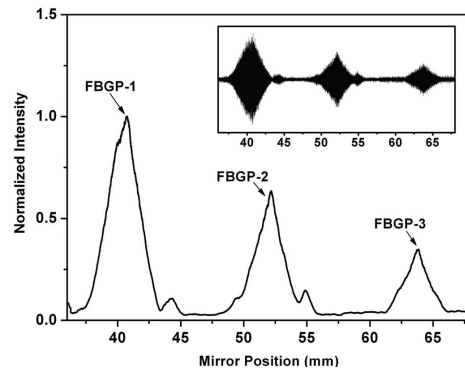


Fig. 5. Well-separated signals of the three FBGPs. The inset shows the original interferograms.

Fig. 5. One can see three peaks of the envelope at around 40.5, 52.1, and 63.7 mm, which agree well with the theoretical analysis in Section II. The maximal interference intensity occurs at  $z \cong n_{\text{eff}} l_{c-c}$  for each FBGP. The peak intensity decreases due to the optical loss induced by a  $\sim 15\%$  reflection in each preceding grating.

To test the performance of our sensing system in terms of sensitivity and crosstalk, some experiments on temperature sensing are carried out here. In each FBGP, one of the FBGs is shielded from the measurand (as the reference), and the other is exposed to the measurand for sensing, which is the local temperature for this example. Obviously, the measurand will induce some mismatch between the central reflection wavelengths of two FBGs in the FBGP. The wavelength mismatch

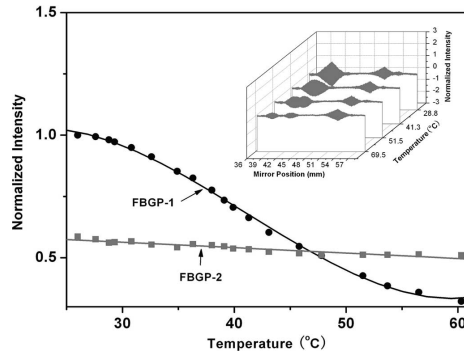


Fig. 6. Interference intensities for FBGP-1 (in an increasing local temperature; circle marks fit with a dark line) and FBGP-2 (kept in a constant-temperature environment; rectangle marks fit with a gray line). The inset shows the evolution of the interferograms for these two FBGPs.

can be detected by monitoring the corresponding interference intensity (i.e., the maximal value of the interference envelope), as we have discussed before. We increase the local temperature of the sensing FBG in FBGP-1 while keeping the reference FBG shielded from any temperature variation. From Fig. 6, one sees that the interference intensity of FBGP-1 decreases as the local temperature increases, and sensitivity can be as high as  $-1.92\%/^{\circ}\text{C}$ . A small change in temperature (less than  $0.1^{\circ}\text{C}$ ) can be determined over a range of  $35^{\circ}\text{C}$ . For comparison, the temperature around FBGP-2 (i.e., around both the sensing and reference FBGs) remains unchanged. The interference intensity of FBGP-2 is relatively kept stable (see Fig. 6). The slow decrease of the intensity is due to the shift of the spectrum of the sensing FBG in FBGP-1 as the surrounding temperature increases from  $25^{\circ}\text{C}$  to  $60^{\circ}\text{C}$ . The slope of a crosstalk-induced decrease is less than  $0.23\%/^{\circ}\text{C}$  (which can be reduced further if gratings of lower reflectivity are employed). The above experimental results indicate that our sensing system can be employed to demultiplex distributed FBGP sensors with high sensitivity and low crosstalk.

## V. DISCUSSION

Obviously, the maximal number of distributed FBGP sensors is  $2n_{\text{eff}}[\max\{l_{\text{c-c}}\} - \min\{l_{\text{c-c}}\}]/l_{\text{co}}$ , where  $\max\{l_{\text{c-c}}\}$  and  $\min\{l_{\text{c-c}}\}$  are the longest and shortest  $l_{\text{c-c}}$  of the FBGPs to be demultiplexed, respectively.  $\max\{l_{\text{c-c}}\}$  should not be larger than  $2 \times \min\{l_{\text{c-c}}\}$ ; otherwise, the interferogram of the shortest FBGP, corresponding to two round trips of OPD, will overlap with the interferogram of the longest FBGP, corresponding to one round trip of OPD. Therefore, the maximal number of distributed FBGP sensors is  $2n_{\text{eff}} \min\{l_{\text{c-c}}\}/l_{\text{co}}$ . Several tens of sensors can be multiplexed in our system since  $\min\{l_{\text{c-c}}\}$  is in the order of centimeters, while  $l_{\text{co}}$  is in the order of millimeters. If more sensors are to be multiplexed, one can increase  $\min\{l_{\text{c-c}}\}$  or decrease  $l_{\text{co}}$ . As mentioned before, the coherence length  $l_{\text{co}}$  is inversely proportional to the bandwidth

of the reflectance spectrum. Thus, we can also design an FBG with a wider reflection bandwidth (through, e.g., chirped gratings) to reduce the coherence length  $l_{\text{co}}$  and consequently increase the total number of sensing elements to be multiplexed. However, on the other hand, too wide bandwidth will degrade the sensitivity of the present FBGP sensor.

Another factor that limits the multiplexing ability of our system is the optical loss induced in each sensor. The interference visibility of the last sensor will be influenced by the reflections of the preceding sensors. From Fig. 5, we can clearly see that the signal-to-noise ratio of the interferogram corresponding to the last sensor is more worse than that corresponding to the first one. Therefore, one should use gratings of low reflectivity if many sensors are to be multiplexed in the present system. In addition, the low reflection in each sensing FBG can also minimize the crosstalk among the sensors in series. By considering the sensitivity of the photodiode, a reflectivity of  $2\%$ – $3\%$  for each grating is enough. This is also the standard value for the reflective devices used in a conventional coherence multiplexing sensing system [10].

Compared with the light source used in a WDM or TDM system for distributed FBG sensors, a cheaper CW light source with a bandwidth of about  $1\text{ nm}$  (typical bandwidth of a diode or fiber laser) can be used in our coherence multiplexing system. Although the proposed sensing system requires twice more gratings than a conventional system, the fabrication cost is reduced since the gratings used are identical and can be fabricated simply with a single phase mask. Our coherence multiplexing system is quite different from a conventional one, in which only the variation of the OPD (i.e., the peak position of the interferogram) is measured for each sensing interferometer. In our system, the variation of the measurand induces a mismatch between the central reflection wavelengths of the sensing and reference FBGs in an FBGP and consequently reduces the corresponding interference intensity (i.e., the peak value of the interferogram). Each sensor in our system is pretty sensitive to the variation of the measurand since the slopes of the reflectance spectra for the two FBGs are quite sharp; thus, their overlap is quite sensitive to any relative shift of the central reflection wavelengths for the two FBGs. Besides sensitivity, the stability of our system should also be considered. One can make the spectra of the grating pair in each sensor stable over a long time using, e.g., the annealing processing and mechanical package.

## VI. CONCLUSION

We have proposed a coherence multiplexing system for distributed FBGP sensors for the first time (to the best of our knowledge). As an example, a sensing system of three distributed FBGPs (with different grating intervals) has been demonstrated to show its good performance in sensing temperature (a high sensitivity of  $-1.92\%/^{\circ}\text{C}$  has been achieved).

## ACKNOWLEDGMENT

The authors would like to thank Dr. A. P. Zhang and B. Zhou for their helpful discussion.

## REFERENCES

- [1] A. D. Kersey, M. A. Davis, H. J. Patrick, M. LeBlanc, and K. P. Koo, "Fiber grating sensors," *J. Lightw. Technol.*, vol. 15, no. 8, pp. 1442–1463, Aug. 1997.
- [2] A. D. Kersey, T. A. Berkoff, and W. W. Morey, "Multiplexed fiber Bragg grating strain-sensor system with a fiber Fabry-Pérot wavelength filter," *Opt. Lett.*, vol. 18, no. 16, pp. 1370–1372, Aug. 1993.
- [3] M. A. Davis and A. D. Kersey, "Application of a fiber Fourier transform spectrometer to the detection of wavelength-encoded signals from Bragg grating sensors," *J. Lightw. Technol.*, vol. 13, no. 7, pp. 1289–1295, Jul. 1995.
- [4] M. A. Davis and A. D. Kersey, "All-fiber Bragg grating strain-sensors demodulation technique using a wavelength division coupler," *Electron. Lett.*, vol. 30, no. 1, pp. 75–76, Jan. 1994.
- [5] R. S. Weis, A. D. Kersey, and T. A. Berkoff, "A four-element fiber grating sensor array with phase-sensitive detection," *IEEE Photon. Technol. Lett.*, vol. 6, no. 12, pp. 1469–1471, Dec. 1994.
- [6] J. L. Brooks, R. H. Wentworth, R. C. Youngquist, M. Tur, B. Y. Kim, and H. J. Shaw, "Coherence multiplexing of fiber-optic interferometric sensors," *J. Lightw. Technol.*, vol. LT-3, no. 5, pp. 1062–1072, Oct. 1985.
- [7] W. V. Sorin and D. M. Baney, "Multiplexed sensing using optical low-coherence reflectometry," *IEEE Photon. Technol. Lett.*, vol. 7, no. 8, pp. 917–919, Aug. 1995.
- [8] L. Yuan and J. Yang, "Two-loop-based low-coherence multiplexing fiber-optic sensor network with a Michelson optical path demodulator," *Opt. Lett.*, vol. 30, no. 6, pp. 601–603, Mar. 2005.
- [9] Z. G. Guan, A. P. Zhang, M. Jiang, and S. He, "Low-coherence interrogation scheme for multiplexed sensors based on long-period-grating Mach-Zehnder interferometers," *IEEE Photon. Technol. Lett.*, vol. 18, no. 7, pp. 832–834, Apr. 2006.
- [10] Z. G. Guan, B. Zhou, G. Liu, and S. He, "Quasi-distributed absorption sensing system based on a coherent multiplexing technique," *IEEE Photon. Technol. Lett.*, vol. 19, no. 10, pp. 792–794, May 2007.
- [11] U. Wiedmann, P. Gallion, and G. H. Duan, "A generalized approach to optical low-coherence reflectometry including spectral filtering effects," *J. Lightw. Technol.*, vol. 16, no. 7, pp. 1343–1347, Jul. 1998.
- [12] T. Erdogan, "Fiber grating spectra," *J. Lightw. Technol.*, vol. 15, no. 8, pp. 1277–1294, Aug. 1997.



**Zu-Guang Guan** was born in Zhejiang, China, in 1981. He received the B.S. degree in optical engineering (with honors) from Zhejiang University, Hangzhou, China, in 2004. He is currently working toward the Ph.D. degree at the Center for Optical and Electromagnetic Research, Zhejiang University.

His main research interests include multiplexed fiber-optic sensor systems and fiber-grating devices.



**Daru Chen** was born in Wenzhou, China, in 1982. He received the B.S. degree from Zhejiang University, Hangzhou, China, in 2004. He is currently working toward the Ph.D. degree at the Center for Optical and Electromagnetic Research, Zhejiang University.

His current research interests include fiber lasers, optical fiber amplifiers, and fiber sensors.



**Sailing He** (M'92–SM'98) received the Licentiate of Technology and Ph.D. degrees from the Royal Institute of Technology, Stockholm, Sweden, in 1991 and 1992, respectively.

After receiving the Ph.D. degree, he worked at the Royal Institute of Technology as an Assistant Professor, as an Associate Professor, and as a Full Professor. He has been with Zhejiang University, Hangzhou, China, since the time he was appointed by the Ministry of Education of China. He has first-authored one monograph (Oxford University Press) and authored/coauthored over 200 papers in refereed international journals. His current research interests include photonic integration, fiber optical communication, and optical sensing technologies.